JOURNAL OF THE
AEROSPACE SCIENCES

VOLUME 28 FEBRUARY, 1961 NUMBER 2

FEB 16 1961 LIBRARY
PURDUE UNIVERSITY FEB 14 1961 LIBRARY

CONTENTS

The Role of Entropy in the Aerospace Sciences (Daniel and Florence Guggenheim Memorial Lecture) ..... JAKOB ACKERET 81

Radiation From Hot Air and Its Effect on Stagnation-Point Heating ... BENNETT KIVEL 96

Solution of Subsonic Nonplanar Lifting Surface Problems by Means of High-Speed Digital Computers ..... L. J. KULAKOWSKI AND R. N. HASKELL 103

The Supersonic Boom of a Projectile Related to Drag and Volume ..... I. L. RYHMING 113

An Analytic Extension of the Shock-Expansion Method ..... GEORGE D. WALDMAN AND RONALD F. PROBSTEIN 119

The Dynamics of Rolling Aircraft ..... F. W. NIEDENFUHR 133

Plasma Flow Over a Thin Charged Conductor ..... HIDEO YOSHIHARA 141

High-Speed Viscous Corner Flow ..... MARTIN H. BLOOM AND STANLEY RUBIN 145

Readers' Forum 158

Published by
INSTITUTE OF THE AEROSPACE SCIENCES, INC.

JOURNAL OF THE AEROSPACE SCIENCES

Editor: W. R. SEARS
Director, Graduate School of Aeronautical Engineering, Cornell University

Associate Editor: ROBERT R. DEXTER *Managing Editor:* RITA J. TURINO

Editorial Assistant: CHARLOTTE C. ROBB

IAS Aerospace Technology Panels

Paul J. Burr, Technical Services Director, Coordinator

The members of the IAS Aerospace Technology Panels shown here are to be available, collectively or as individuals, to assist and advise IAS committees, Sections, and staff members as to currently interesting and important technical topics related to their specialties and as to people most qualified to speak or write on such topics. The panels will also stimulate thought and scientific papers of potential value for the future, and they should be sensitive to technical activity of other professional groups, seeking through joint action the enlightenment of all having professional aerospace interests. Panel chairmen are indicated with an asterisk (*).

Aerodynamics and Fluid Mechanics

Lester Lees*
Dean R. Chapman
Antonio Ferri
Paul Germain
Wayland C. Griffith
Hans W. Liepmann
C. C. Lin
W. R. Sears
John R. Sellars
R. T. Whitcomb
Hideo Yoshihara

Aeroelasticity

R. L. Bisplinghoff*
Y. C. Fung
I. E. Garrick
Martin Goland
Kurt H. Hohenemser
J. C. Houbolt
W. P. Jones
W. J. Mykytow
Robert F. Speaker

Biomedical Sciences

Brig. Gen. D. Flickinger, USAF*
W. Ross Adey
Capt. Wm. Augerson, USA
Hilding Bjurstedt
Stuart Bondurant
A. Scott Crossfield
Cdr. J. H. Ebersole, USN
W. R. Lovelace, II
Capt. Bruce Pinc, USAF
Stanley Roscoe

Communication

P. C. Sandretto*
James M. Bridges
Leonard Jaffe
David S. Little
Cdr. D. O. Mann, USN
William Sen
Arnold Shostack
Teck A. Wilson

Control, Guidance, and Navigation

C. S. Draper*
R. C. Berendsen
B. Paul Blasingame
Robert N. Brown
S. F. Eyestone
Percy Halpert
B. J. O'Connor
S. F. Schmidt
O. Hugo Schuck
H. Philip Whitaker

Energy Conversion

David Altman*
Robert Bromberg
M. U. Clauser
J. Preston Layton
Frank Marble
G. H. Markstein
A. M. Rothrock
Milton M. Slawsky
Martin Summerfield
T. Y. Toong

Flight Mechanics

H. J. Kelley*
Malcolm J. Abzug
H. Julian Allen
A. E. Bryson, Jr.
T. N. Edelbaum
William C. House
Angelo Miele
John D. Nicolaides
Charles B. Westbrook

Instrumentation

R. H. Tripp*
Paul F. Bechberger
J. M. Hungerford
Mac Lowy
Walter McKay
M. David Prince
Charles P. Sonett
George I. Toumanoff
William A. Wildhack

Meteorology

Thomas F. Malone*
Robert D. Fletcher
Henry T. Harrison
Joseph Kaplan
D. S. Perkins
Herbert Riehl
Morris Tepper
Harry Wexler

Nuclear Applications

J. Donald Rauth*
Jack L. Armstrong
Robert W. Bussard
H. M. Dieckamp
Capt. R. L. Duncan, USN
Harold B. Finger
Donald J. Keirn
Frank E. Rom
Raymer E. Schreiber
D. Roy Shoults
T. B. Taylor

Operations

Benjamin S. Kelsey*
Maj. Gen. Otis Benson, USAF (MC)
Ernest A. Cutrell
Capt. E. E. Fawkes, USN
Melvin N. Gough
Franklin W. Kolk
Col. J. L. Marinelli, USA
Richard V. Rhode
W. E. Rhodes
M. B. Spaulding, Jr.
Ernest G. Stout
Maj. Gen. D. Yates, USAF

Propulsion Systems

Bruce T. Lundin*
Robert H. Boden
George W. Brady
David Cochran
Elliot Mitchell
Perry W. Pratt
C. C. Ross
John G. Wilder, Jr.
Maurice J. Zucrow

Space Physics

H. G. Stever*
John C. Evvard
Herbert Friedmann
Leo Goldberg
C. F. Hansen
Arthur Kantrowitz
Bruno Rossi
S. F. Singer
Leo Steg
Fred L. Whipple

Structures and Materials

Nicholas J. Hoff*
Samuel B. Batdorf
Bruno A. Boley
Pol Duwez
R. R. Heldenfels
Samuel Levy
George N. Mangurian
S. S. Manson
Nathan E. Promisel
Ernest E. Sechler

Vehicle Design

C. E. Pappas*
Ralph Alex
C. H. Christenson
A. J. Eggers, Jr.
E. V. Marshall
Rene H. Miller
John R. Ragazzini
George S. Trimble, Jr.

SUBSCRIPTION RATES

JOURNAL OF THE AEROSPACE SCIENCES, Published Monthly. United States and Possessions: 1 Year, $15.00; Single Copies, $1.50. Foreign Countries Including Canada (American Currency Rates): 1 Year, $16.00; Single Copies, $1.50.

AEROSPACE ENGINEERING, Published Monthly. United States and Possessions: 1 Year, $5.00; Single Copies, $0.50. Foreign Countries Including Canada (American Currency Rates): 1 Year, $6.00; Single Copies, $0.50.

Notices of change of address, which should be sent at least 30 days prior to actual change of address, and correspondence regarding subscrip ions should be sent to the Circulation Department, JOURNAL OF THE AEROSPACE SCIENCES, 2 East 64th Street, New York 21, N.Y.

Manuscripts for publication, proofs, and all correspondence should be addressed to the Editorial Office of the JOURNAL.

© Copyright, 1961, by the Institute of the Aerospace Sciences, Inc.

Publication Office, 20th and Northampton Sts., Easton, Pa. Second-Class Mail Privileges Authorized at Easton, Pa. Acceptance for mailing at a special rate of postage provided for in Section 1103, Act of October 3, 1917, authorized April 29, 1937.

JOURNAL OF THE AEROSPACE SCIENCES

VOLUME 28 FEBRUARY, 1961 NUMBER 2

The Role of Entropy in the Aerospace Sciences

Daniel and Florence Guggenheim Memorial Lecture

JAKOB ACKERET*

IT IS A GREAT HONOR for me to deliver the second Daniel and Florence Guggenheim Memorial Lecture here in Zurich. We all know of the Guggenheims' deep understanding of the value of scientific treatment of the many important and often only partially solved problems in aeronautics, and now also in astronautics. We are most thankful for the moral and financial help research workers enjoy through the Guggenheims' generosity.

In our small country there always exists a modicum of local patriotism, and so we are proud to remember that the Guggenheims stem from an old family which resided more than a hundred years ago at Lengnau, only twenty miles from here, or, in American measure "just around the corner." Meyer Guggenheim was born there in 1828 and emigrated to America in 1847. One of his seven sons was Daniel Guggenheim.

Our eminent Professor von Kármán delivered the first Guggenheim lecture in Madrid in 1958, giving one of his famous reviews of the state of the science of aerodynamics. For the poor people who suffer from a deluge of papers and reports, his lectures are an invaluable help, inasmuch as they treat the most recent developments with a truly Latin clarity.

It is clear that other people (for instance, the present speaker) should not simply imitate such a proceeding. I intend, therefore, to follow a somewhat different path. It is my hope that a "Spaziergang" across the wide field of aerothermodynamics in the light of the concept of *entropy* may not bore you too much.

Nearly a hundred years have passed since Rudolf Clausius, then professor at this school, introduced entropy. Since then entropy has always been a favorite theme in Zurich, especially as it concerns engineering applications. I may mention the names of Gustav Zeuner and Aurel Stodola, the latter being my revered teacher. Stodola was able to destroy the fear of this somewhat mystical concept, that befell so many students as he demonstrated how to use it in all sorts of thermodynamic calculations.

There are indeed some rather mysterious conclusions resulting from the entropy laws. Entropy is not conserved, but is constantly increasing. The universe seems bound to run down to an end, the oft-cited "heat death." There are enigmas, and it may be that in this connection cosmology has surprises in store for the

FIG. 1. Nicolaus Léonard Sadi Carnot (1796–1832).

Presented at the Second International Congress of the Aeronautical Sciences, Zurich, Switzerland, September 12, 1960.

* Professor, Institut für Aerodynamik, Eidgenössische Technische Hochschule, Switzerland.

I would like to thank Mr. H. Baumann and Dr. H. Sprenger, of the Institute of Aerodynamics, for their valuable help in the preparation of this lecture and the demonstration.

future. May space flight, one of our goals, help scientists in their difficult task to find a way.

But let us keep to the more homely regions of our science. With the realization of airplane and missile speeds equal to or even surpassing many times the speed of sound, thermodynamics has entered the scene and will never again be absent from our considerations. Finally, re-entry has widened this fascinating field still more, as the tremendous temperatures involved produce chemical and to a certain extent even electrical changes in the composition of the air.

Here entropy plays quite an important part. But there are limits: in principle, the classical definition applies only to the so-called *equilibrium states*, which are not present in extreme cases. A hundred years of development of equilibrium-state physics thus reaches its end, giving way to a much more sophisticated program—the amalgamation of micro- and macrophysics.

The Work of Carnot and Clausius

Thermodynamics is a relatively young branch of the physical sciences. We may date its beginning as the year 1824, when the young Frenchman Nicolaus Sadi Carnot theorized on the "puissance motrice du feu."[1] (Fig. 1.)

Like everyone else at that time, he adhered to the concept of a caloric, some kind of very subtle, indestructible fluid. Notwithstanding, he succeeded in finding very general laws by ingenious use of what we nowadays call "Gedanken-Experimente." First he noticed that the caloric could do work only if there was a drop in temperature in the heat engine. To a certain extent he used the analogy of a hydraulic wheel, assigning to the temperature the role of the water level.

FIG. 2. Water-wheel analogy of a heat engine. If we take the water level as the analog of (absolute) temperature, the "efficiency" $\eta = (H_1 - H_2)/H_1$ translates into $\eta_c = (T_1 - T_2)/T_1$, the Carnot efficiency. But the analogy is only partially correct. Curiously enough, the obviously bad exploitation of the available power in this romantic plant is not worse than the thermodynamic efficiency of the steam process in a rather modern locomotive. The lost head H_2 corresponds to the loss of energy in the steam exhaust.

FIG. 3. Rudolph Clausius (1822–1888).

Fig. 2 immediately suggests some consequences of this analogy: For greatest efficiency, all the water should enter the engine at the highest level and leave it at the lowest level, and no water should pass beside the wheel.

The caloric cannot do work directly, but must be delivered to or taken away from some material substance, preferably in the form of gas or vapor which show great changes in volume upon being heated or cooled. In this way, he stated his famous Carnot cycle consisting of two isothermal and two adiabatic processes working with a constant quantity of fluid. He realized the fundamental possibility of a *reverse* cycle, inventing in the process the *heat pump*, and he showed conclusively that with given upper and lower temperatures and a fixed amount of caloric his cycle would give maximum efficiency.

He could not make further progress, however, as the first (energy) law of thermodynamics had still to be found, which states that heat and work can be transformed into one another in a fixed ratio. This step was taken by Rudolf Clausius[2] in 1850. (Fig. 3.)

Clausius combined the first law with Carnot's ideas. The heat quantity Q_1 enters at the high temperature T_1, and a smaller quantity Q_2 leaves the system at T_2. The difference $Q_1 - Q_2$ is equivalent to the work done, and we have the simple relation

$$Q_1/Q_2 = T_1/T_2$$

or

$$(Q_1/T_1 - Q_2/T_2) = 0 \tag{1}$$

The power is

$$L = Q_1[1 - (T_2/T_1)] = Q_1\eta_c \tag{2}$$

where η_c is the Carnot efficiency.

Thus only a fraction of the heat supplied is transformed into mechanical work. We can see that low temperature of the environment is rather more im-

portant than high temperature on the supply side. Perhaps there are lower temperature atmospheres on other planets which would allow higher efficiency, but that may not be too encouraging, considering other difficulties arising from the diminished comfort for space men.

The next step was a generalization of the Carnot cycle by the introduction of arbitrary but reversible cycles. By the well-known artifice of dissecting such cycles into elementary Carnot cycles (Fig. 4), and taking Q algebraically, we find instead of Eq. (1)

$$\oint \frac{dQ_{rev}}{T} = 0 \tag{3}$$

A simple proof shows that the integral along an arbitrary path from 1 to 2 is always

$$S_2 - S_1 = \int_1^2 \frac{dQ_{rev}}{T} \tag{4}$$

provided that dQ is supplied in a reversible manner. S is therefore a *function of the state*, named, by Clausius in 1865, *entropy* ($\dot{\eta}\ \tau\rho o\pi\dot{\eta}$), "the change."[3]

It is useful to remember that the suffix "reversible" in dQ_{rev} is necessary only for the calculation of entropy. If we have an irreversible process going in some way from 1 to 2, the entropy difference is still determined, but then the heat exchange has no direct connection with the entropy change.

A typical example may be mentioned here—the adiabatic throttling of an ideal gas (Fig. 5). From 1 to 2 the pressure falls but the temperature is constant (as an energy check shows). Entropy increases, hence the process is completely irreversible. In order to calculate the entropy difference we choose a reversible path, first an isentropic cooling from 1 to 1*, followed by heating along an isobar (p_2) from 1* to 2. We get

$$\Delta S_{(T)} = R \ln (p_2/p_1) \tag{5}$$

For an irreversible process we have

$$\int_1^2 \frac{dQ_{irr}}{T} \leqq S_2 - S_1$$

(In our previous example the corresponding integral was zero.) In the case of an irreversible cyclic process,

$$\oint \frac{dQ}{T} \leqq 0 \tag{6}$$

which seems to be the simplest statement of the so-called *second law*.

A process of this sort occurs in any closed wind tunnel mechanically driven from the outside. To secure a steady state inside the tunnel, a cooler is needed. The entropy of the gas at a given position inside does not, of course, change. But the cooler draws heat away, equivalent to the mechanical work done from the outside. Hence the *entropy of the environment* steadily rises. The high-rated mechanical energy is downgraded and can perform practically no work, being at nearly ambient temperature. As there is always some irreversible friction, heat conduction, and radiation "the entropy of the universe" is continuously growing toward a maximum at which all high-grade energy (which is conserved) will have been turned to heat. It was Clausius who first drew this dreary conclusion.

The late Robert Emden, a very ingenious scientist, used to stress that we on earth are not really living from solar energy since, except for negligible amounts, this energy is radiated back into interplanetary space. Instead, we derive life from a deliberate increase of solar entropy.[4] In the words of Léon Brillouin,[5] the sun delivers negative entropy or "negentropy" to the earth, and organic life catches and squanders this most useful gift. But where did negentropy come from? We simply do not know.

Formula (4) gives only entropy differences. This is no drawback, if we consider only one element or compound. But if there are chemical changes, the so-called absolute entropies must be known. In 1906, before the advent of quantum statistics which gives absolute entropies more or less directly, a more indirect way was found by Nernst who introduced the so-called

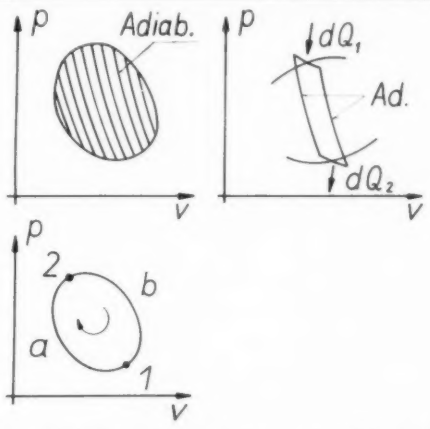

FIG. 4. Dissection of an arbitrary reversible cycle into elementary Carnot cycles. Since the integral $\oint dQ_{rev}/T$ equals zero, the entropy difference

$$\int_1^2 dQ_{rev}/T$$

is independent of the integration path and entropy appears as a state function.

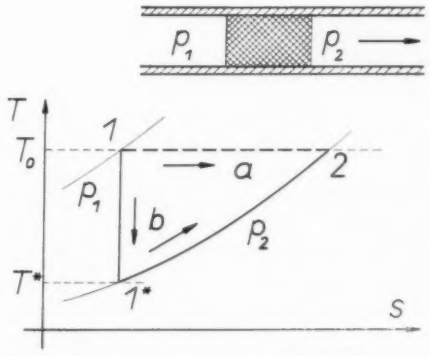

FIG. 5. Adiabatic, irreversible throttling of an ideal gas. No heat is exchanged, but entropy increases.

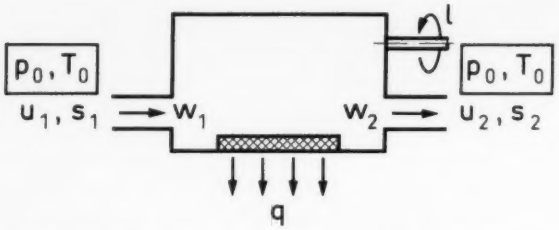

FIG. 6. Ideal, reversibly working propulsion mechanism using chemical propellents.

"third law of thermodynamics." A somewhat simplified version of this law reads: "The entropy of a substance disappears at absolute zero temperature."

Since specific heats and heats of fusion and evaporation are known to a considerable extent, absolute entropies can be calculated in a straightforward manner. Usually the values are given for one gram mole in a standard state, the latter being taken for the convenience of the physical chemist as $p^* = 1$ atm. and $T = 298.1°K$.

The figures in Table 1 show the orders of magnitude of absolute entropies.

Let me mention the well-known formula for the entropy of an ideal gas for constant specific heats:

$$s_2 - s_1 = c_v\{\ln (p_2/\rho_2^\gamma) - \ln (p_1/\rho_1^\gamma)\} \qquad (7)$$

where $$\gamma = c_p/c_v$$

In most cases specific heat is dependent on temperature and, to a lesser extent, on pressure, and so we have

$$s_2 - s_1 = \int_1^2 c_p \frac{dT}{T} - R \ln \frac{p_2}{p_1} \qquad (8)$$

Often real gases have quite complicated equations of state $F(p,v,T) = 0$, when the density grows to larger values. There are long equations for steam involving not less than 20 empirical constants.

As an example, and considering its importance in aeronautical science, I shall mention the formula for the velocity of sound a in a real gas.

Generally, we have from mechanical considerations

$$a^2 = (\partial p/\partial \rho)_{s = \text{const.}} \qquad (9)$$

Since entropy is a state function,

$$ds = (\partial s/\partial p)_v\, dp + (\partial s/\partial v)_p\, dv$$

which can be transformed into

$$ds = \frac{c_v}{T}\left(\frac{\partial T}{\partial p}\right)_v dp + \frac{c_p}{T}\left(\frac{\partial T}{\partial v}\right)_p dv = 0 \qquad (10)$$

TABLE 1*

Substance	s^*/R_m
C (graphite)	0.684
Fe (solid)	3.27
H_2 (gas)	15.71
O_2 (gas)	24.66
H_2O (liquid)	8.43

* R_m the molar gas constant = 8.317×10^7 ergs/°K.

hence

$$a^2 = \gamma[-(\partial T/\partial \rho)_p/(\partial T/\partial p)_\rho]$$

from which, with the use of a well-known thermodynamic formula the simple result appears:

$$a^2 = \gamma(\partial p/\partial \rho)_{T = \text{const.}} \qquad (11)$$

For ideal gases this gives the classical value

$$a^2 = \gamma(p/\rho) \qquad (12)$$

Real gases can be treated most practically with the help of entropy charts or diagrams. Often used are temperature-entropy (T,s) and Mollier enthalpy-entropy (h,s) diagrams.

Enthalpy and Free Enthalpy; the Ideal Heat Engine

In our jet or rocket motors, chemical energy is transformed into mechanical energy. For instance, in a turbojet the entering air is accelerated, the change in momentum producing the thrust. But we know also that the jet is hot, and that thereby quite a considerable amount of energy is lost. The question raised is how much mechanical (or electrical) work can the motor do at best?

We imagine a hypothetical apparatus working continuously and delivering mechanical or electrical power (Fig. 6). Within the "box" an unspecified type of chemical reaction is going on. On the left, the fuel (air + hydrocarbon, oxygen + hydrogen, etc.) flows in steadily, while the products leave on the right, both flows taking place at pressure p_0 and temperature T_0 of the surroundings. As we intend to have the best possible device, we naturally cannot afford a direct loss of heat at relatively high temperature. If heat exchanges with the environment are necessary, they should take place reversibly at T_0. Mechanical work should be extracted through a shaft and coupling, and/or in the form of kinetic energy of the exhaust. Transformation to electrical energy is another alternative.

The first law gives immediately

$$l + \frac{w_2^2 - w_1^2}{2} = (u_1 + p_0 v_1) - q - (u_2 + p_0 v_2) \qquad (13)$$

where w is velocity, l mechanical or electrical work, u the (internal) energy, and v the volume, all taken for one gram.

The second law is used in the following way: To secure a maximum of efficiency we assume that the internal processes work reversibly (combustion, expansions, compressions, etc.), and as mentioned before also, the heat exchange q. Then $q = -T_0(s_2 - s_1)$, and we have

$$l + \frac{w_2^2 - w_1^2}{2} = (u_1 + p_0 v_1 - T_0 s_1) - (u_2 + p_0 v_2 - T_0 s_2) = g_{1_0} - g_{2_0} \qquad (14)$$

where g is Gibbs' *free enthalpy*,

$$g = (u + pv - Ts) = h - Ts \qquad (15)$$

specialized for $T_1 = T_2 = T_0$ and $p_1 = p_2 = p_0$, (h = enthalpy). The part $h_1 - h_2$ is called heat of reaction at p_0, T_0, and $(s_2 - s_1)$ is the change in absolute entropy, since in general we have a change in chemical composition.

Gouy and Stodola (Fig. 7) were, to my knowledge, the first to apply free enthalpy to the evaluation of heat-engine processes.[6,7] When absolute values of entropies were available, the maximum output for a given fuel input could be calculated. For the reactions

$$\begin{aligned} C + O_2 &= CO_2 \\ CO + {}^1/_2\, O_2 &= CO_2 \\ H_2 + {}^1/_2\, O_2 &= H_2O \end{aligned}$$

the output can be nearly 100 per cent of the heat of reaction. There are even reactions in which more than 100 per cent can be gained. In these, heat is taken from the surroundings and transformed to work. There is no contradiction to the second law, since we do not have a cyclic process but use up the fuel.

The crux is the assumed reversibility of the chemical changes. Normal fuel-air combustion is rather irreversible (look at a film, run in reverse, of a gasoline-air explosion!).

Quantum chemistry has shown that a chemical reaction means a rearrangement of the outermost electrons. Without further restraint the reaction products gain kinetic energy on the order of one electron volt. But one electron volt corresponds to a "temperature" of 7,740°K. (1.6×10^{-12} erg $= {}^3/_2\, kT$). The next few collisions with inert molecules (N_2, etc.) lead to a degradation of this mechanical energy which is irreversible, causing rise in entropy.

We should be able to firmly hold in the reaction products and divert their energy slowly outwards. This is the process in the ordinary galvanic cell, where an electric field holds back the charged particles. Their efficiency (at low current density) is quite high, very near to maximum. No high temperatures are involved.

You know that this process has undergone a sort of renaissance in the form of the modern fuel cells. Maybe one day the *output density* of these cells will be high enough for practical applications even in the field of space flight. At the moment there is no other way to attain high power output than by irreversible burning.

We can approach reversibility by using pure fuels (LOX + hydrocarbon or hydrogen) and very high temperatures (2,000°–3,000°K.). Here we are nearing an equilibrium between association and dissociation, where burning is reversible. To a certain extent this is realized in rocket combustion chambers; but there we have an input of relatively cold material (even with regenerative cooling) and a corresponding entropy increase during the heating to equilibrium temperature. In principle, we should use isentropic precompression up to this temperature, but the practical difficulties are obvious and need no further comment.

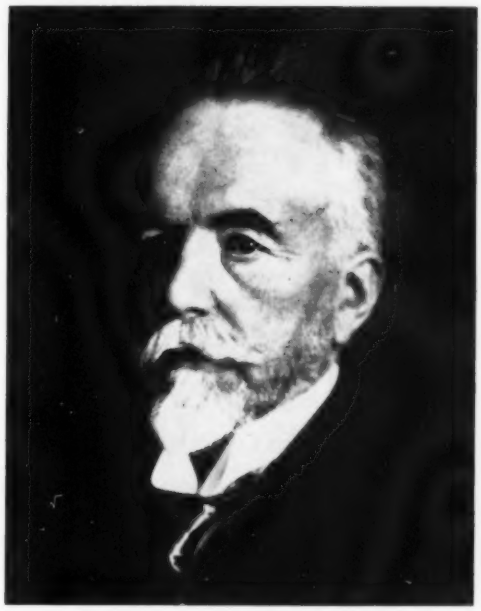

FIG. 7. Aurel Stodola (1859–1942).

Propulsion in the Void

In interplanetary space the environment is different in several respects. The pressure is practically zero, and temperature is not defined.

Problems appear if there is a need for dissipation of heat. Several new propulsion systems, such as ionic drive or plasma jets, include thermal machinery, i.e., steam or gas turbines working with closed cycles more or less along the Carnot cycle. The high temperature T_1 is limited as usual by material properties, but the lower temperature is not fixed. We would naturally strive for a low T_2. But as there is no convection, *radiation* takes its place and the energy radiated (per cm.^{2} per sec.) increases as the fourth power of T_2 (the Stefan-Boltzmann law). A low T_2 means a bigger radiation surface and leads to better efficiency than a high T_2. A simple calculation shows that for an ideal Carnot process the smallest radiation surface demands the temperature ratio

$$T_2/T_1 = 3/4$$

The corresponding Carnot efficiency would be 0.25, a relatively low figure. But it is supposed that in all the projects there is plenty of heat available, the heat source being a nuclear reactor.

Similar results can be seen in Fig. 8. Here a closed-cycle gas turbine with regenerator is considered. Some allowance was made for losses in the turbine, compressor, and heat exchanger. The hatched line gives the minimum specific radiation surface for different pressure ratios. T_{max} is fixed at 1,200°K. The radiation surface per megawatt of power is smallest for $T_2 = {}^1/_2 T_1$. Even then the absolute area is rather large, and construction may be quite a problem.

In rockets, the diminishing counterpressure makes a

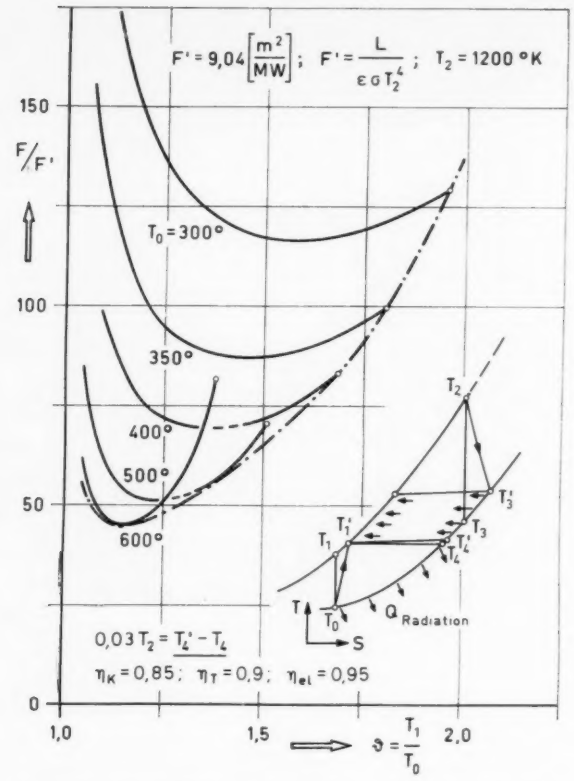

FIG. 8. Closed-cycle gas turbine generator working with nuclear reactor heat. Radiator area as a function of radiator temperature T_0 and ideal temperature ratio in the compressor. η_K = isentropic compressor efficiency, η_T = turbine efficiency, η_{el} = efficiency of electric generator.

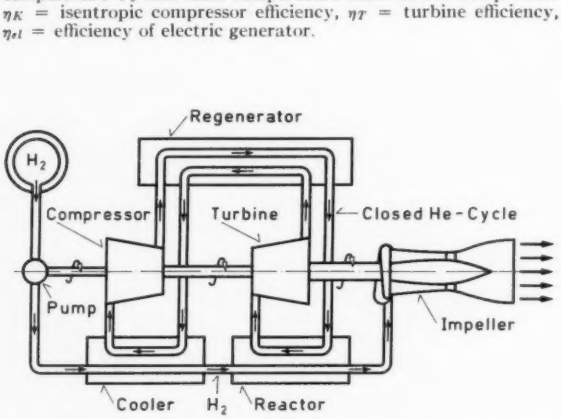

FIG. 10. A turbine rocket drive after the proposal of N. Rott and E. L. Resler. Helium is used in a closed-cycle process with very low inlet temperature. The power is transformed into electrical or mechanical work to accelerate a hydrogen jet.

FIG. 12. Boundary layer along a flat plate in a uniform stream of gas. According to the theorem of Oswatitsch, drag is connected with the entropy flux.

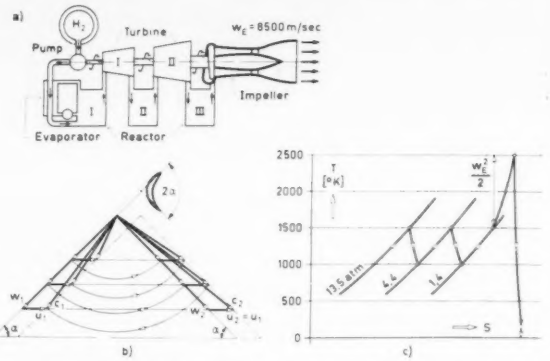

FIG. 9. Scheme of a turbine-driven rocket. Liquid hydrogen is evaporated at relatively high pressure, heated and reheated by nuclear reactors. Work is drawn out by turbines during the expansion and delivered to a mechanical impeller in the form of a multistage compressor. As compressor efficiency is not critical, the blade arrangement can be made for acceleration rather than for pressure rise. Alternatively, the mechanical work could be transformed into electrical power for further use in a hydrogen plasma device. This gives an approximation to isothermal expansion.

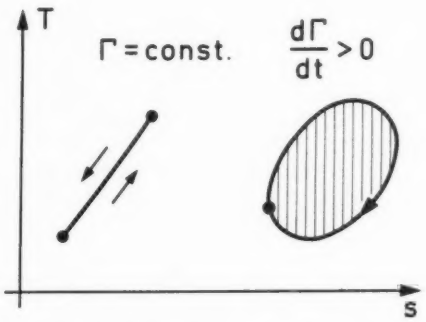

FIG. 11. The circulation theorem in the T,s diagram. The area circumscribed by the process line is proportional to the rate of change of circulation along a closed fluid line.

FIG. 13. Entropy rise in normal and oblique shocks.

useful contribution to the specific impulse, but the theoretical limit is well known. An *isentropic* expansion from a chamber temperature T_1 to $T_2 = 0$ gives an exhaust speed of

$$w_{max} = \sqrt{2c_pT_1} \tag{16}$$

where for simplicity constant specific heat was assumed. w_{max} is independent of the chamber pressure; in fact, the theoretical pressure ratio would be infinite anyway. It is well known that this limit cannot be reached in practice because of finite nozzle dimensions, wall friction, energy losses due to incomplete combustion, etc.

With the introduction of nuclear heating and the use of isentropic expansion of hydrogen, very high exhaust velocities are possible. However, the reactor temperatures must be extremely high, at least by present standards (some 1,600–2,000°K. or even more). It is therefore interesting to remember that considering the nearly unlimited supply of heat and the infinite pressure ratio, an *isothermal* expansion could give any desired specific impulse.[8] Indeed, the formula

$$w_{isoth} = \sqrt{2RT \ln (p_1/p_2)} \tag{17}$$

tends to ∞ as $p_2 \to 0$.

The simplest scheme would be a system of long nozzles surrounded by a nuclear reactor. Heat would be exchanged through the walls. Contrary to expectation, friction would not alter the exhaust speed; only a change in dimension would be necessary for the same thrust. But there is another limit which destroys all hope.[9] Wall friction is intimately connected with heat production in the boundary layer. If the so-called recovery factor is equal to one (as is nearly the case in turbulent boundary layers), we find by a simple calculation that the maximum velocity is exactly the same as with isentropic expansion. The reason for this is that at a certain velocity in the center of the nozzle the boundary-layer temperature caused by frictional heating reaches the wall temperature and heat exchange ceases [see Section (1) of the Appendix].

Something like an isothermal expansion can nevertheless be realized by a more complicated arrangement.[10] The scheme is seen in Fig. 9. A light substance (He or H) in liquid state is vaporized and passed through a first reactor. After heating there is expansion in a turbine, which delivers mechanical work. The process can be repeated and after the last passage through the reactor the effective temperature of the gas is increased by transmission of the work of the turbines in electrical or even mechanical form to the gas. In Fig. 9 the second type of transmission is illustrated. It is interesting to note that the efficiency of the mechanical accelerator need not be high; hence we could use quite uncommon blade shapes, turning angles, velocities and, most important, some high-melting ceramic material. For very high temperatures electrical transmission would be more promising, but this would require the successful development of ultralight electrical machinery.

A highly interesting alternative has been proposed by Resler and Rott[11] (Fig. 10). They also use a turbine and an electrical (or mechanical) drive; in addition, however, they intend to use a regenerative helium cycle inserted in the process, with a heat sink at the temperature of liquid hydrogen. This closed-cycle machine would truly give the utmost Carnot efficiency, the temperature ratio being something like 50 to 1.

With both arrangements, speeds of some 7,000–8,000 m./sec. may be produced at reactor gas temperatures in the region of 1,200 to 1,500°K. If reactor gas temperatures of 2,000°K. or even 2,500°K. are possible, the direct heating will of course be more practical.

Entropy in Gas Flow

(a) Nonviscous Flow; Vortex Theorems

In nonviscous flow the well-known Helmholtz-Kelvin theorem applies:

$$\frac{d\Gamma}{dt} = -\oint \frac{dp}{\rho} \tag{18}$$

where Γ is the circulation along a line moving with the gas. This theorem can be written in terms of entropy and enthalpy. With

$$ds = (du + pdv)/T = dq/T$$

and

$$h = u + pv$$

the integral transforms to

$$\frac{d\Gamma}{dt} = \oint \{Tds - dh\}$$

As h is a single-valued function of the state, the second term drops out and we have

$$\frac{d\Gamma}{dt} = \oint Tds \tag{19}$$

a formula which has been much used in meteorology since Bjerknes first introduced it.

In the T, s diagram, the integral is given by the area circumscribed. If p and ρ are in a single-valued relation, this area disappears and there is no change in circulation (Fig. 11).

Another interesting theorem was developed by Luigi Crocco.[12] He started with Euler's equation for inviscid compressible gases,

$$(\partial \mathbf{w}/\partial t) - \mathbf{w} \times \text{rot } \mathbf{w} + \text{grad } (w^2/2) = - \text{grad } h + T \text{ grad } s \tag{20}$$

If now the flow is assumed to be stationary and of constant energy over the whole field, then

$$h + (w^2/2) = \text{const.}$$

a condition which is fulfilled even if shock waves are present. It follows that

$$\text{grad } (w^2/2) + \text{grad } h = 0$$

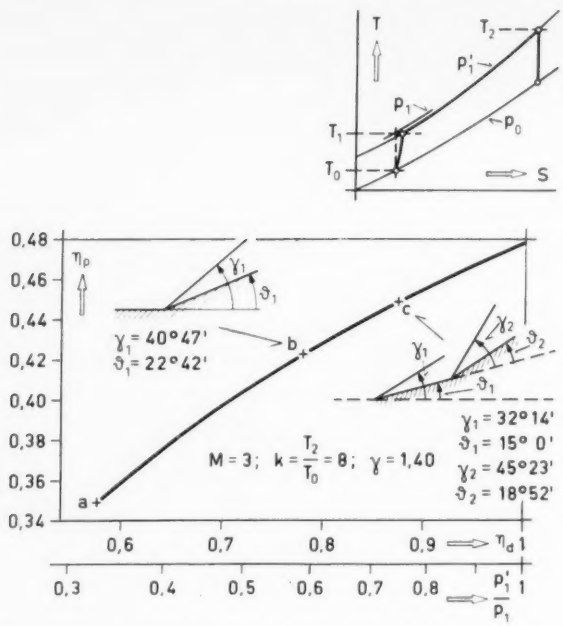

FIG. 14. Two-dimensional ramjet with shock diffusors. *a*, normal shock; *b* and *c*, oblique shock compression.

η_p = propulsion efficiency
$\eta_d = \dfrac{(T_1/T_0)(p_1'/p_1)^{(\gamma-1)/\gamma} - 1}{(T_1/T_0) - 1}$
= diffusor efficiency

and therefore

$$\mathbf{w} \times \text{rot } \mathbf{w} = -T \text{ grad } s \tag{21}$$

The following conclusions can be drawn:

(1) A stationary gas flow, irrotational and with constant energy, is an isentropic flow;

(2) If there are entropy changes within the field, vortices (vortex sheets) will generally appear.

The last consequence is important, for instance, in the case of shock waves in front of a blunt body. Vortex sheets will be formed whose strength will decrease with increasing distance from the body.

(b) Entropy in Boundary Layers; Oswatitsch's Theorem

Entropy is produced in boundary layers at a relatively high rate, as the dissipation is concentrated in these layers. Let us consider the simple case of a plate parallel to a stream of constant velocity (Fig. 12). We further assume that the Prandtl number

$$Pr = \mu c_p/\lambda$$

(where λ = heat conductivity) is unity, if the boundary layer is laminar. In the turbulent case the equivalent ratio Pr^* of "apparent" coefficients also has this value, even if Pr is not exactly one. Busemann has shown that for Pr or $Pr^* = 1$ the simple relation applies:

$$h + (w^2/2) = c_pT + (w^2/2) = \text{const.} \tag{22}$$

where w is the velocity parallel to the plate.

The entropy flux can now be calculated for a section relatively far downstream (section 3 in Fig. 12). The index 1 applies to the undisturbed flow, the index 2 to the profile at the end of the plate. As the pressure is constant, the specific entropy in section 3 is given (with s_1 taken as zero) by

$$s_3 = c_p \ln (T_3/T_1) = c_p \ln \left(1 + \frac{w_1^2 - w_3^2}{2c_pT}\right) \tag{23}$$

As w_3 is quite near to w_1, we get for the entropy flux:

$$S_3 = c_p \int_0^\infty \rho_3 w_3 \frac{w_1 + w_3}{2} \frac{w_1 - w_3}{c_pT_1}\, dy$$

$$= \frac{1}{T_1} \int_0^\infty \rho_2 w_3 w_1 (w_1 - w_3)\, dy$$

We now compare this formula with the momentum equation which gives us the frictional drag D of the plate:

$$D = \int_0^\infty \rho_2 w_3 (w_1 - w_3)\, dy$$

So we see that

$$Dw_1 = T_1 S_3 \tag{24}$$

This is a special case of the important theorem of Oswatitsch.[13]

An interesting question arises when we carry out our flux calculation on section 2. S_2 is different from S_3 ($S_2 < S_3$). What does T_1S_2 mean? Nothing other than the minimum power needed for propulsion. We can think of a sophisticated propulsion mechanism that leaves behind the plate a wake which possesses (in an absolute system) no visible kinetic energy, undisturbed temperature, and undisturbed entropy. To obtain this effect we have to apply two mechanisms: (1) a Carnot-cycle heat engine which utilizes the temperature difference $T_2 - T_1$ and transforms it into power, as a consequence of which the entropy of the environment increases; (2) an isentropic compressor which accelerates the air from w_2 to $w_3 = w_1$.

The work (a) is sensibly smaller than (b) [see Section (2) of the Appendix]. Sets of such equipment would have to be installed in great numbers, namely, one for every fluid filament. The gain in power is considerable but such complicated machinery is of course an absurdity. In certain applications of boundary-layer suction, however, the second part of this effect may well be present.

In the last instance it is the *sticking* of molecules to solid surfaces that initiates boundary layers. Sticking is physically quite different from the mechanism of internal friction. It may be that one day an ingenious inventor will find an antisticking device; at the moment nothing of this kind is in sight. The next step toward the reduction of frictional resistance will be laminarization. The latest results of Pfenninger seem to be encouraging.[14]

Entropy in Shock Waves

When Riemann discovered shock waves by theoretical reasoning, he assumed an isentropic change of state

This is nearly true for weak shocks, but not for strong ones.

The Hugoniot-Rankine equation

$$\frac{\gamma}{\gamma-1}\left(\frac{p_2}{\rho_2}-\frac{p_1}{\rho_1}\right)=\frac{\rho_2+\rho_1}{2\rho_1\rho_2}(p_2-p_1) \qquad (25)$$

(where the suffixes 1 and 2 refer to in front of and behind the shock) can be transformed into the simple Kármán relation:

$$\frac{p_2-p_1}{\rho_2-\rho_1}=\gamma\frac{p_2+p_1}{\rho_2+\rho_1} \qquad (26)$$

which, by the way, is equal to the square of the so-called critical velocity a^*.

For extremely weak shocks this becomes in the limit

$$dp/d\rho=\gamma(p/\rho) \qquad (27)$$

the common isentropic equation.

In stronger shocks the entropy increases. We find

$$\frac{s_2-s_1}{R}=\frac{1}{\gamma-1}\ln\left[1+\frac{2\gamma}{\gamma+1}(M_1^2-1)\right]+\frac{\gamma}{\gamma-1}\ln\left[1-\frac{2}{\gamma+1}\left(1-\frac{1}{M_1^2}\right)\right] \qquad (28)$$

where

$$M_1=w/a_1$$

in which w is the gas velocity in front of the shock relative to the shock front, and a_1 is the speed of sound in this region.

The stagnation pressure is reduced, while the stagnation temperature (as a consequence of the first law) remains constant. We have

$$p_{0_2}/p_{0_1}=e^{-(s_2-s_1)/R} \qquad (29)$$

For weak shocks an approximation gives

$$\frac{s_2-s_1}{R}\to\frac{\gamma+1}{12\gamma^2}\left(\frac{p_2-p_1}{p_1}\right)^3=\frac{2}{3}\frac{\gamma}{(\gamma+1)^2}(M_1^2-1)^3 \qquad (30)$$

From this formula it is evident that the irreversibility is quite small near $M_1\approx 1$.

Oblique shocks can be treated in much the same way. Here only the velocity component normal to the shock front undergoes a change. The formula is

$$\frac{s_2-s_1}{R}=\frac{1}{\gamma-1}\ln\left[1+\frac{2\gamma}{\gamma+1}(M_1^2\cos^2\varphi-1)\right]+\frac{\gamma}{\gamma-1}\ln\left[1-\frac{2}{1+\gamma}\left(1-\frac{1}{M_1^2\cos^2\varphi}\right)\right] \qquad (31)$$

Fig. 13 shows the substantial reduction in the entropy increase. According to Oswatitsch's theorem, drag can be reduced by sweeping back the shock front; the same principle explains the advantage of Oswatitsch's multishock diffusor inlet. An infinite number of shocks with vanishing strength give as a limit isentropic compression, but even with a very limited multiplicity a considerable gain is made, as is exemplified in the case of a (plane) ramjet where the propulsive efficiency is improved (Fig. 14). Well-designed intake diffusors are of great importance for the realization of economic supersonic airliners.

The Structure of Shock Waves

Shock waves are not real discontinuities, although sometimes they are very thin. An attempt can be made to apply the one-dimensional Navier-Stokes equation combined with the energy and continuity equations. Besides the heat conduction $\lambda(dT/dx)$, the compressional viscous stress π_{xx} enters the equations

$$\pi_{xx}=-2\mu(\partial w_x/\partial x)+(2/3)\mu\ \mathrm{div}\ \mathbf{w}-(2/3)\mu'\ \mathrm{div}\ \mathbf{w} \qquad (32)$$

with μ as normal, and μ' as bulk viscosity. For the one-dimensional case

$$\pi_{xx}=-\left(\frac{4}{3}\mu+\frac{2}{3}\mu'\right)\frac{\partial w_x}{\partial x} \qquad (33)$$

If there is no bulk viscosity,

$$\pi_{xx}=-(4/3)\mu(\partial w_x/\partial x)$$

A very crude order-of-magnitude argument shows immediately that the thickness of the shock turns out to be really small in normal cases. We can assume that π_{xx} must be comparable to the total pressure difference, say $^1/_2(p_2-p_1)$. Then we find for the thickness d

$$d=(8/3)(\nu/a_1)(1/M_1)\qquad(M_1>1) \qquad (34)$$

which gives for atmospheric air and for medium Mach numbers something on the order of 10^{-5} cm., quite comparable with the free-path length.

Many people have given exact solutions on the basis of the Navier-Stokes equation. One of the first was R. Becker.[15] He neglected the change of the viscosity- and heat-conduction coefficients with temperature, and assumed a gas with Prandtl number 3/4 to simplify the calculations. Fig. 15 shows the transition in the shock. The entropy first rises, and then there is a small reduction. M. Roy has shown that the entropy maximum corresponds to the abscissa where the velocity curve is steepest.[16] The different terms of the energy equation are plotted separately. By introducing entropy, this equation can be transformed into the simple form:

$$(\rho w)\,T\,(ds/dx)=\mu(dw/dx)^2+\lambda(d^2T/dx^2) \qquad (35)$$

If we call $(\rho w)s=S$ an *entropy flux*, the left-hand side means T div S, and the right-hand side contains the *entropy sources*. Both concepts play an important role in the new science of *irreversible thermodynamics*.

Thomas included the variability of the coefficients of heat conduction and viscosity ($\mu\sim\sqrt{T}$), and found values for the thickness little differing from Becker's.[17] His values for air ($T_1=300°$K., $\gamma=1.4$) and different Mach numbers are given in Table 2.

TABLE 2

M	Thickness, cm. $\times 10^{-7}$
2	173.8
3	106.6
4	87.6
5	79.5
∞	65.8

The finite limit comes from the indefinite growth of viscosity and heat conductivity with shock strength. Green, Cowan, and Hornig were able to measure the thickness by an interesting light reflection method,[18,19] and Sherman did the same using a temperature probe in a relatively weak shock at reduced density.[20] Some results are shown in Fig. 16 (after Patterson) compared with different theories, especially with different laws of temperature dependence of viscosity ($\mu \sim T^N$).[21] Mott-Smith's theory is different, in that he uses a mixture of two Maxwellian distributions.[22] The most astonishing conclusion is that the macroscopic Navier-Stokes treatment does not apply too badly, and that other theories do not seem to show much improvement.

The application of shock tubes for the study of supersonic and hypersonic gas flow is well known. Here I shall consider only a simple case of shock reflection, the so-called resonance tube.[23] A cylindrical tube completely or nearly closed at one end and open at the other end is used. A supersonic air jet is directed towards the open end. Long ago Hartmann found that this device produces a periodic flow of gas in and out of the tube, and intense ultrasonic waves outside.[24] He was chiefly interested in the latter, but the phenomena inside the tube are no less interesting. The part of the tube near the closed end is heated to a considerable temperature. An elementary explanation may be found by considering the movement of shock waves

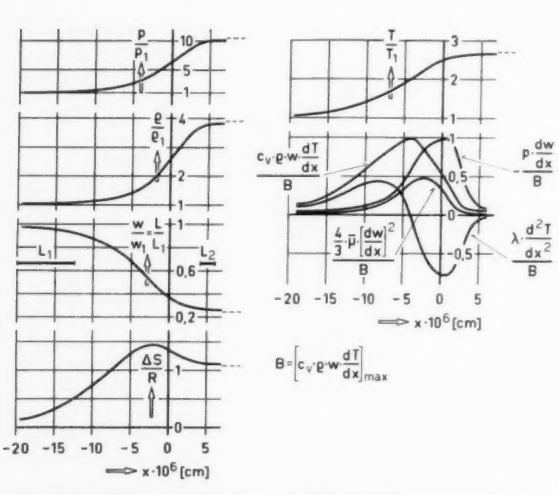

FIG. 15. Values of the state variables inside a normal shock, after R. Becker. L is free path length. The different terms of the energy equation are drawn separately in the last diagram. $M_1 = 3$, $T_1 = 295°$K., $p_1 = 10^6$ dynes/cm.², $\bar{\mu} = 2.85 \times 10^{-4}$ gm./cm.-sec. Energy equation:

$$c_v \rho w \frac{dT}{dx} = -\left(p - \frac{4}{3}\mu \frac{dw}{dx}\right)\frac{dw}{dx} + \lambda \frac{d^2T}{dx^2}$$

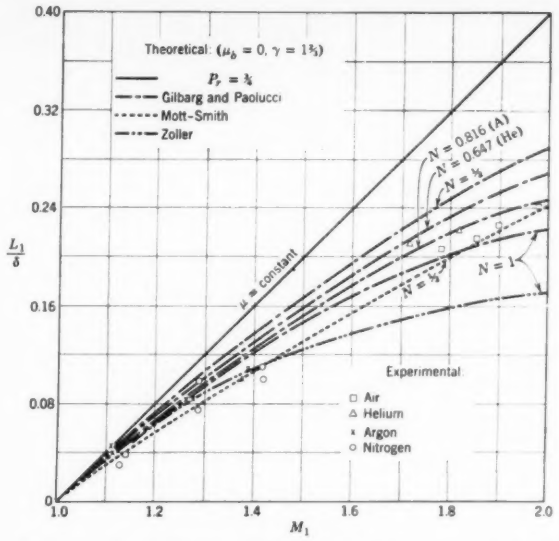

FIG. 16. Shock thickness (after Patterson). μ = constant applies to Becker's solution. The other curves are obtained by variation of the exponent N for the viscosity-temperature dependence. Experimental points confirm the order of magnitude.

inside the tube (Fig. 17). The influence of the impinging jet may be represented by a massless piston which is driven by a constant pressure from outside. A shock wave (b) is built up which is reflected at the closed end (c). After a certain time the reflected wave reaches the piston. From that time on a relatively slow expansion takes place until the original volume is regained. Then a new cycle starts. The entropy as well as the temperature have increased, since the shocks were irreversible. If there were no heat extraction, the temperature would rise to:

$$T_{max}/T_1 = p_2/p_1$$

independent of γ. With heat extraction the process will be stationary at some intermediate temperature. We can *demonstrate* the effect quite simply. A thin tube of platinum is fixed in an evacuated lamp bulb (Fig. 18). Air of about 4 atmospheres absolute, at room temperature, leaves a cylindrical nozzle as a free jet. The tube heats up and glows at about 700°C. There is some indication that certain accidents with high-pressure valves may have been caused by similar phenomena.

Connections Between Entropy and Molecular Theory

Thus far we have used the classical definition of entropy, which is sufficient for most practical problems. Very early, however, phenomena not explicable by macroscopic theory were observed. For instance, there was the riddle of the specific heats of diatomic gases, where one degree of freedom is evidently not in action, contrary to the otherwise well-established equipartition theorem. This "cloud over the mechani-

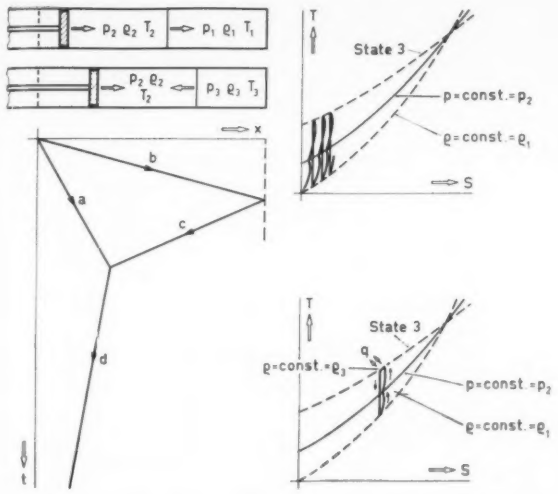

FIG. 17. Shock wave propagation in the tube. Schematic entropy diagrams for the assumed thermal processes: *above*, without energy removal; *below*, with radiation, resulting in a stationary process. Entropy increases per cycle:

$$\frac{\Delta s}{R} = \frac{1}{\gamma - 1} \ln \frac{p_2}{p_1} - \frac{\gamma}{\gamma - 1} \ln \frac{\rho_2}{\rho_1}$$

cal theory of heat," in the words of Lord Kelvin, was dispersed much later by quantum theory.

A very curious conclusion was drawn quite early by Gibbs.[25] He considered the mixing of different gases (Fig. 19). If we have two volumes of gases at the same pressure and temperature and let them mix, the process is clearly irreversible, and total entropy increases. To calculate the entropy increase in the classical way, we have to perform the mixing reversibly, which can be done, at least in principle, with the use of semipermeable pistons. Heat has to be added and work is done. If for example we use one mole of each gas, entropy is increased by

$$\Delta s = R2 \ln 2$$

as a simple calculation shows. But the formula contains an astonishing paradox, as the nature of the gases does not affect the result. Thus two gases of identical nature would show the same entropy increase upon being mixed, which is contrary to experience: nothing happens if a wall dividing a mass of gas is withdrawn.

The paradox is that the slightest difference gives an effect, but complete identity gives none. This suggests that the calculation of entropy must in reality be a counting process. As an illustration, let us imagine two coin specimens from different countries but of equal monetary value. They may be equal in weight. In normal times, to keep track of your fortune, you might simply weigh the whole lot. This is a "macroscopic" method. But if monetary perturbations occur, it might be wiser to make a closer inspection and count the coins "microscopically"—in our case, to consider the molecules.

First I would like to mention an experiment by Kantrowitz, as simple as it is interesting.[26] Carbon dioxide is a gas consisting of linear triatomic molecules. In normal equilibrium the molecules have translational, rotational, and to a certain extent also vibrational energy. Kantrowitz let the gas flow under some pressure from a receiver through a nozzle and impinge on a very small pitot head (Fig. 20). One would expect the pitot to show the exact pressure of the gas in the receiver; but with CO_2 the pitot measurement was visibly smaller. The explanation is as follows: Since the compression before the pitot occurs in a very short time, oscillation does not follow immediately; some 30,000 impacts are needed to excite vibration. For a short time the gas behaves as if it possessed a smaller number of degrees of freedom, and during this time its temperature rises. But immediately afterwards vibrations are excited continuously up to the equilibrium level. This means an irreversible temperature drop and consequently an entropy rise. But we know that greater entropy at the same equilibrium temperature means lower stagnation pressure, which corresponds to the Kantrowitz observation.

This "relaxation" phenomenon is well known also from experiments on the "dispersion" of the velocity of sound in CO_2, i.e., the change of sound velocity with frequency. A fine confirmation of the relaxation was given by Bleakney[27] who measured interferometrically the density variation in a shock in CO_2. The total entropy change is invariably given by Eq. (28), but immediately behind the shock, a zone of relaxation is clearly visible (Fig. 21).

It is plausible to assume that a similar entropy increase will occur in the vicinity of any object put into

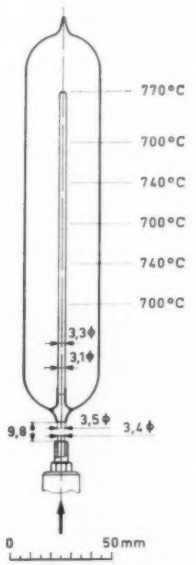

FIG. 18. Resonance tube. Air with a pressure of about 4.1 atmospheres absolute and with a stagnation temperature of 20°C. flows as a small jet against the opening of a straight circular platinum tube closed at the other end. Shock waves are running into the tube and are reflected at the closed end. Depending on pressure, there may be several shocks simultaneously in the tube. The tube is thermally insulated by an evacuated bulb, and glows. Surface temperatures are about 1000°K., and the light emitted is quite appreciable.

a stream of CO_2. According to Oswatitsch's theorem an additional drag will result.[28] It would be interesting to obtain an experimental verification of this conclusion.

There seems to be a connection between relaxation and the aforementioned bulk viscosity μ'. Busemann,[29] taking into consideration that a change in specific volume changes first the translational degrees of freedom and then the others after a certain small relaxation time, gave an approximate formula:

$$\mu' = [(5 - 3\gamma)/2]\mu \tag{36}$$

It follows that the bulk viscosity should be zero for monatomic gases (since $\gamma = 5/3$), and experiments seem to confirm this conclusion. Multiatomic gases ($\gamma \to 1$) would show, according to the formula, a bulk viscosity equal to the normal viscosity ($\mu' = \mu$). But it seems that the whole question of bulk viscosity has not as yet been settled. There are indications that for CO_2 μ' is in reality much bigger than μ. In this case the relaxation time is much greater for vibration than for rotation, and Busemann's formula cannot be applied without change.

Chemical Equilibrium

In rocket combustion chambers, temperatures are so high that dissociation occurs. In chambers where flow velocities are relatively low, the state of the gas mixture approaches equilibrium. Here, at least, entropy is well defined and if the standard entropy values for the different components are known, the whole state is theoretically determined. For the sake of simplification, we shall discuss the example of dissociating hydrogen,

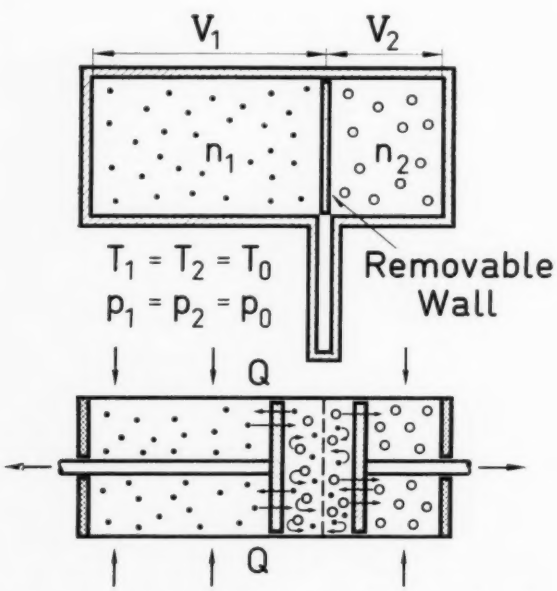

FIG. 19. *Above:* Irreversible mixing of gases. *Below:* Redersible mixing by means of semipermeable pistons. Work is vone and heat has to be added.

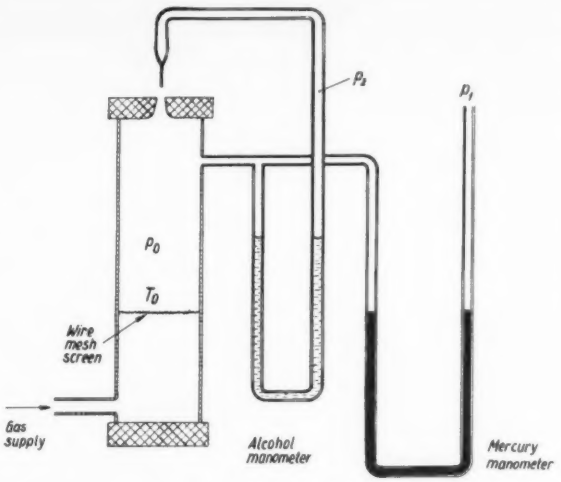

FIG. 20. Experiment of Kantrowitz, showing loss of stagnation pressure in consequence of an entropy increase by relaxation.

$$H_2 \rightleftarrows H_1 + H_1$$

We consider a mixture of H_2 and H_1 with a total mass of one mole H_2 (= 2 gm.), at a pressure p_{total}. With α designating the proportion of H_2 molecules which are dissociated, we have the following molar amounts of the components: H_2, $(1 - \alpha)$; H_1, 2α; and hence for the mixture, $(1 + \alpha)$. α depends on p_{total} and on the temperature T.

The free enthalpies of the different constituents are

$$g_i = u_i + p_i v - T s_i$$

where p_i is the partial pressure of the ith component. The total free enthalpy is given by

$$g = \sum_i g_i$$

Now the equilibrium composition is that for which the entropy is maximum—i.e., the composition for which the variation δg of g is zero for small changes in α. The equilibrium formula is found to be

$$\ln K_p = \ln\left(\frac{p_{H_1}^2}{p_{H_2}}\right) = -\frac{Q_p}{RT} + \frac{(2s_{H_1} - s_{H_2})_{abs}}{R} \tag{37}$$

Q_p, the heat of reaction at constant pressure and at the temperature T, can be found from calorimetric measurements and the known values of specific heats. s_{H_1} and s_{H_2} are the absolute entropies. α is related to K_p by

$$\alpha = \sqrt{K_p/(K_p + p_{total})} \tag{38}$$

For example, at $p_{total} = 1$ atm. and $T = 4{,}000°\text{K}$.:

$$K_p = 2.768 \qquad \alpha = 0.64$$

Fig. 22 is a temperature-entropy chart for hydrogen in equilibrium state. α and the enthalpy are included.

Much more complicated reactions have been treated analogously; charts are available for air and combustion products up to 15,000°K.

A most interesting consequence of quantum theory is the possibility of calculating the entropy of an element or compound in the gaseous state without using details of fusion or vaporization or even specific heats.

For a monatomic gas (and also for an electron gas), the absolute entropy for the aforementioned standard state (T^*,p^*) is

$$\frac{s^*}{R_m} = \frac{5}{2} + \frac{3}{2}\ln M + \frac{5}{2}\ln T^* - \ln p^* + \ln\left\{\left(\frac{2\pi}{N}\right)^{3/2}\frac{k^{5/2}}{h^3}\right\} \quad (39)$$

Here R_m is the gas constant for one mole, M is the molecular weight, N is Avogadro's number, k is Boltzmann's constant, and h is Planck's constant. For the derivation of Eq. (39), see Section (3) of the Appendix.

For more complicated molecules, further terms including moments of inertia, vibration frequencies, etc., are to be added; spectroscopy is generally able to deliver the necessary data.

Nonequilibrium States

Up to now we have considered, for the most part, equilibrium states. Chemical thermodynamics does not go any further. But nonequilibrium states are of growing importance, for strictly speaking, exact equilibrium occurs only relatively seldom in gas dynamics. However, a rational theory of nonequilibrium states must necessarily be extremely complicated. There are two courses that may lead to further progress which are being pursued now with great vigor.

First, a theory of steady *irreversible thermodynamsic* (Jaumann, Onsager, de Groot,[31] Prigogine and others), a partially phenomenological approach, has been very successful in the treatment of phenomena in which different effects operate simultaneously, for instance heat conduction plus diffusion. For a simple gas flow at high speed there is not much progress to be mentioned at present, since equations of the type of formula (35) result, whereby entropy flux and sources of entropy can

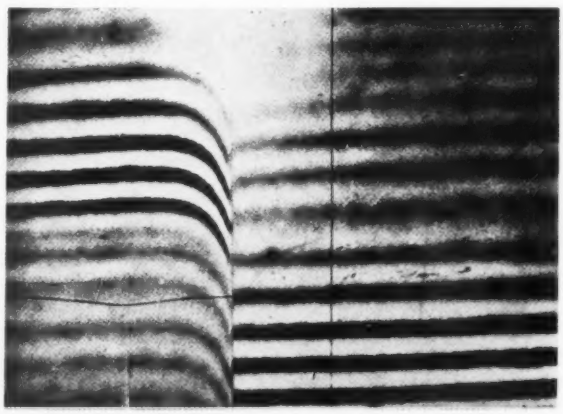

FIG. 21. Relaxation in a plane shock in CO_2, after Bleakney. The adjustment of vibrational energy takes a certain time, and the corresponding length for transition is clearly visible. Flow direction from right to left.

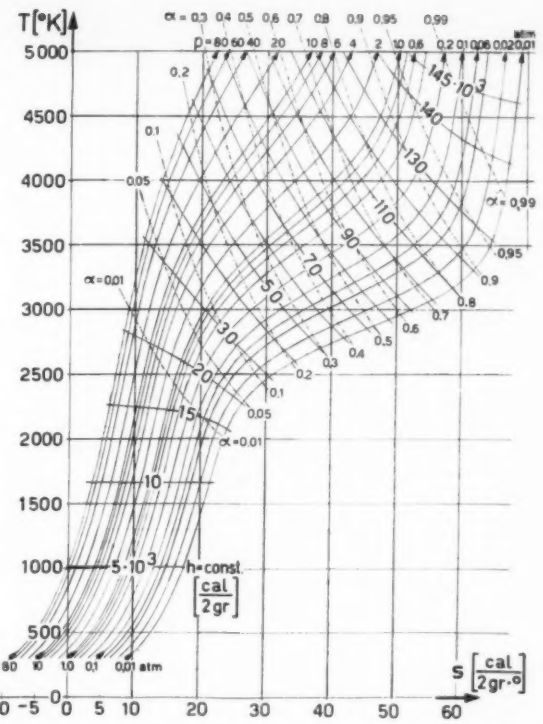

FIG. 22. Entropy chart for hydrogen gas taking dissociation into account. α is the degree of dissociation, h the enthalpy for one gram mole of H_2 (2 gm.).

be calculated directly. But we may expect that important developments will materialize in time.

The second course is more fundamental. It starts from the kinetic theory of nonuniform gases, using the Maxwell-Boltzmann equation. Entropy is given a new definition which in the limit leads to the classical equilibrium relations.

Thus we see that a new era is beginning in thermodynamics, one rather more adapted to practical phenomena in which viscosity, heat conduction, diffusion and chemical reactions all act at the same time. It may be that the old generation will be disappointed at the growing complexity of the subject, but then we have the young scientists well acquainted with abstract thinking and with the tremendous possibilities of electronic calculation. The development of theory may be slow at times, but there is always some way out of the difficulties. Let us just remember that at the beginning of this century viscous flow at high Reynolds numbers was practically intractable with the old methods, especially if turbulence occurred, but that thanks to the work of Prandtl, von Kárámn, Taylor, Dryden and so many others, these problems are now solved to a considerable extent. So there is never room for despair.

Appendix

(1) *Isothermal Expansion*

Take the recovery factor equal to one, for simplicity; then the temperature T_{g_w} of the gas near the wall is

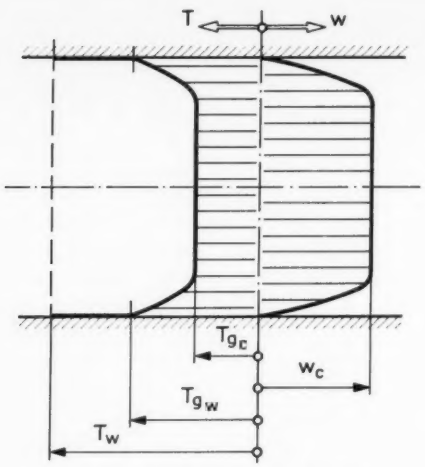

FIG. 23. See Appendix, Section(1).

higher than the gas temperature T_{g_c} in the nearly undisturbed center by the amount $w_c^2/2c_p$ (Fig. 23). Heat transfer from the wall stops if

$$T_g + (w_c^2/2c_p) = T_w$$

From this point on, an adiabatic expansion to zero pressure gives

$$(w_{max}^2 - w_c^2)/2c_p = T_{g_c}$$

so that $$\frac{w_{max}^2}{2c_p} = T_{g_c} + (w_c^2/2c_p) = T_w$$

This means that there is no gain over the simple isentropic expansion [Eq. (16) of the text].

(2) *Minimum Propulsive Power*

Step (*a*). Power is produced through utilization of the temperature difference between T_2 and T_1 in a Carnot cycle, the pressure and velocity of the gas remaining constant. We have to take away continuously the heat (per unit mass)

$$dq = -c_p dT$$

The Carnot efficiency is equal to

$$\eta_c = 1 - (T_1/T)$$

Integration between the limits T_2 and T_1 yields

$$\Delta A = c_p\{(T_2 - T_1) - T_1 \ln (T_2/T_1)\}$$

Summed up over the whole boundary layer, the power gained is:

$$L_a = \int_0^{\delta_2} \rho_2 w_2 c_p\{(T_2 - T_1) - T_1 \ln (T_2/T_1)\}\, dy$$

Step (*b*). The gas at uniform temperature T_1 and variable velocity w_2 is now accelerated to w_1 by isentropically working fans. The power needed is simply

$$L_b = \int_0^{\delta_2} \rho_2 w_2 \left(\frac{w_1^2 - w_2^2}{2}\right) dy = \int_0^{\delta_2} \rho_2 w_2 c_p (T_2 - T_1)\, dy$$

The total propulsive power is the difference $L_b - L_a$:

$$L_p = L_b - L_a = c_p T_1 \int_0^{\delta_2} \rho_2 w_2 \ln \left(\frac{T_2}{T_1}\right) dy$$

$$= c_p T_1 \int_0^{\delta_2} \rho_2 w_2 \ln \left(1 + \frac{w_1^2 - w_2^2}{2c_p T_1}\right) dy$$

On the other hand, the entropy flux S_2 is given by the following integral:

$$S_2 = c_p \int_0^{\delta_2} \rho_2 w_2 \ln \left(\frac{T_2}{T_1}\right) dy$$

Hence we have

$$L_p = T_1 S_2$$

We can introduce an equivalent drag, $D' = T_1 S_2/w_1$ which is smaller than D by the factor S_2/S_3. As a simplified example we may take a laminar boundary layer with $Pr = 1$ and $\gamma = 1.40$, at Mach 2 where the velocity profile is approximately linear. In this example the ratio D'/D equals 0.62 and the ratio L_a/L_b is 0.18.

(3) *Absolute Entropy of a Monatomic Gas*

A relatively simple method for the calculation of the entropy from first principles, due to H. A. Lorentz,[30] can be modified to include quantum effects. For simplicity, we take one gram atom of a monatomic gas. Its volume v then contains N atoms, where $N = 6.025 \times 10^{23}$ (Avogadro's number).

For a detailed description of the state of this complicated mechanical system we should know $3N$ positional coordinates $(q_1, q_2, \ldots, q_{3N})$ and $3N$ momentum components $(p_1, p_2, \ldots, p_{3N})$.

We shall imagine a $6N$-dimensional "phase space" (q,p). The microscopic state of the gas is then represented by one single point in this space. If v and T are fixed, this point can move only in a limited region, the so-called phase volume. This volume is given by the integral

$$\phi' = \ldots \iiint dq_1\, dq_2 \ldots dq_{3N}\, dp_1\, dp_2 \ldots dp_{3N}$$

which can be divided into a spatial factor

$$\phi'_{sp} = \ldots \iiint dq_1\, dq_2 \cdots dq_{3N}$$

and a momentum factor

$$\phi'_{mom} = \ldots \iiint dp_1\, dp_2 \cdots dp_{3N}$$

as coordinates and momenta are independent.

ϕ'_{sp} is simply equal to v^N, as every molecule has the full spatial range v. ϕ'_{mom} requires a special consideration. The total energy E of the gas is kinetic, as we exclude interaction of the atoms other than impacts in collisions. Therefore the momenta have to fulfill the condition

$$\frac{p_1^2}{2m} + \frac{p_2^2}{2m} + \ldots + \frac{p_{3N}^2}{2m} = E = \frac{3}{2} R_m T$$

m being the mass of one atom. In other words, the representative point moves on a spherical surface in

the momentum space (p) with radius

$$P = \sqrt{p_1^2 + p_2^2 + \ldots + p_{3N}^2} = \sqrt{2mE}$$

Now it is important to note that the volume enclosed by a many-dimensional sphere is practically concentrated in an extremely thin surface shell. Indeed, if we write for the total volume

$$J = \text{const.} r^n$$

a surface layer of small thickness Δr has the partial volume

$$\Delta J = \text{const.}(nr^{n-1}\Delta r)$$

the ratio being

$$\Delta J/J = n(\Delta r/r)$$

As n is of the order 10^{24}, ΔJ is comparable to J even if the thickness Δr is only the 10^{24}th part of r. Therefore, we can take the whole volume of the p-sphere instead of a very thin surface layer.

According to a well-known calculation, the volume of such a hypersphere turns out to be

$$\phi'_{mom} = [\pi^{3N/2}/(3N/2)!]P^{3N}$$

The total phase volume is now

$$\phi' = \phi'_{xp}\,\phi'_{mom} = v^N\,\phi'_{mom}$$

If we take classical mechanics to the last consequence, it does not make sense to substitute an infinitesimally thin sheet for a volume. But with Heisenberg's principle of indeterminacy, quantum mechanics has brought a certain latitude (Δp, Δq) into the fixation of momenta and coordinates. For one degree of freedom, for instance, we have

$$\Delta x \cdot \Delta p_x = h = \text{Planck's constant}$$

For $3N$ degrees of freedom, the elementary volume of phase space is therefore not infinitesimal but equal to h^{3N}.

We have to measure the phase volume in this unit (Sackur-Tetrode-Brody), and the surface layer has a small but finite thickness. So we find:

$$\phi'' = (\phi'/h^{3N})$$

as a natural measure of phase volume. This is not the end. Another quantum phenomenon enters: the indistinguishability of the atoms. If we interchange the nth and the mth atoms, the representative point changes place in the surface layer if the atoms are considered as distinct. But if they are indistinguishable, both points represent the same physical reality, and consequently the accessible phase volume is reduced. We can exchange every atom with every other in $N!$ ways, and the phase volume that really counts is

$$\phi = \phi''/N!$$

Entropy is now defined as being proportional to the logarithmic measure of the accessible phase volume, the constant factor being Boltzmann's

$$k = R_m/N$$

and so we obtain the following formula for the absolute entropy:

$$s = k \ln \phi = k \ln \left\{ \frac{v^N \pi^{3N/2} P^{3N}}{(3N/2)!\, h^{3N} N!} \right\}$$

As N is an extremely great number, we can use Stirling's formula with good approximation:

$$\ln n! = n(\ln n) - n$$

and after some simple algebraic manipulation, we find

$$s/R_m = \ln v + \ln \pi^{3/2} + \ln \left(\frac{2mE}{h^2}\right)^{3/2} + \frac{5}{2} - \frac{5}{2} \ln N - \frac{3}{2} \ln \frac{3}{2}$$

Substituting p (pressure) and T for v and $E = (3/2)R_m T$, we obtain Eq. (39) of the text.

References*

[1] Carnot, N. S., *Réflexions sur la puissance motrice du feu et sur les machines propres à développer cette puissance*, Bachelier, Paris, 1824.

[2] Clausius, R., *Ueber die bewegende Kraft der Wärme*, Poggendorffs Annalen, Vol. 79, pp. 368–397, 500–524, 1850.

[3] Clausius, R., *Ueber verschiedene für die Anwendung bequeme Formen der Hauptgleichungen der mechanischen Wärmetheorie*, Poggendorffs Annalen, Vol. 125, pp. 353–400, 1865.

[4] Emden, R., Nature, Vol. 141, pp. 908–909, 1938.

[5] Brillouin, L., *Science and Information Theory*, Academic Press, New York, 1956.

[6] Gouy, J., Physique, Vol. 8, p. 501, 1889.

[7] Stodola, A., Zeitschrift des Vereins deutscher Ingenieure, Vol. 42, p. 1088, 1898.

[8] Winterberg, F., Proceedings of the IXth International Astronautical Congress (Amsterdam, 1958), Vol. 1, p. 181; Springer Verlag, Vienna, 1959.

[9] Stingelin, V., *Isotherme Düsenströmungen*, Astronautica Acta, Vol. 6, pp. 61–74, 1960.

[10] Ackeret, J., *A System of Rocket Propulsion Using Reactors and Gas Turbines*, Proceedings of the IXth International Astronautical Congress (Amsterdam, 1958), Vol. 1, pp. 277–281, Springer Verlag, Vienna, 1959.

[11] Resler, E. L., and Rott, N., *On Rocket Propulsion with Nuclear Power*, Preprint ARS Semiannual Meeting, Los Angeles, Calif., 1960.

[12] Crocco, L., *Eine neue Stromfunktion für die Erforschung der Bewegung der Gase mit Rotation*, ZAMM, Vol. 17, pp. 1–7, 1937.

[13] Oswatitsch, K., *Der Luftwiderstand als Integral des Entropiestromes*, Nachr. Ges. Wiss. Göttingen. Math. Phys. Kl., pp. 88–90, 1945.

[14] Pfenninger, W., *Design Considerations of Large Subsonic Long-Range Transport Airplanes with Low Drag Boundary-Layer Suction*, Norair Division of Northrop Corp. Report No. NAI-58-529 (BLC-111), 1958. (Revised April, 1959.)

[15] Becker, R., *Stosswelle und Detonation*, Zeitschrift für Physik, Vol. 8, pp. 321–362, 1922.

[16] Roy, M., *Analyse énergétique de la structure de l'onde de choc*, Compt. rend. Acad. Sci., Vol. 251, pp. 178–181, 1960.

(*Continued on page 102*)

* References: As entropy is treated in many books on physics, physical chemistry, and gasdynamics, there is no need for a general survey of literature. Therefore only a few books and papers immediately connected with the substance of this lecture are cited.

Radiation From Hot Air and Its Effect on Stagnation-Point Heating†

BENNETT KIVEL*

Avco-Everett Research Laboratory

Summary

The heating of the stagnation region of a blunt body by radiation from the hot air in the shock layer is investigated for flight speeds up to 50,000 ft./sec. by using experimental shock-tube data, supplemented by theoretical estimates. Nonequilibrium effects which modify the radiation predictions at high altitudes ($\geq$30 miles) are pointed out. The radiation is compared with the aerodynamic heating and is found to be important at high velocities ($\geq$30,000 ft./sec.) and low altitudes ($\leq$25 miles). For this flight regime the dominant radiation results from the capture of electrons by nitrogen ions.

Symbols

A	= area
c	= constant
E	= energy
h	= enthalpy
I	= radiated power per unit volume
k	= Boltzmann's constant 8.62×10^{-5} ev./deg.
n	= integer
N	= particle density
p	= pressure
q	= heat transfer
r	= distance
R	= nose radius
π	= 3.1416
ρ	= mass density
σ	= 5.67×10^{-12} watts/cm.^{2} deg.^{4}
T	= temperature
v	= flight velocity
V	= volume
W	= weight
Z	= effective electric charge

Subscripts

aero.	= aerodynamic
D	= drag
i	= radiation species
rad.	= radiation
ST	= stagnation region
0	= sea level
∞	= free stream

Received December 7, 1959.

† This work was sponsored jointly by Ballistic Missile Division, ARDC, USAF, under Contract AF-04(647)-278, and Army Rocket and Guided Missile Agency, AOMC, USA, under contract DA-19-020-ORD-4862 under ARPA order 39-59 Task 6.

* Principal Research Scientist.

The author is indebted to the director of the Avco-Everett Research Laboratory, Dr. Arthur Kantrowitz, without whose guidance these results would not have been produced. Drs. M. C. Adams, J. C. Keck, N. H. Kemp, and J. D. Teare stimulated the writing of this manuscript and offered critical comments. The graphs were made under the supervision of H. Hidalgo and H. Kachadorian; J. Hayes provided the trajectories, and C. Lindenmeier estimated the Kramer's radiation in high-temperature air.

Introduction

THE PROBLEM of aerodynamic heat transfer at the stagnation point in dissociated air has been a subject of considerable interest in high-speed re-entry problems.[1] The literature deals with the conduction of energy through the boundary layer, taking into account the effects of diffusion and recombination of atomic species. Very little has been published[2] about the energy carried to the body by radiation from the high-temperature air outside the boundary layer. In this paper we apply recent shock-tube measurements of the emissivity of high-temperature air to the problem of estimating this radiative heat transfer. We compare radiation with aerodynamic heat transfer and find that radiation is dominant at high flight speeds and low altitudes.

The radiation heat transfer to the nose of re-entering IRBM's and ICBM's can be estimated using the results of shock-tube measurements. Until recently, this radiation was not predictable because the rate at which the molecular constituents of high-temperature air radiated was unknown. It was soon realized that nitric oxide was a potent possibility even though there is only a few per cent of NO present, because a relatively large fraction of these molecules can radiate.[3] This is not true of N_2 which is more plentiful. On the other hand, O_2 is strongly dissociated at high temperatures. As we will note below, it turns out that NO has a low rate of radiation[4] so that the radiation from air is not important in the ballistic-missile re-entry regime.

Recent interest in higher re-entry speeds, such as might be encountered on a return from an elliptic orbit around Mars,[5] has revived the radiation heating problem. A theoretical study of this problem indicates that for high re-entry velocities and high performance, radiation heat transfer may be orders of magnitude greater than the aerodynamic heat transfer. In this case the important radiation source is the recombination of nitrogen ions and electrons, for which reasonably accurate theoretical estimates can be made.

In the next section we summarize the basic physics of high-temperature air radiation. These results are applied to the problem of estimating the energy radiated by air at stagnation conditions. We then set forth several limitations on the use of our results. Finally, we apply the results to the calculation of stagnation-point heat transfer during re-entry of typical ICBM and Mars probe vehicles.

Radiation From High-Temperature Air

The shock tube is an extremely useful tool for determining absolute radiation intensities. Spectroscopists have determined the spectral locations of the radiation from the important molecules in high-temperature air. However, there exists only limited knowledge about the corresponding rate of radiation because of the complicated nonequilibrium light sources that are conventionally employed. The shock tube has the advantage of providing a source of high-temperature gas of known temperature and density. With this source it was a straightforward job to calibrate the radiation emission from high-temperature air in the regime important for IRBM and ICBM re-entry. These measurements are summarized in a recent paper by Keck, et al.[4] For example, the measured radiation at 8,000°K. and one atmosphere of density is ~7 per cent per centimeter of gas thickness of the total black body radiation (σT^4) or ~1.6 kilowatts per cm.^{2} There is no single dominant radiation source. The radiation comes primarily from the diatomic molecules, N_2, O_2, and NO. About 10 per cent of the radiation comes from the capture of electrons by atomic oxygen to form negative oxygen ions.

The experimental uncertainty indicated by the internal consistency of the shock-tube measurements is about 30 per cent. However, the possibility of systematic errors has not been completely eliminated and uncertainties as large as a factor 2 cannot be ruled out.[17]

Scaling laws based on statistical mechanics have been used by Kivel and Bailey[6] to make predictions at temperatures and densities where measurements have not been made. However, as the temperature and density deviate appreciably from the region where measurements are made, the uncertainty increases because the important radiating species change. Fig. 1 is a graph of the energy radiated per unit volume as a function of temperature for constant values of the density from Kivel and Bailey. Their estimate uses the composition, according to statistical mechanics for thermodynamic equilibrium, rough but reasonably correct statistical scaling factors for the temperature dependence of the fraction of radiating molecules, an adjustment of the radiation rates to agree with shock-tube measurements and rough estimates for the radiation rates where measurements are not available. The radiation is computed as a sum of contributions expressed as

$$I_i = N_i c_i T^{n_i} e^{-E_i/kT}$$

where N_i is the density of the radiating species, and c_i a constant adjusted to available experimental information. E_i is the energy of the excited molecular level of the radiation transition and n_i is an appropriate integer: -1 for NO and O_2, 0 for other diatomic and triatomic radiation considered and $+1$ for the Kramer's radiation. The Kramer's radiation results from the deceleration of electrons by atoms or ions; if the electron is captured it is called recombination, if just deflected then it is called Bremsstrahlung.

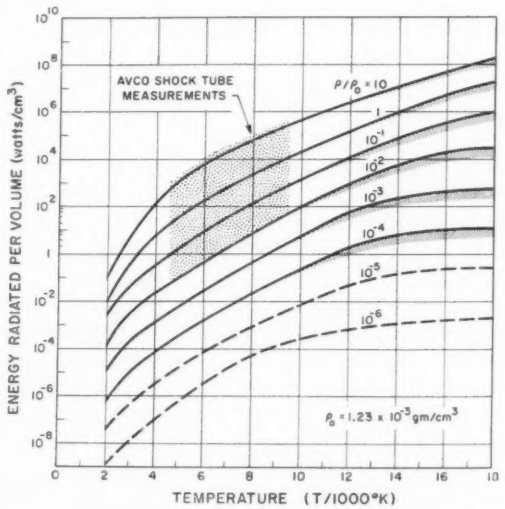

FIG. 1. Total emitted radiation energy per unit volume of high-temperature air in full equilibrium as a function of temperature for constant values of the density.

The region where shock-tube measurements determine the radiation level is indicated by the shaded area in Fig. 1. It covers temperatures from 5,000–9,000°K. and density ratios from 10^{-2} to 10 atmospheres.

In the low temperature region one must consider the triatomic molecules as NO_2, O_3, and CO_2. There is also a strong radiation from the NO vibration-rotation transitions—an infrared radiation in which the radiated energy comes only from the vibration and rotation degrees of freedom and not from the electronic excitation of the molecule, as in the other cases. The magnitude of this radiation is reasonably well determined.[7] Near, 1,000°K., the CO_2 vibration-rotation radiation is dominant.[8]

In Fig. 1 we have dashed the theoretical curves at very low densities, 10^{-5} and 10^{-6} atmospheres, because the "collision limiting" effect,[4] which has not been taken into account, will reduce the radiation level except where NO vibration-rotation radiation is important. The collision limiting depends on the ratio of the rate of radiation for the important species to the rate of excitation by collision of this radiation. At low densities, the rate of excitation will not be sufficient to maintain the statistical population of radiating states against the cooling by radiation emission. For NO vibration-rotation which is readily excited and a slow radiator, the effect will not become important until lower densities are reached. The recombination radiation has not been investigated carefully but we estimate it to be collision limited at $\rho/\rho_0 = 10^{-4}$ which is coincidental with our estimate for the diatomics based on investigations by Keck, et al.[4]

In Fig. 1 we have shaded the region below the Kivel and Bailey estimate indicating the uncertainty in the Kramer's radiation from $N^+ + e$. We have paid special attention to the accuracy of this radiation pre-

diction because the radiative heat transfer is important for very high speed re-entry. Our prediction of radiation heat transfer in this regime is primarily theoretical. However, an adequate theory is more feasible in this case than at lower temperatures where molecular rates dominate. To a reasonable approximation, the Kramer's radiation can be treated by a hydrogen-like model for which an exact solution exists.[9] Lindenmeier[10] has recently reviewed this problem and suggests that the effective charge for nitrogen ions capturing electrons is $Z = \sqrt{1.5}$. This result predicts a radiation energy emission rate which is a factor one-half less than the original estimate in Kivel and Bailey. The high estimate in Kivel and Bailey was made intentionally to be consistent with a shock-tube measurement of the Kramer's radiation from argon.[11] The uncertainties in the theory used by Lindenmeier center around (1) the many atomic lines in the spectrum and (2) the suppression of the ionization potential by collisions in the high-temperature gas. Both these corrections increase the estimate made by Lindenmeier. However, he indicates that the increase is not sufficient to reach the earlier estimate of Kivel and Bailey. Because of this uncertainty it would be well to obtain experimental values prior to making engineering decisions affected by this radiation level.

Oxygen contributes about 1/10 as much radiation as nitrogen corresponding to the ratio of their ion densities. The nitrogen is favored by the fact that there is more nitrogen in air and by statistical factors which favor N^+ over O^+ by 81/16. On the other hand, the ionization potential of oxygen is slightly lower.

In order to predict the radiation heat transfer one should integrate the energy radiated per unit volume, which depends on the local temperature and density $[I(T, \rho)]$, over that volume of the bow shock which can radiate to the point of interest. The expression for the heat transfer per unit area is approximately

$$q_{\text{rad.}} = \frac{1}{4\pi} \int \frac{I(T, \rho)}{r^2} \, dV \qquad (1)$$

where r is the distance from the surface to volume element (dV). The factor $4\pi r^2$, the area of a sphere with

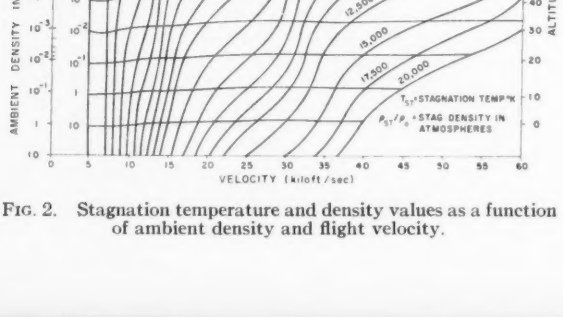

FIG. 2. Stagnation temperature and density values as a function of ambient density and flight velocity.

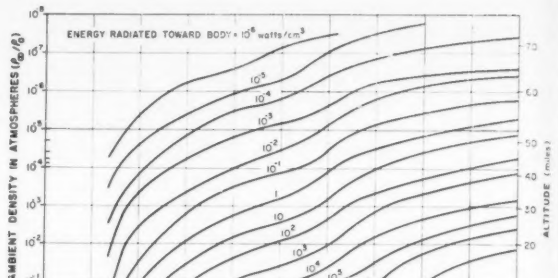
ENERGY RADIATED TOWARD BODY × 10^6 watts/cm^3
AMBIENT DENSITY IN ATMOSPHERES (ρ_∞/ρ_0)
ALTITUDE (miles)
VELOCITY (kilofeet/sec)

FIG. 3. One-half of the emitted radiation energy per unit volume from the stagnation region for full equilibrium as a function of ambient density and flight velocity.

radius r, is introduced to give the radiation per unit area at a distance r from an isotropic source.

Since the detachment distance is approximately equal to the radius of curvature of the vehicle nose divided by the density ratio at the shock, which is of order 10, the detachment distance is small compared to the radius of curvature. Consequently, we can treat the radiation to the stagnation point as if it came from a semi-infinite plane, with the thickness equal to the detachment distance. Then we can approximate for the stagnation region

$$q_{\text{rad.}} \doteq I(T_{ST}\rho_{ST})R\rho_\infty/2\rho_{ST} \qquad (2)$$

where the factor 2 enters, since half of the energy leaves each side of the semi-infinite plane. We see that the radiation heat transfer goes as the nose radius because the detachment distance is proportional to R. This is in contrast with the aerodynamic heat transfer which is inversely proportional to $\sqrt{R}$.

Stagnation-Point Radiation Heat Transfer

The stagnation temperature and density as a function of altitude and flight velocity is given in Fig. 2. It is convenient for scaling nonequilibrium effects to work in terms of the ambient density instead of the altitude, hence our figures use the ratio of air density to sea level density as the linear coordinate. The corresponding altitude in miles from the ARDC atmosphere, revised slightly above 60 miles by Carleton,[13] is given on the right-hand side of the figure. The stagnation values are obtained for speeds under 25,000 ft./sec. from tables of Feldman[12] and over that speed from recent calculations at Avco-Everett Research Laboratory by Keeler and Winkler.* Keeler and Winkler have calculated the equation of state of high-temperature air—i.e., they have determined the enthalpy and pressure of air for given values of temperature and density. In order to relate the temperature and density to the flight speed and altitude, we have used the following approximations. First, we take the stagnation en-

* C. L. Keeler and H. B. Winkler, private communication of unpublished results.

thalpy per unit mass to be equal to one-half the square of flight speed, $h_{ST} = v^2/2$. Having determined the flight velocity, we find the ambient density corresponding to the stagnation pressure by approximating $p_{ST} = \rho_\infty v^2$. The constant temperature lines contain kinks in the regions where oxygen and nitrogen dissociation and ionization are changing rapidly.

Fig. 3 is a plot of the radiation energy per unit volume, found by combining the information given in Figs. 1 and 2, which is emitted toward the body in the stagnation region. From Fig. 1 we obtain the energy radiated per unit volume as a function of temperature and density and from Fig. 2, the stagnation temperature and density. To convert from the total energy radiated to the energy radiated toward the body it is necessary to divide by 2 because half of the radiation leaves each side from a thin slab of radiating gas. In order to make estimates for radiative heat transfer, it is necessary to place the flight trajectory on this altitude-velocity map and multiply the energy radiated per unit volume by the detachment distance in cm. As a first approximation, one can take the detachment distance to be 1/10 of the nose radius. For more accurate work, the density ratio across the shock can be obtained from Fig. 2.

As can be seen in Fig. 3, the radiation heating increases rapidly with increasing flight velocity and decreasing altitude. A body that re-enters at high speed and high drag can avoid the high radiation region because it decelerates at high altitudes. In the subsequent discussion we will pursue the question of the magnitude of radiation heating for typical trajectories.

In Fig. 4, we give three typical trajectories corresponding to the re-entry of an ICBM, a satellite and Mars probe. The ICBM has a 5,500 nautical mile minimum energy trajectory with $W/C_DA = 400$. The satellite trajectory is in accord with the NASA specifications for Project Mercury with a $W/C_DA = 28$ and a 2° re-entry angle at 60 nautical miles. The Mars probe has an elliptic orbit, which passes around Mars, has a $W/C_DA = 50$ and re-enters vertically. On this figure we also show several limitations on the radiation predictions which will be amplified later. It is seen that the low W/C_DA satellite flies above the equilibrium line. As a result, the radiation heating will be greater than indicated by the predictions of Figs. 1 and 3. This increase is somewhat compensated by the "collision limiting" effect. Also shown are lines that indicate when the aerodynamic heat transfer is 1/10 of, equal to, and 10 times the radiation heating for a nose radius of 1 ft. It is seen that the ICBM trajectory does not cross the line where the radiation heating become equal to the aerodynamic for $R = 1$ ft. For this reason, the radiation heating can be neglected, except for the highest performance cases.

This is not true for the return from Mars. In this case, the radiation heating in the neighborhood of the peak heat-transfer region exceeds the aerodynamic heat transfer.

Conditions of Validity and Approximations

The equilibrium predictions of radiation intensity given in Figs. 1 and 3 are subject to several limitations. These limitations, which are important at higher altitudes, are delineated in Fig. 4. At very high altitudes a shock wave is not formed in front of the reentering vehicle—a condition described as free molecule flow. Our predictions are of no use in computing radiation in this regime. In the figure, we have separated this region by a line labeled "free molecule flow" at which the mean distance a molecule from the surface travels before a collision with an incident air molecule equals the nose radius; $R = \lambda_\infty \bar{c}/v$, where R is the nose radius; λ_∞ is the mean distance between collisions in the ambient air; $\bar{c}$ is the mean speed of particles leaving the surface; and v is the flight speed of the vehicle. At this altitude, almost all of the particles incident on the vehicle suffer at least one collision before being intercepted.[14] The line is drawn for a nose radius of 1 ft., assuming that the particles leave the surface with a mean speed corresponding to the surface temperature of 300°K. and the collision cross section is 3×10^{-15} cm.^{2} This line will occur at higher altitudes for larger vehicles and will scale so the product of nose radius and ambient air density is a constant. Somewhere below this altitude a detached shock forms in front of the vehicle. In this region the surface will have a strong cooling effect on the gas behind the shock. At a somewhat lower altitude the viscous part of the shock layer is sufficiently thin so that there is a high-temperature inviscid region. According to Adams and Probstein,[15] this inviscid flow appears when $R \doteq 10^2 \lambda_\infty v/(26{,}000$ ft./sec.). This line, labeled "no inviscid region" also scales so that $R\rho_\infty =$ constant.

The next correction to be considered is the diminution of radiation because the radiation-producing collisions are too infrequent compared to the rate of emitted radiation. This phenomena, which has already been described, is called collision limiting, and depends primarily on the gas density. It also depends on the time for molecular radiation, which varies in the neighborhood of 10^{-6} to 10^{-8} sec. for air components.

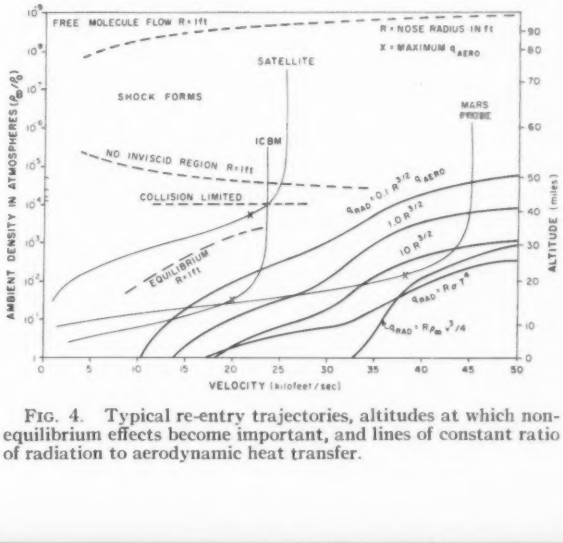

FIG. 4. Typical re-entry trajectories, altitudes at which non-equilibrium effects become important, and lines of constant ratio of radiation to aerodynamic heat transfer.

A mean height for the onset of collision limiting is indicated in Fig. 4 by the "collision limited" line drawn by assuming a mean radiation lifetime of 10^{-7} sec. and a de-excitation collision cross section of 10^{-15} cm.^{2} Above this line the radiation decreases more rapidly by a factor ρ because of collision limiting. This altitude is independent of R.

Another nonequilibrium correction occurs because of the finite relaxation zone at the shock front. In this region, the molecular constituents are excited to vibration equilibrium and dissociated by gas kinetic collisions. When the time to relax is long compared to the time a particle takes to flow along a streamline from the shock front through the shock layer, then consideration of nonequilibrium phenomena becomes essential. The radiation from this region may overshoot the corresponding equilibrium value. This is because of the high nonequilibrium translational temperature. At high Mach numbers a strong overshoot of nonequilibrium radiation is observed in shock tubes.[16] This overshoot disappears at lower speeds and lower altitudes. In Fig. 4 the line labeled "equilibrium" gives the altitude at which the relaxation time is approximately equal to the time it takes a gas particle to pass through the shock layer. It is only below this altitude that the equilibrium predictions of Fig. 3 are correct. This line scales so that $R\rho_\infty \doteq$ constant.

There are two further restrictions on using the results presented in Figs. 1 and 3 about which the reader should be cautioned. The first is that the radiation intensity will not exceed the statistical maximum called the Planck or black-body radiation intensity (σT^4). This condition is

$$q_{\text{rad.}} < \sigma T^4 = 56.7\ (T/10^{4\circ}\text{K.})^4 \text{kilowatts/cm.}^2 \quad (3)$$

the limiting case in which they are equal for $R = 1$ ft. is plotted on Fig. 4. This statistical limit arises because the molecules which radiate also absorb radiation with the consequence that all of the radiation radiated does not leave a radiating gas. When the radiation intensity approaches the black-body limit, the radiation is calculated using a transfer theory which accounts for both emission and absorption. When making estimates of radiation heating, it is sufficient to neglect the absorption and assume that the emission increases linearly with the detachment distance until the black-body limit is reached. One should use the black-body limit for greater thicknesses. This approximation gives a slight overestimate ($\sim$20 per cent) when the radiation intensity is close to the black-body limit.

The second correction deals with the attenuation of the energy in the shock layer by radiation.* When the radiation level is comparable with the energy in the flow it must be considered in determining the temperature distribution in the stagnation region. It is therefore required that

$$\left.\begin{array}{l} 2q_{\text{rad.}} < \rho_\infty v^3/2 = 1.7 \times 10^3(\rho_\infty/\rho_0) \\ (v/10^4 \text{ ft./sec.})^3 \text{ kilowatts/cm.}^2 \end{array}\right\} \quad (4)$$

The factor 2 is introduced since the gas is cooled by the total radiation emitted. The line $q_{\text{rad.}} = R\rho_\infty v^3/4$ is plotted on Fig. 4 with R in feet.

Both of these effects become important at the higher velocities and lower altitudes of Fig. 3. In fact, for the Mars probe the peak value of $q_{\text{rad.}}$ is about 1/3 of σT^4 and $2q_{\text{rad.}}$ is about 1/3 of $\rho v^3/2$.

We have assumed that the radiating gas has a uniform temperature and density. In fact, the temperature falls off as the gas flows around the body. As a result, the effective temperature for predicting the radiation at the stagnation point is somewhat less than the stagnation temperature. Since the radiation is sensitive to temperature, this is a correction that should be made when requiring an accuracy better than $\sim$30 per cent.

The radiation must pass through the boundary layer before reaching the surface of the vehicle. It is possible that the boundary layer, in view of its high density, will absorb some of the radiation incident on the body. However, as is well known, cold air is a good transmitter of light so that, coupled with the thinness of the boundary layer, we do not predict appreciable boundary-layer absorption. In passing, we note that this effect is less important at higher altitudes since the boundary-layer thickness increases as $\rho^{-1/2}$ while the absorption decreases roughly as ρ^2. The latter factor arises because the density of molecules in a dissociating gas goes roughly as ρ^2; one power because there are fewer particles and one because of increased dissociation.

While the problem of heating with both ablation and radiation is a complicated one which remains to be solved, we note that the ablated vapors may absorb appreciable amounts of the incident radiation. In this way, ablation might produce a decrease in radiative heat transfer. Thus, there are several possible situations, depending on the radiation intensity: (1) a small amount of radiation increases the rate of ablation and consequently decreases the aerodynamic heat transfer tending to cancel the effect of radiation; (2) an intermediate intensity of radiation, which is not compensated for by the blowing and decreased aerodynamic transfer, so that the ablating material is not as effective as against pure aerodynamic heating of the same total magnitude; and (3) a larger amount of radiation so that the rapid ablation produces an absorbing vapor which may protect the surface.

Applications

In Figs. 5 and 6, we compare the aerodynamic and radiative heating for an ICBM and a Mars probe. We have estimated the aerodynamic heating using

$$q_{\text{aero.}} \doteq 10^3(\rho_\infty/\rho_0)^{1/2}(v/10^4 \text{ ft./sec.})^3 R^{-1/2} \text{ watts/cm.}^2 \quad (5)$$

where v is the flight speed in ft./sec. and R is the nose

* See Goulard, R., *A Comment on "Radiation From Hot Air and Its Effect on Stagnation-Point Heating,"* Journal of the Aerospace Sciences, Readers' Forum, Vol. 28, No. 2, pp. 158–159, February, 1961.

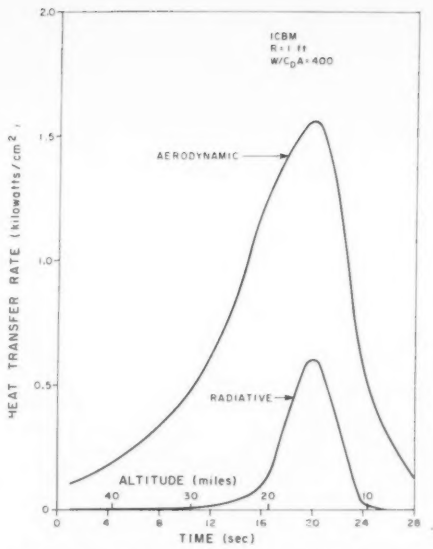

FIG. 5. Comparison of aerodynamic and radiation heat transfer during re-entry for a typical ICBM.

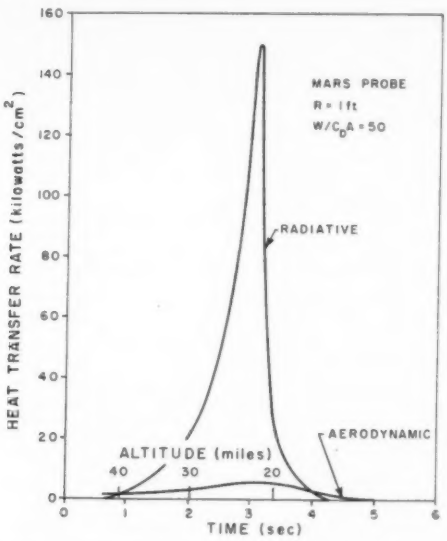

FIG. 6. Comparison of radiation and aerodynamic heat transfer during re-entry for a Mars probe.

radius in feet, which is consistent with shock-tube measurements of Rose and Stark.[1] These measurements of aerodynamic heat transfer do not extend to the high-velocity regime of interest for the Mars probe. In this region one may question the simple formula because there is appreciable ionization and the electrons may effect the heat conductivity. While we do not have the solution to this problem, Eq. (5) is adequate for illustrative purposes and may actually be correct.* At higher flight speeds and lower altitudes, this expression should require revision.

The radiative heat transfers are obtained using Fig. 3 with the trajectories shown in Fig. 4. We have not done the calculation for the satellite because it flies in the nonequilibrium region and, as a result, the radiation in the region of peak heating is larger than indicated in Fig. 3. We defer this to a future publication when an adequate description of the nonequilibrium radiation is available. In both the ICBM and Mars probe calculations, the peak in the radiative transfer precedes that of the aerodynamic heating. This is because the radiation is more strongly dependent on the flight speed than the aerodynamic heat transfer.

In the case of the 5,500 nautical mile minimum energy ICBM with a nose radius of 1 ft. and $W/C_DA = 400$, the peak radiative heat-transfer rate is about 1/3 of the aerodynamic. The total radiation heating is seen in Fig. 5 to be about 1/10 of the aerodynamic. This is because the radiative falls roughly as the density squared, while the aerodynamic goes as the density to the 1/2 power. As a result, the radiation becomes important at lower altitudes; it also diminishes more rapidly while the vehicle decelerates. For the Mars probe (Fig. 6) with $R = 1$ ft., $W/C_DA = 50$, and vertical re-entry, the radiative heating is much larger than the aerodynamic in both peak and total values. In this case the radiative heat-transfer rate reaches 150 kw./cm.^{2} and is more than 10 times the peak aerodynamic value. The condition of validity that $2q_{rad.} < \rho v^3/2$ causes concern. This effect of radiation cooling has not been computed and deserves further study. Since the correction reduces the radiation, we must consider our result as a conservative overestimate. The radiative rate is about 100 times the aerodynamic peak of 1.5 kw./cm.^{2} found for the ICBM example.

The high radiative heat transfer in the Mars probe can be avoided to some extent. One may use a smaller nose radius since the radiative transfer goes in proportion to R, and the aerodynamic in proportion to $R^{-1/2}$. For example, a 3-in. nose radius in our example would receive a peak radiative heat-transfer rate of 50 kw./cm.^{2} while the aerodynamic rate would only be increased by a factor 1.7 to about 10 kw./cm.^{2} A second change would be to slow the vehicle down at a higher altitude, which may be accomplished by using a lower performance or a shallower re-entry angle.

It might be well to remind the reader of the uncertainty in the radiation prediction for the Mars probe. The important radiation from the stagnation region is the Kramer's recombination of electrons and nitrogen ions which is uncertain in absolute magnitude by about a factor 2. A measurement of the absolute radiation intensity should be made. The value used in our prediction is probably high and may be considered conservative.

References

[1] Rose, P. H., and Stark, W. I., *Stagnation Point Heat-Transfer Measurements in Dissociated Air*, Journal of the Aeronautical Sciences, Vol. 25, No. 2, pp. 86–97, February, 1958. Kemp, N. H., and Riddell, F. R., *Heat Transfer to Satellite Vehicles Re-*

* M. C. Adams, private communication.

entering the Atmosphere, Jet Propulsion, Vol. 27, pp. 132–137, February, 1957. Fay, J. A., Riddell, F. R., and Kemp, N. H., *Stagnation Point Heat Transfer in Dissociated Air Flow*, Jet Propulsion, Vol. 27, No. 6, pp. 672–674, June, 1957. Detra, R. W., Kemp, N. H., Riddell, F. R., *Addendum to Heat Transfer to Satellite Vehicles Re-Entering the Atmosphere*, Jet Propulsion, Vol. 27, p. 1256, December, 1957. Fay, J. A., and Riddell, F. R., *Theory of Stagnation Point Heat Transfer in Dissociated Air*, Journal of the Aeronautical Sciences, Vol. 25, No. 2, pp. 73–85, 121, February, 1958. Kemp, N. H., Rose, P. H., and Detra, R. W., *Laminar Heat Transfer Around Blunt Bodies in Dissociated Air*, Journal of the Aero/Space Sciences, Vol. 26, No. 7, pp. 421–430, July, 1959. This is only a partial list, being limited to works with which the author is familiar. However, these articles contain more complete reference lists.

[2] Meyerott, R. E., *Radiation Heat Transfer to Hypersonic Vehicles*, Lockheed Aircraft Corporation Missile Systems Division, Palo Alto, California, LMSD-2264, November, 1957.

[3] Kivel, B., Mayer, H., and Bethe, H., *Radiation from Hot Air—Part I, Theory of Nitric Oxide Absorption*, Annals of Physics, Vol. 2, No. 1, pp. 57–80, July, 1957. See also, Thompson, A., *Emmissivity Estimates for Heated NO*, Technical Report No. 6, Contract AF 18(603)-2, California Institute of Technology, 1957.

[4] Keck, J. C., Camm, J. C., Kivel, B., and Wentink, T., Jr., *Radiation from Hot Air—Part II, Shock Tube Study of Absolute Intensities*, Annals of Physics, Vol. 7, No. 1, pp. 1–38, May, 1959. Keck, J., Camm, J., and Kivel, B., *Absolute Emission Intensity of Schumann-Runge Radiation from Shock Heated Oxygen*, J. Chem. Phys., Vol. 28, No. 4, pp. 723–724, April, 1958. Wentink, Jr., T., Planet, W., Hammerling, P., and Kivel, B., *Infrared Continuum Radiation from High-Temperature Air*, J. Appl. Phys., Vol. 29, No. 4, pp. 742–743, April, 1958.

[5] Battin, R. H., *The Determination of Round-Trip-Planetary Reconnaissance Trajectories*, Journal of Aero/Space Sciences, Vol. 26, No. 9, pp. 545–567, September, 1959.

[6] Kivel, B., and Bailey, K., *Radiation from High Temperature Air*, Avco-Everett Research Laboratory, Research Report 21, January, 1958.

[7] Penner, S. S., *The Emission of Radiation from Diatomic Gases—I. Approximate Calculations*, J. Appl. Phys., Vol. 21, pp. 685–695, July, 1950. Benitez, L. E., and Penner, S. S., *The Emission of Radiation from Nitric Oxide: Approximate Calculations*, J. Appl. Phys., Vol. 21, pp. 907, 908, September, 1950.

[8] Hottel, H. C., *Radiant-Heat Transmission*, Heat Transmission, Adams, W. H., (Ed.), Chap. 4, McGraw-Hill Book Co., Inc., New York, 1954.

[9] Unsold, A., *Physik der Sternatmospharen*, Springer, Berlin, 1938.

[10] Lindenmeier, C. W., *Kramer's Radiation from Hot Air*, Avco-Everett Research Laboratory, Research Note 157, September, 1959.

[11] Petschek, H., Rose, P. H., Glick, H. S., Kane, A., and Kantrowitz, A., *Spectroscopic Studies of Highly Ionized Argon Produced by Shock Waves*, J. Appl. Phys., Vol. 26, pp. 83–95, January, 1955.

[12] Feldman, S., *Hypersonic Gas Dynamic Charts for Equilibrium Air*, Avco-Everett Research Laboratory, January. 1957.

[13] Carleton, N. P., *Bibliography on Upper Atmosphere; Summary of Current Knowledge of Basic Properties of the Upper Atmosphere*, Avco-Everett Research Laboratory, Research Note 91, September, 1958.

[14] Hammerling, P., and Kivel, B., *Heat Transfer to a Sphere at the Transition from Free Molecule Flow*, The Physics of Fluids, Vol. 1, No. 4, p. 357, July–August, 1958.

[15] Adams, M. C., and Probstein, R. F., *On the Validity of Continuum Theory for Satellite and Hypersonic Flight Problems at High Altitudes*, Jet Propulsion, pp. 86–89, February, 1958.

[16] Camac, M., Camm, J., Feldman, S., Keck, J., and Petty, C., *Chemical Relaxation in Air, Oxygen and Nitrogen*, Paper presented at the Hypersonic Aerodynamics Session, IAS 26th Annual Meeting, New York, January 27–30, 1958. Camac, M., Camm, J., Keck, J., Petty, C., *Relaxation Phenomena in Air Between 3,000 and 8,000°K.*, Avco-Everett Research Laboratory, Research Report 22, March, 1958.

[17] Penner, S. S., *Quantitative Molecular Spectroscopy and Gas Emissivities*, Addison-Wesley Publishing Co., Inc., Reading, Mass., 1959.

✦ ✦ ✦

The Role of Entropy (*Continued from page 95*)

[17] Thomas, L. H., J. Chem. Phys., Vol. 12, p. 449, 1944.

[18] Greene, E. F., Cowan, G. R., and Hornig, D. F., J. Chem. Phys., Vol. 19, p. 427, 1951.

[19] Greene, E. F., and Hornig, D. F., J. Chem. Phys., Vol. 21, p. 617, 1953.

[20] Sherman, F. S., *Low Density Wind-Tunnel Study of Shock-Wave Structure and Relaxation Phenomena in Gases*, NACA TN 3298, 1955.

[21] Patterson, G. N., *Molecular Flow of Gases*, p. 113; John Wiley & Sons, Inc., New York, 1956.

[22] Mott-Smith, H. M., *The Solution of the Boltzmann Equation for a Shock Wave*, Phys. Rev., Vol. 82, p. 885, 1951.

[23] Sprenger, H., *Ueber thermische Effekte in Resonanzrohren*, Mitteilungen aus dem Institut für Aerodynamik ETH, No. 21, pp. 18–35, 1954.

[24] Hartmann, J., *Modus Operandi of the Air-Jet Pulsator*, (Vorträge Aachen 1929), pp. 169–183; Springer Verlag, Berlin, 1930.

[25] Gibbs, J. W., (1875), *Collected Works*, p. 166; Longmans, Green and Co., New York, 1928.

[26] Kantrowitz, A., *Heat-Capacity Lag in Gasdynamics*, J. Chem. Phys., Vol. 14, p. 150, 1946.

[27] Bleakney, W., *Transient Phenomena in Supersonic Flow*, in *Modern Physics for the Engineer*, L. Ridenour, ed., p. 362; New York, 1954.

[28] Ackeret, J., *Ueber Widerstände, die durch gasdynamische Relaxation hervorgerufen werden*, ZFW., Vol. 4, pp. 14–17, 1956.

[29] Busemann, A., *Handbuch der Experimentalphysik*, Vol. 4, Part 1, pp. 357–358, Leipzig, 1931.

[30] Lorentz, H. A., *Les théories statistiques en thermodynamique*, pp. 9–10 and 80–81; Teubner, Leipzig, 1916.

[31] de Groot, S. R., *Thermodynamics of Irreversible Processes*, North-Holland Publishing Co., Amsterdam, 1951.

✦ ✦ ✦

Solution of Subsonic Nonplanar Lifting Surface Problems by Means of High-Speed Digital Computers

L. J. KULAKOWSKI* AND R. N. HASKELL**

Convair, A Division of General Dynamics Corporation

Summary

The method proposed in this paper is based on an approximate solution of the integral equation which represents the potential flow about a finite wing, with no restrictions beyond those necessary for linearization. After assuming the usual series representation of the wing surface vorticity distribution, the solution is achieved by approximating portions of the kernels of the transformed integral equation by single and double Fourier series and performing termwise integrations analytically. This is followed by the routine inversion of the aerodynamic influence coefficient matrix, after satisfying appropriate boundary conditions at selected control points. In this procedure the number of control points used is limited only by the storage capacity of the computer. Control points may be located so as to cover the entire wing surface, with due regard to certain physical requirements, permitting the accurate representation of complicated mean surface shapes.

An evaluation of the proposed method is included. Comparisons with other theoretical methods and electrical analogy tank results are used to substantiate the accuracy of the proposed method when applied to plane wings. A final evaluation involves a comparison of calculated surface pressure distribution with wind-tunnel measurements on a swept, tapered wing with a cambered and twisted mean surface. The agreement evidenced in the latter comparison has the same order of overall accuracy as similar comparisons on plane wing planforms. In either case, the results given by the proposed method are within the accuracy requirements for most aircraft design studies.

Symbols

$A_{k,l}$ = coefficients in Fourier series
AR = wing aspect ratio, $4s^2/S$
$a_{\mu,\,n}$ = vorticity series coefficients
c = wing chord at any span station
c_R = wing root chord
M = Mach number
Δp = pressure differential across the wing mean surface, $p_{\text{lower}} - p_{\text{upper}}$
q = free-stream dynamic pressure, $(1/2)\rho V^2$
R = $\sqrt{(x - x_0)^2 + \beta^2(y - y_0)^2}$
R_0 = $\sqrt{(x - x_0)^2 + (y - y_0)^2}$
S = total wing area
s = wing semispan
V = free-stream velocity
w = perturbation velocity component parallel to the z axis, positive downward
x_0, y_0 = Cartesian coordinates of wing surface control points
β = Prandtl-Glauert factor, $\sqrt{1 - M^2}$
Γ = total circulation about any wing span station
η, ξ = axes in the transformed coordinate system
θ = arc cos $(-\xi)$
Λ = sweep angle of the wing mid-chord line, positive for sweepback
λ = wing taper ratio
μ = index in vorticity series, even for antisymmetric loading, odd for symmetric loading
ρ = free-stream density
σ = ratio of wing root chord to span, $c_R/2s$
τ = $1 - \lambda$
φ = arc cos η

Received December 9, 1959.

* Design Specialist, Aero Sciences Group, Convair—Fort Worth.

** Project Aerodynamics Engineer, Aero Sciences Group, Convair—Fort Worth.

Introduction

AT LEAST thirty different methods for the calculation of subsonic loadings on finite, lifting wings have been presented in the literature since Prandtl's initial attack on the problem in 1918. Most of these methods rely on specializations of the basic, linearized integral equation for the lifting surface and are thus restricted to particular ranges of aspect ratios or planforms.

An early method which used the integral equation for a continuous distribution of vorticity in the plane of the wing and wake was presented by Blenk.[1] More recently, the development of true lifting surface methods was stimulated by the advent of low aspect ratio, swept wing planforms. Some such methods are those developed by Weissinger[2] (F method), Multhopp,[3] and van de Vooren.[4] The method proposed in this paper is based on van de Vooren's form of the integral equation and uses an original scheme for the solution, which is readily adaptable to high-speed digital computing equipment. The principal advantage of the proposed method is that the surface control points may be located so as to cover the entire wing, with due regard to physical requirements, and are limited in number only by the storage capacity of the computing machine. Consequently, the subsonic aerodynamic characteristics of cambered and twisted wings may readily be determined. The proposed method is of particular value in ascertaining the subsonic aerodynamic characteristics of aircraft employing wings with warped mean surfaces designed, say, to improve their supersonic performance. It has additional utility in the calculation of airloads for static aeroelastic analyses on wings with appreciable chordwise deformation.

The proposed method is based on a solution of the linearized differential equation for the perturbation

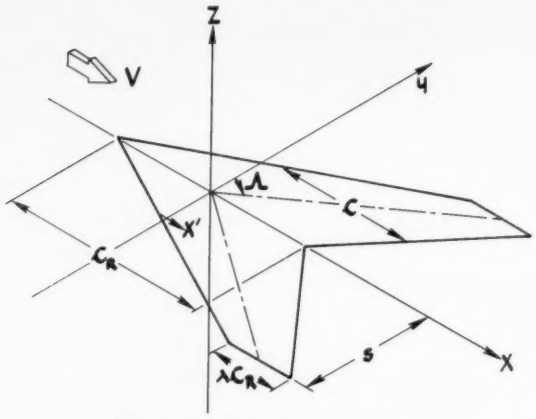

FIG. 1. Wing planform geometry.

velocity potential, which governs the subsonic compressible flow of an ideal fluid. As such, the method is limited by the following linearizing restrictions:

(1) The flow is potential.
(2) The perturbation velocities are small compared to the free-stream velocity.
(3) The wing is made up of thin (line) airfoil sections.
(4) The vertical displacement of the wing surface is so small that the tangential flow boundary conditions may be satisfied in the $z = 0$ plane.

Some consequences of these restrictions are discussed elsewhere in this paper.

The Integral Equation

Consider a lifting wing immersed in an incompressible, potential flow field. The wing may be represented by a continuous distribution of vorticity within the wing surface (S) and wake (W), with the induced downwash being given by application of the Biot-Savart law,

$$w(x_0, y_0) = -\frac{1}{4\pi}\left\{\iint_S \frac{(x - x_0)\gamma_y}{R_0^3}\,dxdy - \iint_{S+W} \frac{(y - y_0)\gamma_x}{R_0^3}\,dxdy\right\} \quad (1)$$

where γ_x and γ_y are components of the local vorticity vector parallel to the x and y axes, respectively. A complete derivation of Eq. (1) is given by Bisplinghoff, Ashley, and Halfman.[5]

Eq. (1) has never been inverted analytically. Its direct use for even an approximate evaluation of downwash results in certain mathematical difficulties. Van de Vooren[4] avoided these difficulties by applying the transformation

$$x = f(\eta) + \xi(c/2), \quad y = \eta s \quad (2)$$

where $f(\eta)$ represents the equation of the wing midchord line. Eq. (2) transforms the wing planform from the x, y plane into a square in the ξ, η plane.

After substituting Eq. (2) and performing a number of manipulations, van de Vooren converted Eq. (1) to the form

$$w(\xi_0, \eta_0) = -\frac{1}{4\pi s}\left[\frac{1}{2}\int_{-1}^{1}\int_{-1}^{1} c\gamma_y \frac{\partial J'}{\partial \eta}\,d\xi d\eta + \int_{-1}^{1} \frac{d\Gamma/d\eta}{\eta - \eta_0}\,d\eta\right] \quad (3)$$

where, by definition,

$$J'(\xi_0, \eta_0; \xi, \eta) = -s^2 \int \frac{x - x_0}{R_0(y - y_0)^2}\,d\eta \quad (4)$$

Eqs. (3) and (4) define the surface downwash for all types of wing planforms. However, if the planform boundaries are curved, application of these expressions will generally require the evaluation of some complicated, singular, elliptic-type integrals. Only trapezoidal wing planforms with straight edges, like that illustrated in Fig. 1, are considered in this paper. For trapezoidal planforms the transformation (2) may be written as

$$x = |\eta| s \tan \Lambda + (\xi/2)c_R(1 - \tau|\eta|), \quad y = \eta s \quad (5)$$

The relationship between the Cartesian and ξ, η coordinates is illustrated in Fig. 2.

The function J' has a finite discontinuity at wing span stations where either the leading or trailing edge of the planform has a sudden change in slope—e.g., the root chord of a swept, trapezoidal wing. In this case, a more tractable form of Eq. (3) is derived by a partial integration of the first term with respect to η,

$$w(\xi_0, \eta_0) = \frac{1}{4\pi s}\left\{\frac{1}{2}\int_{-1}^{1}\int_{-1}^{1} J' \frac{\partial(c\gamma_y)}{\partial \eta}\,d\eta d\xi - \int_{-1}^{1} \frac{d\Gamma/d\eta}{\eta - \eta_0}\,d\eta + \frac{1}{2}\int_{-1}^{1} [J'(\xi_0, \eta_0; \xi, 0^+) - J'(\xi_0, \eta_0; \xi, 0^-)](c\gamma_y)_{\eta=0}\,d\xi\right\}, \quad \eta_0 \neq 0 \quad (6)$$

A solution for the wing loading requires that the tangential flow boundary conditions be satisfied at certain surface control points (ξ_0, η_0). Since the method is based on linearized theory, the principle of superposition may be applied to determine asymmetric loadings from combinations of symmetric and antisymmetric loadings. Consequently, the control points are always located on the right wing panel ($\eta_0 > 0$).

To determine the J' functions for trapezoidal planforms, consider the control point ξ_0, η_0 illustrated in Fig. 2. For field points located in the right wing panel, Eqs. (5) yield

$$\left.\begin{aligned} x - x_0 &= (\eta - \eta_0)s \tan \Lambda + (1/2)c_R[\xi - \xi_0 - \tau(\eta\xi - \eta_0\xi_0)] \\ R_0 &= \sqrt{\{(\eta - \eta_0)s \tan \Lambda + (1/2)c_R[\xi - \xi_0 - \tau(\eta\xi - \eta_0\xi_0)]\}^2 + (\eta - \eta_0)^2 s^2} \end{aligned}\right\} \quad 0 \leq \eta \leq 1 \quad (7)$$

and, for field points located in the left wing panel,

$$\left.\begin{aligned} x - x_0 &= -(\eta - \eta_0)s \tan \Lambda + (1/2)c_R[\xi^* - \xi^*_0 + \tau(\eta\xi^* + \eta_0\xi^*_0)] \\ R_0 &= \sqrt{\{-(\eta - \eta_0)s \tan \Lambda + (1/2)c_R[\xi^* - \xi^*_0 + \tau(\eta\xi^* + \eta_0\xi^*_0)]\}^2 + (\eta - \eta_0)^2 s^2} \end{aligned}\right\} \quad -1 \leq \eta \leq 0 \qquad (8)$$

where

$$\xi^*_0 = \frac{\sigma(1 - \tau\eta_0)\xi_0 + 2\eta_0 \tan \Lambda}{\sigma(1 + \tau\eta_0)}$$

Introducing $t = \eta - \eta_0$, the indefinite integral (4) may be written as

$$J' = -\int \frac{A + Bt}{t^2\sqrt{(A + Bt)^2 + s^2t^2}}\, dt = \frac{\sqrt{(A + Bt)^2 + s^2t^2}}{At}$$

Upon defining A and B by comparison with Eqs. (7) and (8), it follows that

$$\left.\begin{aligned} J'(\xi_0, \eta_0; \xi, \eta^+) &= \frac{\sqrt{\{\sigma(1 - \tau\eta_0)(\xi - \xi_0) + (\tan \Lambda - \sigma\tau\xi)(\eta - \eta_0)\}^2 + (\eta - \eta_0)^2}}{\sigma(1 - \tau\eta_0)(\xi - \xi_0)(\eta - \eta_0)} \\ J'(\xi_0, \eta_0; \xi^*, \eta^-) &= \frac{\sqrt{\{\sigma(1 + \tau\eta_0)(\xi^* - \xi^*_0) - (\tan \Lambda - \sigma\tau\xi^*)(\eta - \eta_0)\}^2 + (\eta - \eta_0)^2}}{\sigma(1 + \tau\eta_0)(\xi^* - \xi^*_0)(\eta - \eta_0)} \end{aligned}\right\} \qquad (9)$$

The above summary of van de Vooren's approach was included here to indicate the background of the proposed method and to establish a point of demarcation from van de Vooren's analysis of the problem. Solution of the problem requires the inversion of Eq. (6). This is achieved in an approximate manner by assuming a series representation for the vorticity distribution, performing the integrations of Eq. (6) and then inverting a matrix formed by satisfying the boundary conditions at a number of discrete control points within the wing planform.

The Vorticity Distribution

Before discussing the form of the vorticity distribution it is advantageous to make a further transformation to angular coordinates,

$$\xi = -\cos \theta, \quad \eta = \cos \varphi \qquad (10)$$

Note that $\theta = 0$ at the leading edge and π at the trailing edge, while $\varphi = 0$ at the right wing tip and π at the left wing tip. The form of vorticity distribution assumed in most lifting surface methods is

$$c\gamma_y = c\Delta p/\rho V = 2g_0(\varphi) \cot (\theta/2) + 4 \sum_{n=1}^{\bar{n}-1} g_n(\varphi) \sin n\theta \qquad (11)$$

where

$$g_n(\varphi) = (4sV/\pi) \sum_{m=1}^{\bar{m}} a_{\mu,\, n} \sin \mu\varphi$$

with $\mu = 2m - 1$ for symmetric loadings and $\mu = 2m$ for antisymmetric loadings. This amounts to the combination of spanwise series with the chordwise loading terms suggested by Birnbaum[6] for two-dimensional airfoils.

The series (11) adequately represents the vorticity distribution for rectangular wings and for antisymmetric loadings on all trapezoidal wings. However, for symmetric loading problems on planforms having kinked edges (such as the root chord of a swept wing), three-dimensional effects cause localized loading errors

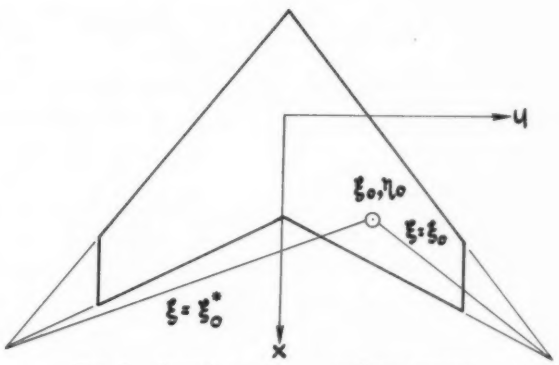

FIG. 2. Cartesian and ξ, η coordinate systems.

if (11) is used to represent the vorticity distribution. These errors are caused by the difficulty in making (11) satisfy the symmetry requirement that lines of constant vorticity (isobars) must be orthogonal to the root chord.

A number of authors have proposed several artifices to satisfy the symmetry requirement at the root chord. For example, Multhopp[3] essentially solved for the loading on a planform whose kink was rounded off, while Falkner[7] adopted a local modification to the surface vorticity distribution. As noted previously, using the proposed method for planforms with rounded edges produces some rather formidable integrals. On the other hand, modifying the vorticity distribution leads to the problem of selecting a series having the proven convergence properties of (11). One vorticity modification was attempted in the study of the proposed method. It consisted of adding terms of the form

$$\sum_{n=1}^{N} h_n(\varphi)[1 + \cos (2n - 1)\theta]$$

where

$$h_n(\varphi) = 4sV \sum_{m=1}^{\bar{m}+1} b_{2m-1,n}\,(1 - |\cos\varphi|)\sin(2m-1)\varphi$$

to (11) and satisfying an analytical orthogonal isobar condition at N discrete points on the root chord. This approach was abandoned when the rate of convergence proved inadequate.

For the purposes of this paper, the localized loading error associated with using the series (11) is accepted. The fact that this assumption does not lead to significant errors is established by comparisons of the proposed method with other theoretical and experimental results. The total circulation about any wing span station caused by the vorticity distribution (11) is

$$\Gamma(\varphi) = (1/2)\int_{-1}^{1} c\gamma_y d\xi = \pi[g_0(\varphi) + g_1(\varphi)] \quad (12)$$

This result is used, with Eq. (11), in the integration of Eq. (6).

Solution of the Integral Equation

A direct integration of Eq. (6) is impractical because of the complicated nature of the J' functions and the line singularities which occur on the lines $\xi = \xi_0$, $\xi^* = \xi^*_0$, and $\eta = \eta_0$. An alternate integration procedure, which takes advantage of the rapid convergence properties of Fourier series, is outlined below.

If the singular terms in the J' functions are split off, the resulting expressions are continuous. These expressions are the J functions,

$$\left.\begin{aligned} J(\xi_0, \eta_0; \xi, \eta^+) &= \frac{\sqrt{\{\sigma(1-\tau\eta_0)(\xi-\xi_0) + (\tan\Lambda - \sigma\tau\xi)(\eta-\eta_0)\}^2 + \beta^2(\eta-\eta_0)^2}}{\sigma(1-\tau\eta_0)} \\ J^*(\xi_0, \eta_0; \xi^*, \eta^-) &= \frac{\sqrt{\{\sigma(1+\tau\eta_0)(\xi^*-\xi^*_0) - (\tan\Lambda - \sigma\tau\xi^*)(\eta-\eta_0)\}^2 + \beta^2(\eta-\eta_0)^2}}{\sigma(1+\tau\eta_0)} \end{aligned}\right\} \quad (13)$$

The Prandtl-Glauert factor, β, accounts for compressibility effects and was included in the J functions by applying the similarity rules given by Dickson.[8] It is of interest to note that

$$R = \sigma(1-\tau\eta_0)J = \sigma(1+\tau\eta_0)J^*$$

Hence, for sets of J and J^* values appropriate to a specified planform and control point, these equations represent right, elliptic cones in the J, x, y space, with major axes parallel to the y axis and apexes located at the control point.

With the substitution of Eq. (13), Eq. (6) may be written in the form

$$w(\xi_0, \eta_0) = \frac{1}{8\pi s}\left\{\int_{-1}^{0}\int_{-1}^{1} \frac{J^*(\xi_0, \eta_0; \xi^*, \eta)}{(\xi^* - \xi^*_0)(\eta - \eta_0)} \frac{\partial(c\gamma_y)}{\partial\eta}\, d\xi^* d\eta + \int_{0}^{1}\int_{-1}^{1} \frac{J(\xi_0, \eta_0; \xi, \eta)}{(\xi - \xi_0)(\eta - \eta_0)} \frac{\partial(c\gamma_y)}{\partial\eta}\, d\xi d\eta\right\} -$$
$$\frac{1}{4\pi s}\int_{-1}^{1} \frac{d\Gamma/d\eta}{\eta - \eta_0}\, d\eta - \frac{1}{8\pi s\eta_0}\int_{-1}^{1}\left[\frac{J(\xi_0, \eta_0; \xi, 0^+)}{\xi - \xi_0} - \frac{J^*(\xi_0, \eta_0; \xi, 0^-)}{\xi - \xi^*_0}\right](c\gamma_y)_{\eta=0}\, d\xi, \quad \eta_0 \neq 0 \quad (14)$$

The restriction $\eta_0 \neq 0$ imposed on control point locations stems from the indeterminate form of the last term in Eq. (14). As will be seen later, locating control points precisely on the root chord is not necessary to achieve solutions by the proposed method. The various integrals of (14) may be evaluated analytically if the J functions are represented by Fourier series, after using the transformation (10). Hence,

$$\bar{J}(\xi_0, \eta_0; \xi, \eta) = \sum_{k=0}^{h-1}\sum_{l=0}^{j-1} \epsilon_k\epsilon_l \bar{A}_{k,l} \cos k\theta \cos l\varphi \quad (15)$$

and

$$\bar{J}(\xi_0, \eta_0; \xi, 0) = \sum_{k=0}^{h-1} \epsilon_k \bar{A}_k \cos k\theta \quad (16)$$

where $\epsilon_0 = 1/2$ and $\epsilon_k = \epsilon_l = 1$ for $k \neq 0, l \neq 0$. In these expressions $\bar{J}$ represents J or J^* while $\bar{A}$ represents A or A^*, respectively. The series coefficients are determined by means of double and single harmonic analyses—i.e.,

$$\bar{A}_{k,l} = \frac{4}{hj}\sum_{\alpha=0}^{h-1}\sum_{\delta=0}^{j-1} \bar{J}\left[\xi_0, \eta_0; -\cos\frac{(2\alpha+1)\pi}{2h}, \cos\frac{(2\delta+1)\pi}{2j}\right]\cos\frac{k(2\alpha+1)\pi}{2h}\cos\frac{l(2\delta+1)\pi}{2j} \quad (17)$$

and

$$\bar{A}_k = \frac{2}{h}\sum_{\alpha=0}^{h-1} \bar{J}\left[\xi_0, \eta_0; -\cos\frac{(2\alpha+1)\pi}{2h}, 0\right]\cos\frac{k(2\alpha+1)\pi}{2h} \quad (18)$$

By this procedure both J functions are approximated in the entire region $0 \leq \theta \leq \pi$, $0 \leq \varphi \leq \pi$, even though each is used within only a portion of this region in (14). This step eliminates a spanwise normalization which would complicate the integrations.

After transforming to the θ, φ plane by applying Eq. (10) and substituting Eqs. (11), (12), (15), and (16), Eq. (14) becomes

$$\frac{w}{V}(\xi_0, \eta_0) = \sum_{m=1}^{\bar{m}} \sum_{n=0}^{\bar{n}-1} a_{\mu,n} \, Wa_{\mu,n}, \quad \eta_0 \neq 0 \tag{19}$$

where

$$Wa_{\mu,0} = \frac{1}{\pi} \sum_{k=0}^{h-1} \sum_{l=0}^{j-1} \mu\epsilon_k\epsilon_l [A_{k,l} I_{l,\mu} G_k + A^*_{k,l} I^*_{l,\mu} G^*_k] + \mu \frac{\sin \mu\varphi_0}{\sin \varphi_0} + \frac{\sin (\mu\pi/2)}{\pi \cos \varphi_0} \sum_{k=0}^{h-1} \epsilon_k (A_k G_k - A^*_k G^*_k)_{\eta=0}$$

$$Wa_{\mu,1} = \frac{2}{\pi} \sum_{k=0}^{h-1} \sum_{l=0}^{j-1} \mu\epsilon_k\epsilon_l [A_{k,l} I_{l,\mu} H_{k,1} + A^*_{k,1} I^*_{l,\mu} H^*_{k,1}] + \mu \frac{\sin \mu\varphi_0}{\sin \varphi_0} + \frac{2 \sin (\mu\pi/2)}{\pi \cos \varphi_0} \sum_{k=0}^{h-1} \epsilon_k (A_k H_{k,1} - A^*_k H^*_{k,1})_{\eta=0}$$

$$Wa_{\mu,n} = \frac{2}{\pi} \sum_{k=0}^{h-1} \epsilon_k \left\{ \sum_{l=0}^{j-1} \mu\epsilon_l [A_{k,l} I_{l,\mu} H_{k,n} + A^*_{k,l} I^*_{l,\mu} H^*_{k,n}] + \frac{\sin (\mu\pi/2)}{\cos \varphi_0} (A_k H_{k,n} - A^*_k H^*_{k,n})_{\eta=0} \right\}, \quad n > 1$$

In Eq. (19) the coefficients of similar unknowns have been grouped to facilitate computation. New symbols introduced in these expressions represent chordwise and spanwise integrals. The chordwise integrals are

$$\bar{G}_k = \frac{1}{\pi} \int_0^\pi \frac{(1 + \cos \theta) \cos k\theta}{\cos \theta + \bar{\xi}_0} \, d\theta, \quad \bar{H}_{k,n} = \frac{1}{\pi} \int_0^\pi \frac{\cos k\theta \sin n\theta \sin \theta}{\cos \theta + \bar{\xi}_0} \, d\theta$$

where $\bar{G}_k$ represents G_k or G^*_k when $\bar{\xi}_0$ is ξ_0 or ξ^*_0, respectively, with the same rule applying to $\bar{H}_{k,n}$. The spanwise integrals are

$$I_{l,\mu} = \int_0^{\pi/2} \frac{\cos l\varphi \cos \mu\varphi}{\cos \varphi - \cos \varphi_0} \, d\varphi, \quad I^*_{l,\mu} = \int_{\pi/2}^{\pi} \frac{\cos l\varphi \cos \mu\varphi}{\cos \varphi - \cos \varphi_0} \, d\varphi$$

All of these integrals are evaluated below.

Consider the integrals $\bar{G}_k$, which may be written in the form

$$\bar{G}_k = \frac{1}{\pi} \int_0^\pi \frac{\cos k\theta + (1/2) \cos (k-1)\theta + (1/2) \cos (k+1)\theta}{\cos \theta + \bar{\xi}_0} \, d\theta$$

All three terms in the integrand represent standard integrals given by Grobner and Hofreiter.[9] It follows that

$$\left.\begin{aligned} \bar{G}_0 &= 1; \quad \bar{G}_k = \sin k\theta_0 \cot (\theta_0/2), \quad k > 0 \qquad -1 < \bar{\xi}_0 \leq +1 \\ \bar{G}_k &= (1/\sqrt{\bar{\xi}_0^2 - 1})[K_0^k + (1/2)(K_0^{|k-1|} + K_0^{k+1})], \quad \bar{\xi}_0 > +1 \\ &= [(-1)^k/\sqrt{\bar{\xi}_0^2 - 1}][-K_0^k + (1/2)(K_0^{|k-1|} + K_0^{k+1})], \quad \bar{\xi}_0 < -1 \end{aligned}\right\} k \geq 0 \tag{20}$$

where

$$K_0 = \sqrt{\bar{\xi}_0^2 - 1} - |\bar{\xi}_0|$$

Furthermore, taking the limit at the leading edge,

$$\lim_{\bar{\xi}_0 \to -1} \bar{G}_k = 2k, \quad k > 0$$

The latter equation is only used for the parameter ξ^*_0 (when the wing has a swept forward leading edge), since the control points are never located precisely on the leading edge. An analogous evaluation technique is used for the $\bar{H}_{k,n}$ integrals. After writing

$$\bar{H}_{k,n} = \frac{1}{4\pi} \int_0^\pi \frac{\cos (n-1-k)\theta + \cos (n-1+k)\theta - \cos (n+1-k)\theta - \cos (n+1+k)\theta}{\cos \theta + \bar{\xi}_0} \, d\theta$$

it can be shown that

$$\left.\begin{aligned} \bar{H}_{k,n} &= -\cos k\theta_0 \cos n\theta_0, \quad n > k \\ &= -(1/2)(2 \cos^2 k\theta_0 - 1), \quad n = k \\ &= \sin k\theta_0 \sin n\theta_0, \quad n < k \end{aligned}\right\} -1 \leq \bar{\xi}_0 \leq +1$$

$$\left.\begin{aligned} &= [1/(4\sqrt{\bar{\xi}_0^2 - 1})](K_0^{|n-1-k|} + K_0^{n-1+k} - K_0^{|n+1-k|} - K_0^{n+1+k}), \quad \bar{\xi}_0 > +1 \\ &= [(-1)^{n+k}/4\sqrt{\bar{\xi}_0^2 - 1}](K_0^{|n-1-k|} + K_0^{n-1+k} - K_0^{|n+1-k|} - K_0^{n+1+k}), \quad \bar{\xi}_0 < -1 \end{aligned}\right\} \tag{21}$$

This completes the evaluation of the chordwise integrals for all possible control point locations.

The spanwise integrals may be evaluated by first considering an integral of the form

$$I_{m'} = \int_{\varphi_1}^{\varphi_2} \frac{\cos m'\varphi}{\cos \varphi - \cos \varphi_0} d\varphi$$

which may be evaluated by use of the recursion formula

$$I_{m'+1} = (2/m')(\sin m'\varphi_2 - \sin m'\varphi_1) + 2I_{m'} \cos \varphi_0 - I_{m'-1}, \quad m' > 0 \tag{22}$$

and the initial values

$$\left.\begin{aligned} I_0 &= \frac{1}{\sin \varphi_0} \ln \frac{\sin (1/2)(\varphi_2 + \varphi_0) \sin (1/2)\,|\varphi_1 - \varphi_0|}{\sin (1/2)\,|\varphi_2 - \varphi_0| \sin (1/2)(\varphi_1 + \varphi_0)}, \quad \varphi_0 \neq \varphi_1, \varphi_2 \\ I_1 &= \varphi_2 - \varphi_1 + I_0 \cos \varphi_0 \end{aligned}\right\} \tag{23}$$

With use of a trigonometric substitution,

$$I_{l,\mu} = (1/2)(I_{l+\mu} + I_{|l-\mu|}) \tag{24}$$

so that, after letting m' be $l + \mu$ and $|l - \mu|$ in turn, the recursion formula (22) may be used to evaluate the spanwise integrals.

This completes the definition of all data required to compute the downwash at any control point by means of Eq. (19). The vorticity series coefficients $a_{\mu,n}$ may then be determined by solving the set of simultaneous equations formed in satisfying the tangential flow boundary conditions,

$$(w/V)(\xi_0, \eta_0) = -(\partial z/\partial x)(\xi_0, \eta_0) \tag{25}$$

at $\bar{m}\cdot\bar{n}$ control points located on the right wing panel. In matrix notation, these equations are

$$[W]\{a_{\mu,n}\} = \{-(\partial z/\partial x)\} \tag{26}$$

The choice of suitable control point locations is discussed in the following section.

Control Point Locations

The choice of control point locations for solving problems by the proposed method should, in general, be governed by the following practical considerations:

(1) Control points should be located at stations which would yield the best curve fit to the wing surface slopes.

(2) The density of control points should be greater in regions where the loading is varying rapidly—e.g., near the wing tips.

(3) Control points should not be located on the wing planform boundaries since these lines are loci of slope discontinuities between the wing and free stream.

The restriction against locating control points precisely at the root chord has already been mentioned. In the computer programing of the method control points located at the root are admissible since the program, after making appropriate tests, shifts these points to $\eta_0 = 0.01$. This step involves the tacit assumption that the last term of (14) approaches a finite value as η_0 tends to zero, a point which is open to argument. In the rigorous sense this assumption is quite invalid since, by applying an analysis similar to that given by Ursell[10] to a lifting, swept wing, it may be shown that the surface isobars must be orthogonal to the root chord if a finite downwash is to exist there. The assumption is justified only when it is considered as part of the localized error introduced by the chosen vorticity series (11).

In many lifting surface theories the author lists preferred control point locations chosen to yield relatively accurate solutions with the least computing effort. The means of defining preferred control point locations for the proposed method is not explicit. It was learned by experience that solutions derived from low-order matrices (20 control points, or less) are relatively unaffected by control point locations. However, solutions involving high-order matrices were often grossly in error when the control points were located in a random fashion, probably because of matrix error sensitivity.

These errors apparently originate in the integration scheme used to compute the surface downwash. As noted previously, the J functions describe right, elliptic cones with apexes at the given control point. The Fourier series (15) used to approximate the J functions are fitted at the points

$$\xi = -\cos \frac{(2\alpha + 1)\pi}{2h}, \quad \eta = \cos \frac{(2\delta + 1)\pi}{2j}$$

In general, the Fourier series approximation will tend to round off the J function in the vicinity of the apex. The largest error caused by rounding occurs when a surface control point exactly coincides with one of the fitting points. Conversely, a very good representation of the J functions will result if the control points are all located halfway between the fitting points—i.e.,

$$\left.\begin{aligned} \xi_0 &= -\cos \frac{\alpha\pi}{h} \cos \frac{\pi}{2h}, \quad \alpha = 0, 1 \ldots h - 1 \\ \eta_0 &= \cos \frac{\delta\pi}{j} \cos \frac{\pi}{2j}, \quad \delta = 0, 1 \ldots j - 1 \end{aligned}\right\} \tag{27}$$

A number of problems having up to 56 control points have been solved by the proposed method. All problems in which the control points were oriented as indicated by (27) resulted in accurate solutions. This is not to imply that the control point orientation given by (27) is an absolute guarantee of an accurate solution, since a singular downwash matrix may occasionally be written by chance.

Thanks to the rapid convergence of Fourier series, no particular advantage results from using different values for h and j. Consequently, it was assumed that $h = j$ in the computer programing of the proposed method.

For this case, Eqs. (27) yield the preferred control point locations listed in Table 1.

Only even values of $h = j$ are shown, to allow locating control points at the root chord. It should be emphasized that all of the control points listed in Table 1 for a specified h need not be used to solve a given problem, particularly if the surface slope distribution is fairly simple.

TABLE 1
Preferred Control Point Locations

h, j	$\pm\xi_0, \eta_0$	h, j	$\pm\xi_0, \eta_0$	h, j	$\pm\xi_0, \eta_0$
6	0	8	0	10	0
	0.48297		0.37533		0.30522
	0.83652		0.69353		0.58055
			0.90613		0.79906
					0.93935
12	0	14	0	16	0
	0.25660		0.22112		0.19411
	0.49572		0.43115		0.38076
	0.70106		0.61957		0.55278
	0.85862		0.77691		0.70355
	0.95766		0.89530		0.82729
			0.96880		0.91923
					0.97586

Aerodynamic Characteristics

After the vorticity series coefficients have been determined, the wing aerodynamic characteristics may be determined with use of relationships derived by elementary methods. Only the final results for the pertinent aerodynamic characteristics are given here, for both the symmetric and antisymmetric loading problems.

Local Pressure Coefficient

The local pressure coefficient at any point of the wing surface is given by

$$\frac{\Delta p}{q} = \frac{2\gamma_y}{V} = \frac{16s}{\pi c} \sum_{m=1}^{\bar{m}} \left(a_{\mu,0} \cot \frac{\theta}{2} + 2 \sum_{n=1}^{\bar{n}-1} a_{\mu,n} \sin n\theta \right) \sin \mu\varphi \quad (28)$$

where $s/c = 1/[2\sigma(1 - \tau|\eta|)]$

Section Lift Coefficient

The local lift coefficient at any span station is

$$c_l = (8s/c) \sum_{m=1}^{\bar{m}} (a_{\mu,0} + a_{\mu,1}) \sin \mu\varphi \quad (29)$$

Note that only the first two terms of the vorticity series (11) contribute to the lift.

Wing Lift Coefficient

The lift coefficient for the entire wing is determined from the expression

$$C_L = \pi AR(a_{1,0} + a_{1,1}) \quad (30)$$

Spanwise Load Distribution

Distribution of wing span loading is given by the relationship

$$\frac{c_l c}{c_{avg}} = 4AR \sum_{m=1}^{\bar{m}} (a_{\mu,0} + a_{\mu,1}) \sin \mu\varphi \quad (31)$$

where $c_{avg} = S/2s$ is the average wing chord length.

Spanwise Center of Pressure

Since only symmetric and antisymmetric loadings are considered, the spanwise center of pressure need be defined for only the right wing panel—i.e.,

$$\eta_{c.p.} = \frac{AR}{C_L^*} \left[\frac{\pi}{4} (a_{2,0} + a_{2,1}) - 2 \sum_{m=1}^{\bar{m}}{}'' (a_{\mu,0} + a_{\mu,1}) \frac{\sin(\mu\pi/2)}{\mu^2 - 4} \right] \quad (32)$$

where C_L^* is the lift coefficient for the right wing panel, given by

$$C_L^* = 2AR \left[\frac{\pi}{4} (a_{1,0} + a_{1,1}) - \sum_{m=1}^{\bar{m}}{}' (a_{\mu,0} + a_{\mu,1}) \frac{\mu \cos(\mu\pi/2)}{\mu^2 - 1} \right] \quad (33)$$

The single and double primes on the summation signs above mean that the terms with $\mu = 1$ and 2, respectively, are excluded from the series.

Induced Drag

The induced drag is calculated by application of Munk's Stagger Theorem, which states (in part) that the induced drag of a single wing is independent of the chordwise location of its lifting elements. Hence, after the loading is transferred to a line lying in the wing plane and parallel to the y axis, the induced drag is determined by a spanwise integration. The resulting drag coefficient is given by

$$C_{D_i} = \pi AR \sum_{m=1}^{\bar{m}} \mu(a_{\mu,0} + a_{\mu,1})^2 \quad (34)$$

Local Chordwise Center of Pressure

The distance to the local center of pressure, measured positive aft of the leading edge at any wing span station, is

$$\frac{x'_{c.p.}}{c} = \frac{1}{2} - \frac{\sum_{m=1}^{\bar{m}} (a_{\mu,0} + a_{\mu,2}) \sin \mu\varphi}{4 \sum_{m=1}^{\bar{m}} (a_{\mu,0} + a_{\mu,1}) \sin \mu\varphi}, \quad 0 < \varphi < \frac{\pi}{2} \quad (35)$$

This expression is valid at the root chord for symmetric loading problems. Taking the limit at the wing tip yields

$$\frac{x'_{c.p.}}{c} = \frac{1}{2} - \frac{\sum_{m=1}^{\bar{m}} \mu(a_{\mu,0} + a_{\mu,2})}{4 \sum_{m=1}^{\bar{m}} \mu(a_{\mu,0} + a_{\mu,1})}, \quad \varphi = 0$$

At the root chord, for antisymmetric loading problems,

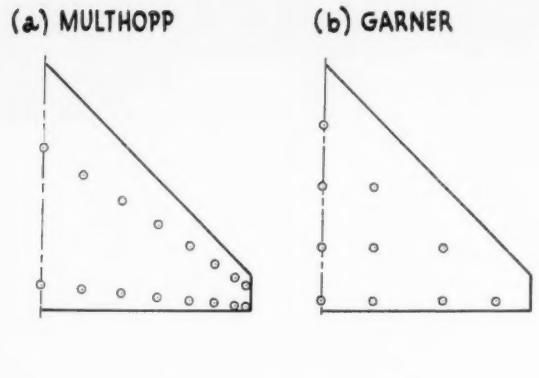

FIG. 3. Delta wing control point locations.

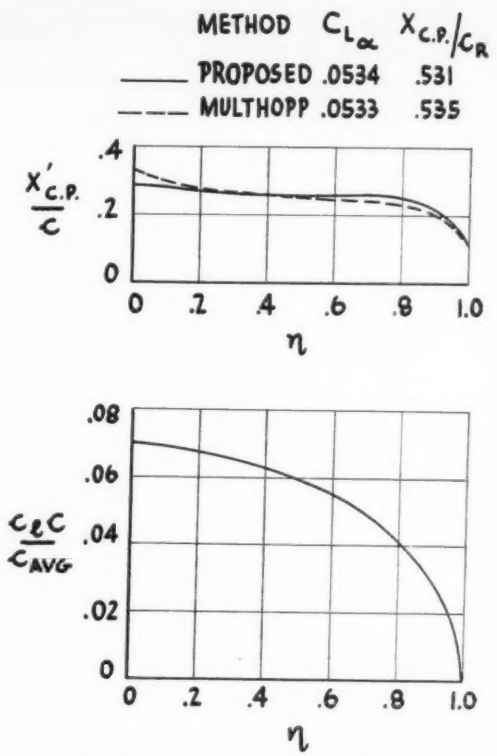

FIG. 4. Comparison of delta wing solutions—I.

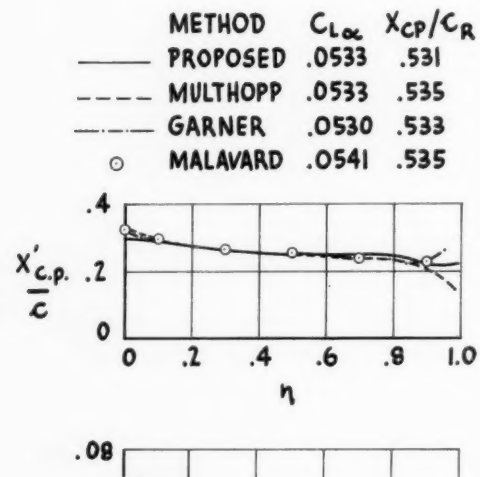

FIG. 5. Comparison of delta wing solutions—II.

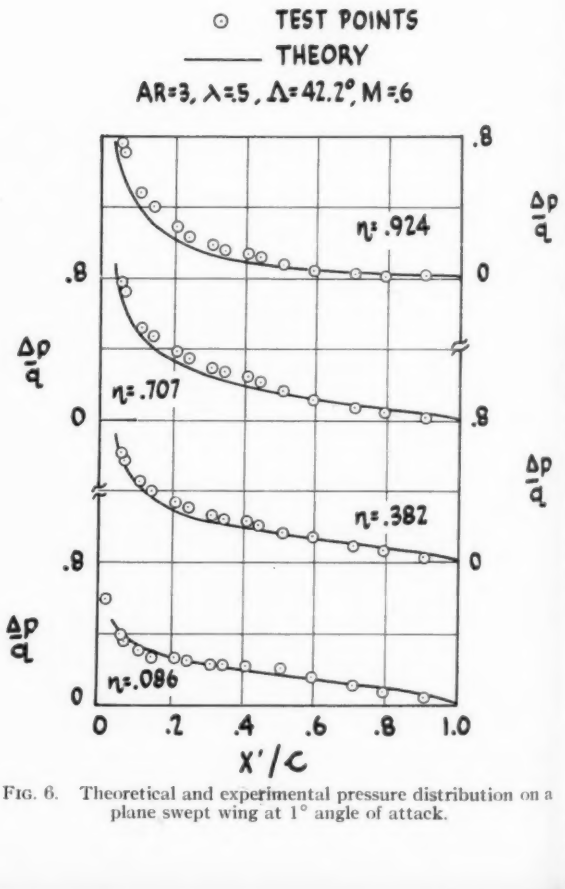

FIG. 6. Theoretical and experimental pressure distribution on a plane swept wing at 1° angle of attack.

$$\frac{x'_{c.p.}}{c} = \frac{1}{2} - \frac{\sum_{m=1}^{\bar{m}} m(a_{2m,0} + a_{2m,2})\ (-1)^m}{4 \sum_{m=1}^{\bar{m}} m(a_{2m,c} + a_{2m,1})\ (-1)^m}, \quad \varphi = \frac{\pi}{2}$$

Note that only the first three terms of the vorticity series (11) affect the chordwise center of pressure.

Wing Chordwise Center of Pressure

Like the spanwise center of pressure, the wing chordwise center of pressure is derived only for the right wing panel. The resulting expression is

$$\frac{X_{c.p.}}{c_R} = \frac{1}{2} + \frac{\eta_{c.p.}}{\sigma} \tan \Lambda - \frac{AR}{2C_L^*} \left\{ \frac{\pi}{4} [a_{1,0} + a_{1,2} + (\tau/2)(a_{2,0} + a_{2,2})] - \sum_{m=1}^{\bar{m}}{}' \frac{\mu(a_{\mu,0} + a_{\mu,2})}{\mu^2 - 1} \cos \frac{\mu\pi}{2} - \tau \sum_{m=1}^{\bar{m}}{}'' \frac{a_{\mu,0} + a_{\mu,2}}{\mu^2 - 4} \sin \frac{\mu\pi}{2} \right\} \quad (36)$$

where $X_{c.p.}$ is the distance from the leading edge of the root chord to the center of pressure, measured positive when the center of pressure lies aft of the reference point.

Rolling Moment Coefficient

The total rolling moment coefficient caused by an antisymmetric load distribution is given by

$$C_l = -C_L^* \eta_{c.p.} \quad (37)$$

where a positive rolling moment is defined as one which tends to lower the right wing tip.

Evaluation of the Method

The validity of the proposed method was ascertained by means of comparisons with other theoretical solutions, electrical analogy tank results, and wind-tunnel measurements. A discussion of these comparisons is given below.

An initial check involved a comparison with Multhopp's solution[3] for the plane delta wing illustrated in Fig. 3. This wing had an aspect ratio of 3, a leading-edge sweep of 45°, and a taper ratio of 1/7. The integral equation solved by Multhopp is equivalent to Eq. (1), but Multhopp's method for the inversion is quite different from that proposed here. Another significant difference in the two solutions is Multhopp's correction at the root chord, which was described above. For this comparison, a solution was computed by the proposed method, using $h = 6$ and Multhopp's control points, as illustrated in Fig. 3(a) (with $\eta_0 = 0.01$ instead of zero at the root). Results of the two solutions are shown in Fig. 4, where the agreement in span loading and lift curve slope, C_{L_α}, is seen to be excellent. As expected, the largest discrepancy between the two solutions was in the local center of pressure near the root chord.

The popularity of the delta planform described above suggested an additional comparison between Multhopp's solution, Garner's solution,[11] Malavard's electrical analogy tank results,[12] and a more elaborate solution by the proposed method. Control points used in the three analytical methods are shown in Fig. 3.

3. Garner's solution was accomplished by numerical integrations for the downwash produced by a continuous distribution of doublets in the wing and wake. His solution is unique since the integrations are performed in the x, y coordinates and the series assumed for the doublet strength satisfies the orthogonal isobar condition identically along the entire root chord. Malavard's electrolytic tank essentially simulates the infinitely thin wing postulated in the linear theory. The solution by the proposed method had $h = 10$ and 25 control points ($\xi_0 = 0, \pm 0.58055, \pm 0.93935$; $\eta_0 = 0, 0.30522, 0.58055, 0.79906, 0.93935$).

A comparison of results derived from the four methods is shown in Fig. 5. The agreement in span loading and lift curve slope leaves little to be desired.

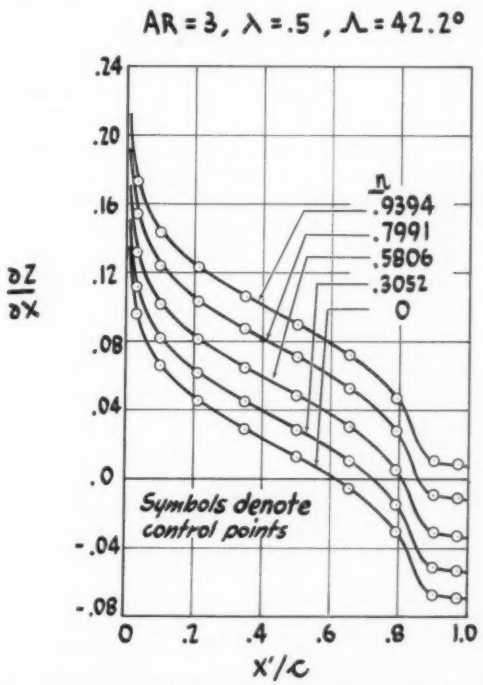

FIG. 7. Streamwise surface slopes of the cambered and twisted wing.

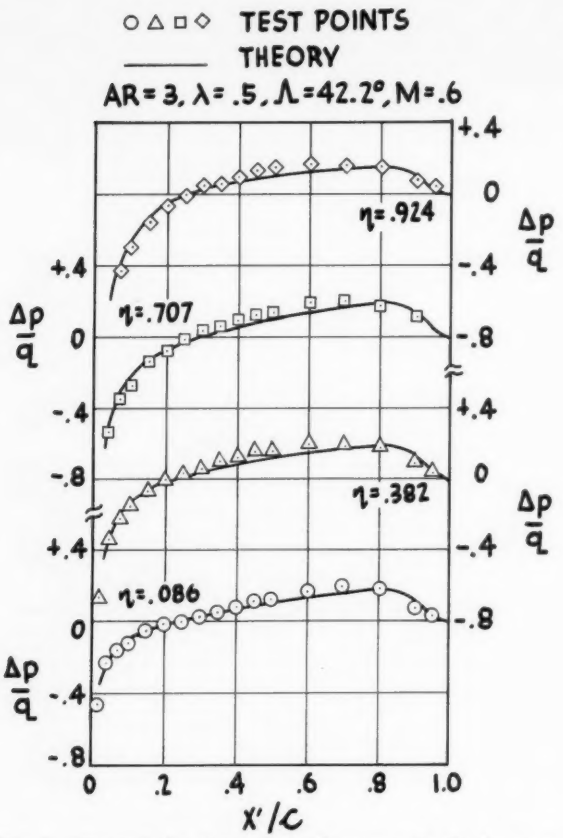

FIG. 8. Theoretical and experimental pressure distribution on a cambered and twisted wing at 0° angle of attack.

Though the error is somewhat less than that of the solution having $h = 6$, the proposed method gives the expected forward center of pressure at the root, where all of the other three methods show good agreement. Near the wing tip the proposed method indicates a fairly constant spanwise variation of center of pressure, the Multhopp solution indicates a forward shift, while the Garner solution indicates an aft shift. Since the Multhopp and proposed solutions given in Fig. 4 indicated the same trend in center of pressure near the tip, it may be concluded that both the Multhopp and Garner solutions suffer locally from lack of sufficient chordwise control points near the tip. That is, one or two control points are inadequate for the definition of the wing mean surface shape in the vicinity of the wing tip, where the vorticity has a large gradient.

The good agreement in span loading and lift curve slope between the solutions by the proposed method shown in Figs. 4 and 5 is a tribute to the convergence properties of Fourier series. A study of a number of solutions by the proposed method indicated that, with appropriate control points, accurate span loading and lift curve slope results are given for values of h greater than or equal to 6.

No really adequate theoretical methods for the calculation of loadings on arbitrarily cambered and twisted wings are available. For this reason, the evaluation of solutions for such wings was based on comparisons with wind-tunnel measurements. Wing surface pressure data given by Kolbe and Boltz[13, 14] were selected for this comparison because their results included measurements on the same swept wing planform, with both a cambered and twisted and a plane mean surface. A Mach number of 0.6 was selected at random.

Fig. 6, showing the theoretical and experimental pressure distribution for the plane wing, was prepared for purposes of orientation. The theoretical solution had $h = 10$ and all 45 control points given in Table 1. While the overall agreement between test and theory is good, sizeable local discrepancies are apparent. These discrepancies are caused by higher order and viscous effects, which are eliminated by the linearizing process. The overall agreement indicated in Fig. 6 is of the same order as the comparison shown by Garner.[11] It is of interest to note that, though the experimental pressure data never exceed a finite peak while the theoretical results rise to infinity at the leading edge, the integrated local lift coefficients agree very well.

Fig. 7 shows the streamwise mean surface slopes of the cambered and twisted wing. This wing, designed by the so-called simple sweep theory, had a modified NACA $a = 0.8$ camber distribution with a design lift coefficient of 0.4, oriented perpendicular to the quarter-chord line of the equivalent straight wing. The twist amounted to 5° of washout at the tip, with a spanwise variation given by

$$\frac{\partial z(\eta)}{\partial x} = \frac{\lambda\eta \sin(5°)}{\sqrt{[1 - \eta(1 - \lambda)]^2 - \lambda^2\eta^2 \sin^2(5°)}}$$

This type of twist yields linear surface elements along constant percent chord lines. Symbols shown in Fig. 7 denote the locations of the control points used, which are the same as those for the plane wing solution of Fig. 6. Though a number of these 45 points are superfluous for the plane wing case, all were used since the computer program has provisions for retaining the inverted downwash matrix $[W]^{-1}$, and this solution was available for a small amount of computer time.

A comparison of theoretical and experimental results for the cambered and twisted wing is shown in Fig. 8. Data shown are for zero angle of attack, measured relative to the manufacturer's chord line at the root

(*Continued on page 176*)

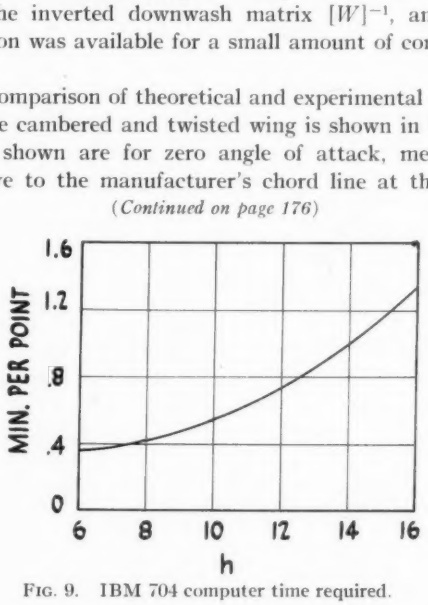

FIG. 9. IBM 704 computer time required.

The Supersonic Boom of a Projectile Related to Drag and Volume

I. L. RYHMING*

Boeing Scientific Research Laboratories

Summary

The Whitham theory predicting the far-flow field around a projectile is used to derive body shapes which produce extreme bow shock-wave pressure jump or "boom," subject to constraining conditions regarding the drag due to the bow shock and fineness ratio of the bodies. It is found that the minimum drag body is also the minimum boom body. The body-volume effect and the effect of discontinuities in slope of the body meridian section on the boom intensity is investigated.

As a general result of the investigation, it can be said that the boom of a projectile for given Mach number and flight altitude is primarily determined by its length and fineness ratio. The maximum variation in the boom intensity for pointed bodies with given length and fineness ratio is of the order of 10 per cent. The geometry of the bodies is thus found to play a minor role.

(1) Introduction

IN A PREVIOUS PAPER by Whitham,[1] a method was developed for determining the flow field and the shock pattern of a supersonic projectile. The present paper investigates the stationary character of the integral giving the bow-shock pressure jump subject to different subsidiary conditions.

According to reference 1, the wave drag of a supersonic projectile and the bow-shock pressure jump are two quantities which can be related to the same universal function, the F-function, describing the flow field. In the first part of the investigation that part of the wave drag which is due to the bow shock only is chosen as a subsidiary condition. A second subsidiary condition giving the maximum body thickness in terms of the F-function is also imposed on the problem.

The body-volume effect on the bow shock and the effect of discontinuities in slope of the body meridian section are investigated in the second part of the paper. The variation of the boom in connection with volume for a certain family of bodies is studied.

(2) General Considerations

The formula predicting the pressure rise in the bow shock or the "boom" of a projectile is given in reference 1:

$$s = \frac{p - p_\infty}{p_\infty} = h(\gamma, M_\infty, r)\left[\int_0^{y_0} F(y)\,dy\right]^{1/2} \quad (1)$$

where p is the pressure immediately behind the bow shock, p_∞ the pressure in the free stream, and $h(\gamma, M_\infty, r)$ is

$$h(\gamma, M_\infty, r) = 2^{1/4}\,\gamma(\gamma+1)^{-1/2}(M_\infty^2 - 1)^{1/8}\,r^{-3/4} \quad (2)$$

In Eq. (2), γ is the ratio of the specific heats, M_∞ is the Mach number in the free stream, and r is the radial distance in the x, r coordinate system shown in Fig. 1.

Under the assumption that the cross-sectional area of the projectile $S(x)$ possesses continuous first and second derivatives $S'(x)$ and $S''(x)$ and, further, that $S'(x)$ and $S''(x)$ have a bounded variation, the function $F(y)$ has the following form:

$$F(y) = \frac{1}{2\pi}\int_0^y \frac{S''(x)dx}{\sqrt{y-x}} \quad (3)$$

For Eq. (3) to be valid, it is also assumed that the projectile has a pointed nose, that is, $S(0) = S'(0) = 0$. The variable y appearing in the above formulas is defined as the characteristic variable. On each characteristic it has the value of $x - \alpha r$ at the point where the characteristic meets the body surface, α being the

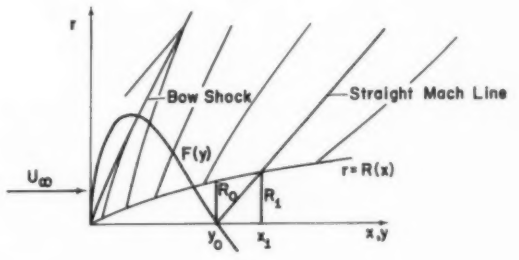

Fig. 1a

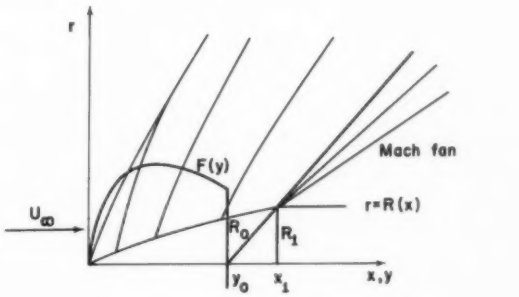

Fig. 1b

FIG. 1. Continuous and discontinuous F(y)-functions related to actual body geometry.

Received December 22, 1959.

* Staff Scientist, Flight Sciences Laboratory. Now, Fluid Dynamics Research Group, Convair (San Diego).

The author would like to thank Dr. Y. A. Yoler for his valuable criticism during the preparation of this paper.

value of $(M_\infty^2 - 1)^{1/2}$. The upper limit of the integral in Eq. (1) is defined as the first zero of the function $F(y)$ apart from $y = 0$ itself, that is,

$$F(y_0) = \frac{1}{2\pi}\int_0^{y_0} \frac{S''(x)dx}{\sqrt{y_0 - x}} = 0 \tag{4}$$

Eq. (4) holds for those bodies that have a continuously varying slope of the meridian section $R(x)$ of the body in the interval $0 < x \leq y_0 + \alpha R_1 = x_1$ (see Fig. 1a). For this class of bodies it is seen that the value of y_0 is dependent upon $S(x)$. However, in this paper we want to consider also another kind of a first zero of the F-function, namely, a zero which occurs when the F-function exhibits a jump at y_0 due to a discontinuity in slope of $R(x)$ at $x_1 = y_0 + \alpha R_1$ (see Fig. 1b). For such bodies, Eq. (4) does not hold. In the following we want to consider both types of bodies.

The physical situation together with typical F-functions is shown in Fig. 1. The shock wave starts at the pointed nose. All characteristics leaving the body surface up to the point x_1,R_1 eventually coalesce with the shock wave in the far field. That is, all disturbances created by the body surface up to that point feed into the shock wave and determine its pressure jump in the far field. The integral in Eq. (1) expresses this statement as the area under the F-curve up to the point y_0. On the other hand, the drag of the body up to the point x_1,R_1 can be determined by integrating all pressure disturbances along the body surface itself. Another way of determining the drag is to take the integral of the entropy jump along the shock wave.[1] Thus, using the Whitham theory for the *front* shock only, the drag of the body up to the point x_1,R_1 is given by

$$D = \pi\rho_\infty U_\infty^2 \int_0^{y_0} F^2(y)\, dy \tag{5}$$

where ρ_∞ and U_∞ are the free-stream density and velocity, respectively. This formula, giving the drag due to the bow shock, is different from the general drag formula for a body of revolution.[2] This can be seen if Eq. (3) is substituted in Eq. (5) and one integration over y is performed. In the following, we shall use this formula to deduce relations between body shape, drag, and pressure jump of the bow shock in the far field.*

(3) Bow Shock-Wave Drag and Boom Relations

The first problem to be considered may be formulated as follows: Determine the cross-sectional area distribution $S(x)$ in the interval $0 \leq x \leq x_1$ of a pointed body of revolution which has a specified maximum section at $x = x_1$, such that this body gives an extreme value of the integral in Eq. (1) subject to the further condition that the drag of the bow shock given by Eq. (5) is prescribed. Thus, we want to find the stationary character of the integral

$$T = \int_0^{y_0} F(y)\, dy \tag{6}$$

when the argument function $F(y)$ is subject to the subsidiary conditions:

$$\frac{D}{\pi\rho_\infty U_\infty^2} = \int_0^{y_0} F^2(y)\, dy = \text{a given constant } C_1 \tag{7}$$

$$(3/8)S(y_0) = \text{a given constant } C_2 \tag{8}$$

A further condition which must be fulfilled by the F-function is

$$F(y) \geq 0 \quad \text{for} \quad 0 \leq y \leq y_0 \tag{9}$$

where the equalities may only occur simultaneously.

In order to express the second subsidiary condition in terms of the F-function, Eq. (3), treated as an Abel integral equation, can be written as

$$S''(x) = 2\frac{d}{dx}\int_0^x \frac{F(t)\, dt}{\sqrt{x - t}} \tag{10}$$

The boundary conditions which can be specified for the pointed body are

$$S(0) = 0 \quad \text{and} \quad S'(0) = 0 \tag{11}$$

Performing two integrations of Eq. (10) and using the boundary conditions, Eq. (11) gives

$$S(x) = \frac{8}{3}\left[F(0)\, x^{3/2} + \int_0^x F'(t)(x - t)^{3/2}\, dt\right] \tag{12}$$

It is to be observed that the F-function is not necessarily zero for $y = 0$.

The second subsidiary condition now takes the form

$$\frac{3}{8}\, S(y_0) = F(0)y_0^{3/2} + \int_0^{y_0} F'(t)(y_0 - t)^{3/2}\, dt = C_2$$

Introduce two Lagrange multipliers, λ and μ; the integral to be studied is thus

$$I = \int_0^{y_0} F(y)\, dy + \lambda\int_0^{y_0} F^2(y)\, dy + \mu F(0)y_0^{3/2} + \mu\int_0^{y_0} F'(y)(y_0 - y)^{3/2}\, dy \tag{13}$$

Suppose first that Eq. (4) holds; namely, $F(y)$ is continuous through y_0 and $F(y_0) = 0$. Then the variable y_0 is dependent upon $S(x)$. Therefore, when the varied function $F(y, \epsilon)$ is introduced, ϵ being a parameter, y_0 is changed and becomes a function of ϵ, since Eq. (4) must also be satisfied for the varied function $F(y, \epsilon)$. Thus, not only the integrands but also the limits of the integrals in Eq. (13) depend upon ϵ. The total first variation of Eq. (13) can now be calculated and, in view of Eq. (4), we obtain

$$\delta I = \int_0^{y_0} [\delta F + 2\lambda F\delta F + \mu\delta F'(y_0 - y)^{3/2}]\, dy + \frac{3}{2}\mu\,\delta y_0\left[\int_0^{y_0} F'(y)(y_0 - y)^{1/2}\, dy + F(0)y_0^{1/2}\right] = 0 \tag{14}$$

* The author is indebted to Dr. G. B. Whitham for his suggestion to use Eq. (5) as a representation for the drag of the body.

where δI, δF, etc., are defined by:

$$\delta I = \epsilon \left.\frac{dI(\epsilon)}{d\epsilon}\right|_{\epsilon=0} \qquad \delta F = \epsilon \left.\frac{\partial F(y,\epsilon)}{\partial \epsilon}\right|_{\epsilon=0}$$

First, let y_0 be fixed and put the differential $\delta y_0 = 0$. After a partial integration of the third term in the first integral of Eq. (14), the Euler equation of the problem becomes

$$F(y) = -\frac{3}{4}\frac{\mu}{\lambda}(y_0 - y)^{1/2} - \frac{1}{2\lambda} \tag{15}$$

Then, by letting y_0 vary, we see that the remaining expression in Eq. (14) is equal to zero:

$$\frac{3}{2}\mu\,\delta y_0\left[\int_0^{y_0} F'(y)(y_0 - y)^{1/2}\,dy + F(0)y_0^{1/2}\right] = 0$$

This expression cannot be zero, however, unless δy_0 itself is zero, since the expression within the brackets is the slope of the S-function at y_0, and generally it is not zero. Therefore, y_0 can be regarded simply as a constant in the calculation, which is to be determined a posteriori.

Next, suppose that Eq. (4) does not hold; that is, suppose there is a jump in the F-curve at y_0. In this case y_0 can immediately be regarded as a constant, and as a consequence Eq. (14) remains unchanged except for the last term which is automatically zero.

The Lagrangian multipliers μ and λ are determined by means of Eqs. (7) and (8):

$$\mu = -(16/9y_0^2)[C_2\lambda + (1/2)y_0^{3/2}] \tag{16}$$

$$\lambda = \pm(1/2)(y_0)^{1/2}/(9C_1y_0^2 - 8C_2^2)^{1/2} \tag{17}$$

Eqs. (15), (16), (17), and (9) now describe the solution completely.

In the following, the constant C_2 will be assigned the value

$$C_2 = (3/8)S(y_0) = (3/8)\pi R_0^2 \tag{18}$$

Now, there exists a variety of solutions according to the value of C_1 in Eq. (17) which satisfy the condition stated by Eq. (9) when the negative value of λ is used. The lowest possible value which C_1 can take, according to Eq. (17), is

$$C_1 = (1/8)(\pi^2R_0^4/y_0^2) \tag{19}$$

Also, there exists an upper limit for the value of C_1 which can be found by combining Eqs. (15), (16), and (17) with Eq. (9). This value of C_1 is:

$$C_1 = (3/8)(\pi^2R_0^4/y_0^2) \tag{20}$$

The F-functions for the C_1 values given by Eqs. (19) and (20) are, respectively,

$$F(y) = \frac{\pi}{2}\frac{R_0^2}{y_0^{3/2}}\left(1 - \frac{y}{y_0}\right)^{1/2} \tag{21}$$

$$F(y) = \frac{3\pi}{2}\frac{R_0^2}{y_0^{3/2}}\left[1 - \left(1 - \frac{y}{y_0}\right)^{1/2}\right] \tag{22}$$

In general, the value of the integral T in Eq. (6) is found by substituting Eqs. (15) and (16) in Eq. (6):

$$T = (\pi/3)(R_0^2/y_0^{1/2}) - (y_0/18\lambda) \tag{23}$$

When λ is an admissible negative quantity, it is seen that T reaches its least value when λ is as large as possible. The minimum value actually occurs when λ tends to infinity, that is, when C_1 has its least value. The least value of C_1 given by Eq. (19) is, however, the minimum wave drag due to the bow shock for a given maximum thickness of the body. This can readily be seen from Eqs. (17), (16), (15), and (14). According to these equations there exists only one Lagrange multiplier, say ν, as $\lambda \to -\infty$ with the value

$$\nu = \mu/\lambda = -(16/9y_0^2)C_2$$

The second variation of Eq. (13) is then:

$$\delta^2 I = 2\int_0^{y_0} (\delta F)^2\,dy > 0$$

Thus, it can be concluded that the minimum-boom body for given bow-shock wave drag and maximum body thickness is also the minimum drag body due to the bow shock for a given maximum body thickness.

When λ goes through the range of admissible values, the value of T increases monotonically and reaches its maximum value when C_1 obtains the value given in Eq. (20):

$$T_{max} = (\pi/2)(R_0^2/y_0^{1/2}) \tag{24}$$

The geometry of the noses which produce minimum and maximum boom or drag can now be found from Eq. (12). These bodies are, respectively,

$$\left.\begin{aligned} R^2(x)_{min} &= \frac{1}{2}R_0^2\left[\left(\frac{x}{y_0}\right)^{1/2}\left(1 + \frac{x}{y_0}\right) - \left(\frac{x}{y_0} - 1\right)^2 \tanh^{-1}\left(\frac{x}{y_0}\right)^{1/2}\right] \\ &= R_0^2 f\left(\frac{x}{y_0}\right) \end{aligned}\right\} \tag{25}$$

and

$$\left.\begin{aligned} R^2(x)_{max} &= \frac{1}{2}R_0^2\left[\left(\frac{x}{y_0}\right)^{1/2}\left(5\frac{x}{y_0} - 3\right) + 3\left(\frac{x}{y_0} - 1\right)^2 \tanh^{-1}\left(\frac{x}{y_0}\right)^{1/2}\right] \\ &= R_0^2 g\left(\frac{x}{y_0}\right) \end{aligned}\right\} \tag{26}$$

However, these bodies are to be extended up to the point x_1 (see Fig. 1 or 2), where the body radius is R_1. In order to be able to compare the results, it is therefore convenient to refer the bodies to the same body radius R_1 at $x = x_1$. Beyond the point x_1, the body may be continued with, for example, a cylindrical portion without affecting the bow shock. At the point x_1, there is then a discontinuity in slope of the body meridian section. This discontinuity causes the fluid to expand rapidly and gives rise to a recompression which appears as the tail shock in the far field, the drag of

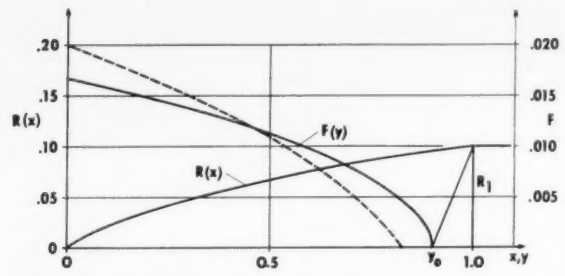

FIG. 2a. Geometry of minimum boom body and its F-curve; $M_\infty = \sqrt{2}$. The dotted curve is the F-curve for the minimum drag body.[3]

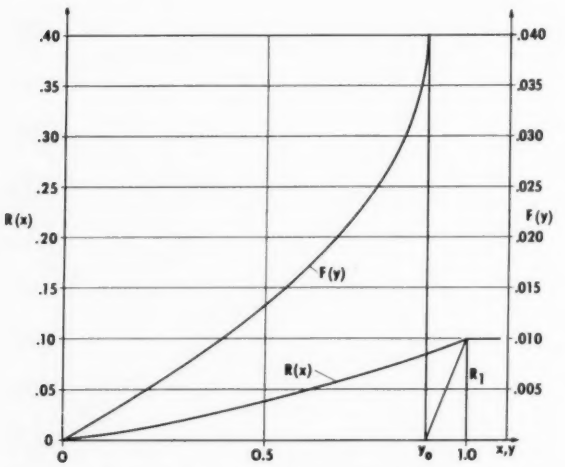

FIG. 2b. Geometry of maximum boom body and its F-curve; $M_\infty = \sqrt{2}$.

which is given by

$$D_{\text{rear shock}} = \pi \rho_\infty U_\infty^2 \int_{y_0}^{\infty} F^2(y)\, dy$$

This drag, however, has no significance in the present problem because we are concerned with the front part of the body exclusively. As a result of the discontinuity in slope at x_1, the F-curve exhibits a jump at y_0. The F-function then can take a manifold of different values at the same place, indicating a Mach fan at the shoulder of the body.

Now for $x = x_1$,

$$R^2(x_1)_{min} = R_1^2 = R_0^2 f\left(\frac{x_1}{y_0}\right) = R_0^2 f_1$$

and

$$R_0^2 = R_1^2/f_1 \tag{27}$$

Substituting R_0^2 from Eq. (27) in Eq. (25) gives the equation for the body radius in terms of x_1 and R_1. For a given Mach number, the proper value of y_0 then can be found from the relation:

$$y_0 = x_1 - \alpha R_1$$

It is seen that the functions f_1 and g_1 are functions of the product of α and the fineness ratio τ, defined by

$$\tau = R_1/x_1$$

The functions f_1 and g_1 are

$$2f_1 = \frac{2 - \alpha\tau}{(1 - \alpha\tau)^{3/2}} - \frac{(\alpha\tau)^2}{(1 - \alpha\tau)^2} \tanh^{-1}(1 - \alpha\tau)^{1/2} \tag{28}$$

$$2g_1 = \frac{2 + 3\alpha\tau}{(1 - \alpha\tau)^{3/2}} + \frac{3(\alpha\tau)^2}{(1 - \alpha\tau)^2} \tanh^{-1}(1 - \alpha\tau)^{1/2} \tag{29}$$

The minimum and maximum values of T given by Eq. (6) are as follows:

$$\left.\begin{aligned} T_{min} &= \frac{\pi}{3}\frac{R_0^2}{y_0^{1/2}} = \frac{\pi}{3}\frac{1}{f_1}\left(\frac{x_1}{y_0}\right)^{1/2} \tau^2 x_1^{3/2} \\ T_{max} &= \frac{\pi}{2}\frac{R_0^2}{y_0^{1/2}} = \frac{\pi}{2}\frac{1}{g_1}\left(\frac{x_1}{y_0}\right)^{1/2} \tau^2 x_1^{3/2} \end{aligned}\right\} \tag{30}$$

Also, the drag of the bodies are:

$$\left.\begin{aligned} C_{D_{min}} &= \frac{D_{min}}{(1/2)\rho_\infty U_\infty^2 \pi R_1^2} = \frac{\pi^2}{4}\frac{R_0^4}{y_0^2 R_1^2} = \frac{\pi^2}{4}\left(\frac{x_1}{y_0}\right)^2 \frac{1}{f_1^2}\tau^2 \\ C_{D_{max}} &= \frac{D_{max}}{(1/2)\rho_\infty U_\infty^2 \pi R_1^2} = \frac{3\pi^2}{4}\frac{R_0^4}{y_0^2 R_1^2} = \frac{3\pi^2}{4}\left(\frac{x_1}{y_0}\right)^2 \frac{1}{g_1^2}\tau^2 \end{aligned}\right\} \tag{31}$$

For comparison, we choose the Mach number $M_\infty = \sqrt{2}$ and $\tau = 0.1$. The values of T_{min}, T_{max}, $C_{D_{min}}$, and $C_{D_{max}}$ then are:

$$T_{min} = 1.002\tau^2 x_1^{3/2} \qquad T_{max} = 1.200\tau^2 x_1^{3/2}$$

$$C_{D_{min}} = 2.511\tau^2 \qquad C_{D_{max}} = 4.802\tau^2$$

As given by Eq. (1), the boom of the body is proportional to the square root of T. The ratio of extreme boom intensities then is

$$\left(\frac{T_{max}}{T_{min}}\right)^{1/2} = \left(\frac{3f_1}{2g_1}\right)^{1/2} = \left(\frac{3}{2}\right)^{1/2} \times \left(1 - \alpha\tau + \frac{25}{16}(\alpha\tau)^2 - \frac{5}{8}(\alpha\tau)^2 \ln\frac{4}{\alpha\tau} + \ldots\right) \tag{32}$$

where the functions f_1 and g_1 given by Eqs. (28) and (29) have been expanded for $\alpha\tau$ small compared to unity. For $\alpha\tau = 0.1$, for example,

$$(T_{max}/T_{min})^{1/2} = 1.095$$

Thus, for slender bodies at supersonic speed it can be stated that the maximum variation of the boom intensity is of the order of 10 per cent.

According to Eqs. (30) and (31), a general form of C_D and T for any pointed body of revolution is

$$C_D = C_1(\alpha\tau)\,\tau^2$$

$$T = C_2(\alpha\tau)\,\tau^2 x_1^{3/2}$$

where $C_1(\alpha\tau)$ and $C_2(\alpha\tau)$ are functions of $\alpha\tau$. Therefore, the boom of a projectile can be written in the form

$$s = H[\gamma, M_\infty, (r/x_1), \alpha\tau]\, C_D^{1/2} \tag{33}$$

showing that s is proportional to the square root of C_D. In Fig. 2, the minimum and maximum boom body geometry is shown together with the F-curves of the bodies for $\tau = 0.1$ and $M_\infty = \sqrt{2}$.

(4) The Boom of Minimum Total Wave-Drag Bodies

The results in the preceding section suggest that the minimum wave-drag bodies, according to the investigations by Lighthill,[3] Sears[4] and Haack,[5] also are minimum boom bodies. The minimum wave drag for a projectile with given maximum thickness and satisfying Eqs. (11) is, according to reference 3,

$$C_D = 4\tau^2$$

The F-curve for this body is

$$F(y) = (4/\pi)(R_1^2/x_1^{3/2})(2E - K) \tag{34}$$

where E and K are complete elliptic integrals with modulus

$$k = (y/x_1)^{1/2}$$

The F-curve given by Eq. (34) is very much like the F-curve given by Eq. (21) (see Fig. 2a). The value of the integral T for this body is*

$$T = 0.983\tau_1^2 x_1^{3/2} \tag{35}$$

(5) Volume Effect on Bow-Shock Pressure Jump

In this section we want to consider the volume of the projectile as another parameter of interest relative to the supersonic boom. The problem is to determine the distribution of a given total volume along a given length, such that the body thickness never exceeds a certain value, and the boom produced by this body is a minimum. In the following, we consider projectiles that possess only one expansive zero of the F-function. For this class of bodies, the problem can be stated as an isoperimetric variational problem of Eq. (6) with the volume up to point y_0 given, since the bow shock is influenced only by the nose of the body up to y_0. However, this problem, when analyzed, gives only the trivial solution $S = 0$, which is in contradiction to the subsidiary condition imposed on the problem. Therefore, there is no real physical solution to this problem.

However, it is interesting to study the behavior of the relative minima for certain given families of bodies. Consider, for example, the family of pointed bodies defined by

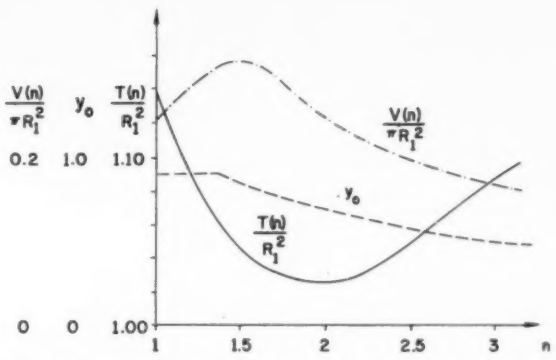

FIG. 3. $T(n)$, $y_0(n)$ and $V(n)$ for a family of bodies given by Eq. (36); $M_\infty = \sqrt{2}$.

$$\begin{aligned} R(x) &= R_1[1 - (1 - x)^n] \qquad n \geq 1, \quad 0 \leq x \leq 1 \\ R(x) &= R_1 \qquad x > 1 \end{aligned} \tag{36}$$

Find the exponent n for which the integral

$$\begin{aligned} T(n) &= \int_0^{y_0} F(y)\, dy \\ &= 2R_1^2 n \int_0^{y_0} [(2n - 1)(1 - x)^{2(n-1)} - \\ &\qquad (n - 1)(1 - x)^{n-2}]\sqrt{y_0 - x}\, dx \end{aligned} \tag{37}$$

has its minimum value. The upper limit $y_0(n)$ in Eq. (37) is generally to be determined from

$$\begin{aligned} F(y_0) = (2n - 1) \int_0^{y_0} \frac{(1 - x)^{2(n-1)}}{\sqrt{y_0 - x}}\, dx - (n - 1) \times \\ \int_0^{y_0} \frac{(1 - x)^{n-2}}{\sqrt{y_0 - x}}\, dx = 0 \end{aligned} \tag{38}$$

This equation is true for all n, which gives

$$0 < y_0 \leq 1 - \alpha R_1 \tag{39}$$

If Eq. (38) gives $y_0 > 1 - \alpha R_1$, then $y_0 = 1 - \alpha R_1$ in Eq. (37). Thus, for a given Mach number we have two equations with two unknown variables n and y_0 together with the inequality (39). This problem has been solved numerically for Mach number $\sqrt{2}$. The results are shown in Fig. 3 with $T(n)$ plotted against n. The volume of the bodies up to the point y_0 is given by

$$\begin{aligned} V(n) = \pi R_1^2 \Big[y_0 + \frac{2}{n + 1}(1 - y_0)^{n+1} - \frac{1}{2n + 1} \times \\ (1 - y_0)^{2n+1} - \frac{3n + 1}{(n + 1)(2n + 1)} \Big] \end{aligned}$$

This function together with $y_0(n)$ is also plotted in Fig. 3.

The minimum of Eq. (37) occurs in the neighborhood of $n = 2$, for which $T(2) = 1.025R_1^2$. As can be expected from the foregoing discussion, the minimum is very flat. The volume change around $n = 2$ is

$$dV(n)/dn\big|_{n=2} \sim 0.13\pi R_1^2$$

which is considerable. The integral in Eq. (6) is thus insensitive to changes in the nose volume, being de-

* It is believed that this value of T is the lowest possible for any body of revolution with given maximum thickness and satisfying the Eq. (11). A proof of this statement is, however, very difficult to give and is omitted here.

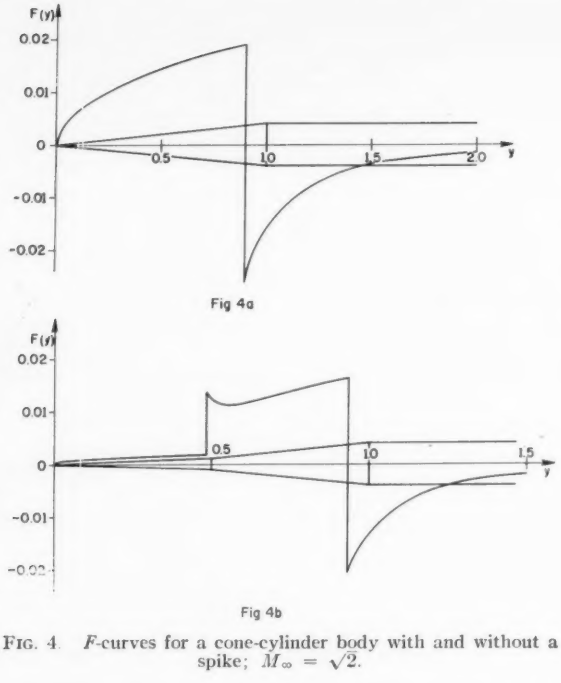

FIG. 4. *F*-curves for a cone-cylinder body with and without a spike; $M_\infty = \sqrt{2}$.

pendent primarily on the fineness ratio and body length. In this connection, it is interesting to examine the Sears-Haack body producing minimum wave drag for a given body volume. The meridian section is given by

$$R(x) = R_1[1 - (1 - x)^2]^{3/4} \qquad 0 \leq x \leq 2$$

where $$R_1 = (8V/3\pi^2)^{1/2}$$

V being the volume of the body. It is found that T has the following value for this body:

$$T = 0.988R_1^2$$

This value is very close to that given in Eq. (35).

(6) Effect of a Discontinuity in Slope of the Meridian Section of the Nose on the Bow-Shock Pressure Jump

In the preceding discussion we have considered bodies that have a continuously varying cross-sectional area with continuous first and second derivatives in the interval $0 \leq y \leq y_0$. In this section, the effect of a discontinuity in $S'(x)$ on the bow-shock pressure jump is studied. For such bodies the F-function cannot be calculated with Eq. (3). Instead, the F-function must be evaluated with the Stieltjes integral[1]:

$$F(y) = \int_0^\infty \left(\frac{2}{\alpha R(x)}\right)^{1/2} h\left(\frac{y - x}{\alpha R(x)}\right) \frac{dS'(x)}{2\pi} \qquad (40)$$

where $h[(y - x)/\alpha R(x)]$ is a function given in reference 1.

In order to study this question, consider a very slender cone (a spike) added to the bodies discussed in the foregoing section. At the spike-body junction, there is a sudden change in $S'(x)$, giving rise to a second shock attached to the body. In Figs. 4 and 5, respectively, the F-curves for the cases $n = 1$ and $n = 3$ are compared with the original F-curves for the bodies. The ratio of the boom intensity of the original and the spiked bodies for the two cases is

$$n = 1 \qquad \frac{S_{\text{cone}}}{S_{\text{sp. cone}}} = 0.986$$

$$n = 3 \qquad \frac{S_{\text{ogive}}}{S_{\text{sp. ogive}}} = 1.021$$

Thus, a spike has very little effect on the boom and may lead to an increase in boom intensity, as in the case $n = 1$.

(7) Conclusion

The boom of a projectile for given Mach numbers and flight altitudes is determined primarily by its length and fineness ratio [see, e.g., Eqs. (30) and (35)]. The geometry of the projectile plays a minor role. For pointed bodies with given length and fineness ratio, the maximum variation in the boom intensity for a given Mach number and flight altitude is of the order of 10 per cent. The minimum wave-drag bodies *thereby* also are the minimum boom bodies. A general relation between the drag coefficient and the boom for any pointed body of revolution shows that the boom is proportional to the square root of the drag coefficient.

(*Continued on page 157*)

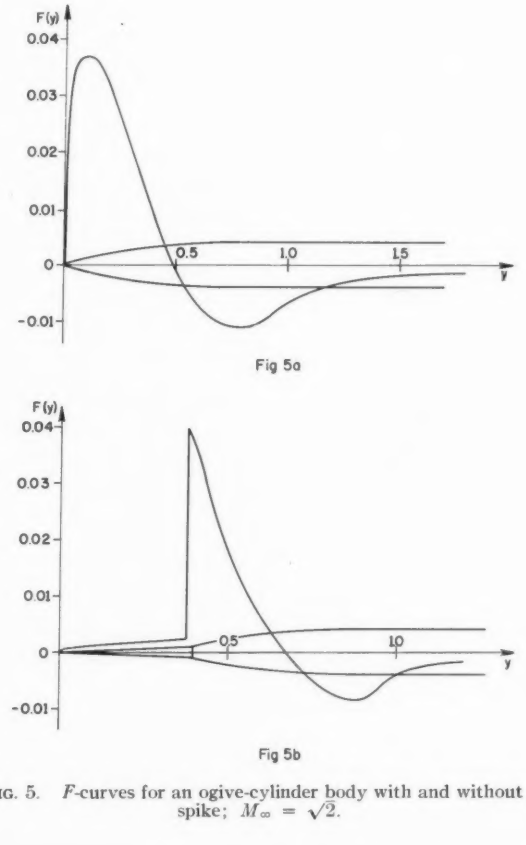

FIG. 5. *F*-curves for an ogive-cylinder body with and without a spike; $M_\infty = \sqrt{2}$.

An Analytic Extension of the Shock-Expansion Method†

GEORGE D. WALDMAN* AND RONALD F. PROBSTEIN**

Brown University

Summary

The problem is considered of calculating approximately the inviscid rotational flow field and pressure distribution about a smooth two-dimensional airfoil with sharp leading and trailing edges in a uniform supersonic or hypersonic stream. The assumption of a perfect gas is made, and the basic flow pattern for the analysis is taken to be given by the simple isentropic shock-expansion method with straight characteristics. An elementary characteristics treatment is discussed to show when the simple shock-expansion method should be satisfactory for computing the surface pressure distribution, and under what circumstances it may be expected to break down. By utilizing characteristic variables the isentropic shock-expansion method is then formulated analytically, and an analytic result is obtained for the shock shape corresponding to this zero-order approximation. In the special case where hypersonic similitude is applicable, that is, for slender bodies and high Mach numbers, the shock-shape expression for large distances is found to reduce to the result previously given by Mahony, which for weak shocks and slender bodies in turn reduces to the simple-wave result first given by Friedrichs.

Employing the analytic form of the isentropic shock-expansion method as a zero-order approximation, an analytically consistent perturbation method is developed by expanding the dependent flow variables in the exact partial differential equations in powers of the reflection coefficient for simple waves interacting with an oblique shock. The scheme by its nature helps to define those regions in which shock expansion can be used, in addition to taking into account in a perturbation sense the factors neglected in simple shock-expansion theory, namely, the curvature and reflection of the Mach waves and the correct boundary conditions at the shock wave. Analytic solutions are obtained for the first-order corrections, including the surface pressure distribution. The necessary numerical computation of the integrals involved is considerably simpler than a direct application of the method of characteristics. To illustrate the method and its accuracy, the zero-order shock shape and first-order pressure distribution are calculated for a family of parabolic arc airfoils at an infinite free-stream Mach number. These results are compared with rotational characteristic solutions where available, and the present method is found to be in excellent agreement.

Symbols

a = function defined by Eq. (4.5)
C_p = pressure coefficient, $(p - p_\infty)/{}^1/_2\rho_\infty q_\infty{}^2$
c_p = specific heat at constant pressure
c_v = specific heat at constant volume
F = function defined by Eqs. (3.11), (3.12)
G = function defined by Eqs. (3.11), (3.12)
H = function defined by Eqs. (3.11), (3.12)
K = function defined by Eq. (3.21)
M = Mach number
$M(\theta_n)$ = function defined by Eq. (5.11)
N = $K\, d\theta/d\varphi$
p = pressure
q = velocity
s = entropy measured from free-stream conditions, divided by c_v
t = time
x = abscissa measured parallel to the free-stream direction with origin at the nose of the airfoil, divided by the airfoil chord length
y = ordinate measured perpendicular to the free-stream direction with origin at the nose of the airfoil, divided by the airfoil chord length
α = $\gamma M^2/\sqrt{M^2 - 1}$
γ = c_p/c_v
Γ = function defined by Eq. (5.1)
δ = reflection coefficient for a simple wave at a shear layer, Eq. (2.5)
ϵ = reflection coefficient for a simple wave at a shock wave, Eq. (2.1a)
ζ = characteristic variable which is constant along reflected Mach lines
η = ${}^1/_2(\theta + \nu)$
θ = flow deflection angle
λ = function defined by Eq. (2.1b)
μ = Mach angle, arc sin $1/M$
ν = Prandtl-Meyer angle measured from sonic conditions
ξ = ${}^1/_2(\theta - \nu)$
ρ = density
φ = angle between shock wave and free-stream direction
ψ = surface-pressure gradient ratio at the nose of the airfoil, $[(dp/dz)_{\text{exact}}/(dp/dz)_0]_n$, where z is arc length measured along the body
ω = $\varphi - \theta$

Subscripts

b = conditions at the airfoil surface
n = conditions at the airfoil nose
s = conditions at the shock wave
t = conditions at stagnation
0 = isentropic shock-expansion quantities
i = 1, 2, . . . , ith order perturbation quantities
∞ = conditions in the free stream

$\sim$ signifies asymptotically equal

(I) Introduction

IN THE PRESENT PAPER the problem is considered of calculating the inviscid flow field about a two-dimensional airfoil with sharp leading and trailing edges in a uniform supersonic or hypersonic stream. The angle of attack and the Mach number of the inci-

Received December 29, 1959.

† This investigation was supported by the Fluid Dynamics Research Branch of the Aeronautical Research Laboratory, Wright Air Development Center, USAF, under Contract No. AF 33(616)-5442.

* Research Assistant, Division of Applied Mathematics. Presently, Associate Scientist, Research and Advanced Development Division, Avco Corporation, Wilmington, Mass.

** Professor of Engineering.

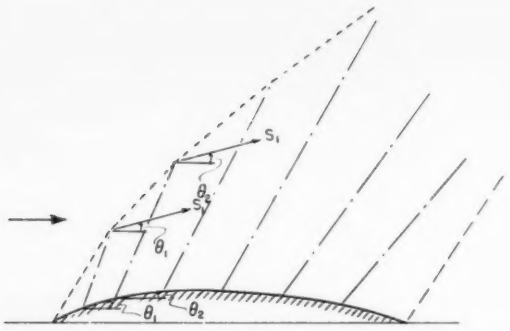

FIG. 1. Flow field obtained by the shock-expansion method utilizing an isentropic Prandtl-Meyer flow and matching the flow deflection at the shock.

dent stream, M_∞, are so limited that the deflections of the stream through angles concave to the flow which are made at the leading and trailing edges are achieved with the aid of attached shocks separating regions of supersonic flow. The gas is assumed to be ideal with a constant ratio of specific heats; the generalization of the treatment to include real gas effects, however, presents no essential difficulty, particularly if the flow behind the shock may be considered in thermodynamic equilibrium with an appropriate constant average isentropic exponent.

Depending on the body geometry and flight Mach number, a variety of approximate schemes for calculating such flows are available. Epstein[1] suggested the so-called shock-expansion method, in which conditions are presumed to be those associated with a uniform shock generated by a wedge inclined at the leading-edge angle, followed by an isentropic Prandtl-Meyer expansion over the airfoil surface. Such a scheme gives the surface pressure and one may calculate the shape of the shock wave by assuming no wave reflection from the shock and, say, matching shock-flow deflection with the constant-flow deflection along the straight characteristics emanating from the airfoil surface (Fig. 1); alternatively, one can match pressure in the same way. Clearly this model is not quite correct, since the expansion waves produced by the curvature of the airfoil will interact with the shock wave, curving and decaying it and giving rise to a nonisentropic flow field. Thus, not taken into account are the facts that the forward-facing Mach lines are curved due to their interaction with and subsequent partial reflection from the vortex lines given off by the shock, that Mach waves are reflected from the shock, and that the shock shape is in error because of the impossibility of satisfying all the Rankine-Hugoniot conditions.

Eggers and Syvertson[2,3] have attempted to correct one of the deficiencies of this method. In their generalized shock-expansion method they still consider only a single family of Mach lines, neglecting both the reflections from the shock wave and from the vortex lines in the flow, but they do not require the field to be isentropic; thus there is a Mach number gradient along the characteristics, so that they are no longer straight. This allowed Eggers and Syvertson to develop an initial-value procedure similar to but much simpler than the method of characteristics. The procedure utilizes the conditions that, downstream of the shock wave, the entropy is constant along streamlines and the pressure is constant along forward-facing Mach lines; in place of the latter statement one can also assume that the flow inclination angle is constant along forward-facing Mach lines—both conditions are equally valid under the authors' assumptions. Unfortunately both conditions taken together overdetermine the flow field: although the pressure distribution on the body is unaffected, they predict, for example, two slightly different values of the shock angle at each point of the shock. The authors get partly around this difficulty resulting from the large degree of arbitrariness by employing the arithmetic mean of the constant-pressure procedure and the constant-flow deflection procedure. In Hayes and Probstein (reference 18, p. 266) it is shown that the choice of the arithmetic mean is not irrational and removes the arbitrariness of the method.

The generalized shock-expansion method is fairly satisfactory for a good portion of the range of supersonic and hypersonic flight conditions; certain errors, however, occur for values of the hypersonic similarity parameter (the maximum flow deflection angle multiplied by the free-stream Mach number) of the order of unity, a range of considerable practical interest.

(II) Preliminary Considerations

In an attempt to determine the accuracy of the shock-expansion method, Rand[4] poses the problem of finding that rotational stream which would be compatible with an irrotational Prandtl-Meyer flow over a planar wedge with an afterbody; thus he requires all flow properties to be constant along the principal characteristics behind the shock. The results he found show that except at extremely high Mach numbers the effect of entropy variation behind the shock is small and may be neglected for deflection angles less than about 10°. As will be noted later, the range of applicability turns out to be wider than indicated by this analysis because of cancellation effects entering into the calculation of the exact flow problem. Other work in this direction has been carried out by Munk and Prim[5] who, following the earlier analysis by Crocco[6] of the relation between shock wave and body curvature at the nose of a body, performed calculations of the ratio of the exact surface-pressure gradient to the pressure gradient obtained by use of the shock-Prandtl-Meyer method for various leading-edge angles and values of M_∞. Kraus[7] has extended their computations and plotted the surface-pressure gradient ratio, which he denotes by ψ, as a function of leading-edge angle θ_n. An examination of his results indicates that, except near detachment, the exact surface-pressure gradients are less than those resulting from a Prandtl-Meyer flow for Mach numbers greater than

about 3, though the absolute difference even at infinite Mach number is no greater than 12%, except near shock detachment. Although this investigation answers some of the questions regarding the influence of the reflected waves in the leading-edge region, the problem of the influence of the reflected disturbances on the downstream flow field as a whole still remained; for example, it is clear that the pressure changes caused by the reflected waves are not important in that portion of the flow field where the local pressure ratio p/p_∞ is large, but they might conceivably have considerable influence on the surface pressures some distance downstream of the leading edge, where $(p - p_\infty)/p_\infty$ is small.

Lighthill[8] and Chu[9] have obtained an exact reflection coefficient for the reflection of a simple wave at a shock front. The coefficient denoted by ϵ is defined as the pressure change across the reflected wave to the pressure change across the incident wave. As expressed by Chu, it may be written

$$\epsilon = (\tan \lambda - \tan \mu_s)/(\tan \lambda + \tan \mu_s) \quad (2.1a)$$

where

$$\tan \lambda = \frac{\left(1 + \frac{\gamma - 1}{2} M_s^2 \sin^2 \omega\right) \sin 2\omega}{\left(1 - \frac{1}{M_s^2}\right)\left(1 + \frac{\gamma - 1}{2} M_s^2 \sin^2 \omega\right) + \left(\gamma M_s^2 \sin^2 \omega - \frac{\gamma - 1}{2}\right) \cos^2 \omega} \quad (2.1b)$$

and where μ_s and M_s are, respectively, the Mach angle and Mach number behind the shock wave, and ω is the angle the shock wave makes with the flow direction at the shock. As shown by Lighthill this coefficient increases initially with angle as the cube of the flow deflection at the shock, but later somewhat more slowly. Of course there is an interaction between the simple wave and its reflection at the shock, so that although their results give the exact form at the shock, they cannot predict how the wave will propagate. It should be noted, as pointed out in reference 10, that Lighthill's limiting expression for the reflection coefficient at infinite Mach number is incorrect.

In Hayes and Probstein (reference 18, p. 270) it is shown that the limiting value of the reflection coefficient for $M_\infty = \infty$ takes on a particularly simple form which is independent of the deflection angle and dependent only on the state of the gas behind the shock. With γ_s the specific heat ratio behind the shock when the gas behind the shock is considered as perfect, this reflection coefficient may be written

$$\epsilon = \frac{2\sqrt{\gamma_s - 1} - \sqrt{2\gamma_s}}{2\sqrt{\gamma_s - 1} + \sqrt{2\gamma_s}} \quad (2.2)$$

We see from this relation that as $\gamma_s \to 1$ the reflection coefficient approaches -1, whence an expansion wave reflects from the shock as a compression wave of undiminished strength. To give an idea of the magnitude of the reflection, values of ϵ for various γ_s are presented in Table 1 (taken from reference 18, p. 270). Certainly it is revealing to note that even in this extreme case, except for specific heat ratios very close to 1, the absolute value of the reflection coefficient is never very large, implying that the disturbances are in fact absorbed to a great extent by the shock wave and only weakly reflected.

Complete calculations for all values of the flow deflection angle were first given correctly by Eggers and Syvertson[2] who showed that for a specific heat ratio of 1.4 the waves reflected from the shock are always weak, except near detachment. They take as a measure of the strength of these reflected waves the ratio of the rate of variation of flow angle along the incident waves to that along the reflected waves; this "disturbance strength ratio," $(\partial\theta/\partial C_1)/(\partial\theta/\partial C_2)$, is related to the pressure change along incident and reflected char-

TABLE 1
Reflection Coefficient at Shock for $M_\infty = \infty$ in a Perfect Gas

γ_s	1.4	1.3	1.2	1.1	1.05	1.0
ϵ	−0.14	−0.19	−0.27	−0.40	−0.53	−1.0

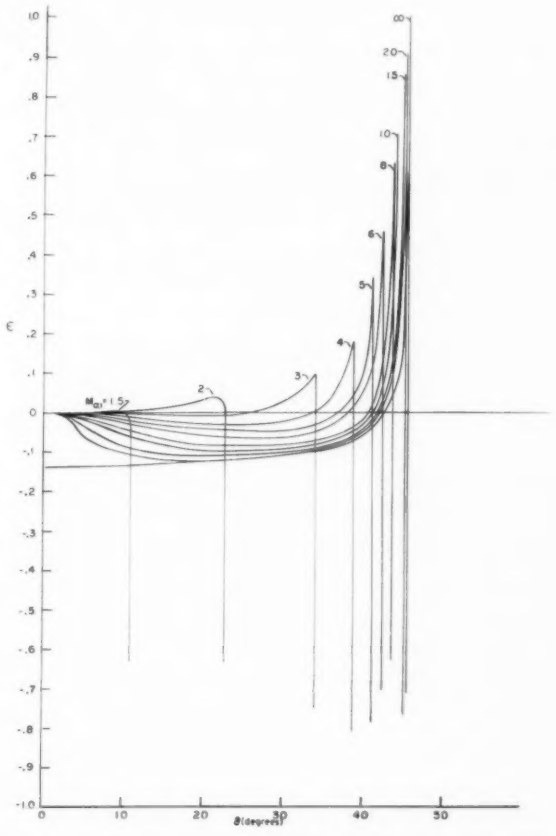

FIG. 2. Reflection coefficient as a function of deflection angle; $\gamma = 1.4$.

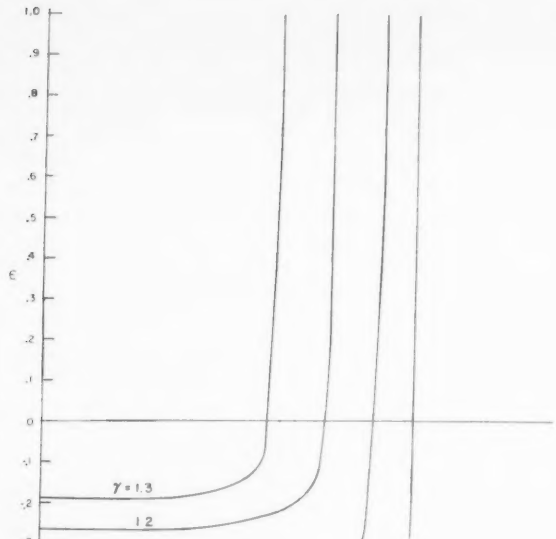

FIG. 3. Reflection coefficient as a function of deflection angle for $M_\infty = \infty$.

acteristics and the surface-pressure gradient ratio at the nose by

$$(\partial\theta/\partial C_1)/(\partial\theta/\partial C_2) = -(\partial p/\partial C_1)/(\partial p/\partial C_2) = -(\psi - 1)/(\psi + 1) \quad (2.3)$$

For a Prandtl-Meyer flow the ratio is of course zero. It can be shown that this parameter is related to the reflection coefficient ϵ by

$$\epsilon = -[(\partial\theta/\partial C_1)/(\partial\theta/\partial C_2)]\,\frac{\sin(\mu_s + \varphi - \theta_s)}{\sin(\mu_s - \varphi + \theta_s)} \quad (2.4)$$

where φ is the angle the shock makes with the free-stream direction and θ_s is the flow-deflection angle behind the shock. Utilizing the tabulated results of Kraus[7] for ψ (with $\gamma = 1.4$), ϵ has been computed from Eq. (2.4) and plotted in Fig. 2. It is interesting to note that even in the limiting case $M_\infty \to \infty$, the absolute value of ϵ is never larger than 0.14 for $\theta_s < 44°$, and is practically independent of the nose angle, a result which we have already seen from the large Mach number analysis. Also computed from the same source and shown in Fig. 3 is ϵ for infinite free-stream Mach number for various values of γ between 1.0 and 1.4. These results are also seen to check with the computations in Table 1.

The shock reflection coefficient, however, does not by itself tell the whole story, since it does not involve the interaction of the simple wave from the airfoil surface and the vorticity in the flow between the airfoil and shock. Some insight into the magnitude of this effect can be obtained by calculating the reflection of a simple wave from an idealized supersonic shear layer; this has previously been carried out by Marble[11] and an alternative derivation is indicated in reference 18 (p. 271). A schematic picture of the model used in this calculation is shown in Fig. 4. The result gives for the ratio of pressure rise across the wave reflected from the shear layer to the pressure rise across the incident simple wave

$$\delta = \frac{(\Delta p)_{\text{reflected}}}{(\Delta p)_{\text{incident}}} = \frac{1 - (\alpha_1/\alpha_2)}{1 + (\alpha_1/\alpha_2)} \quad (2.5)$$

where $\alpha = \gamma M^2/\sqrt{M^2 - 1}$. Clearly, when the shear layer is very weak ($M_2 \to M_1$), then $\alpha_2 \to \alpha_1$, so that $\delta \to 0$ and there is no reflection of the incident wave. On the other hand, if there is a very strong shear layer ($M_2 \gg M_1$), then $\alpha_2 \gg \alpha_1$ provided M_1 is not too close to unity ($\sqrt{M_1^2 - 1} \ll M_2$), so that $\delta \to 1$. In such a case the change in pressure across the reflected wave is equal to that across the incident wave, so that an expansion reflects as if from a solid wall. Therefore if no wave cancellation were to take place in the field, we see that an effect of this magnitude would clearly invalidate the shock-expansion method and place a limitation upon its region of applicability which might be even more severe than the reflection effect from the shock wave would indicate.

Hence, in considering the applicability of shock-expansion theory by itself, we must not be misled into treating the influence on the surface pressure of either one of the reflections mentioned as characterizing the validity of the method. This follows from the fact that the effect of each of these reflections is to cancel one another on the average over the surface. Thus an expansion reflects from a shear layer as an expansion, whereas an expansion reflects from the shock as a compression. This annulment thus tends to make the shock-expansion method, at least insofar as surface-pressure distribution is concerned, more accurate than

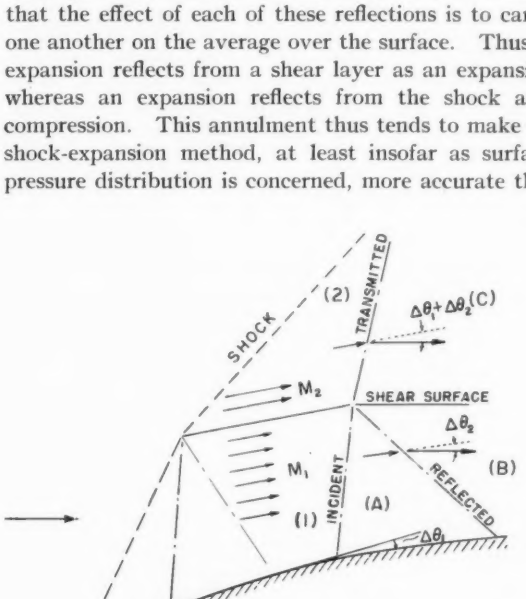

FIG. 4. Schematic picture of wave reflection from a shear surface.

a consideration of either one of the inherent errors by itself would indicate.

In the present paper we propose to develop a perturbation scheme for the flow variables in which the first approximation is isentropic shock-expansion theory and subsequent approximations are expanded in powers of the parameter ϵ. Our choice of the shock reflection coefficient as the expansion parameter is quite arbitrary and is used only as an indication of the deviation from the zero-order approximation. Such a scheme should provide an accurate and mathematically meaningful way of determining the flow variables, and by its nature help to define those regions in which the shock-expansion method may be used with confidence; it takes into account in the perturbation sense all the neglected factors, for example, the curvature and reflection of the principal characteristics and the correct boundary conditions at the shock.

Another analysis concerned with an analytic correction to shock-expansion theory has been given by Mahony.[12] He treats the unsteady one-dimensional piston problem, and in particular the case of the uniformly retarded piston, by an iteration technique starting with the shock-expansion solution. The results are carried over to the steady two-dimensional hypersonic thin-body problem by means of the Tsien-Hayes equivalence principle,[13, 14] thus restricting the analysis to the region of applicability of hypersonic similarity.

Mahony recognizes in his treatment the dominant role played by the principal characteristics in contrast to the secondary role of the reflected Mach lines, and introduces as independent variables a "dummy" characteristic parameter defined by the requirement that it be constant along reflected Mach lines, and a "near" characteristic parameter, related to the flow deflection angle, which is constant along forward-facing Mach lines if the conditions of isentropic shock-expansion theory are met. Having established the basic shock-simple-wave solution, he then applies an iteration in which the characteristic coordinates are held fixed but an entropy distribution is allowed to propagate from the known conditions at the shock along the streamlines, whence the corrected pressure distribution at the airfoil is obtained by integrating back along the reflected characteristics from the shock. He finds that at least for air ($\gamma = 1.4$) and helium ($\gamma = 5/3$) the predictions of shock-expansion theory are remarkably accurate within the hypersonic similarity range, owing partly to a tendency of errors to cancel, which is observed in his iteration procedure.

Independent of the present analysis Mahony and Skeat,[21] following the method of reference 12, treated the problem considered in the present paper without recourse to the hypersonic equivalence principle. Because of their different approach, their method results in a numerical evaluation of an iteration scheme, in constrast to the analytical results of the present analysis. However, the final numerical results should be equivalent to those obtained in the present paper although a direct analytical comparison is not apparent.

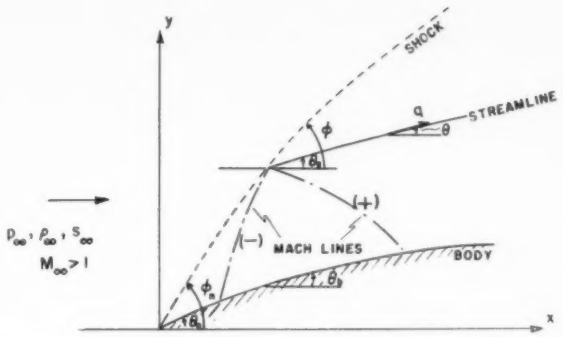

FIG. 5. Coordinate system and flow variables.

The authors point out that it is difficult with their scheme to determine the orders of magnitude of the errors in the theory.

Before proceeding to the analysis we might note that Meyer[15] has formulated the generalized shock-expansion method analytically. Since in this case the flow-deflection angle θ is constant along minus Mach lines and the flow field is determined by the interaction between streamlines carrying entropy changes downstream from the shock and principal characteristics, Meyer logically chooses as independent variables the characteristic coordinates (θ, ψ), where ψ is the stream function. Hence the generalized shock-expansion solution can in principle be built up in a simple rectangular network in the plane of the independent variables. The determination of the shock shape $\psi = \psi_s(\theta)$ is not, however, quite so straightforward, and it must be found by an iteration procedure using the isentropic shape as the zero-order approximation. One may observe that this particular difficulty is avoided by choosing entropy s instead of stream function ψ as one of the characteristic variables, but unfortunately other difficulties just as formidable are encountered.

(III) Basic Equations

As outlined in Section I the problem to be considered is the steady two-dimensional supersonic rotational field of flow generated behind an attached shock wave by a smooth convex body oriented in the direction of a uniform stream of Mach number M_∞. In general the motion may be characterized by the flow-deflection angle θ that the local velocity vector q makes with the free-stream direction, the local Mach angle $\mu = \text{arc sin } 1/M$, and the entropy s, together with the constant ratio of specific heats γ (Fig. 5).

For an isentropic two-dimensional flow the field is completely characterized by the characteristic variables

$$2\xi = \theta - \nu \tag{3.1}$$

$$2\eta = \theta + \nu \tag{3.2}$$

where ν is the Prandtl-Meyer turning angle defined by the differential relation

$$d\nu = [(\cot \mu)/q]\, dq \tag{3.3a}$$

The above equation can be integrated to give the usual

relation for the Prandtl-Meyer angle in an isentropic field as a function of Mach angle

$$\nu = \sqrt{\frac{\gamma+1}{\gamma-1}} \arctan\left(\sqrt{\frac{\gamma-1}{\gamma+1}} \cot \mu\right) - \left(\frac{\pi}{2} - \mu\right) \tag{3.3b}$$

where we require $\nu = 0$ at sonic conditions $\mu = \pi/2$.

Since the Prandtl-Meyer solution serves as the "building block" even for a rotational flow, let us express the compatibility relations for the three sets of characteristics in a rotational flow in terms of the variables ξ and η (see, e.g., reference 16):

On minus Mach lines or principal characteristics

$$\left.\begin{aligned} dy/dx &= \tan(\theta + \mu) \\ d\xi &= [(\sin 2\mu)/4\gamma(\gamma-1)]\, ds \end{aligned}\right\} \tag{3.4}$$

whereas on plus Mach lines or reflected characteristics

$$\left.\begin{aligned} dy/dx &= \tan(\theta - \mu) \\ d\eta &= -[(\sin 2\mu)/4\gamma(\gamma-1)]\, ds \end{aligned}\right\} \tag{3.5}$$

while along streamlines

$$\left.\begin{aligned} dy/dx &= \tan\theta \\ ds &= 0 \end{aligned}\right\} \tag{3.6}$$

Here the entropy s represents the difference between local and free-stream entropy s_∞, nondimensionalized with respect to the specific heat at constant volume c_v, and x, y are rectangular Cartesian coordinates with origin at the leading edge of the body, nondimensionalized with respect to the airfoil chord length.

If the subscript b is used to denote conditions at the body, then the boundary condition on the body can be expressed as

$$(dy/dx)_b = \tan\theta_b \tag{3.7}$$

If the subscript s is used to denote conditions directly behind the shock, then the boundary conditions on the shock

$$(dy/dx)_s = \tan\varphi$$

can be expressed as

$$\theta_s = \arctan\left[\frac{M_\infty^2 \sin 2\varphi - 2\cot\varphi}{2 + M_\infty^2(\gamma + \cos 2\varphi)}\right] \tag{3.8}$$

$$\mu_s = \arcsin\left\{\frac{[(2\gamma M_\infty^2 \sin^2\varphi - (\gamma-1)][(\gamma-1)M_\infty^2 \sin^2\varphi + 2]}{(\gamma+1)^2 M_\infty^4 \sin^2\varphi - 4(M_\infty^2 \sin^2\varphi - 1)(\gamma M_\infty^2 \sin^2\varphi + 1)}\right\}^{1/2} \tag{3.9}$$

$$s_s = \log\left[\frac{2\gamma M_\infty^2 \sin^2\varphi - (\gamma-1)}{\gamma+1}\right] - \gamma \log\left[\frac{(\gamma-1)M_\infty^2 \sin^2\varphi}{(\gamma-1)M_\infty^2 \sin^2\varphi + 2}\right] \tag{3.10}$$

The dominant feature of Eqs. (3.4)–(3.6) is their nonlinearity, the characteristics depending on the solution. In addition, the shock shape itself depends on the solution, through Eqs. (3.8)–(3.10). If, on the basis of the discussion in Section II, the generalized shock-expansion assumption is made that disturbances incident on the shock wave along minus Mach lines are completely absorbed, and the reflections from the streamlines are neglected, then the flow field behind the shock consists of an interaction between streamlines and principal characteristics, along the latter of which both flow-deflection angle θ and pressure p are constant. But even with this assumption it can be seen from Eq. (3.4) that the calculation is still nonlinear since both s and μ vary along the principal characteristics, though the numerical work is made much simpler.

If, however, the further assumption is made that the flow field behind the shock is isentropic, the nonlinearity vanishes; $d\mu = 0$ (because $d\nu = 0$) along principal characteristics, which are straight. Since η is constant along both minus and plus Mach lines, it has the constant value η_0 in the entire flow field. The corresponding shock shape can then be obtained by matching the flow deflection at the body, which is propagated unchanged along principal characteristics, with the flow deflection caused by the shock. The pressure distribution at the body is simply that given by a Prandtl-Meyer expansion from the pressure behind the attached leading-edge shock, and the value of the entropy s_0 is that computed at the leading edge behind the shock.

Because of its analytic simplicity, as has been mentioned, it is this isentropic shock-expansion method which will be utilized as the zero-order approximation in our perturbation scheme. It is most conveniently studied by transforming to characteristic coordinates. We may write for a general flow

$$dx = F\, d\zeta + H\, d\xi \tag{3.11}$$

$$dy = (F + G)\tan(\theta + \mu)\, d\zeta + H \tan(\theta - \mu)\, d\xi \tag{3.12}$$

F, G, and H being defined by these relations under the condition that $d\zeta = 0$ along plus Mach lines. Note that here a line $d\xi = 0$ is given by $dy/dx = [(F + G)/F]\tan(\theta + \mu)$; hence the function G measures the divergence between the principal characteristics and the lines ξ = constant. But ξ is a characteristic variable along these minus Mach lines, and so $G \equiv 0$, under the assumptions of shock-expansion theory. Mahony[12] first introduced this coordinate approach in the one-dimensional unsteady flow problem.

Flow conditions are now characterized by the dependent variables θ, μ, s, F, G, and H, with independent variables ξ and ζ. The transformation of Eqs. (3.4)–(3.6) to these new coordinates results in the following equations:

$$G\tan(\theta + \mu) + \frac{\sin 2\mu}{4\gamma(\gamma-1)}\left\{H[\tan(\theta - \mu) - \tan(\theta + \mu)]\frac{\partial s}{\partial \zeta} - G\tan(\theta + \mu)\frac{\partial s}{\partial \xi}\right\} = 0 \tag{3.13}$$

$$\frac{\partial \eta}{\partial \xi} + \frac{\sin 2\mu}{4\gamma(\gamma - 1)} \frac{\partial s}{\partial \xi} = 0 \tag{3.14}$$

$$H[\tan(\theta - \mu) - \tan\theta] \frac{\partial s}{\partial \zeta} + [F \tan\theta - (F + G)\tan(\theta + \mu)] \frac{\partial s}{\partial \xi} = 0 \tag{3.15}$$

where, since dx, dy are perfect differentials,

$$\partial H/\partial \zeta = \partial F/\partial \xi \tag{3.16}$$

$$(\partial/\partial\zeta)[H \tan(\theta - \mu)] = (\partial/\partial\xi)[(F + G)\tan(\theta + \mu)] \tag{3.17}$$

The equations of the boundaries must also be expressed in the new variables. Since the equation of the body is the equation of a streamline, it is

$$\frac{d\zeta}{d\xi} = \left[\frac{H[\tan(\theta - \mu) - \tan\theta]}{F\tan\theta - (F + G)\tan(\theta + \mu)}\right]_b \tag{3.18}$$

Further, let the equation of the body be $x = X(\theta) = X(\xi + \eta)$: then on eliminating $d\zeta/d\xi$ we can express H_b as

$$H_b = X'\left[\frac{[F\tan\theta - (F+G)\tan(\theta+\mu)][1 + (\partial\eta/\partial\xi)]}{F\tan(\theta-\mu) - (F+G)\tan(\theta+\mu) + X'[\tan\theta - \tan(\theta-\mu)](\partial\eta/\partial\zeta)}\right]_b \tag{3.19}$$

The equation of the shock may be written as

$$\frac{d\zeta}{d\xi} = \left[\frac{H[\tan(\theta - \mu) - \tan\varphi]}{F\tan\varphi - (F + G)\tan(\theta + \mu)}\right]_s$$

The function G can be eliminated from the above equation by using the identities $d\xi/d\zeta = (d\xi/d\varphi)(d\varphi/d\zeta)$ and $ds/d\zeta = (ds/d\varphi)(d\varphi/d\zeta)$, together with the compatibility equations, which yield a quadratic in $d\varphi/d\zeta$ with the roots

$$d\varphi/d\zeta = -(F/H)_s(d\varphi/d\xi)$$

and

$$d\varphi/d\zeta = -(F/H)_s K(\varphi) \tag{3.20}$$

where

$$K(\varphi) = \left\{\frac{[\tan(\theta+\mu) - \tan\varphi][\tan\theta - \tan\varphi]}{[\tan(\theta-\mu) - \tan\varphi]\left\{\frac{\sin 2\mu}{4\gamma(\gamma-1)}[\tan(\theta+\mu) - \tan\theta]\frac{ds}{d\varphi} + [\tan\theta - \tan\varphi]\frac{d\xi}{d\varphi}\right\}}\right\}_s \tag{3.21}$$

The shock equation then is Eq. (3.20). That it is the correct root can be seen from the fact that it reduces to the original equation for $d\zeta/d\xi$ under the assumptions, say, of isentropic shock-expansion theory ($G = 0$, $ds/d\varphi = 0$).

(IV) Analytic Formulation of Shock-Expansion Method

With the differential equations and boundaries in the transformed coordinates, we can now determine the zero-order isentropic shock-expansion solution in these coordinates to be used in the perturbation procedure. The resulting shock shape and the original body can then be used as boundaries determining the first-order corrections to the flow field characteristics and the surface-pressure distribution; and from these corrections a perturbed shock shape can in turn be found, etc.

The zero-order results are obtained in the following manner: In accordance with our previous remarks,

$$\nu_0 = \eta_0 - \xi \qquad \theta_0 = \eta_0 + \xi$$

$$\mu_0 = \mu_0(\eta_0 - \xi)$$

η_0 being a constant, where we distinguish quantities associated with the isentropic shock-expansion method by a subscript 0. Hence ν_0, θ_0, and μ_0 are functions only of ξ, the principal characteristic variable. Under these circumstances Eqs. (3.13)–(3.15) are identically zero. The solution is provided by the nontrivial Eqs. (3.16) and (3.17), which become

$$\partial F_0/\partial\xi = \partial H_0/\partial\zeta \tag{4.1}$$

$$(\partial F_0/\partial\xi)\tan[\eta_0 + \xi + \mu_0(\eta_0 - \xi)] + F_0\sec^2[\eta_0 + \xi + \mu_0(\eta_0 - \xi)][1 + (d\mu_0/d\xi)] = (\partial H_0/\partial\zeta)\tan[\eta_0 + \xi - \mu_0(\eta_0 - \xi)] \tag{4.2}$$

Eliminating H_0 between these two equations,

$$\frac{1}{F_0}\frac{\partial F_0}{\partial\xi} = -\frac{\sec^2(\theta_0 + \mu_0)[1 + (d\mu_0/d\xi)]}{\tan(\theta_0 + \mu_0) - \tan(\theta_0 - \mu_0)} \tag{4.3}$$

Upon integration we have

$$\log[C(\zeta)F_0] = -\int \frac{[(d\xi/d\mu_0) + 1]\,d\mu_0}{\tan 2\mu_0} - \int \frac{\tan(\theta + \mu_0)d[\tan(\theta_0 + \mu_0)]}{1 + \tan^2(\theta_0 + \mu_0)}$$

where we have used the identity

$$\tan(\theta_0 - \mu_0) = \frac{\tan(\theta_0 + \mu_0) - \tan 2\mu_0}{1 + \tan(\theta_0 + \mu_0)\tan 2\mu_0}$$

Differentiating the Prandtl-Meyer relation, Eq. (3.3b),

$$(d\xi/d\mu_0) + 1 = (\gamma + 1)/(\gamma - \cos 2\mu_0)$$

On substituting the above relation and integrating, we obtain

$$F_0(\xi) = \frac{\cos(\theta_0 + \mu_0)\,[(\gamma - \cos 2\mu_0)/2]^{\gamma/2(\gamma-1)}}{(\cos\mu_0)^{1/2}(\sin\mu_0)^{(\gamma+1)/2(\gamma-1)}} \tag{4.4}$$

Here we have set $C(\zeta) = 1$, which is possible because ζ

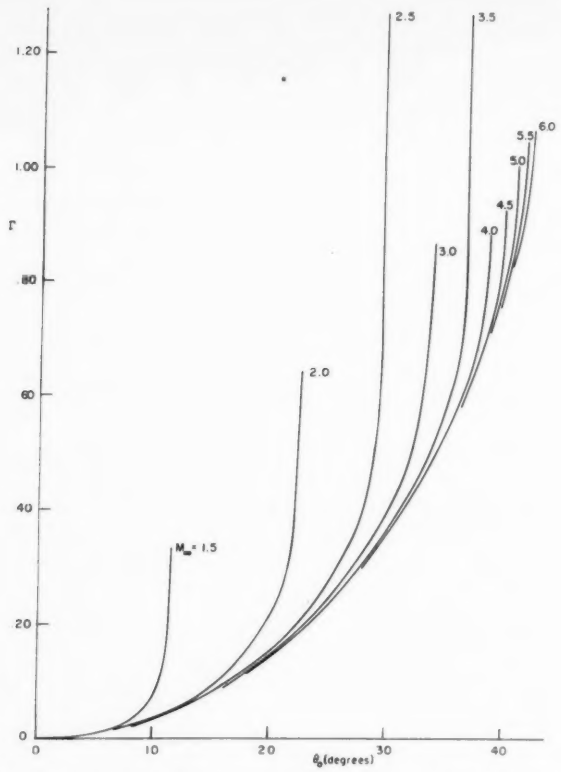

FIG. 6. Integrating factor as a function of deflection angle; $\gamma = 1.4$.

previously has only been specified along plus Mach lines.

With $F_0(\xi)$ known, Eq. (4.1) can be integrated to give

$$H_0(\xi, \zeta) = F_0'(\xi)\zeta + a(\xi) \tag{4.5}$$

The function $a(\xi)$ is determined by the boundary condition at the body given by Eq. (3.19),

$$(H_0)_b = (1/2)X'(1 + \tan \theta_0 \tan \mu_0)_b \tag{4.6}$$

The body shape in the present coordinates follows from Eq. (3.18), and is

$$d\zeta/d\xi = (1/2)X'[(1 - \tan \theta_0 \tan \mu_0)/F_0]_b \tag{4.7}$$

(V) Shock Shape and Pressure Distribution According to Isentropic Shock-Expansion Theory

With the zero-order solutions represented by Eqs. (4.4)–(4.7) we can now find any of the properties of the flow field. One of the main points of interest is the shock shape—Eq. (3.20)—which, inserting the value of H given by Eq. (4.5), is governed by the differential equation

$$d\zeta/d\varphi_0 = -[(F_0'/F_0)\zeta + (a/F_0)]_s[1/K_0(\varphi_0)]$$

An integrating factor of this equation is

$$\Gamma(\varphi_0) = \exp\left\{-\int \frac{1}{K_0} \frac{(d/d\xi)[\tan(\theta_0 + \mu_0)]}{\tan(\theta_0 + \mu_0) - \tan(\theta_0 - \mu_0)} d\varphi_0\right\}_s \tag{5.1}$$

which reduces it to

$$(d/d\varphi_0)(\zeta\Gamma) = (-a\Gamma/F_0K_0)_s$$

On integrating the above relation, the equation of the shock in characteristic coordinates is

$$\zeta = -\frac{1}{\Gamma(\varphi_0)} \int_{\varphi_n}^{\varphi_0} \left[\frac{a(\xi)}{F_0(\xi)} \frac{\Gamma(\varphi_0)}{K_0(\varphi_0)}\right]_s d\varphi_0 \tag{5.2}$$

In physical variables, note from Eqs. (2.11) and (2.12) that any line $\zeta = \zeta(\xi)$ is written

$$dx = \{(d/d\xi)(F_0\zeta) + a\}\, d\xi \tag{5.3}$$

$$dy = \left\{F_0 \frac{d\zeta}{d\xi} \tan(\theta_0 + \mu_0) + (F_0'\zeta + a) \tan(\theta_0 - \mu_0)\right\} d\xi \tag{5.4}$$

Hence, integrating Eq. (5.3) between the origin and an arbitrary point on the shock and substituting relation (5.2) for ζ, the shock equation may be written

$$x = \left[-\frac{F_0}{\Gamma} \int_{\varphi_n}^{\varphi_0} \frac{a}{F_0} \frac{\Gamma}{K_0} d\varphi_0 + \int_{\varphi_n}^{\varphi_0} a \frac{d\theta_0}{d\varphi_0} d\varphi_0\right]_s \tag{5.5}$$

a relation between abscissa x and inclination φ_0. Finding the ordinate y would require integration of Eq. (5.4).

If we wish to evaluate the integrals in Eq. (5.5), however, we must investigate more fully the properties of the integrating factor Γ. In particular, Γ vanishes in regions where the shock has decayed to negligibly small strength. It is most convenient in such regions to use θ_0 as independent variable, since the usual expansions of quantities associated with weak shocks are carried out with respect to flow-deflection angle.

Thus we write Eq. (5.1) in the form

$$\Gamma(\varphi_0) = \Gamma_1(\theta_0) = \exp\left\{-\int \frac{1}{N_0(\theta_0)} \frac{(d/d\xi)[\tan(\theta_0 + \mu_0)]}{\tan(\theta_0 + \mu_0) - \tan(\theta_0 - \mu_0)} d\theta_0\right\}_s \tag{5.6}$$

where $N_0(\theta_0) = (d\theta_0/d\varphi_0)_s K(\varphi_0)$. In the appendix the integrand in the exponent is evaluated for small θ_0, with the result

$$\left[\frac{1}{N_0(\theta_0)} \frac{(d/d\xi)[\tan(\theta_0 + \mu_0)]}{\tan(\theta_0 + \mu_0) - \tan(\theta_0 - \mu_0)}\right]_s = \left[-\frac{2}{\theta_0} - L(\theta_0)\right]_s \tag{5.7}$$

where $L(\theta_0)$, which is defined by this equation, is a quantity of order 1 in θ_0:

$$L(0) = (M_\infty^2 - 1)^{-3/2}[(\gamma - 1)M_\infty^2 + 2]$$

We see that the integrand consists of a singular part plus a nonsingular part near $\theta_0 = 0$. The exponent then becomes

$$-\int \left[-\frac{2}{\theta_0} - L(\theta_0)\right]_s d\theta_0 = \int L(\theta_0) d\theta_0 + 2(\log \theta_0)_s$$

and $$\Gamma_1(\theta_0) = (\theta_0)_s^2 \exp\left\{\int_0^{\theta_0} L(\theta_0)\, d\theta_0\right\} \qquad (5.8)$$

This form is most convenient for computational purposes.

The integrating factor Γ is shown in Fig. 6 as a function of θ_0 with M_∞ as a parameter for $\gamma = 1.4$. It is seen that for all free-stream Mach numbers and flow-deflection angles except for those adjacent to the condition for shock detachment, the values of Γ are close to those computed with $M_\infty = \infty$. Although an analytic expression for Γ is beyond reach for arbitrary M_∞, the case $M_\infty = \infty$ is integrable. The solution can be expressed in the following form:

$$[\Gamma_1(\theta_0)]_{M_\infty=\infty} = 2\left\{\frac{F_0 \sin(\theta_0 + \mu_0 - \varphi_0)\sin\varphi_0}{\cos(\theta_0 + \mu_0)}\left[\tan\frac{\varphi_0}{2}\right]^{\sqrt{2\gamma/(\gamma-1)}} \times \left[\frac{\tan\mu_0 + \sqrt{(\gamma-1)/(\gamma+1)}\tan\varphi_0}{\tan\mu_0 - \sqrt{(\gamma-1)/(\gamma+1)}\tan\varphi_0}\right]^{\gamma/\sqrt{\gamma^2-1}} \times \left[-\frac{(\gamma-1)\cot(\varphi_0/2) + (\gamma+1)\cot\varphi_0 - \sqrt{2\gamma(\gamma-1)}\cot\mu_0}{(\gamma-1)\cot(\varphi_0/2) - (3\gamma-1)\cot\varphi_0 - \sqrt{2\gamma(\gamma-1)}\cot\mu_0}\right]^{\sqrt{\gamma/2(\gamma-1)}}\right\}_s \qquad (5.9)$$

Here, the integration constant which multiplied $\Gamma_1(\theta_0)$ has been evaluated numerically and found equal to 1/2.

The asymptotic shock shape far away from the leading edge, where the shock is weak, may easily be developed from the expressions in the appendix: the flow-deflection angle is small, and both Mach angle and shock angle tend to the value arc sin $(1/M_\infty)$. We write the shock equation (5.2)

$$\zeta = -\frac{1}{\Gamma_1(\theta_0)}\left[\int_{\theta_n}^{0}\frac{a}{F_0}\frac{\Gamma_1}{N_0}\,d\theta_0 + \int_0^{\theta_0}\frac{a}{F_0}\frac{\Gamma_1}{N_0}\,d\theta_0\right]_s$$

But for sufficiently small θ_0, $\Gamma_1 \sim \theta_0^2$ by Eq. (5.8), and $N_0 = 0(\theta_0)$ as shown in the appendix; hence the second integral is $0(\theta_0^2)$, and we have

$$\zeta \sim \left\{[M(\theta_n)/\theta_0^2][1 + 0(\theta_0^2)]\right\}_s \qquad (5.10)$$

where

$$M(\theta_n) = \int_0^{\theta_n}\left(\frac{a}{F_0}\frac{\Gamma_1}{N_0}\right)_s d\theta_0 \qquad (5.11)$$

Inverting (5.10),

$$\theta_0 \sim \sqrt{M(\theta_n)}\,\zeta^{-1/2} + 0(\zeta^{-3/2}) \qquad (5.12)$$

Now we write the shock shape in physical variables from Eq. (2.11) as

$$x = \int_0^\zeta\left\{F_0\left[1 + \frac{H_0}{F_0}\frac{d\xi}{d\zeta}\right]\right\}_s d\zeta = \int_0^\zeta \left\{F_0(\xi)[1 - N_0(\theta_0)]\right\}_s d\zeta \qquad (5.13)$$

by Eq. (3.20). Writing $N_0(\theta_0) \sim p\theta_0 + q\theta_0^2$ (see appendix) and expanding $F_0(\xi)$ in Taylor series about its value $F_0(-\eta_0)$ at $\theta_0 = 0$, the above equation becomes

$$x \sim \int_0^\zeta\left\{F_0(-\eta_0)\left[1 + \left\{-p + \frac{F_0'(-\eta_0)}{F_0(-\eta_0)}\right\}\theta_0 + \left\{-q - p\frac{F_0'(-\eta_0)}{F_0(-\eta_0)} + \frac{1}{2}\frac{F_0''(-\eta_0)}{F_0(-\eta_0)}\right\}\theta_0^2\right]\right\}_s d\zeta$$

Then substituting Eq. (5.12) yields

$$x \sim \int_0^\zeta\left\{F_0(-\eta_0)\left[1 + \left\{-p\sqrt{M(\theta_n)} + \frac{F_0'(-\eta_0)}{F_0(-\eta_0)}\sqrt{M(\theta_n)}\right\}\zeta^{-1/2} + \left\{-qM(\theta_n) - p\frac{F_0'(-\eta_0)}{F_0(-\eta_0)}M(\theta_n) + \frac{1}{2}\frac{F_0''(-\eta_0)}{F_0(-\eta_0)}M(\theta_n)\right\}\zeta^{-1} + 0(\zeta^{-3/2})\right]\right\}_s d\zeta \qquad (5.14)$$

From the information in the appendix we may readily evaluate $F_0'(-\eta_0)/F_0(-\eta_0)$. By Eq. (4.3),

$$\left(\frac{F_0'}{F_0}\right)_{\theta_0=0} = \left\{\frac{-\sec^2(\theta_0+\mu_0)[1 + (d\mu_0/d\xi)]}{\tan(\theta_0+\mu_0) - \tan(\theta_0-\mu_0)}\right\}_{\theta_0=0} = -\frac{\gamma+1}{4}\frac{M_\infty^4}{(M_\infty^2-1)^{3/2}} = 2p$$

Hence, integrating Eq. (5.14),

$$x \sim \left\{F_0(-\eta_0)\left[\zeta + 2p\sqrt{M(\theta_n)}\,\zeta^{1/2} - \left(2p^2 + q - \frac{1}{2}\frac{F_0''(-\eta_0)}{F_0(-\eta_0)}\right)M(\theta_n)\zeta\left(\frac{\log\zeta}{\zeta}\right) + 0(\zeta^{-1/2})\right]\right\}_s$$

Since $(\log\zeta)/\zeta = 0(1/\zeta)$,

$$x \sim \left\{F_0(-\eta_0)\,\zeta[1 + 2p\sqrt{M(\theta_n)}\,\zeta^{-1/2} + 0(\zeta^{-1})]\right\}_s$$

Using Eq. (5.10) and solving for θ_0, we obtain for the asymptotic shock decay

$$\theta_0 \sim \left\{\sqrt{F_0(-\eta_0)M(\theta_n)}\,x^{-1/2} \times [1 + p\sqrt{F_0(-\eta_0)M(\theta_n)}\,x^{-1/2} + 0(x^{-1})]\right\}_s \qquad (5.15)$$

This reduces to Mahony's form[12]

$$\theta_0 \sim \left\{\sqrt{F_0(-\eta_0)M(\theta_n)}\,t^{-1/2} \times [1 - (\Lambda/2)\sqrt{F_0(-\eta_0)M(\theta_n)}\,t^{-1/2} + 0(t^{-1})]\right\}_s$$

in the event that hypersonic similitude applies ($\tan\theta \ll 1$, $\tan\mu \ll 1$). Here, t is the time nondimensionalized with respect to the airfoil chord length divided by the free-stream sound speed, and Mahony's $\Lambda \to -2p$.

This relation in turn reduces to Friedrichs' form[20] if the shock is everywhere weak.

The pressure at the body is of course just the Prandtl-Meyer pressure distribution. In general this may be found implicitly from Eq. (3.3b) which can be solved to give a relation $\mu_0 = \mu_0(\nu_0) = \mu_0(\eta_0 - \xi)$. Probstein[17] has shown that with $\gamma = 5/3$ or $5/4$ this relation can be given explicitly. Since we know the distribution of ξ at the body, we have, say, $(\mu_0)_b = f(x_b)$; then

$$\frac{(p_0)_b}{p_{t_\infty}} = \left[\left(1 + \frac{\gamma - 1}{2 \sin^2 (\mu_0)_b}\right) \times \left(\frac{(\gamma - 1)M_\infty^2 \sin^2 \varphi_n + 2}{(\gamma + 1)M_\infty^2 \sin^2 \varphi_n}\right)\right]^{-\gamma/(\gamma-1)} \times \left[\frac{\gamma + 1}{2\gamma M_\infty^2 \sin^2 \varphi_n - (\gamma - 1)}\right]^{1/(\gamma-1)} \tag{5.16}$$

(VI) First-Order Perturbation on Isentropic Shock-Expansion Method

Having analytically formulated the zero-order results, we are now in a position to obtain an improvement on this solution by means of a perturbation. As we noted previously, the dependent variables will be expanded in power series in the maximum value of the shock reflection coefficient ϵ, the series coefficients being functions of ξ and ζ. These expansions are then substituted into the flow equations, first-order terms are equated, and the first-order solutions are subjected to the boundary conditions at the zero-order shock. In this way entropy differences, the introduction and subsequent curvature of both families of Mach lines, and the interactions between the characteristics themselves are permitted.

The quantity ϵ described in Section II is a logical expansion parameter since it is small when the assumptions of shock-expansion theory are valid, and becomes of order 1 or greater when they are not. The reader should recall, however, that relatively large deviations of the dependent variables from their normal values in isentropic shock-expansion theory do not necessarily indicate a breakdown in the approximation procedure, as was shown in Section II.

We now write

$$\left.\begin{aligned} F &= F_0 + \epsilon F_1 + \epsilon^2 F_2 + \dots \\ G &= \epsilon G_1 + \epsilon^2 G_2 + \dots \\ H &= H_0 + \epsilon H_1 + \epsilon^2 H_2 + \dots \\ s &= s_0 + \epsilon s_1 + \epsilon^2 s_2 + \dots \\ \eta &= \eta_0 + \epsilon\eta_1 + \epsilon^2\eta_2 + \dots \\ \theta &= \theta_0 + \epsilon\theta_1 + \epsilon^2\theta_2 + \dots = \\ &\qquad (\xi + \eta_0) + \epsilon\eta_1 + \epsilon^2\eta_2 + \dots \\ \mu &= \mu_0 + \epsilon\mu_1 + \epsilon^2\mu_2 + \dots = \mu(\nu) = \\ &\qquad \mu([-\xi + \eta_0] + \epsilon\eta_1 + \epsilon^2\eta_2 + \dots) \end{aligned}\right\} \tag{6.1}$$

where s_0 and η_0 are constants. Substituting these in Eqs. (3.13)–(3.17) and equating coefficients of ϵ, we obtain, respectively, the first-order equations

$$G_1 \tan(\theta_0 + \mu_0) + H_0[(\sin 2\mu_0)/4\gamma(\gamma - 1)] \times [\tan(\theta_0 - \mu_0) - \tan(\theta_0 + \mu_0)](\partial s_1/\partial\zeta) = 0 \tag{6.2}$$

$$(\partial\eta_1/\partial\xi) + [(\sin 2\mu_0)/4\gamma(\gamma - 1)](\partial s_1/\partial\xi) = 0 \tag{6.3}$$

$$H_0[\tan(\theta_0 - \mu_0) - \tan\theta_0](\partial s_1/\partial\zeta) + F_0[\tan\theta_0 - \tan(\theta_0 + \mu_0)](\partial s_1/\partial\xi) = 0 \tag{6.4}$$

$$\partial H_1/\partial\zeta = \partial F_1/\partial\xi \tag{6.5}$$

$$(\partial/\partial\zeta)\{H_1 \tan(\theta_0 - \mu_0) + H_0(\theta_1 - \mu_1) \times [1 + \tan^2(\theta_0 - \mu_0)]\} = (\partial/\partial\xi)\{(F_1 + G_1)\tan(\theta_0 + \mu_0) + F_0(\theta_1 + \mu_1)[1 + \tan^2(\theta_0 + \mu_0)]\} \tag{6.6}$$

The variables θ_1 and μ_1 may be expressed in terms of η_1 by expanding the last two of Eqs. (6.1) in ϵ, with the help of Eq. (3.3b):

$$\theta_1 = \eta_1 \tag{6.7}$$

$$\mu_1 = -(1/2)[(\gamma + 1)\tan^2\mu_0 + \gamma - 1]\eta_1 \tag{6.8}$$

Note that the relation between Prandtl-Meyer angle and Mach angle [Eq. (3.3b)] holds in a nonisentropic flow provided the critical speed of sound is everywhere constant (as it is in this problem). Substituting these two relations in Eq. (6.6) and carrying out the differentiations, the following equation results:

$$\frac{\partial F_1}{\partial\xi}[\tan(\theta_0 + \mu_0) - \tan(\theta_0 - \mu_0)] + \frac{\partial G_1}{\partial\xi}\tan(\theta_0 + \mu_0) + (F_1 + G_1)\frac{d}{d\xi}[\tan(\theta_0 + \mu_0)] - \frac{1}{2}\frac{\partial\eta_1}{\partial\xi}[(\gamma + 1)\tan^2\mu_0 + \gamma - 3]F_0 \sec^2(\theta_0 + \mu_0) - \frac{1}{2}\frac{\partial\eta_1}{\partial\zeta}[(\gamma + 1)\tan^2\mu_0 + \gamma + 1]H_0 \sec^2(\theta_0 - \mu_0) - \frac{1}{2}\eta_1\left[\{(\gamma + 1)\tan^2\mu_0 + \gamma - 3\}\left\{\frac{d}{d\xi}[F_0 \sec^2(\theta_0 + \mu_0)] + F_0' \sec^2(\theta_0 - \mu_0)\right\} + 4F_0' \sec^2(\theta_0 - \mu_0) + (\gamma + 1)F_0 \sec^2(\theta_0 + \mu_0)\frac{d}{d\xi}(\tan^2\mu_0)\right] = 0 \tag{6.9}$$

The boundary conditions (3.7)–(3.10), together with the necessary specifications of H_1 and F_1, are for the first order as follows:

On the body,

$$dy/dx = (dy/dx)_b$$

$$(\theta_0 + \epsilon\theta_1)_b = \arctan(dy/dx)_b \tag{6.10}$$

$$(H_1)_b = 0 \tag{6.11}$$

and on the shock,

$$dy/dx = \tan\varphi_0$$

$$(\theta_1)_s = 0 \tag{6.12}$$

$$(\mu_1)_s = 0 \tag{6.13}$$

$$(s_0 + \epsilon s_1)_s = \log\left[\frac{2\gamma M_\infty^2 \sin^2\varphi_0 - (\gamma - 1)}{\gamma - 1}\right] - \gamma \log\left[\frac{(\gamma - 1)M_\infty^2 \sin^2\varphi_0}{(\gamma - 1)M_\infty^2 \sin^2\varphi_0 + 2}\right] \quad (6.14)$$

$$(F_1)_s = 0 \quad (6.15)$$

The method of solving these equations follows. Since s_0 is a constant, the characteristic equation resulting from Eq. (6.4) gives the streamlines s_1 = constant to the first order in the characteristic plane: using Eq. (4.5),

$$\frac{d\zeta}{(F_0'\zeta + a)[\tan(\theta_0 - \mu_0) - \tan\theta_0]} = \frac{-d\xi}{F_0[\tan(\theta_0 + \mu_0) - \tan\theta_0]}$$

$$\zeta = \left[\int \frac{a}{\cos(\theta_0 - \mu_0)} \left\{\frac{1 - \cos 2\mu_0}{\gamma - \cos 2\mu_0}\right\}^{(\gamma+1)/2(\gamma-1)} d\zeta + C\right] \frac{(\cos\mu_0)^{1/2}\,[(\gamma - \cos 2\mu_0)/2]^{1/2(\gamma-1)}}{(\sin\mu_0)^{(\gamma+1)/2(\gamma-1)}} \quad (6.17)$$

$$= \zeta_T(\xi, C)$$

with the constant C distinguishing separate streamlines.

If we call a general point in the flow field $P(\xi, \zeta)$ and the point on the shock wave determined by the streamline through P, $Q(\xi_Q, \zeta_Q)$, then writing the zero-order equation of the shock $\zeta = \zeta_s(\xi)$ we may obtain the point Q from the equality

$$\zeta_T(\xi_Q, C) = \zeta_s(\xi_Q)$$

But at this point we know the entropy contribution $s_1 = (s_1)_Q$ from Eq. (6.14). Hence the entropy distribution is determined from

$$s_1(\xi, \zeta) = (s_1)_Q \quad (6.18)$$

The distribution of η_1 may be found from Eq. (6.3):

$$\eta_1 = \frac{-1}{4\gamma(\gamma - 1)} \int \sin 2\mu_0 \frac{\partial s_1}{\partial \xi}\, d\xi + h(\zeta) = \frac{-1}{4\gamma(\gamma - 1)} \left[s_1 \sin 2\mu_0 - 2\int s_1 \cos 2\mu_0 \frac{d\mu_0}{d\xi}\, d\xi\right] + h(\zeta)$$

where $h(\zeta)$ is determined by Eqs. (6.7) and (6.12):

$$\eta_1 = \frac{-1}{4\gamma(\gamma - 1)} \left\{\left[s_1 \sin 2\mu_0\right]_{\xi_s(\zeta)}^{\xi} - 2\int_{\xi_s(\zeta)}^{\xi} s_1 \cos 2\mu_0 \frac{d\mu_0}{d\xi}\, d\xi\right\} \quad (6.19)$$

From Eq. (6.2) G_1 is found directly, where, if we consider $(s_1)_Q = (s_1)_Q(C)$, by Eq. (6.17)

$$\frac{\partial s_1}{\partial \zeta} = \frac{d(s_1)_Q}{dC}\frac{\partial C}{\partial \zeta} = \frac{d(s_1)_Q}{dC}\left\{\frac{(\sin\mu_0)^{(\gamma+1)/2(\gamma-1)}}{(\cos\mu_0)^{1/2}[(\gamma - \cos 2\mu_0)/2]^{1/2(\gamma-1)}}\right\}$$

From Eq. (6.9) we deduce F_1, which has the form

or $$d\zeta/d\xi = g\zeta + f \quad (6.16)$$

where the functions g and f so defined, depending only on ξ, may be evaluated from Eqs. (4.3) and (4.4) as

$$g = -\frac{F_0'}{F_0}\left[\frac{\tan(\theta_0 - \mu_0) - \tan\theta_0}{\tan(\theta_0 + \mu_0) - \tan\theta_0}\right] = -\frac{1 + (d\mu_0/d\xi)}{\sin 2\mu_0} = -\frac{\gamma + 1}{2\sin 2\mu_0 \cos^2\mu_0}$$

$$f = -\frac{a}{F_0}\left[\frac{\tan(\theta_0 - \mu_0) - \tan\theta_0}{\tan(\theta_0 + \mu_0) - \tan\theta_0}\right] = \frac{a\cos(\theta_0 + \mu_0)}{F_0\cos(\theta_0 - \mu_0)} = a\frac{(\cos\mu_0)^{1/2}(\sin\mu_0)^{(\gamma+1)/2(\gamma-1)}}{\cos(\theta_0 - \mu_0)[(\gamma - \cos 2\mu_0)/2]^{\gamma/2(\gamma-1)}}$$

This differential equation has the solution

$$(\partial F_1/\partial\xi) + m(\xi)F_1 + n(\xi, \zeta) = 0$$

whence

$$F_1 = \left[-\int n(\xi, \zeta)e^{\int m(\xi)d\xi}\, d\xi + k(\zeta)\right] e^{-\int m(\xi)d\xi}$$

$k(\zeta)$ being determined by Eq. (6.15):

$$F_1 = e^{-\int m(\xi)d\xi}\int_{\xi}^{\xi_s(\zeta)} n(\xi, \zeta)e^{\int m(\xi)d\xi}\, d\xi \quad (6.20)$$

From Eq. (6.5) it follows that

$$H_1 = \int \frac{\partial F_1}{\partial \xi}\, d\zeta + l(\xi) = -\int [n(\xi, \zeta) + m(\xi)F_1]d\zeta + l(\xi)$$

$l(\xi)$ being determined by Eq. (6.11). Hence

$$H_1 = \int_{\zeta}^{\zeta_b(\xi)} [n(\xi, \zeta) + m(\xi)F_1]d\zeta \quad (6.21)$$

The shock equation in characteristic coordinates is, of course, Eq. (5.2). Due to the straining of coordinates involved in the perturbation, however, the body shape is slightly disturbed in the characteristic plane. But if we assume that this disturbance can be neglected (as can be proved), we may easily obtain an expression for the pressure correction at the body. Under these conditions, from Eq. (6.19)

$$(\eta_1)_b = \frac{-1}{4\gamma(\gamma - 1)} \left\{\left[\left[s_1 \sin 2\mu_0\right]_{\xi_s}^{\xi_b} - 2\int_{\xi_s}^{\xi_b} s_1 \cos 2\mu_0 \frac{d\mu_0}{d\xi}\, d\xi\right\}\right. \quad (6.22)$$

Thus Eq. (6.8) gives the distribution of $(\mu_1)_b$. The total body pressure is then

$$\frac{(p_0 + \epsilon p_1)_b}{p_{t\infty}} = \left[\left(1 + \frac{\gamma - 1}{2 \sin^2 (\mu_0 + \epsilon\mu_1)_b}\right) \times \left(\frac{(\gamma - 1)M_\infty^2 \sin^2 \varphi_n + 2}{(\gamma + 1)M_\infty^2 \sin^2 \varphi_n}\right)\right]^{-\gamma/(\gamma-1)} \times \left[\frac{\gamma + 1}{2\gamma\, M_\infty^2 \sin^2 \varphi_n - (\gamma - 1)}\right]^{1/(\gamma-1)} \tag{6.23}$$

so that we have for the first-order contribution

$$(p_1)_b = \left[2\gamma\, p_0 \cos 2\mu_0 \left(\frac{1 + \cos 2\mu_0}{\gamma - \cos 2\mu_0}\right)\mu_1\right]_b \tag{6.24}$$

at each point on the body with inclination $\theta_b = \xi_b + \eta_0 + \epsilon(\eta_1)_b$.

It is evident that the amount of labor required to obtain higher order approximations using this system may be rather large. Yet various results, in particular the first-order pressure distribution, fall out quite readily.

(VII) Numerical Calculations and Discussion

To illustrate the method we have just developed, numerical computations were carried out for the case of $M_\infty = \infty$ and $\gamma = 1.4$. In particular a family of symmetric parabolic airfoils was selected with latus recta parallel to the free stream. If such airfoils are (100 b) per cent thick and pass through the points (0,0) and (1,0) in the xy-plane, their equation is

$$y - (1/2)b = -2b[x - (1/2)]^2$$

or

$$\left.\begin{aligned} x = X(\theta) &= (1/2) - (1/4b) \tan\theta \\ X'(\theta) &= -(1/4b) \sec^2\theta \end{aligned}\right\} \tag{7.1}$$

It was decided to calculate the body and shock shapes in the characteristic plane by numerical integration, although a numerical-graphical procedure might prove easier in the absence of automatic computing equipment. The body shape $\zeta_b(\xi)$ is obtained from Eq. (4.7), and Eqs. (4.5) and (4.6) then serve to determine the function $a(\xi)$. The shock shape $\zeta_s(\xi)$ is then computed from Eq. (5.2) with the aid of the integrating factor of Eq. (5.9).

Note that if we eliminate $(H_0)_b$ and X' from Eqs. (4.5)–(4.7) we obtain the following expression for $a(\xi)$:

$$a = \frac{d\zeta_b}{d\xi} \frac{\cos(\theta_0 - \mu_0)}{\cos(\theta_0 + \mu_0)} F_0 - \zeta_b F_0'$$

Substituting this into Eq. (6.16) yields the first-order streamline equation

$$\frac{d\zeta}{d\xi} - \frac{d\zeta_b}{d\xi} = -\frac{\gamma + 1}{2 \sin 2\mu_0 \cos^2 \mu_0} [\zeta - \zeta_b(\xi)] \tag{7.2}$$

which is particularly simple for our purposes, since it allows rapid numerical-graphical computation of the streamline pattern. A number of appropriate points on the shock in the characteristic plane are chosen and through these are drawn lines ξ = constant to the body, along which lines the various coefficients in Eq. (7.2) are constant and can be determined once and for all. The streamlines are then built up, starting from the shock, as line segments between the lines ξ = constant with slopes determined by Eq. (7.2).

At each point on the shock $(s_1)_s$ is determined from Eq. (6.14). This equation must be expanded for large M_∞ in the present case. The dominating term is the first logarithm, which is asymptotically

$$\log\left[\frac{2\gamma M_\infty^2 \sin^2 \varphi_0 - (\gamma - 1)}{\gamma - 1}\right] \sim \log\left[\frac{2\gamma M_\infty^2 \sin^2 \varphi_0}{\gamma - 1}\right] - \frac{\gamma - 1}{2\gamma M_\infty^2 \sin^2 \varphi_0}$$

The function $(s_0)_s$ consists substantially of this term evaluated at the leading edge ($\varphi_0 = \varphi_n$). Hence taking the limit $M_\infty \to \infty$,

$$\epsilon(s_1)_s = 2 \log(\sin \varphi_0 / \sin \varphi_n) \tag{7.3}$$

Since entropy differences are propagated along streamlines, we now know the entropy distribution along lines ζ = constant, and we can proceed to evaluate $(\eta_1)_b$ from Eq. (6.22) and hence $(p_1/p_0)_b$ from Eqs. (6.8) and (6.24). The pressure coefficient for infinite free-stream Mach number is

$$C_p = \frac{2p/p_\infty}{\gamma M_\infty^2}$$

The zero-order pressure distribution may be written

$$\left(\frac{p_0/p_\infty}{M_\infty^2}\right)_b = \left(\frac{p_0}{p_t}\frac{p_t}{p_n}\frac{p_n/p_\infty}{M_\infty^2}\right)_b = \left(\frac{p_0}{p_t}\right)_b \left(1 + \frac{M_n^2}{5}\right)^{7/2} \left(\frac{7}{6}\sin^2 \varphi_n\right)$$

by the oblique shock relations, for $\gamma = 7/5$, whence we have for the zero- and first-order pressure coefficients at the body, respectively,

$$C_{p_0} = \left[\frac{10}{7}\frac{p_0/p_\infty}{M_\infty^2}\right]_b$$

$$C_{p_1} = \left[\left(1 + \frac{\epsilon p_1}{p_0}\right) C_{p_0}\right]_b$$

The computations were carried out for 10%- and 30%-thick parabolic airfoils, and the results of these calculations are given in graphical form in Figs. 7–11. One notes from Fig. 7 that the shock wave in the characteristic plane bends over at the point which corresponds along a line ζ = constant to the value $\theta_0 = 0$ on the body. Physically this point represents the end of the region of influence of the body on the shock wave in isentropic shock-expansion theory, since the principal characteristic $\theta_0 = 0$ never meets the shock wave in the physical plane. Mathematically it represents a limit to the applicability of the present theory, since disturbances cannot be propagated from the shock to the body beyond this point.

Figs. 8 and 10, which show the pressure coefficient on the parabolic airfoils, present the most important

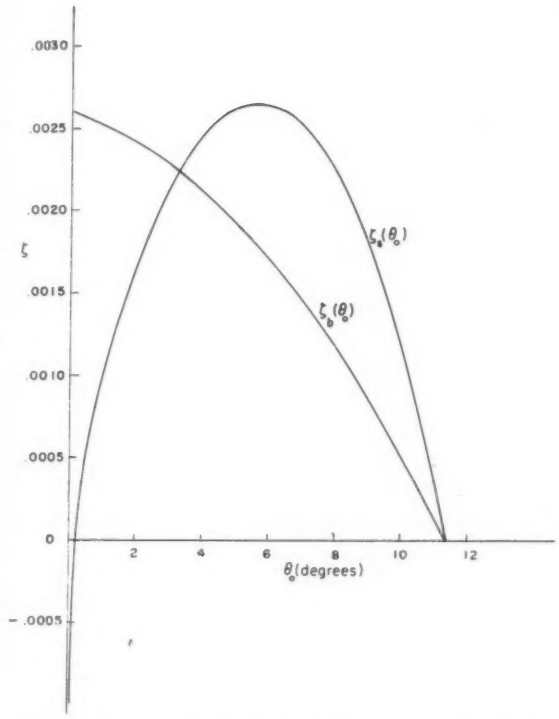

FIG. 7. Shock and body shapes in the characteristic plane for 10%- thick parabolic-arc airfoil; $M_\infty = \infty$, $\gamma = 1.4$.

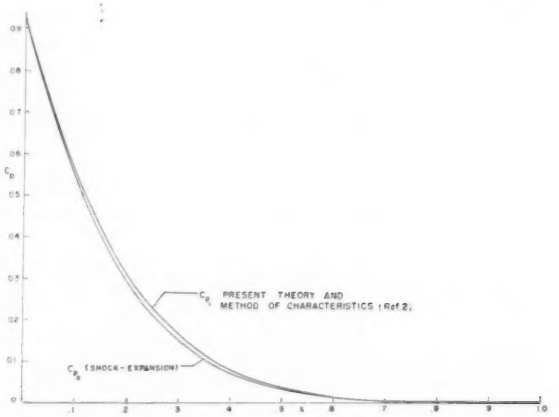

FIG. 8. Zero- and first-order pressure coefficients for 10%-thick parabolic-arc airfoil; $M_\infty = \infty$, $\gamma = 1.4$.

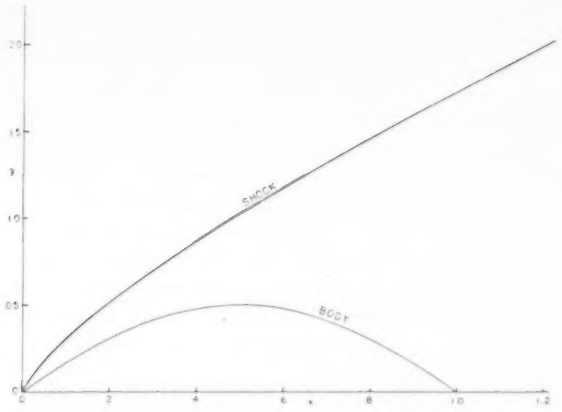

FIG. 9. Shock and body in physical plane for 10%-thick parabolic-arc airfoil; $M_\infty = \infty$, $\gamma = 1.4$.

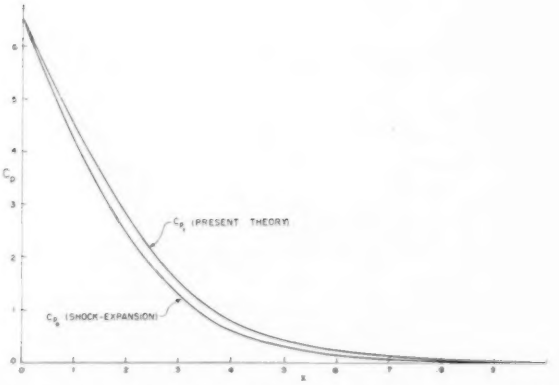

FIG. 10. Zero- and first-order pressure coefficients for 30%-thick parabolic-arc airfoil; $M_\infty = \infty$, $\gamma = 1.4$.

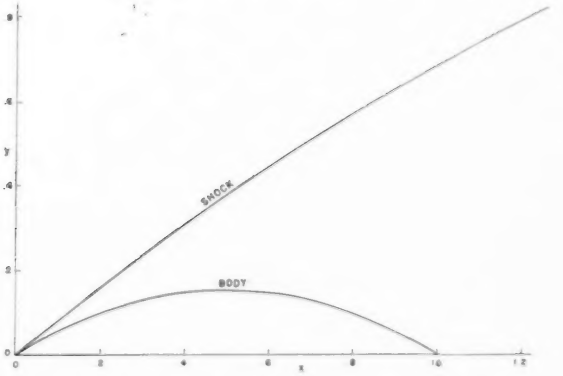

FIG. 11. Shock and body in physical plane for 30%-thick parabolic-arc airfoil; $M_\infty = \infty$, $\gamma = 1.4$.

results of the calculations. In particular, Fig. 8 compared with the method of characteristics (reference 2) shows us that the pressure correction at the body given by the present scheme for all practical purposes accounts for any difference between the shock-expansion method and the "exact" method of characteristics. Unfortunately, rotational characteristics results with which to compare our calculations were not available for the 30%-thick airfoil. From Fig. 10, however, we see that the correction to the pressure coefficient afforded by the present scheme is of the order that might be expected from the results for the more slender airfoil.

Appendix: Form of Integrating Factor Γ for Small Flow-Deflection Angles

For small flow deflections (see, e.g., reference 19) we have

$$\tan \varphi_0 \sim \frac{1}{\sqrt{M_\infty^2 - 1}} + A\theta_0 + C\theta_0^2$$

where

$$A = \frac{\gamma + 1}{4}\left(\frac{M_\infty^2}{M_\infty^2 - 1}\right)^2$$

$$C = \frac{(\gamma + 1)M_\infty^4[(\gamma + 1)M_\infty^4 + 4(\gamma - 1)M_\infty^2 + 8]}{32(M_\infty^2 - 1)^{7/2}}$$

and

$$\tan \mu_0 \sim \frac{1}{\sqrt{M_\infty^2 - 1}} + f\theta_0 + g\theta_0^2$$

where

$$f = \frac{M_\infty^2[(\gamma - 1)M_\infty^2 + 2]}{2(M_\infty^2 - 1)^2}$$

$$g = \frac{M_\infty^2[\gamma(\gamma - 1)M_\infty^4 + (3\gamma - 1)M_\infty^2 + 2]}{2(M_\infty^2 - 1)^{7/2}}$$

Substituting these expressions into

$$N_0(\theta_0) = (d\theta_0/d\varphi_0)_s K(\varphi_0)$$

with $K(\varphi_0)$ defined by Eq. (3.21), we find

$$N_0(\theta_0) = \frac{\tan(\theta_0 + \mu_0) - \tan \varphi_0}{\tan(\theta_0 - \mu_0) - \tan \varphi_0} \sim p\theta_0 + q\theta_0^2$$

where

$$p = -\frac{(\gamma + 1)M_\infty^4}{8(M_\infty^2 - 1)^{3/2}}$$

$$q = \frac{(\gamma + 1)M_\infty^4[(\gamma - 1)M_\infty^4 - (3\gamma - 1)M_\infty^2 - 2]}{16(M_\infty^2 - 1)^3}$$

In the same way we evaluate

$$\frac{1}{N_0(\theta_0)} \frac{(d/d\xi)[\tan(\theta_0 + \mu_0)]}{\tan(\theta_0 + \mu_0) - \tan(\theta_0 - \mu_0)} \sim -\frac{2}{\theta_0} - L(0)$$

where

$$L(0) = [(\gamma - 1)M_\infty^2 + 2]/(M_\infty^2 - 1)^{3/2}$$

The remarks in the text leading to Eq. (5.8) follow immediately.

References

[1] Epstein, P. S., *On the Air Resistance of Projectiles*, Proc. Natl. Acad. Sci., Vol. 17, p. 532, 1931.

[2] Eggers, A. J., Jr., and Syvertson, C. A., *Inviscid Flow about Airfoils at High Supersonic Speeds*, NACA TN 2646, 1952. Superseded by NACA TR 1123, 1953.

[3] Eggers, A. J., Jr., *On the Calculation of Flow about Objects Traveling at High Supersonic Speeds*, NACA TN 2811, 1952.

[4] Rand, R. C., *Prandtl-Meyer Flow behind a Curved Shock Wave*, J. Math. and Phys., Vol. 29, No. 2, p. 124, 1950.

[5] Munk, M. M., and Prim, R. C., *Surface-Pressure Gradient and Shock-Front Curvature at the Edge of a Plane Ogive With Attached Shock Front*, Journal of the Aeronautical Sciences, Vol. 15, No. 11, p. 691, November, 1948.

[6] Crocco, L., *Singolarita della Corrente Gassosa Iperacustica nell' Intorno di una Prora a Diedro*, L'Aerotecnica, Vol. 17, No. 6, p. 519, 1937.

[7] Kraus, S., *An Analysis of Supersonic Flow in the Region of the Leading Edge of Curved Airfoils, Including Charts for Determining Surface-Pressure Gradient and Shock-Wave Curvature*, NACA TN 2729, 1952. Superseded by NACA TR 1123, 1953.

[8] Lighthill, M. J., *The Flow behind a Stationary Shock*, Phil. Mag., Vol. 40, p. 214, 1949.

[9] Chu, B. T., *On Weak Interaction of Strong Shock and Mach Waves Generated Downstream of the Shock*, Journal of the Aeronautical Sciences, Vol. 19, No. 7, p. 433, July, 1952.

[10] Eggers, A. J., Jr., Savin, R. C., and Syvertson, C. A., *The Generalized Shock-Expansion Method and Its Application to Bodies Traveling at High Supersonic Air Speeds*, Journal of the Aeronautical Sciences, Vol. 22, No .4, pp. 231–238, 248, April, 1955.

[11] Marble, F., *The Reflection of a Weak Shock from a Supersonic Shear Layer*, Problems on Shock Reflection, Section III, GALCIT Transonic Research Group, Contract No. W33-038 ac-1717 (11592), U. S. Army Air Force, July, 1948.

[12] Mahony, J. J., *A Critique of Shock-Expansion Theory*, Journal of the Aeronautical Sciences, Vol. 22, No. 10, pp. 673–680, 720, October, 1955.

[13] Tsien, H. S., *Similarity Laws of Hypersonic Flows*, J. Math. and Phys., Vol. 25, No. 3, p. 247, 1946.

[14] Hayes, W. D., *Hypersonic Similitude*, Quart. Appl. Math., Vol. 5, p. 105, 1947.

[15] Meyer, R. E., *On Supersonic Flow Behind a Curved Shock*, Quart. Appl. Math., Vol. 14, p. 433, 1957.

[16] Isenberg, J. S., and Lin, C. C., *The Method of Characteristics in Compressible Flow—Part I (Steady Supersonic Flow)*, Tech. Rep. No. F-TR-1173A-ND, Air Materiel Command, December, 1947.

[17] Probstein, R. F., *Inversion of the Prandtl-Meyer Relation for Specific Heat Ratios of 5/3 and 5/4*, Journal of the Aeronautical Sciences, Vol. 24, No. 4, pp. 316–317, April, 1957.

[18] Hayes, W. D., and Probstein, R. F., *Hypersonic Flow Theory*, Academic Press, New York, 1959.

[19] Lighthill, M. J., *Higher Approximations* in *General Theory of High-Speed Aerodynamics*, ed. W. R. Sears, Princeton University Press, Princeton, 1954.

[20] Friedrichs, K. O., *Formation and Decay of Shock Waves*, Comm. Pure and Appl. Math., Vol. 1, p. 211, 1948.

[21] Mahony, J. J., and Skeat, P. R., *The Flow Around a Supersonic Airfoil*, Aero. Note 147, Aero. Research Labs., Dept. of Supply, Australia, October, 1955.

✦ ✦ ✦

The Dynamics of Rolling Aircraft†

F. W. NIEDENFUHR*
Ohio State University

Summary

Some modern aircraft have mass distribution characteristics which lead to peculiar behavior under certain extreme maneuver conditions. In particular, the so-called "roll inertia coupling effect" has been observed. This report presents an elementary analysis of the dynamic couplings between rigid- and flexible-body aircraft motions introduced by a rapid steady roll. It is shown that rotating elastic systems exhibit several types of instability and "subharmonic response," and these motions are explained. Some new stability criteria for high-speed aircraft are introduced.

(1) A Rigid Airplane With Pitch and Yaw Freedom

THE DYNAMICS of a rigid airplane which is permitted only to pitch, yaw, and roll has been investigated by Phillips.[1] By neglecting the aerodynamic damping forces and considering a typical long, slim high-speed aircraft which is performing steady rapid roll, Phillips obtains a system which is equivalent to the mechanical system of Fig. 1. This system consists of a slim rod pivoted at one point and supported by a pair of springs. The rod is considered to be rolling about its undeflected axis (the x axis), and the springs rotate with it. In the absence of roll, oscillation of the rod against the action of spring K_1 corresponds to the short-period yaw mode of an airplane, while oscillation against spring K_2 corresponds to the short-period pitch mode of an airplane. This equivalent system is shown in its deflected form in Fig. 2, where the springs are omitted for clarity.

Assuming the system to be rotating about the x axis at a constant roll rate $\dot{\varphi}$, the velocity components of an element in the rotating axis system are $-x\dot{\theta}$ and $x\dot{\psi}$ as shown, but relative to space-fixed axes the velocity components are $(x\dot{\psi} + x\theta\dot{\varphi})$ and $(-x\dot{\theta} + x\psi\dot{\varphi})$. With dm as the mass of the element and these absolute velocity components, the kinetic energy can be written as follows:

$$\begin{aligned} T &= (1/2)\int[(x\dot{\psi} + x\theta\dot{\varphi})^2 + (x\dot{\theta} - x\psi\dot{\varphi})^2]dm \\ &= (1/2)[(\dot{\psi} + \theta\dot{\varphi})^2 + (\dot{\theta} - \psi\dot{\varphi})^2]\int x^2 dm \\ &= (B/2)[(\dot{\psi}^2 + \dot{\theta}^2) + 2\dot{\varphi}(\dot{\psi}\theta - \dot{\theta}\psi) + \dot{\varphi}^2(\psi^2 + \theta^2)] \end{aligned} \tag{1}$$

where B is the moment of inertia of the rod (fuselage) about either the y or z axis.

The potential energy of the system can be written:

$$V = -(1/2)[M_\theta\theta^2 + N_\psi\psi^2] \tag{2}$$

where M_θ and N_ψ are the usual pitch and yaw moments caused by unit θ and ψ motions, respectively. For static stability these quantities must be negative.

The Lagrange equations of motion,

$$(d/dt)(\partial L/\partial\dot{q}_i) - (\partial L/\partial q_i) = 0 \tag{3}$$

where $L = T - V$, can be applied to this system with the following result:

$$\left.\begin{aligned} \ddot{\psi} + (\omega_2^2 - \dot{\varphi}^2)\psi + 2\dot{\varphi}\dot{\theta} = 0 \\ -2\dot{\varphi}\dot{\psi} + \ddot{\theta} + (\omega_1^2 - \dot{\varphi}^2)\theta = 0 \end{aligned}\right\} \tag{4}$$

where $\omega_1^2 = -M_\theta/B$ and $\omega_2^2 = -N_\psi/B$ are the squares of the circular pitch and yaw frequencies of the nonrolling system.

(2) A Flexible Airplane With No Rigid-Body Freedom

Before proceeding with the solution of Eq. (4), let us consider the aeroelastic equivalent of the system of Fig. 1. Idealizing the fuselage to a uniform beam which is allowed to bend and rotate (at constant $\dot{\varphi}$) about its nominal axis we obtain the system of Fig. 3, where $Y(x, t)$ and $Z(x, t)$ represent elastic deformation of the fuselage. In the figure, the line OA represents the deformed centerline of the fuselage. Relative to space-fixed axes the velocity components of an elemental length of the deflected beam are $(\dot{Y} - Z\dot{\varphi})$ and $(\dot{Z} + Y\dot{\varphi})$. The kinetic energy of the rotating beam is therefore

$$T = 1/2\int[(\dot{Y} - Z\dot{\varphi})^2 + (\dot{Z} + Y\dot{\varphi})^2]dm \tag{5}$$

This integral is most easily evaluated if the so-called normal modes of the beam are introduced. Write, therefore,

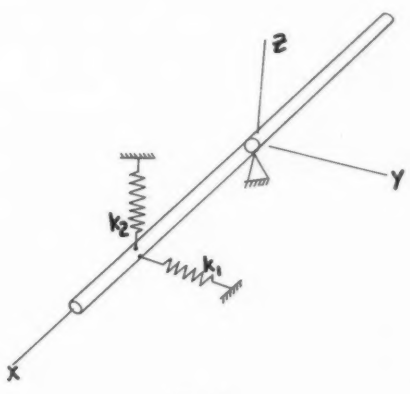

FIG. 1.

Received October 9, 1959. Revised and received October 3, 1960.

† This paper is based on North American Aviation, Inc., Columbus Division Report No. NA59H-148, April, 1959, of the same title.

* Associate Professor of Engineering Mechanics; also, Senior Technical Specialist, North American Aviation, Inc.

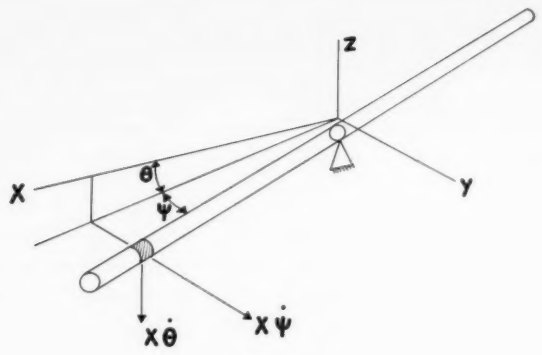

FIG. 2.

$$\begin{aligned} Y(x, t) &= Y_i(t)\eta_i(x) \\ Z(x, t) &= Z_i(t)\zeta_i(x) \end{aligned} \tag{6}$$

where Y_i and Z_i are the normal coordinates, η_i, ζ_i are the *in vacuo* normal mode shapes, and the summation convention has been employed, i.e.,

$$Y_i\eta_i = Y_1\eta_1 + Y_2\eta_2 + \ldots = \sum_i Y_i\eta_i \tag{7}$$

[The summation convention in (6) consists of agreeing not to write the big sigma used in the identity (7).]

Introducing (6) into (5), and expanding, we find that the kinetic energy can be written as follows:

$$\begin{aligned} 2T = \dot{Y}_i^2 \int \eta_i^2 dm + \dot{Z}_i^2 \int \zeta_i^2 dm + \\ 2\dot{\varphi}(Y_i\dot{Z}_j - \dot{Y}_i Z_j) \int \eta_i\zeta_j\, dm + \\ \dot{\varphi}^2 Y_i^2 \int \eta_i^2\, dm + \dot{\varphi}^2 Z_i^2 \int \zeta_i^2 dm \end{aligned} \tag{8}$$

In (8) use has been made of the orthogonality properties of the normal mode shapes, viz.:

$$\int \eta_i\eta_j\, dm = \int \zeta_i\zeta_j\, dm = 0 \quad \text{if} \quad i \neq j \tag{9}$$

The potential energy of this system can be written in terms of the normal modes in the form:

$$2V = Y_i^2 \int EI_z(\eta_i'')^2 dx + Z_i^2 \int EI_y(\zeta_i'')^2 dx \tag{10}$$

For a first look at the behavior of the rotating beam we may satisfy ourselves with only one term of the expansion (7)—i.e., with only one normal mode to represent the deflection of the beam. In this case, the equations of motion for the system become:

$$\left.\begin{aligned} \ddot{Y}_1 + (\omega_1^2 - \dot{\varphi}^2)Y_1 + 2\dot{\varphi}\dot{Z}_1 k_{12} = 0 \\ -2\dot{\varphi}\dot{Y}_1 k_{21} + \ddot{Z}_1 + (\omega_2^2 - \dot{\varphi}^2)Z_1 = 0 \end{aligned}\right\} \tag{11}$$

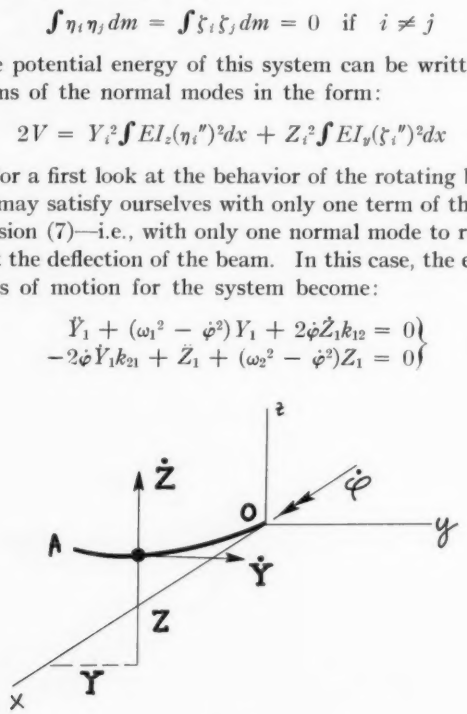

FIG. 3.

where
$$\begin{aligned} \omega_1^2 &= \int EI_z(\eta_1'')^2 dx / \int \eta_1^2 dm \\ \omega_2^2 &= \int EI_y(\zeta_1'')^2 dx / \int \zeta_1^2 dm \\ k_{12} &= \int \eta_1\zeta_1 dm / \int \eta_1^2 dm \\ k_{21} &= \int \eta_1\zeta_1 dm / \int \zeta_1^2 dm \end{aligned}$$

Observe that Eqs. (11) for the rotating beam are of exactly the form of Eqs. (4) for the rotating spring rod, provided $k_{12} = k_{21} = 1$, i.e., $\eta_1(x) = \zeta_1(x)$. This symmetry property of the mode shapes will be assumed for the present, and its removal will be discussed later.

(3) A Simple Mechanical Analogy

A simpler mechanical system, analogous to the two already studied, is a point mass elastically sprung to a rigid frame which rotates at constant velocity. This system is shown in Fig. 4. It is introduced here because it is a bit easier to think about than its distributed-mass analogies discussed above.

In Fig. 4, X, Y is a spaced-fixed coordinate system, while x, y are axes which rotate with the rigid frame. K_1 and K_2 are the constants of the mounting springs which connect the mass, m, to the rotating frame. In the rotating coordinate system (xy space, which corresponds to airplane wind axes) the *absolute* velocity components of the mass are $(\dot{x} - y\dot{\varphi})$ and $(\dot{y} + x\dot{\varphi})$, so that the kinetic energy is

$$\begin{aligned} T &= (m/2)[(\dot{x} - y\dot{\varphi})^2 + (\dot{y} + x\dot{\varphi})^2] \\ &= (m/2)[\dot{x}^2 + \dot{y}^2 + 2\dot{\varphi}(\dot{y}x - \dot{x}y) + \dot{\varphi}^2(x^2 + y^2)] \end{aligned} \tag{12}$$

and the potential energy is

$$V = (1/2)[k_1x^2 + k_2y^2] \tag{13}$$

Application of the Lagrange equations yields

$$\left.\begin{aligned} \ddot{y} + (\omega_2^2 - \dot{\varphi}^2)y + 2\dot{\varphi}\dot{x} &= 0 \\ -2\dot{\varphi}\dot{y} + \ddot{x} + (\omega_1^2 - \dot{\varphi}^2)x &= 0 \end{aligned}\right\} \tag{14}$$

where $\omega_i^2 = k_i/m \qquad i = 1, 2$

That Eqs. (14) are equivalent to Eqs. (4) or Eqs. (11) is apparent, and this fact establishes that the rotating-frame sprung-mass system is a rigorous analog of the two systems previously discussed.* For this reason we may confine our further attentions to Fig. 4 and Eqs. (14).

Let us begin the discussion of this system with the completely symmetrical case obtained by setting $k_1 = k_2 = k$ so that $\omega_1^2 = \omega_2^2 = \omega^2$ in Eqs. (14). Let us call this condition "dynamic isotropy."

Now in this case it is very much simpler to rewrite the equations of motion in the space-fixed X, Y coordinate system. We have immediately that

$$T = (m/2)[\dot{X}^2 + \dot{Y}^2] \text{ and } V = (k/2)[x^2 + y^2] \tag{15}$$

but $$x^2 + y^2 = X^2 + Y^2$$

* Another mechanical system governed by the same set of differential equations is the column simultaneously bent and twisted. See S. Timoshenko, "Theory of Elastic Stability," pp. 167–169, McGraw-Hill Book Company, Inc., New York, 1936.

so that $$V = (k/2)[X^2 + Y^2] \tag{16}$$

Since the kinetic- and potential-energy expressions do not contain cross-product terms, the equations of motion are uncoupled in XY space. Therefore, the equations of motion are

$$\left.\begin{aligned} \ddot{X} + \omega^2 X &= 0 \\ \ddot{Y} + \omega^2 Y &= 0 \end{aligned}\right\} \tag{17}$$

Note that the rate of rotation, $\dot{\varphi}$, does not appear in Eqs. (17), so that these equations are the same whether the frame is rotating or not. This means that the motion of the mass (as viewed in XY space) is unaffected by the "roll" of the frame. The extrapolation of this result to aircraft dynamics is obvious, viz.: *An observer on the ground cannot tell whether or not a dynamically isotropic airplane is rolling.*

As an example, consider a fuselage which is a long slender rod of circular cross section. Let this rod vibrate in the horizontal plane and then begin to roll at a constant rate. As the roll proceeds, the vibration remains in the horizontal plane, and an observer on the ground will be unaware that roll is taking place, since all he sees is continued vibration in the horizontal plane. To the pilot, however, the situation will appear quite differently, and to see this we must study the solution in xy space.

If we set $\omega_1^2 = \omega_2^2$, and $y = Ae^{\lambda t}$, $x = Be^{\lambda t}$ in Eq. (14), we obtain (as a condition for the existence of a nontrivial solution) the secular equation

$$\Delta = \begin{vmatrix} [\lambda^2 + (\omega^2 - \dot{\varphi}^2)] & 2\dot{\varphi}\lambda \\ -2\dot{\varphi}\lambda & [\lambda^2 + (\omega^2 - \dot{\varphi}^2)] \end{vmatrix} = 0 \tag{18}$$

This is a quadratic equation in λ^2, and has the solutions

$$\lambda_{1,2}^2 = -(\omega \pm \dot{\varphi})^2 \tag{19}$$

Denote the two natural frequencies of the system by p_1 and p_2, where

$$p_1 = \omega - \dot{\varphi}, \qquad p_2 = \omega + \dot{\varphi} \tag{20}$$

The solution for general motion of the mass within the frame is thus given by (21):

$$\left.\begin{aligned} x &= A\cos p_1 t + B\sin p_1 t + C\cos p_2 t + D\sin p_2 t \\ y &= B\cos p_1 t - A\sin p_1 t - D\cos p_2 t + C\sin p_2 t \end{aligned}\right\} \tag{21}$$

The mass may be started vibrating in a horizontal plane (while the frame rotates) by using the initial conditions:

$$\left.\begin{aligned} x(0) &= Q, \quad \dot{x}(0) = 0 \\ y(0) &= 0, \quad \dot{y}(0) = -\dot{\varphi}Q \end{aligned}\right\} \tag{22}$$

When these conditions are impressed, the general solution (21) becomes

$$\begin{aligned} x &= (Q/2)[\cos p_1 t + \cos p_2 t] \\ y &= (Q/2)[\sin p_1 t - \sin p_2 t] \end{aligned} \tag{23}$$

Let θ be the instantaneous angular orientation of the displaced mass point relative to the rigid frame, i.e.,

$$\tan\theta = x/y \tag{24}$$

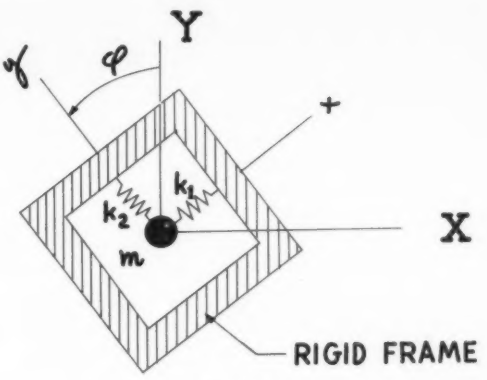

FIG. 4.

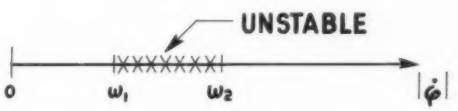

FIG. 5.

Inserting (23) in (24) and differentiating, one readily finds

$$\dot{\theta} = -\dot{\varphi} \tag{25}$$

Eq. (25) states that an observer in xy space sees a precession of the plane of vibration of the mass, and that this precession is equal and opposite to the rotation of the x, y coordinate system—i.e., this observer sees the plane of vibration of the mass remaining fixed relative to the x, y coordinates. It should be emphasized that this conclusion is valid only for the dynamically isotropic system.

The more usual case in practice will be $k_1 \neq k_2$. We have already written the equations of motion for this system, Eqs. (14). Before making an analysis of them we shall look briefly at the equations in terms of the space-fixed X, Y axis system. The transformation relations between the two coordinate systems of Fig. 4 are

$$\left.\begin{aligned} x &= X\cos\dot{\varphi}t + Y\sin\dot{\varphi}t \\ y &= -X\sin\dot{\varphi}t + Y\cos\dot{\varphi}t \end{aligned}\right\} \tag{26}$$

The potential energy of the system can then be written as

$$V = (1/2)[k_1(X\cos\dot{\varphi}t + Y\sin\dot{\varphi}t)^2 + k_2(-X\sin\dot{\varphi}t + Y\cos\dot{\varphi}t)^2] \tag{27}$$

Eq. (27), together with the kinetic energy of Eq. (15), can be put into the Lagrange equations to yield the equations of motion of the system relative to the space-fixed axes. It can be seen that these equations will have periodic coefficients with period $2\pi/\dot{\varphi}$. The study of such equations is rather tedious and in fact the general solution is not known.

Fortunately, the description of the system is phrased in terms of equations with constant coefficients [Eq. (14)] in the rotating x, y coordinates. Accordingly, we turn our attention to the solution of Eq. (14). Assuming, as before, solutions of the form $y = Ae^{\lambda t}$, $x = Be^{\lambda t}$,

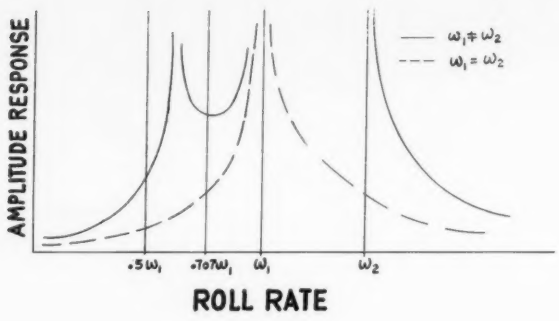

FIG. 6.

we find the secular equation:

$$\Delta = \begin{vmatrix} [\lambda^2 + (\omega_2^2 - \dot{\varphi}^2)] & 2\lambda\dot{\varphi} \\ -2\lambda\dot{\varphi} & [\lambda^2 + (\omega_1^2 - \dot{\varphi}^2)] \end{vmatrix} = 0$$

or,

$$\lambda^4 + 2\lambda^2\left[\left(\frac{\omega_1^2 + \omega_2^2}{2}\right) + \dot{\varphi}^2\right] + (\omega_1^2 - \dot{\varphi}^2)(\omega_2^2 - \dot{\varphi}^2) = 0 \quad (28)$$

The roots of this quadratic are

$$\lambda_{1,2}^2 = -\left[\left(\frac{\omega_1^2 + \omega_2^2}{2}\right) + \dot{\varphi}^2\right] \pm \sqrt{\left[\left(\frac{\omega_1^2 + \omega_2^2}{2}\right) + \dot{\varphi}^2\right]^2 - (\omega_1^2 - \dot{\varphi}^2)(\omega_2^2 - \dot{\varphi}^2)} \quad (29)$$

In order that the motion be stable [i.e., $x(t)$ and $y(t)$ bounded for all t] it is necessary that $\lambda_{1,2}^2$ be negative quantities. This requirement is met if

$$\left.\begin{aligned} &\left[\left(\frac{\omega_1^2 + \omega_2^2}{2}\right) + \dot{\varphi}^2\right]^2 > (\omega_1^2 - \dot{\varphi}^2)(\omega_2^2 - \dot{\varphi}^2) \\ &\text{and} \qquad (\omega_1^2 - \dot{\varphi}^2)(\omega_2^2 - \dot{\varphi}^2) > 0 \end{aligned}\right\} \quad (30)$$

The first of these two inequalities is always satisfied, for it reduces to the positive definite form

$$\left(\frac{\omega_1^2}{\dot{\varphi}^2} - \frac{\omega_2^2}{\dot{\varphi}^2}\right)^2 + 8\left(\frac{\omega_1^2}{\dot{\varphi}^2} + \frac{\omega_2^2}{\dot{\varphi}^2}\right) > 0 \quad (31)$$

The second inequality, however, places some practical restrictions on the operation of the system. It states that the system is unstable if the roll rate $\dot{\varphi}$ lies numerically between ω_1 and ω_2. This is shown in Fig. 5. The endpoints ($\dot{\varphi} = \omega_1$ and $\dot{\varphi} = \omega_2$) are included in the unstable region of Fig. 5, so that even in the case of a dynamically isotropic system ($\omega_1 = \omega_2$) a critical speed exists at $\dot{\varphi} = \omega_1$. This is the familiar critical speed of a rotating circular shaft, for instance. A shaft may be run continuously above or below the critical speed, but at the critical speed it will perform oscillations whose amplitude increases linearly with time. What is less well known is that for a system which is dynamically anisotropic there exists a finite range of continuously distributed critical speeds. Rather unusual behavior for a system with a finite number of degrees of freedom!

Even more unusual behavior can be exhibited, however, if we consider the complete solution of Eq. (14). The conclusions drawn thus far have been based on the so-called complementary solution. A new phenomenon appears if we consider forced motion. For instance, if the system of Fig. 4 is conceived to be in the vertical plane, the potential energy of Eq. (13) must be augmented by a term

$$V' = mgY \quad (32)$$

which accounts for the gravitational forces on the mass. From Eq. (26), however, we find that

$$Y = x \sin \varphi + y \cos \varphi \quad (33)$$

The augmented potential energy for the system then appears in the following form:

$$V = (1/2)[k_1x^2 + k_2y^2] + mg[x \sin \varphi + y \cos \varphi] \quad (34)$$

In combination with the kinetic energy (12) and the Lagrange equations, this yields the nonhomogeneous equations of motion of the system.

$$\left.\begin{aligned} \ddot{y} + (\omega_2^2 - \dot{\varphi}^2)y + 2\dot{\varphi}\dot{x} &= -g \cos \varphi \\ -2\dot{\varphi}\dot{y} + \ddot{x} + (\omega_1^2 - \dot{\varphi}^2)x &= -g \sin \varphi \end{aligned}\right\} \quad (35)$$

Since the roll angle φ is equal to $\dot{\varphi}t$, this is forced motion at circular frequency $\dot{\varphi}$. The complementary solution of Eq. (35) is the same as the solution of Eq. (14) and need not be further discussed. The particular solution of (35) can be seen to be of the form

$$x = A \sin \dot{\varphi}t, \qquad y = B \cos \dot{\varphi}t \quad (36)$$

Substituting (36) into (35) we obtain solutions of the form

$$A = N_A/\Delta, \qquad B = N_B/\Delta \quad (37)$$

where N_A, N_B and Δ are determinants. We see that the motion is unbounded if Δ approaches zero unless N_A and N_B approach zero in the same manner. Upon performing the indicated operations we find

$$\left.\begin{aligned} A = \frac{N_A}{\Delta} &= \frac{g(4\dot{\varphi}^2 - \omega_2^2)}{\omega_2^2\omega_1^2 - 2\dot{\varphi}^2(\omega_1^2 + \omega_2^2)} \\ B = \frac{N_B}{\Delta} &= \frac{g(4\dot{\varphi}^2 - \omega_1^2)}{\omega_2^2\omega_1^2 - 2\dot{\varphi}^2(\omega_1^2 + \omega_2^2)} \end{aligned}\right\} \quad (38)$$

In the case of dynamic isotropy, $\omega_1 = \omega_2$, and Eqs. (38) simplify considerably. Both A and B become equal to $-g/\omega^2$. Thus while Δ may vanish when $\omega_1 = \omega_2$, N_A and N_B also vanish in the same manner and the coefficients A and B remain finite. This case will give us no cause to worry. For $\omega_1 \neq \omega_2$, however, the situation is vastly different, for Δ may vanish quite independent of N_A and N_B. The condition for vanishing Δ is

$$2\dot{\varphi}^2(\omega_1^2 + \omega_2^2) = \omega_1^2\omega_2^2$$

which yields the critical value of $\dot{\varphi}$:

$$1/2\dot{\varphi}_{cr}^2 = (1/\omega_1^2) + (1/\omega_2^2) \quad (39)$$

$\dot{\varphi}_{cr}$ has the following limits (assuming here $\omega_2 > \omega_1$):

(i) As $\omega_2 \to \infty$, $\dot{\varphi}_{cr} \to 0.707\omega_1$

(ii) As $\omega_2 \to \omega_1$, $\dot{\varphi}_{cr} \to 0.5\varphi_1$

Therefore,

$$0.5\omega_L < \dot{\varphi}_{cr} < 0.707\omega_L \tag{40}$$

where ω_L is the least of ω_1, ω_2.

The infinite response to the critical roll rate of Eq. (39) can be exhibited only by a dynamically anisotropic system, and only then when there are forcing terms included in the equations of motion. For instance, a flexible shaft whose principal bending moments of inertia are unequal will exhibit this response when run in a horizontal position, but not if run in a vertical position, for in this latter case the gravity terms are missing from the equation of motion—i.e., there is no static bending deflection due to dead weight of the shaft if it is mounted vertically. Later we shall see the significance of this type of response in the rigid-body airplane performance problem.

The major conclusions here can be briefly summarized in the form of the curve of Fig. 6. Here we have plotted the amplitude responses of the systems of Fig. 1, 2 or 4 vs. the steady roll rate $\dot{\varphi}$. The solid curves are for the case $\omega_1 \neq \omega_2$, while the dashed curves are for the isotropic system, $\omega_1 = \omega_2$.

(4) Transient Roll: Another Equivalent System

The spring and mass system of Fig. 4 immediately brings to mind another system which has the same equations of motion—namely, a particle which slides without friction and under the influence of gravity on the concave side of the surface

$$Z = k_1x^2 + k_2y^2$$

Here we presume that gravity acts in the negative Z direction. The motion analogous to aircraft roll is a rotation of the surface about the z axis. A physically realizable approximation of this idealized problem is a small ball—a marble, say—rolling about in a cup of elliptical cross section. This system is illustrated in Fig. 7.

The ball in a cup is a profitable analogy to introduce because it makes it easier to visualize the x-y motion for variable roll rate $\dot{\varphi}$. As before, let X, Y be a space-fixed axis system and let the x and y axes move with the cup. The kinetic and potential energies of the ball are given by

$$T = (m/2)[\dot{X}^2 + \dot{Y}^2] \tag{41}$$

and

$$V = mgZ = mg[k_1x^2 + k_2y^2] \tag{42}$$

These energy expressions are quite obviously the same as those encountered in the problems previously considered.

Also, the coordinate transformation between the space-fixed and body-fixed axes used here is given by Eq. (26). Thus, the analogy is established.

For the ball in a cup, it is relatively easy to visualize certain simple types of motion. In Eq. (42), let us set $k_2 > k_1$ for definiteness. We may thus talk about the x axis of the cup as the "long axis," or the "weak axis," while the y axis is the "short axis" or "strong axis." Imagine now that with the cup fixed in space the ball is started oscillating along the short axis of the cup. It has some y amplitude, no x amplitude, and rises to a height Z which is a measure of its total energy. If left undisturbed, this motion would continue forever. Now, let the cup begin to turn slowly and then stop. In the transient period, the ball will execute both high-frequency, short-axis (y) oscillations and low-frequency, long-axis (x) oscillations. Any friction in the system will tend to damp the motion, with the highest damping (greatest damping forces) applied to the high-frequency components of motion. When the cup has come to rest again, the motion of the ball will be primarily along the long axis with a much reduced component in the y or short-axis direction, provided the rotation of the cup, $\varphi(t)$, has been chosen properly. An x-y plot of such motion is shown in Fig. 8. This represents the path of the ball as viewed by an observer who rides with the cup and looks down on it from above. The arrowheads on the path indicate the sense of the motion.

A steady-state version of this motion is shown in Fig. 9. The ball is here represented as having been oscillat-

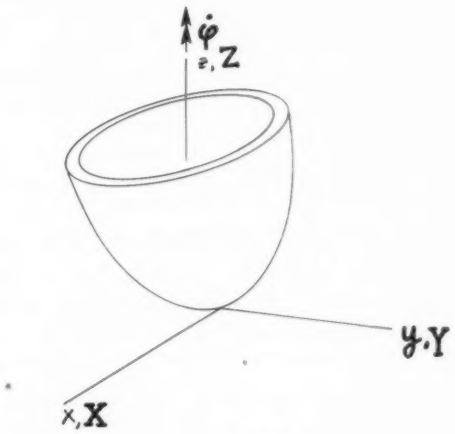

FIG. 7.

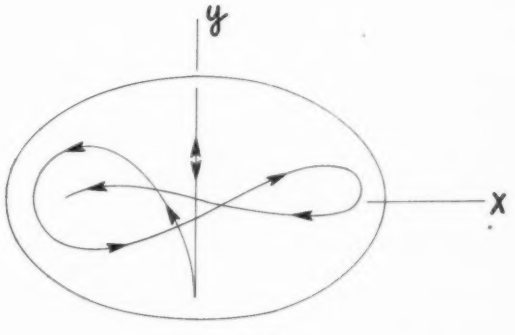

FIG. 8.

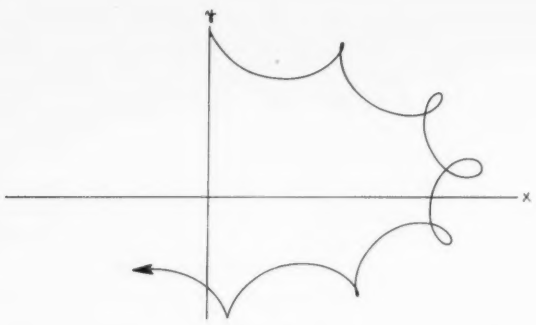

FIG. 9.

ing along the short axis of the cup when a constant roll rate was impressed. Fig. 9 is a replica of an analog computer run in which the relative values of the parameters were $k_2/k_1 = 3/2$ and $m\dot{\varphi}/k_1 = 9/10$.

At least one conclusion regarding aircraft motion can be drawn from these considerations: Consider an airplane fuselage which is stiffer in vertical bending than in lateral bending. Let this fuselage be excited in vertical bending in straight and level flight, and then roll the airplane. The plane of bending will then change from pure vertical to a combination of vertical and lateral bending with a maximum amplitude in the lateral mode. This new motion may have important consequences as regards the stresses in structural components or may affect the function of equipment mounted in the fuselage.

Other simple roll motions of an aircraft may be treated with the aid of the ball-in-cup analogy which should be useful whenever only two degrees of freedom are of primary importance.

(5) The Influence of Mode Shape on the Stability Criteria

In Section 2, the simplified problem of a rolling fuselage was set up in terms of the normal modes of lateral bending (η) and "vertical" bending (ζ). We have thus far assumed in the equations of motion for this problem [Eq. (11)] that the quantities k_{12} and k_{21} are equal to unity,

$$k_{12} = \int \eta_1 \zeta_1 dm / \int \eta_1^2 dm$$

where

$$k_{21} = \int \eta_1 \zeta_1 dm / \int \zeta_1^2 dm$$

Here we examine the possible effects of relaxing this rather stringent assumption.

Let us assume that the mode shapes have been normalized so that

$$\int \eta_1^2 dm = \int \zeta_1^2 dm = 1$$

It then follows that $k_{12} = k_{21}$, and that their common value is less than or equal to one, and we wish to assess the effect on the stability of the system of any variation of this quantity.

Assuming as usual a solution of the form

$$Y_1 = Ae^{\lambda t}, \quad Z_1 = Be^{\lambda t}$$

Eq. (11) yields the secular determinant:

$$\begin{vmatrix} [\lambda^2 + (\omega_1^2 - \dot{\varphi}^2)] & [2\dot{\varphi}\lambda k_{12}] \\ [-2\dot{\varphi}\lambda k_{21}] & [\lambda^2 + (\omega_2^2 - \dot{\varphi}^2)] \end{vmatrix} = 0 \quad (43)$$

The obvious stability criterion is that the real part of λ should not be greater than zero. For the case of $k_{12} = k_{21} = 1$, we found that the criterion reduced to the requirement that $|\dot{\varphi}|$ *not* lie between ω_1 and ω_2. Inspection of Eq. (43) shows that in the other limiting case of $k_{12} = k_{21} = 0$ the stability criterion is that $|\dot{\varphi}|$ be less than both ω_1 and ω_2. That is, if $k_{12} = k_{21} = 0$, the stable region at the right of Fig. 5 does not exist.

Replacing k_{12} and k_{21} by their common value, k, and expanding Eq. (43), we obtain the following equation for λ:

$$\lambda^4 + \lambda^2[\omega_1^2 + \omega_2^2 + \dot{\varphi}^2(4k^2 - 2)] + (\omega_1^2 - \dot{\varphi}^2)(\omega_2^2 - \dot{\varphi}^2) = 0 \quad (44)$$

Thus, in order that λ have a real part not greater than zero, λ^2 must be negative here. This condition is assured if only both coefficients of Eq. (44) are greater than zero. The constant term of (44) being greater than zero implies that $|\dot{\varphi}|$ does not lie between ω_1 and ω_2, which is our original stability criterion. The coefficient of the λ^2 term of (44) will be greater than zero if

$$k^2 \geqslant \frac{1}{2} - \frac{\omega_1^2 + \omega_2^2}{2\dot{\varphi}^2} \quad (45)$$

Eq. (45) is a new stability criterion to be applied if the body-bending mode shapes do not possess the symmetry property $\zeta(x) = \eta(x)$.

If very high roll rates are anticipated, the second term on the right-hand side of (45) may be small. In any event, (45) will always be satisfied if $k^2 \geqslant 1/2$, or $|k| \geqslant 0.707$. Now, it is possible that $|k|$ be less than this value?

The answer is yes, for consider a fuselage whose mass per unit length is constant and which has end-for-end symmetry, as in Fig. 10(a). Then the mode shapes

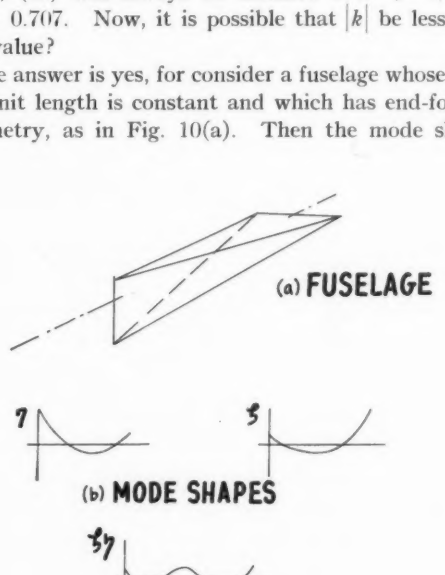

FIG. 10.

will have end-for-end symmetry as in Fig. 10(b) and the product of mode shapes will be as in Fig. 10(c). The parameter k is the net area under the curve of Fig. 10(c), and it is easy to see that this can be made very small by proper choice of the mode shape curves.

An analytical demonstration that systems exist whose first vertical and lateral modes are orthogonal is as follows: Breaking up the fuselage into finite chunks, one can write the equations for lateral and vertical bending

$$\left.\begin{aligned} m_{ij}\ddot{\eta}_j + k_{ij}\eta_j &= 0 \\ m_{ij}\ddot{\xi}_j + \kappa_{ij}\xi_i &= 0 \end{aligned}\right\} \tag{46}$$

where the mass coefficients m_{ij} are the same in both equations, and it is to be determined whether or not $k_{ij} = \kappa_{ij}$. In (46) the summation convention has again been employed. In the notation of Eq. (11) we may write (46) as

$$\begin{aligned} (-m_{ij}\omega_1^2 + k_{ij})\bar{\eta}_j &= 0 \\ (-m_{ij}\omega_2^2 + \kappa_{ij})\bar{\xi}_j &= 0 \end{aligned} \tag{47}$$

where $\bar{\eta}_j$ and $\bar{\xi}_j$ are modal columns and we presume $\omega_1^2 \neq \omega_2^2$. Multiply the first of (47) by $\bar{\xi}_i$ and the second by $-\bar{\eta}_i$ and obtain:

$$\begin{aligned} (-m_{ij}\omega_1^2 + k_{ij})\bar{\eta}_j\bar{\xi}_i &= 0 \\ (m_{ij}\omega_2^2 - \kappa_{ij})\bar{\xi}_j\bar{\eta}_i &= 0 \end{aligned} \tag{48}$$

Since $m_{ij} = m_{ji}$, $k_{ij} = k_{ji}$, and $\kappa_{ij} = \kappa_{ji}$ we may interchange i and j in the second of (48). Doing this, and adding the result to the first of (48), we have

$$[m_{ij}(\omega_2^2 - \omega_1^2) + P_{ij}]\bar{\xi}_i\bar{\eta}_j = 0 \tag{49}$$

where $$P_{ij} = k_{ij} - \kappa_{ij}$$

Now it is easy to see that if

$$P_{ij}\bar{\xi}_i\bar{\eta}_j = 0 \tag{50}$$

then $$m_{ij}\bar{\xi}_i\bar{\eta}_j = 0 \tag{51}$$

since $$\omega_1^2 \neq \omega_2^2$$

If (51) is satisfied, the stability criterion of Eq. (45) may be violated for high enough roll rates, and the satisfaction of (51) requires only the satisfaction of (50). It is well known that (50) does *not* imply that $P_{ij} \equiv 0$, so that in general $k_{ij} \neq \kappa_{ij}$. This establishes the desired result. Until these calculations have been made for several typical airplane configurations we cannot say whether the stability criterion Eq. (45) is of practical importance. To be conservative, then, we should assume $k^2 = 0$ always, and (45) reduces to

$$\dot{\varphi}^2 \leqslant \omega_1^2 + \omega_2^2 \tag{52}$$

For present-day structures the violation of (52) appears unlikely, but we should notice that it *does* modify the conclusions sketched in Fig. 5.

When rigid-body motions are considered, the inclusion of four degrees of freedom may lead to lateral and longitudinal rigid-body mode shapes like those of Fig. 11. These functions may well be orthogonal (in analogy with Fig. 10). In the case of rigid-body aerodynamics, Eq. (52) may be important, for it is well known that ω_1 and ω_2 may become very small at high altitudes. The mode shapes of Fig. 11 correspond to an airplane flying a spiral path in space.

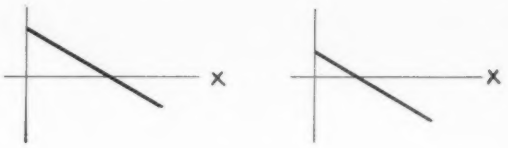

FIG. 11.

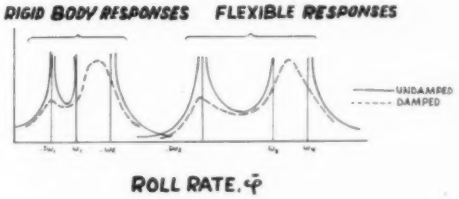

FIG. 12.

(6) Coupling of Pitch, Yaw, and Bending Motions

We have seen that the system may become unstable in two manners, first if $\dot{\varphi}$ lies between ω_1 and ω_2, and second if there is a gravity-induced forcing function and $\dot{\varphi}$ lies between $0.5\omega_L$ and $0.707\omega_L$, where ω_L is the least of ω_1, ω_2. We have thus far separated the bending problem and the rigid-body problem. Superimposing our results, then, we might expect the dynamic response of our system to appear somewhat as in Fig. 12, which assumes that there is no coupling between the rigid and elastic motions. In Fig. 12:

ω_1 = yaw frequency
ω_2 = pitch frequency
ω_3 = vertical body bending frequency
ω_4 = lateral body bending frequency

It is our intent in this section to discover the effect on Fig. 12 of introducing couplings between flexible- and rigid-body airplane modes. As indicated in the figure, the introduction of damping terms into the equations of motion ameliorates but does not eliminate the situation. Since the most probable applications of this theory are in high-speed flight at high altitude where the aerodynamic damping is light, and since our purpose is mainly exploratory, we shall continue to neglect damping. For this reason, the virtual work function that will be presented in this section will not contain a few of the terms that might otherwise be expected.

Following the notation already established, we find that the kinetic energy function for the airplane which is allowed to pitch, yaw, and bend can be written as

$$T = (B/2)[(\dot{\psi}^2 + \dot{\theta}^2) + 2\dot{\varphi}(\dot{\psi}\theta - \dot{\theta}\psi) + \dot{\varphi}^2(\psi^2 + \theta^2)] + (\dot{Y}_1^2 + \dot{\varphi}^2 Y_1^2)\int \eta_1^2\, dm + (\dot{Z}_1^2 + \dot{\varphi}^2 Z_1^2)\int \zeta_1^2\, \mathrm{dm} + 2\dot{\varphi}(Y_1\dot{Z}_1 - \dot{Y}_1 Z_1)\int \eta_1\zeta_1\, dm \tag{53}$$

Eq. (53) follows directly from Eqs. (1) and (8) *after* it has been established that there are no cross-coupling terms.

The potential energy for the system is

$$2V = Y_1^2 \int EI_z(\eta'')^2 dx + Z_1^2 \int EI_y(\zeta_1'')^2 dx \tag{54}$$

The (usually nonconservative) aerodynamic forces are best introduced here by means of a virtual work function, δW. Let $\bar{Y}$ and $\bar{Z}$ represent the (dimensional) lift curve slopes per unit length of the airplane. The corresponding local angles of attack are $[\psi + Y_1\eta_1' + (Y_1/U)\eta_1]$ and $[\theta - Z_1\zeta_1' - (\dot{Z}_1/U)\zeta_1]$ where U is the airspeed. The corresponding virtual displacements are $\delta(\psi x + Y_1\eta_1)$ and $\delta(\theta x - Z_1\zeta_1)$. In terms of these quantities we can write down the virtual work function:

$$\delta W = \int \left\{ \bar{Y}\left(\psi + Y_1\eta_1' + \frac{\dot{Y}_1}{U}\eta_1\right)(x\delta\psi + \eta_1\delta Y_1) + \bar{Z}\left(\theta - Z_1\zeta_1' - \frac{\dot{Z}_1}{U}\zeta_1\right)(x\delta\theta - \zeta_1\delta Z_1) \right\} dx +$$

(other terms dependent on roll rate) (55)

The "other terms" indicated in (55) include the damping in roll, terms arising because lifting-surface centers of pressure do not lie on the fuselage reference line, etc. All these terms may be neglected here as unimportant either because they are small or because the roll rate is constant.

The appropriate form of the Lagrange equation here is

$$\frac{d}{dt}\left(\frac{\partial L}{\partial \dot{q}_i}\right) - \frac{\partial L}{\partial q_i} = \frac{\delta W}{\delta q_i} \tag{56}$$

where $L = T - V$ as usual.

Combining Eqs. (53) through (56) we obtain a set of homogeneous differential equations. As applied to a real airplane these equations should be modified to a nonhomogenous set by the inclusion of right-hand sides to indicate forcing functions. The pertinent forcing functions here have a frequency $\dot{\varphi}$ and arise mainly from two sources, viz., (1) static bending or "droop" of the fuselage and (2) oscillating components of the lift and yaw. These forces are due to the airplane apparent-weight vector rotating with angular velocity $-\dot{\varphi}$ with respect to the body-fixed axes. The particular solution of the equations of motion which corresponds to these oscillating forcing functions can be written in determinental form as:

$$A_\theta = N_\theta/\Delta, \quad A_\psi = N_\psi/\Delta, \quad A_{Z_1} = N_{Z_1}/\Delta, \quad A_{Y_1} = N_{Y_1}/\Delta \tag{57}$$

where A_θ, A_ψ, etc., are the amplitudes of oscillations of θ, ψ, etc., at frequency $\dot{\varphi}$. Eqs. (57) are the four-dimensional analog of Eqs. (37), and as in Eqs. (37) the steady-state response will grow beyond bound if the determinant Δ becomes zero. Without much labor we find, on neglecting rate-damping terms,

$$\Delta = \begin{vmatrix} [\omega_1^2 - 2\dot{\varphi}^2] & [2\dot{\varphi}^2] & a_{13} & 0 \\ [2\dot{\varphi}^2] & [\omega_2^2 - 2\dot{\varphi}^2] & 0 & a_{24} \\ a_{31} & 0 & [\omega_3^2 - 2\dot{\varphi}^2] & [2\dot{\varphi}^2] \\ 0 & a_{42} & [2\dot{\varphi}^2] & [\omega_4^2 - 2\dot{\varphi}^2] \end{vmatrix} \tag{58}$$

In Eq. (58) the columns correspond to θ, ψ, Z_1, and Y_1 in that order. The quantities a_{ij} are the aerodynamic coupling coefficients defined by the virtual work function. ω_1, ω_2, ω_3, and ω_4 are the uncoupled natural frequencies in pitch, yaw, vertical bending, and lateral bending in that order.

Equating Δ to zero and expanding, we obtain

$$4\dot{\varphi}^4[(\omega_1^2 + \omega_2^2)(\omega_3^2 + \omega_4^2) - (a_{24}a_{42} + a_{42}a_{13} + a_{13}a_{31})] +$$
$$2\dot{\varphi}^2[-\omega_1^2\omega_2^2(\omega_3^2 + \omega_4^2) - \omega_3^2\omega_4^2(\omega_1^2 + \omega_2^2) + a_{24}a_{42}(\omega_1^2 + \omega_3^2) + a_{13}a_{31}(\omega_2^2 + \omega_4^2)] +$$
$$[\omega_1^2\omega_2^2\omega_3^2\omega_4^2 - \omega_1^2\omega_3^2a_{24}a_{42} - \omega_2^2\omega_4^2a_{13}a_{31} + a_{31}a_{13}a_{24}a_{42}] = 0 \tag{59}$$

The solutions of Eq. (59) are those critical roll rates at which a "subharmonic response" of the system becomes arbitrarily large. When the a_{ij} are zero, we know the roots to be $\dot{\varphi}_{cr_1}$ and $\dot{\varphi}_{cr_2}$, where

$$1/2\dot{\varphi}_{cr_1}^2 = (1/\omega_1^2) + (1/\omega_2^2)$$

and

$$1/2\dot{\varphi}_{cr_2}^2 = (1/\omega_3^2) + (1/\omega_4^2) \tag{60}$$

Of these, $\dot{\varphi}_{cr_1}$ is the smaller, hence it is the critical limiting roll rate. It would be of interest to know whether the smallest root of (59) is smaller than $\dot{\varphi}_{cr_1}$, for if it were, a more severe limitation of roll rate would be imposed. This information cannot be deduced from (59), however, for the answer depends on the relative signs and magnitudes of the quantities a_{ij}, and these depend in turn on the aerodynamic and elastic properties of the particular airplane being considered. Unfortunately, no general conclusion can be drawn. The advisability of checking this question numerically for a given airplane should be obvious; however, when the problem is reduced to numbers greater accuracy can be achieved than is allowed for in Eq. (59). This increased ac-

(*Continued on page 157*)

Plasma Flow Over a Thin Charged Conductor†

HIDEO YOSHIHARA*

Convair-San Diego, A Division of General Dynamics Corporation

Summary

The flow of a dense plasma over a wavy conducting wall of small amplitude is investigated where magnetic effects are negligible. These results are then used to analyze the flow over a thin conductor with cusped edges. It is found that the Coulomb drag vanishes identically, while the fluid-pressure drag corresponds to the Ackeret value for a neutral particle gas at the reduced-plasma Mach number.

Introduction

WE WILL INVESTIGATE the uniform flow of a dense plasma over thin conducting bodies where the velocity of the free stream is supersonic with respect to the ion thermal speed, but subsonic with respect to the electron thermal speed. Magnetic effects are assumed to be absent and only electrostatic effects are considered. These flow problems are in the category of electrogasdynamics introduced previously by Kraus and Watson.[1]

In reference 2 a simplified case of a plasma flow over a thin, cusped, dielectric body was treated in which an asymptotic form of the basic equations for small Debye distance was used whose order was two less than the exact equation. The boundary-layer effect expected by this singular perturbation was avoided by a special choice of the surface charge on the dielectric. The flow obtained in this case was identical with the Ackeret solution of the neutral-particle supersonic theory with a modified free-stream Mach number.

In the present paper, we shall first investigate the flow over a conducting, infinite, wavy wall (sinusoidal) with a given surface-charge distribution. Here a boundary-layer phenomenon is expected, and the analysis will require the complete fourth-order equation. These results will then be used to analyze the flow over a conducting body with cusped leading and trailing edges.

Formulation of the Problem

The plasma we consider will be composed of electrons and singly charged positive ions; viscosity and heat conductivity will be assumed to be negligible.

The basic continuum equations for the positive ions will be postulated as

$$n^+ M \mathbf{v}\cdot\nabla\mathbf{v} + \nabla p^+ + n^+ e\,\nabla\Phi = 0 \qquad (1)$$

$$\nabla\cdot(n^+\mathbf{v}) = 0 \qquad (2)$$

and

$$p^+ = \text{const.}\ (n^+)^\gamma \qquad (3)$$

where M is the ion mass, n^+ the number density, p^+ the pressure, γ the adiabatic constant, $\mathbf{v}$ the velocity vector of the fluid particle, e the charge of an electron, and Φ the electrostatic potential.

The electrostatic potential fulfills the Poisson equation

$$\nabla^2\Phi = -4\pi e(n^+ - n^-) \qquad (4)$$

where n^- is the electron number density.

For equal electron and ion temperatures the velocity of the electrons (and, therefore, their collision frequency) will be very much larger than that of the ions because of the difference in their masses. Therefore, to a first approximation we can assume that the electrons are aways in thermodynamic equilibrium under the electrostatic force field at the free-stream condition. (Here it is tacitly assumed that the presence of any boundaries in the plasma will not influence the equilibrium distribution of the electron velocities.) Thus, we obtain the Maxwellian distribution function for the electron velocities (see e.g., Chapman and Cowling,[3] and Spitzer[4]) and in particular we obtain as a zero moment

$$n^- = n_0 \exp\,(e\Phi/kT^-)$$

where n_0 is a mean equilibrium density, k is Boltzmann's constant, and T^- is the electron temperature.

Under the equilibrium condition, the temperature T^- will be constant throughout the flow, and the pressure p^- will be given by the equation of state,

$$p^- = kn^- T^- = kT^- n_0 \exp\,(e\Phi/kT^-)$$

We next linearize the above equations by assuming that the flow variables are a small perturbation about a uniform plasma flow with velocity vector $\mathbf{V}_0$ (in the positive abscissa direction), with pressure p_0 and $n^+ = n^- = n_0$. Note that the electrostatic potential Φ will then be a perturbation, and Eq. (5) may be linearized to

$$n^- = n_0[1 + (e/kT^-)\Phi] \qquad (5)$$

If we next introduce a velocity potential P by

$$\mathbf{v} - \mathbf{V}_0 = \nabla P \qquad (6)$$

Eqs. (1) through (4) may be reduced to the coupled equations

$$-\lambda^2 P_{xx} + P_{yy} = (eV_0/a^{+2}M)\Phi_x \qquad (7)$$

$$[\nabla^2 - (a_p/a^+)^2(1/R_D^2)]\Phi = (\omega_p/a^+)^2(V_0 M/e)P_x \qquad (8)$$

and the Bernoulli equation

Received December 29, 1959.

† This report was prepared under ARPA Contract No. AF(604)-554, Order No. 42-59.

* Aerodynamics Group.

$$p - p_0 = -n_0(MV_0P_x + e\Phi) \tag{9}$$

Here $\lambda^2 = (V_0/a^+)^2 - 1$, where V_0 is the absolute value of $\mathbf{V}_0$ and a^+ is the ion sound speed defined by

$$a^{+2} = \gamma p_0/n_0M \tag{10}$$

x and y are the Cartesian coordinates; R_D is the Debye distance given by

$$R_D^2 = kT^-/4\pi n_0e^2 \tag{11}$$

and

$$a_p^2 = a^{+2} + \omega_p^{+2}R_D^2 \tag{12}$$

where the ion plasma frequency ω_p^{+2} is given by

$$\omega_p^{+2} = 4\pi n_0e^2/M \tag{13}$$

Let us next introduce in Eq. (7) through (9) the following scale transformation:

$$\left.\begin{aligned} \xi &= x/c, \qquad \eta = y/c \\ P(x, y) &= cV_0p(\xi, \eta) \\ \Phi(x,y) &= (MV_0^2/e)\bar{\Phi}(\xi, \eta) \end{aligned}\right\} \tag{14}$$

where c is a characteristic macroscopic length of the problem. Assuming an equality of the electron and ion temperatures so that $a^{+2} = \gamma\omega_p^{+2}R_D^2$, we obtain

$$-\lambda^2p_{\xi\xi} + p_{\eta\eta} = M_0^2\bar{\Phi}_\xi \tag{15}$$

$$(\nabla^2 - \sigma^2)\bar{\Phi} = (\gamma + 1)^{-1}\sigma^2p_\xi \tag{16}$$

and

$$C_p = \frac{p - p_0}{(1/2)n_0MV_0^2} = -2(p_\xi + \bar{\Phi}) \tag{17}$$

where

$$\sigma^2 = [(\gamma + 1)/\gamma](c/R_D)^2, \qquad M_0 = V_0/a^+$$

and C_p is the usual pressure coefficient.

Eqs. (15) and (16) can be decoupled to yield the following fourth-order equations for $\bar{\Phi}$ and p:

$$L(\bar{\Phi}) = 0, \qquad L(p) = 0 \tag{18}$$

where L is the operator

$$L = (\nabla^2 - \sigma^2)\left(-\lambda^2\frac{\partial^2}{\partial\xi^2} + \frac{\partial^2}{\partial\eta^2}\right) - (\gamma + 1)^{-1}\sigma^2M_0^2\frac{\partial^2}{\partial\xi^2} \tag{19}$$

Eqs. (15) and (16), or (18), for $\lambda > 0$ (the case in which we are interested), are twofold hyperbolic and twofold elliptic.

For the boundary and Cauchy-type conditions, we shall take the totality of conditions resulting from the purely fluid and electrostatic cases[2]:

(1) At the solid surface the normal velocity must vanish, and the electrostatic potential (since the solid surface is a conductor) must be constant.

(2) Far from the solid surface the velocity and electrostatic potentials must either vanish or be composed of "outgoing waves" (the radiating condition analogous to Sommerfeld's condition).

For the decoupled Eq. (18) one must use all the above conditions expressed in terms of the decoupled dependent variable by means of Eq. (15) or (16).

Plasma Flow Over a Wavy Wall

To obtain a physical insight into a problem that requires a fourth-order equation we consider the simplified case of an infinite, conducting, wavy wall of sinusoidal shape running in the direction of the ξ-axis. Here we expect that the flow will be composed of a thin region adjacent to the solid wall, the Debye boundary layer, and an external flow field. In the latter it is expected that

$$|\nabla^2\Phi/\Phi| \ll R_D^{-2}$$

so that the fourth-order equation as given by Eq. (18) may be reduced to a second-order, modified Prandtl-Glauert equation.[2] It is anticipated that the flow in the external region will not depend on the electrostatic charge of the wall; the external flow is shielded by the Debye boundary layer.

Within the Debye boundary layer we can expect shielding phenomena in which the gradient of the electrostatic potential normal to the wall will be very much larger than that along the wall. The amplitude of the wavy wall will be taken to be sufficiently small (e.g., in comparison to the wavelength) that the normal and tangential gradients can be replaced by gradients in the directions normal and tangential to the mean line of the wall. In the Debye boundary layer, therefore, we can approximate the form of the differential equation by neglecting ξ-derivatives relative to the η-derivatives.

We shall thus seek to simplify the fourth-order differential equation in such a way that in the external flow we obtain the modified Prandtl-Glauert equation used previously[2]; and in the Debye boundary layer we obtain a differential equation which contains only η-derivatives. It is further required that the order of the differential equation not be reduced, and the nature of the differential equations not be radically changed.

With these remarks in mind we shall rewrite the decoupled equations for $\bar{\Phi}$ given by Eq. (18), that is,

$$(\nabla^2 - \sigma^2)(-\lambda_p^2\bar{\Phi}_{\xi\xi} + \bar{\Phi}_{\eta\eta}) - \gamma^{-1}M_p^2\nabla^2\bar{\Phi}_{\xi\xi} = 0 \tag{20}$$

where $M_p = V_0/a_p$, $\lambda_p^2 = M_p^2 - 1$, and a_p is defined in Eq. (12).

Within the boundary layer, we can neglect ξ-derivatives as compared to the η-derivatives. In Eq. (20), therefore, we can neglect the ξ-derivatives in the ∇^2 term. Additionally we can drop the last term as compared to the first. Eq. (20) now becomes

$$\left(\frac{\partial^2}{\partial\eta^2} - \sigma^2\right)\left(-\lambda_p^2\frac{\partial^2}{\partial\xi^2} + \frac{\partial^2}{\partial\eta^2}\right)\bar{\Phi} = 0 \tag{21}$$

This is the desired equation having the correct form in both the Debye boundary layer and the external flow, except for terms of higher order. In the Debye layer

we have departed from consistency by retaining the $\bar{\Phi}_{\xi\xi}$ term in the second factor to obtain the proper form of the equation in the external region. Since we have $\sigma^2 \gg |\bar{\Phi}_{\eta\eta}/\bar{\Phi}|$ in the external region we have essentially $-\lambda_p{}^2 \bar{\Phi}_{\xi\xi} + \bar{\Phi}_{\eta\eta} = 0$, the required differential equation for this region. In Eq. (21) the hyperbolic character of the exact differential equation is retained, while the elliptic character is partially retained by the parabolic character of the first factor and in the change of the propagation speed from λ to λ_p.

The specific wavy wall which we consider is given by

$$\eta = \eta_0(\xi) = \epsilon \sin \alpha\xi \tag{22}$$

where $\epsilon = \text{const.} \ll 1$ and α is a constant related to the wavelength l of the wall by the relation $l = 2\pi/\alpha$ (Fig. 1).

The boundary conditions at the wall become

$$\bar{\Phi}(\xi, \eta_0) = \bar{\Phi}_0 = \text{const.} \tag{23}$$

$$p_\eta(\xi, \eta_0) = \alpha\epsilon \cos \alpha\xi \tag{24}$$

Using Eq. (16) we can express Eq. (24) in terms of $\bar{\Phi}$; we obtain

$$\int_{-\pi/2\alpha}^{\xi} \left(\frac{\partial^2}{\partial\eta^2} - \sigma^2\right) \bar{\Phi}_\eta\,(\bar{\xi}, \eta_0)\, d\bar{\xi} = \frac{\alpha\epsilon\sigma^2}{\gamma + 1} \cos \alpha\xi \tag{25}$$

Before solving the boundary-value problem we shall make a transformation of the ordinate variable such that the origin is taken at the surface of the wall; the abscissa is kept the same. For sufficiently small amplitudes of the wall, the basic Eq. (21) as well as the above boundary conditions remain invariant under the transformation. Instead of introducing new symbols we shall retain the old notation and henceforth measure η from the wall. Thus, the boundary conditions are to be fulfilled at $\eta = 0$.

The solution of Eq. (21) which we use is given in the upper half-plane $\eta \geqq 0$ by

$$\bar{\Phi} = f(\xi - \lambda_p\eta) + g(\xi)e^{-\sigma\eta} \tag{26}$$

where f and g are arbitrary functions of the indicated argument. The argument $(\xi - \lambda_p\eta)$ of f has been selected to obtain the proper behavior of $\bar{\Phi}$ at infinity.

The functions f and g are now determined by the boundary conditions Eq. (23) and (25). The desired solution is

$$\bar{\Phi} = A \cos \alpha(\xi - \lambda_p\eta) + (\bar{\Phi}_0 - A \cos \alpha\xi)e^{-\sigma\eta} \tag{27}$$

where $A = \epsilon\alpha/(\gamma + 1)\lambda_p$ and $\eta \geqq 0$. In Fig. 1 we show qualitatively the electrostatic potential field as given by this expression.

The surface charge distribution $\omega(\xi)$ can be determined from Eq. (27) by the relation

$$\omega(\xi) = (MV_0{}^2/ec)\bar{\Phi}_\eta,$$

or

$$\omega(\xi) = (MV_0{}^2\sigma/ec)(\bar{\Phi}_0 - A \cos \alpha\xi) \tag{28}$$

The surface pressure distribution caused by the positive ions, according to Eq. (17), will be

$$C_p = 2[(\epsilon\alpha/\lambda_p) \cos \alpha\xi - \bar{\Phi}_0] \tag{29}$$

This expression, except for the $\bar{\Phi}_0$ term, is identical with the usual neutral-particle continuum case with the free-stream Mach number equal to M_p.

The Coulomb drag D_c and the fluid pressure drag D_f per wavelength $l = 2\pi/\alpha$ of the wall, are given by

$$D_c = \frac{MV_0{}^2}{e} \int_0^{2\pi/\alpha} \omega(\xi)\bar{\Phi}_\xi\, d\xi$$

and

$$D_f = \int_0^{2\pi/\alpha} (p - p_0) \frac{d\eta_0}{d\xi}\, d\xi$$

(Note that the electron pressures do not affect the drag for the conductor since these pressures are uniform over the body surface.)

In the present case it is found that $D_c = 0$, and D_f is identical with the usual Ackeret value for a neutral-particle gas corresponding to a reduced Mach number M_p.

Lastly, the distribution of the ion number density and velocity vector may be found by using the expression for $\bar{\Phi}$ from Eq. (27) in Eq. (16). It is found that both the ion number density and the velocity vector do not exhibit a boundary-layer phenomenon (as the electrostatic potential does) but possess a hyperbolic character everywhere.

Flow Over a Cusped Body

The results for the wavy wall can be carried over for a conductor with cusped leading and trailing edges by terminating the wall at appropriate points, e.g., $\xi = -\pi/2\alpha$ and $3\pi/2\alpha$. In Fig. 2 we show qualitatively the expected configuration of the equipotential lines. The effect of terminating the wavy wall is confined essentially to a Debye shielding region Σ_d about each edge of the body and to its corresponding region of influence Σ_i formed by the Mach waves emanating from Σ_d (Fig. 3). It is noted that the local behavior of the potential lines in these regions will be identical with that for a flat plate (Fig. 4); the latter may be analyzed in a manner similar to the wavy-wall case after a suitable transformation to elliptic coordinates.* However, from the behavior of the Debye layer for the wavy wall it would follow that the behavior of the potentials near each cusped edge will be locally similar, the behavior being determined primarily by the shielding phenomena. Moreover, this similarity will also extend to the respective regions of influence Σ_i of the two regions Σ_d.

Clearly, with the similarity of the potential in the respective regions Σ_d and Σ_i, reversal of the ξ-axis will yield ξ-derivatives of the velocity and electrostatic potentials of opposite sign. This reversal will be used to determine the change in the Coulomb and fluid-pressure drags caused by terminating the wavy wall.

* The present simplification of the fourth-order equation can be carried over to the flat plate case directly starting from the exact equation (20) in elliptic coordinates.

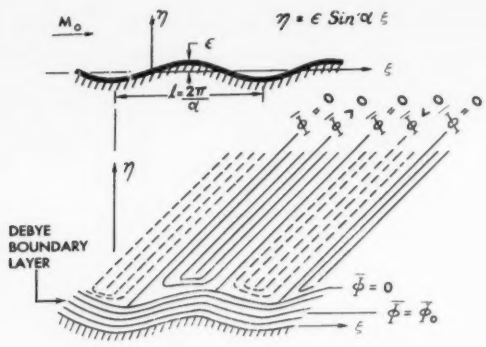

FIG. 1. Equipotential lines for wavy wall.

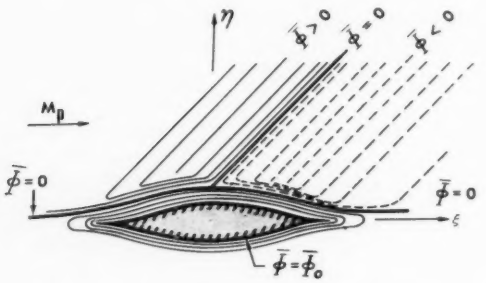

FIG. 2. Equipotential lines for a cusped body.

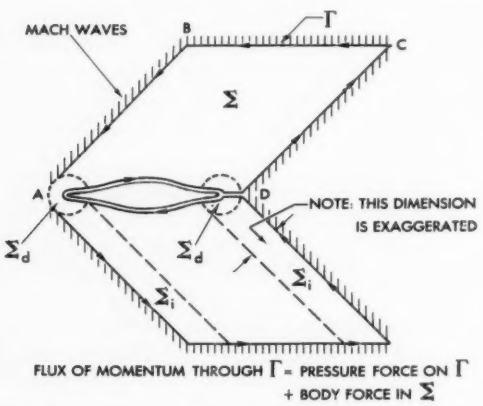

FIG. 3. Control surface for fluid-pressure drag.

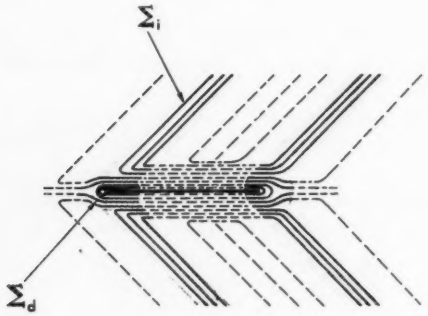

FIG. 4. Equipotential lines for flat plate.

Consider first the Coulomb drag. The preceding discussions lead to equal and opposite contributions of the Coulomb force from the two cusps; the Coulomb drag of the cusped body will thus be zero.

To compute the modification of the fluid-pressure drag we shall use the momentum theorem for the control surface Γ as shown in Fig. 3; Γ here encloses the domain Σ. The momentum theorem states that the flux of the momentum vector through Γ per unit time is equal to the force vector caused by the pressure on Γ plus the Coulomb forces within Σ.

Let us consider first the momentum flux term. In Γ we have taken the Mach waves AB and CD, just upstream and downstream (on the order of the Debye distance), respectively, of the leading- and trailing-edge waves; here essentially free-stream conditions prevail, so that the momentum flux in the ξ-direction through AB and CD will be zero.

The ξ-momentum flux through BC caused by the flow perturbations propagating along the Mach waves in the regions Σ_i from each edge will cancel each other, in accordance with previous considerations; therefore, the only contribution to the momentum flux will be through BC due to the perturbations for the infinite wavy wall.

The Coulomb forces in the regions Σ_i and Σ_d for each edge will cancel each other. The body-force term of the momentum theorem will thus vanish identically in the domain Σ.

Consequently, we obtain the result that the pressure drag for the cusped conductor will be twice that for a wavelength of the infinite wall; that is, it will be equal to the neutral-particle continuum value corresponding to a Mach number equal to M_p.

Final Remarks

Simple two-dimensional electrogasdynamic flow examples were examined, where a fourth-order equation was required. It was found that the electrostatic potential field was divided into two regions: the Debye boundary layer adjacent to the wall, and the external field. Within the Debye layer the electrostatic potential (and, therefore, the number density of the electrons) reflected predominantly an elliptic character (exponential attenuation); the potential was directly related to the charge on the wall. In the external region the character of the potential field was essentially of the hyperbolic type with a modified characteristic speed. The potential field here was independent of the electrostatic state of the wall.

The distributions of the number density and velocity of the positive ions, in contrast to the electrons, were of hyperbolic character throughout the entire flow and did not exhibit any boundary-layer phenomena. The necessary charge separation in the Debye boundary layer required to meet the electrostatic conditions at the wall was accomplished by the electrons with their higher mobility.

(*Continued on page 157*)

High-Speed Viscous Corner Flow†

MARTIN H. BLOOM* AND STANLEY RUBIN**

Polytechnic Institute of Brooklyn

Summary

A boundary-layer integral method analysis is set up for compressible laminar flow in a symmetric corner with varying angle and streamwise pressure gradient. It represents an extension and modification of the constant density analysis of Loitsianskii and Bolshakov.[1] The analysis is applied to the case of constant pressure, constant corner angle, and isothermal surfaces, for which the Crocco velocity-enthalpy relation holds. Although simplifying assumptions limit the quantitative accuracy outside the 60° to 120° angle range, some qualitative trends are probably correct outside this range. The limiting cases near 0° and 180° are not considered.

Favorable agreement between some results obtained by the integral method and by other methods is demonstrated for the isothermal, constant-density case.

Results show an increasingly sharp merger of the outermost isovels of streamwise velocity as the Mach number increases. This sharp merging of the outer isovels is increased by increasing corner angle and by insulation or heating of the surfaces. Within the interior of the viscous layer the spreading or contraction of the disturbed region of merging is influenced by surface heat-transfer conditions. Surface shear and heat flux are decreased in the disturbed region, and are zero at the apex. For cases corresponding roughly to the higher Mach numbers or wider corner angles, the "specific momentum-area" exhibits the same decrease with Mach number as its two-dimensional counterpart, whereas the "specific displacement-area," a measure of stream-tube dilation, increases more rapidly with Mach number than the comparable two-dimensional parameter.

Symbols

A_p = integration area in physical coordinates (Eq. 40a)
A_t = integration area in transformed plane
c = $u_e^2/2h_e$
$g(\xi,\eta)$ = see Eq. (26)
H = stagnation enthalpy, $h + (u^2/2)$
h = static enthalpy
$\bar{h}$ = h/h_e
K = boundary-layer thickness factor
k = thermal conductivity
M = Mach number
$n_1(x)$ = $s_1(x) = \delta_{0P}(x)/\sin\vartheta$
$n_2(s,x)$ = $s_2(n,x)$ = local limit of interference region in physical plane
$n_0(s,x)$ = curve denoting portion of $n_2(s,x)$ which passes through the boundary layer
P = Prandtl number, $\mu c_p/k$
q = heat flux
r = distance along symmetry axis
R_{ex} = Reynolds number, $\rho_e u_e x/\mu_e$
s, n, x, y, z = physical coordinates
u = velocity component in x direction
$\bar{u}$ = u/u_e
V = velocity component in y direction
v = velocity component in s direction
W = velocity component in z direction
w = velocity component in n direction
γ = ratio of specific heats c_p/c_v
Δ^* = displacement area parameter
δ_0 = transformed two-dimensional compressible boundary-layer thickness, $x\sqrt{K/R_{ex}}$
δ_{0P} = physical two-dimensional boundary-layer thickness
δ_0^* = two-dimensional displacement thickness
$\eta_e(\xi, x)$ = curve of outer edge of corner boundary layer [Eq. (31)]
Θ = momentum-area parameter [Eq. (20)]
ϑ = included angle of corner
ϑ_0^* = two-dimensional momentum thickness
λ = station along x axis
μ = absolute viscosity coefficient
ξ, η, x = transformed coordinates
$\xi_1(x)$ = $\eta_1(x) = \delta_0(x)/\sin\vartheta$
$\xi_2(x)$ = $\eta_2(x)$ = local limit of interference region in transformed plane
ρ = density
$\bar{\rho}$ = ρ/ρ_e
τ = shear stress
τ^n = shear stress on surfaces of constant n [Eq. (12)]
φ = interference parameter $n_{2e}/n_1 = \eta_2/\eta_1$
ν = μ/ρ

Subscripts

0 = undisturbed two-dimensional conditions
e = external condition (inviscid)
w = wall condition

Received September 21, 1959. Revised and received July 23, 1960.

† This research was carried out under Contract AF 33(616)-6118, administered by the Aeronautical Research Laboratory of the Air Research and Development Command and partially supported by the Air Force Ballistic Missile Division.

* Professor of Aeronautical Engineering.

** Research Assistant.

(I) Introduction

WE WISH TO EXAMINE the high-speed viscous steady flow within an interior corner formed by the intersection of two semi-infinite surfaces which are effectively planar. The flow proceeds along the line of intersection (Fig. 1).

The classical Prandtl boundary-layer concepts are assumed to apply. Roughly, this means that the transverse velocity components (V, W) and pressure gradients $\partial p/\partial y$, $\partial p/\partial z$ are assumed small in comparison with their respective streamwise counterparts u and $\partial p/\partial x$; whereas transverse gradients of variables other than pressure are assumed large with respect to the corresponding streamwise gradients. Moreover, the intersecting surfaces may be moderately curved in the boundary-layer sense. Following the classical boundary-layer approach, we accord no special treatment to limiting, low Reynolds number phenomena which may occur in the leading-edge regions or very close to the surfaces or very close to the intersection line. Indeed,

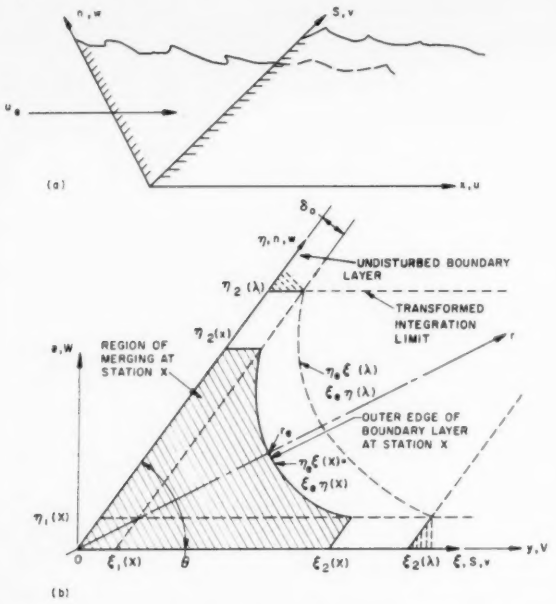

FIG. 1. Coordinates and integration limits for corner flow.

the leading edges may be considered to be blunt, while the intersection region may contain a fillet whose radius is small with respect to the boundary-layer thickness. The latter feature would not be expected to have a significant influence on the dominant characteristics of the boundary layer.

The applicable equations are presented for corner flows with streamwise pressure gradients and for corner angles which vary moderately in the streamwise direction; however, the analysis is completed here only for constant pressure flows with constant corner angles. The solution is accomplished by a one-parameter integral method. In the constant-pressure case the velocity distributions are similar in transverse planes. For a Prandtl number of unity the algebraic Crocco integral relation between enthalpy and velocity is shown to apply. Therefore, for constant pressure, the usual form of Reynolds analogy between heat flux and shear stress holds. The governing equations given here are known to apply also in nonhomogeneous mixtures and chemically reacting flows in which the parameter characterizing the diffusion, say the Lewis number, is unity.

The integral equation derived here may be considered to apply in both laminar and turbulent flow. However, only laminar flows are treated in this paper.

Each of the intersecting surfaces is assumed to possess a boundary-layer region which is essentially undisturbed by the presence of the corner. The corner flow is assumed to merge smoothly with the undisturbed boundary layer in an asymptotic manner if mathematically exact procedures are employed, or in a finite distance from the intersection if integral methods are used. In the integral method used here, this finite distance, which is a measure of the extent of the interference region, is considered to be the single parameter which is finally determined as a function of the streamwise coordinate to complete the solution; this interference length appears nondimensionalized with respect to the undisturbed boundary-layer thickness.

Only flows symmetric with respect to the bisector of the corner are treated here, although nonsymmetric flows may also be of interest.

The present analysis may be considered to be an extension of the work of Loitsianskii and Bolshakov[1] who treated the constant-density case for both laminar and turbulent flow by an integral method. Some minor differences in the procedure employed here for the special case of constant density will be cited in the description of the analysis.

Several other treatments of constant-density flow in a corner can be cited. In all of these the condition is imposed that the corner flow must merge asymptotically with an undisturbed boundary layer at distances sufficiently far from the corner. One of the first studies was that of Carrier,[2] who obtained for a 90° corner an approximate solution of the streamwise component of the momentum equation together with the continuity equation, which he assumed could be split into two equivalent equations. The solution was obtained by a relaxation method. A recent detailed study of mathematically exact solutions for a wide range of corner angles ranging from 0 to 360° has been presented by Levy.[3] Included in Levy's work is a complete literature study which cites attempts by Dowdell[4] and Kemp[5] to obtain more complete solutions along the lines of Carrier's, and a study by Sowerby and Cooke[6] using "Rayleigh's method" of impulsive motion of surfaces. Since the equations of motion are not satisfied when the unsteady flow is transformed to a steady flow in the latter approach, the method is regarded as empirical.

Several criticisms of the integral method solution of Loitsianskii and Bolshakov[1] are mentioned by Levy. It is noted that the outer boundary-layer edge has a discontinuity in slope at its junction with the undisturbed boundary layer. Furthermore, it is cited that one cannot demonstrate that refinements in the choice of profiles will lead to improved results. Finally, it is shown that the second derivative of the velocity profile near the corner intersection point as obtained by the integral method does not agree well with those obtained by more exact solutions of the differential equations. These criticisms of the work of reference 1 would apply to the present analysis as well. However, we may point out that the integral equations derived here by integration of the differential equations (see Analysis) are mathematically exact within the limitations of the boundary-layer approximations, and therefore should be satisfied "exactly" by the most precise possible choice of velocity distributions. Simplifying approximations made for expediency in the analysis may be eliminated if it is deemed necessary. Certainly, it is always of value to check the results of the integral method with exact solutions if possible. However, the integral method is known to yield good

qualitative and even quantitative results in cases where "very peculiar" behavior of the assumed profiles is not expected to occur. Indeed, for improved accuracy additional integral equations may be derived by the use of "weighing factors" in the original differential equations or by piecewise integration, and by the use of additional undetermined parameters to satisfy these equations. A sufficient number of independent integral equations so derived would be equivalent to the governing differential equations.

We may also suggest that the use of the second derivatives of the velocity profiles in judging the accuracy or utility of the integral method forms a very stringent test. Since there is more interest here in the general features of the flow than in its very detailed behavior, perhaps more meaningful comparisons would concern velocity profiles and shear stresses, for example. Such comparisons are discussed further in the body of the paper.

Although the procedure employed here can be used for any corner angle $0 < \vartheta < 180°$, some simplifying assumptions introduced in connection with the use of oblique coordinates are expected to make the solutions inaccurate for angles close to zero and 180°. In this paper primary attention is devoted to the angles $60° < \vartheta < 120°$, while some results are given for $30° < \vartheta < 150°$.

It will be seen that, for a Prandtl number of unity and isothermal surfaces, the Crocco integral of the energy equation, which yields an algebraic relation between the enthalpy and velocity, is applicable. The present paper is limited to cases of this type.

It may be noted here that Gersten[7] has discussed features of constant-density laminar and turbulent corner flow, including some effects of transition to turbulence and of pressure gradients, and has presented some experimental results pertaining to these effects.

Added Note

After the present paper had been completed, a report was issued by Cheng and Levy[9] describing the previously cited work by Levy[3] and giving some additional calculations. Several additional theoretical works relative to laminar corner flow also came to the authors' attention. These were by Krzywoblocki,[10] Oman,[11] and Irvine and Eckert.[12] An experimental investigation by Stainback[8] under laminar and turbulent conditions also was reported.

Krzywoblocki[10] presents a calculation for compressible flow in a 90° corner by a method analogous to Carrier's for constant density. A perturbation in the square of the Mach number is employed to extend the constant-density equations, and a relaxation solution is carried out for the single case of an insulated surface at Mach 2. Isovels are given for values of the velocity ratio $\bar{u} \leqq 0.8$. These indicate at least qualitative agreement with a trend derived in the present work, which shows an increased confinement of the corner influence relative to the undisturbed boundary layer as the Mach number increases. In particular, for Krzywoblocki's isovel $\bar{u} = 0.8$, the ratio of the coordinate point at which corner influence disappears, to the coordinate of $\bar{u} = 0.8$ in the undisturbed Blasius flow, is 2.26 in comparison with the value 2.70 in constant-density flow. The ratio of the latter two values is about 0.84, and may be compared roughly with the value 0.79 obtained from the ratio of analogous values of φ (corresponding to $\bar{u} = 1$) of the present paper. Oman[11] presents an integral method analysis of constant-density flow in a 90° corner including pressure gradient effects. The derived integral equations are the same as those of the present paper for the special case cited. However, the assumed profiles are of asymptotic (exponential integral) type, in the form of products of functions of the coordinates, and are augmented to improve their accuracy at separation. From a computational standpoint the profiles are more difficult to use than the polynomials of the present paper. However, they yield excellent agreement with Carrier's velocity distributions in the isobaric case. In addition, Oman gives some theoretical and experimental results of flow along the inner corners of square tubes with pressure gradients.

Irvine and Eckert[12] present a constant-density, isobaric integral method analysis within grooves with sidewalls of finite extent. Their flows do not necessarily blend with undisturbed two-dimensional flows. They also give a constant-property heat transfer analysis by means of an integral energy equation. However, they do not consider the Crocco relation which is applicable for a Prandtl number of unity, or the Reynolds analogy which it implies.

The experiments reported by Stainback[8] were made at Mach 4.95 at a stagnation temperature of 860°R. and test-section Reynolds numbers per foot between 2×10^6 and 74×10^6. The results, consisting of pressures and surface heat-transfer rates, are difficult to compare with those of the present analysis, since most of the data is in the transitional and turbulent regime. The laminar values, which occur primarily near the leading edge of the model, are influenced by self-induced pressure rises and pressure gradients. Furthermore, preliminary estimates indicate that most of the sensing stations in the experiments cited are marginal or outside the corner-influence region as it is defined in the theoretical analyses cited here.

(II) Analysis

Consider the viscous flow within a corner formed by the intersection of two planar surfaces, the flow being along the line of intersection and symmetric about a center plane (Fig. 1a). A rectangular coordinate system, whose x axis runs along the intersection line, is used for the derivation of the governing equations. It is assumed that the transverse velocity components (V,W in the y,z directions) are small compared with the streamwise component u. Transverse derivatives ($\partial/\partial y$, $\partial/\partial z$) are assumed large with respect to streamwise derivatives ($\partial/\partial x$) except in the case of the trans-

verse pressure gradients ($\partial p/\partial y$, $\partial p/\partial z$) which are assumed negligible compared with the streamwise gradient $\partial p/\partial x$. On the basis of these assumptions the Navier-Stokes, continuity, energy and state equations acquire their Prandtl boundary-layer form. The mathematical procedures required for the derivation of the governing equations by means of series expansions in terms of Reynolds number parameters are discussed in reference 3 for the constant-density case. The aforementioned physical reasoning will suffice for the purpose of this investigation. Therefore the applicable boundary-layer equations in terms of rectangular coordinates are given as follows:

X = wise momentum:

$$\rho u u_x + \rho V u_y + \rho W u_z = -p_x + (\mu u_y)_y + (\mu u_z)_z \quad (1)$$

where p_y and p_z are assumed zero, and $-p_x = \rho_e u_e u_{ex}$;

continuity:

$$(\rho u)_x + (\rho V)_y + (\rho W)_z = 0 \quad (2)$$

energy:

$$\rho u H_x + \rho V H_y + \rho W H_z = \left(\frac{\mu}{P} H_y\right)_y + \left(\frac{\mu}{P} H_z\right)_z + \left[\mu\left(1 - \frac{1}{P}\right) u u_y\right]_y + \left[\mu\left(1 - \frac{1}{P}\right) u u_z\right]_z \quad (3)$$

state (perfect gas):

$$p = \rho R T \quad (4)$$

For $P = 1$ we observe that the usual Crocco integrals hold:

$$\text{for} \quad p_x \neq 0 \quad : \quad H = H_e \quad (5)$$

$$\text{for} \quad p_x = 0 \quad : \quad H - H_w = (H_e - H_w)\bar{u} \quad (6)$$

where H_w and H_e are assumed constant. Only flows in which the Crocco integrals may be used in place of the complete energy Eq. (3) will be considered in this paper.

To facilitate the treatment of flows in corners having angles "not close" to 0 or 180°, oblique coordinates s,n (Fig. 1b) are introduced to replace the transverse coordinates y,z in the momentum and continuity Eqs. (1) and (2). For angles roughly less than 30° or greater than 150°, the use of other coordinate systems would be more suitable. For example, in the constant-density analysis of reference 1, coordinate lines perpendicular to the corner surfaces are used. The present approach is somewhat simpler procedurally in the compressible case. In terms of oblique coordinates, the equations are:

$$\rho u u_x + \rho v u_s + \rho w u_n = -p_x + \frac{1}{\sin^2\vartheta}\left[(\mu u_s)_s + (\mu u_n)_n\right] - \frac{\cos\vartheta}{\sin^2\vartheta}\left[(\mu u_s)_n + (\mu u_n)_s\right] \quad (7)$$

$$(\rho u)_x + (\rho v)_s + \rho w_n = 0 \quad (8)$$

where v and w are the velocity components in the s and n directions, respectively, and again subscripts denote partial differentiation with respect to the indicated variables.

Strictly speaking, up to this point we have been considering the corner formed by flat surfaces intersecting in a straight line. However, in the boundary-layer sense, this requirement may be relaxed somewhat to provide for the consideration of moderately curved surfaces and a moderately curved intersection line. In this case the coordinate planes are families parallel to the solid surfaces, and the coordinates s,n,x are considered to be curvilinear, running along the coordinate planes and the intersection line of the surfaces, respectively. Transverse planes are normal to the intersection line of the solid surfaces, and the local cone angle ϑ in the transverse plane is considered to be a slowly varying function of x. It is emphasized that the analysis is limited to flows in which the streamline curvature parameters do not appear explicitly.

The surfaces forming the corner are assumed to be sufficiently extended laterally that the influence of the junction on the boundary-layer flow on the surfaces is negligible at a sufficient distance from the origin of coordinates. The corner flow blends asymptotically with this undisturbed flow whose properties are assumed known a priori. In terms of the integral method, the extent of the interference flow is assumed to end at a finite distance, say n_2 along n or s_2 along s, in a manner analogous to that of the boundary-layer thickness in usual boundary layers. Of course, the viscous region in the corner is likewise assumed to end at a boundary-layer surface located a finite distance from the intersection. The shape of this bounding surface subsequently will be assumed in a reasonable, although admittedly somewhat arbitrary, fashion.

For the purpose of forming a momentum integral relation from Eqs. (7) and (8), two coordinate planes $n = n_2(\lambda)$ and $s = s_2(\lambda)$ are designated. These planes are located sufficiently far from the origin that they enclose all the corner interference effects which occur prior to a station $x = \lambda$. That is, the values $n_2(\lambda)$ and $s_2(\lambda)$ denote the limits of the interference region at $x = \lambda$. At sections $x < \lambda$ the parameters $n_2(x)$ and $s_2(x)$ denote the local interference limits (see Fig. 1b). When integration of Eqs. (7) and (8) is performed with respect to n and s at a section $x < \lambda$ over the area bounded by $n_2(\lambda)$ and $s_2(\lambda)$, and when the symmetry of the flow is taken into account, the following integral equation is derived:

$$\frac{\partial\Theta}{\partial x} + \left[\left(2 + \frac{\Delta^*}{\Theta}\right)\frac{1}{u_e}\frac{\partial u_e}{\partial x} + \frac{1}{\rho_e}\frac{\partial\rho_e}{\partial x}\right]\Theta - \frac{1}{\rho_e u_e{}^2}\frac{\partial}{\partial x}\left[\rho_e u_e{}^2 \int_0^{n_1(x)} dn \int_0^{s_2(\lambda)} (1 - \bar{u}_0)\bar{\rho}\bar{u}\, ds\right] + \int_0^{n_1(x)} dn \int_0^{s_2(\lambda)} \left[\frac{1}{u_e}\frac{\partial}{\partial x}(u_e - u_0)\right]\bar{\rho}\bar{u}\, ds = \frac{-2}{\rho_e u_e{}^2 \sin\vartheta}\int_0^{s_2(\lambda)} ds \int_0^{n_2(\lambda)} \frac{\partial\tau^s}{\partial n}\, dn \quad (9)$$

where

$$\Theta = \int_0^{s_2(\lambda)} ds \int_0^{n_2(\lambda)} \bar{\rho}\bar{u}(1 - \bar{u})\, dn \quad (10)$$

$$\Delta^* = \int_0^{s_2(\lambda)} ds \int_0^{n_2(\lambda)} (1 - \bar{\rho}\bar{u})\, dn \qquad (11)$$

$$\tau^s = \frac{\mu}{\sin\vartheta}\left(\frac{\partial u}{\partial n} - \cos\vartheta\,\frac{\partial u}{\partial s}\right) \qquad (12)$$

$$\left.\begin{aligned} u_e = u_e(x), \quad \rho_e = \rho_e(x), \quad \vartheta = \vartheta(x), \\ u_0 = u_0(n, x) \quad \text{or} \quad u_0(s, x) \\ \bar{\rho} = \rho/\rho_e, \quad \bar{u} = u/u_e \end{aligned}\right\} \qquad (13)$$

Since the area of an elemental parallelogram in oblique coordinates is $ds\, dn \sin\vartheta$, the quantity $\Theta \sin\vartheta$ represents a "momentum area" analogous to the usual momentum thickness, while $\Delta^* \sin\vartheta$ represents the corresponding "displacement area." The quantity τ^s denotes the shear stress on planes parallel to the s axis. The shear τ^n acting on planes parallel to n has been eliminated by symmetry, but may be obtained from Eq. (12) by interchanging n and s derivatives. The term $n_1(x) \sin\vartheta$ designates the undisturbed boundary-layer thickness δ_{0P}. By symmetry it equals $s_1(x) \sin\vartheta$.

Quantities denoted by the subscript e are functions of x only and may be obtained from the corresponding inviscid flow in the corner. Those denoted by subscript 0 are evaluated in the undisturbed boundary layer, particularly along the limiting coordinate lines $s_2(\lambda)$ and $n_2(\lambda)$ which pierce the undisturbed boundary layers; therefore terms with subscript 0 are functions of x and of either s or n.

For the special case of constant pressure (u_e and ρ_e constant), constant ϑ, and constant density, Eq. (9) should be reduced to the equivalent integral equation presented by Loitsianskii and Bolshakov.[1] However, we observe that two additional terms remain in Eq. (9). These represent the effect of the portion of the control surface which penetrates the undisturbed boundary layer. They apparently have been omitted in reference 1. However, in the constant-pressure, constant-density case treated in reference 1, and in the corresponding constant-pressure, high-speed case to be treated here, the contribution of these terms is found to be negligible.

The integral on the right side of Eq. (9) may be expressed as follows:

$$\int_0^{s_2(\lambda)} ds \int_0^{n_2(\lambda)} \frac{\partial \tau^s}{\partial n}\, dn = -\cot\vartheta \int_0^{s_1(x)} \mu_0 \frac{\partial u_0}{\partial s}\, ds - \frac{1}{\sin\vartheta}\int_0^{s_2(\lambda)} \left(\mu\frac{\partial u}{\partial n}\right)_w ds \qquad (14)$$

In (14) we have taken into account that at $n = n_2(\lambda)$ the shear is negligible for $s > s_1(x)$, while $\partial u/\partial n = 0$ for $s < s_1(x)$, and at $n = 0$, $\partial u/\partial s = 0$. It is noted that terms comparable to the first term on the right side of Eq. (14), expressing the effect of shear through the undisturbed boundary layer, apparently have not been included in the formulation of reference 1. This contribution becomes zero for the special case of $\vartheta = 90°$.

The momentum area parameter Θ may be expressed as

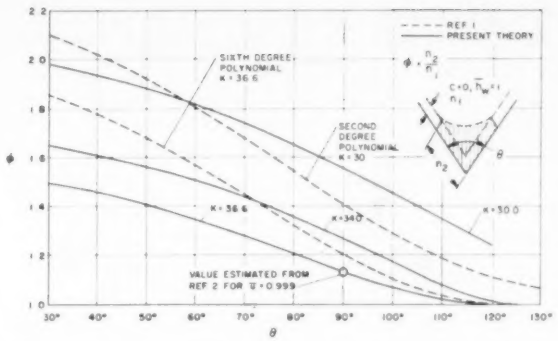

FIG. 2. Interference parameter φ versus corner angle for constant density.

$$\Theta = \int_0^{s_1(x)} ds \int_0^{n_2(\lambda)} \bar{\rho}\bar{u}(1 - \bar{u})dn + \int_{s_1(x)}^{s_2(\lambda)} ds \int_0^{n_e(s,x)} \bar{\rho}\bar{u}(1 - \bar{u})dn \qquad (15)$$

where $n_e(s, x)$ represents the boundary-layer thickness surface whose shape must be prescribed. By symmetry, n and s may be interchanged in Eq. (15). An analogous expression may be written for Δ^*.

In the analysis of reference 1, the outer bounds of the corner flow are chosen to be lines perpendicular to the corner surfaces rather than oblique coordinate lines as in the present analysis. This difference, which disappears for the special case of $\vartheta = 90°$, is indicated by the small shaded regions in Fig. 1b. In the present analysis the point of view of reference 1 would lead to the introduction of the following additional term in Eq. (15):

$$2\int_{s_2(\lambda)}^{[s_2(\lambda)+n_1(\lambda)\cos\vartheta]} ds \times \int_0^{[s_2(\lambda)+n_1(\lambda)\cos\vartheta - s]/\cos\vartheta} \bar{\rho}\bar{u}(1 - \bar{u})dn \qquad (16)$$

Correspondingly, additional shear contributions due to the surface segments $n_1(x) \cos\vartheta$ and $s_1(x) \cos\vartheta$ would appear on the right side of Eq. (9).

A comparison of results obtained for constant density by the present procedures with those obtained by Loitsianskii and Bolshakov[1] is presented in Fig. 2. Only the general trends and qualitative agreement need be noted at this time. The results will be discussed in more detail later.

Density Transformation

In anticipation of the density transformation to be introduced, it should be observed that, in the previous derivation of the integral relations, the control lines which delineate the integration limits over a given section, and which also define the lines of matching of the corner flow and the undisturbed boundary layers, could have been prescribed in the arbitrary symmetric forms $n_2(s, \lambda)$ and $s_2(n, \lambda)$, and $n_2(s, x)$ and $s_2(s, x)$, rather than as the previously indicated straight lines $n_2(\lambda)$, $s_2(\lambda)$, $n_2(x)$, and $s_2(x)$. Indeed, the use of the density transformation is simplified if the curved

limit lines are used, for then it is possible to prescribe that the limit lines in terms of the transformed variables be rectilinear at a given section. This obviates the a priori selection of the physical limit lines, whose form may be determined by means of transformation back to the physical coordinates once a transformed solution has been obtained. The assumed constancy of the transformed limits (at a given x) results in the disappearance of the additional terms which arise in the revised forms of Eqs. (14) and (15) due to the curved nature of the limits n_2 and s_2.

The density transformation of Dorodnitzyn-Howarth type is introduced as follows: at a fixed x,

$$\left.\begin{aligned} \eta &= \int_0^n \bar{\rho}\, dn \quad \text{or} \quad n = \int_0^\eta \frac{1}{\bar{\rho}}\, d\eta \\ \xi &= \int_0^s \bar{\rho}\, ds \quad \text{or} \quad s = \int_0^\xi \frac{1}{\bar{\rho}}\, d\xi \end{aligned}\right\} \tag{17a}$$

where we prescribe the integration limits as:

$$\left.\begin{aligned} \eta_2(\lambda) &= \int_0^{n_2(s,\lambda)} \bar{\rho}\, dn \quad \text{or} \quad n_2(s,\lambda) = \int_0^{\eta_2(\lambda)} \frac{1}{\bar{\rho}}\, d\eta \\ \xi_2(\lambda) &= \int_0^{s_2(n,\lambda)} \bar{\rho}\, dn \quad \text{or} \quad s_2(s,\lambda) = \int_0^{\xi_2(\lambda)} \frac{1}{\bar{\rho}}\, d\xi \end{aligned}\right\} \tag{17b}$$

In particular,

$$\left.\begin{aligned} n_{2w} \equiv n_2(0,x) &= \int_0^{\eta_2(x)} \frac{1}{\bar{\rho}_w}\, d\eta \\ \text{and} \qquad s_{2w} \equiv s_2(0,x) &= \int_0^{\xi_2(x)} \frac{1}{\bar{\rho}_w}\, d\xi \\ n_1(x) = \int_0^{\eta_1(x)} \frac{1}{\bar{\rho}_0}\, d\eta \ &\text{and}\ s_1(x) = \int_0^{\xi_1(x)} \frac{1}{\bar{\rho}_0}\, d\xi \end{aligned}\right\} \tag{18a}$$

where $\bar{\rho}_0 = \bar{\rho}_0(\xi/\xi_1) = \bar{\rho}_0(\eta/\eta_1)$, the density profile in the undisturbed boundary layer, and $\xi_1 \sin\vartheta = \eta_1 \sin\vartheta = \delta_0$, the transformed undisturbed boundary-layer thickness.

Moreover, as a consequence of the assumed form of the profiles, it will be possible to express $\bar{\rho} = \bar{\rho}(g)$, where $g \equiv (\xi/\xi_1)(\eta/\eta_2)$. Considering symmetry, this leads to the relations

$$\begin{aligned} n_{2e} \equiv n_2(s_1,x) &= \eta_2(x) \int_0^1 \left[\bar{\rho}\left(\frac{\eta}{\eta_2}\right)\right]^{-1} d\left(\frac{\eta}{\eta_2}\right) \\ &= \eta_2 \int_0^1 \left[\bar{\rho}_0\left(\frac{\xi}{\xi_1}\right)\right]^{-1} d\left(\frac{\xi}{\xi_1}\right) = \eta_2 s_1/\xi_1 \end{aligned}$$

or

$$n_{2e}/n_1 = \eta_2/\eta_1 \tag{18b}$$

and

$$n_{2e}/n_{2w} = \int_0^1 (\bar{\rho}_0)^{-1}\, d(\eta/\eta_1) \int_0^1 (\bar{\rho}_w)^{-1}\, d(\eta/\eta_2) \tag{18c}$$

Within the undisturbed boundary layer, at $n_2(s,\lambda)$ or $\eta_2(\lambda)$, we may write $u_0 = u_0(\xi, x)$, while at the surface $n = 0$ we must have $\partial u/\partial\xi = 0$. Therefore, if $n_0(s,\lambda)$ denotes the segment of the limit curve $n_2(s,\lambda)$ which penetrates the boundary layer, and $n_e(s,x)$ or $\eta_e(\xi,x)$ represents the corner boundary-layer surface,

$$\begin{aligned} \int_0^{s_2(n,\lambda)} ds \int_0^{n_2(s,\lambda)} \frac{\partial \tau^s}{\partial n}\, dn &= -\cot\vartheta \int_0^{s_1(x)} \mu_0 \frac{\partial u_0}{\partial s}\, ds - \int_0^{s_{2e}(\lambda)} \tau_w^s ds - \int_{s_{2w}}^{s_{2e}} [(\tau^s)_{n_0} - \tau_{w_0}]\, ds = \\ &-\cot\vartheta \int_0^{\xi_1(x)} \mu_0 \frac{\partial u_0}{\partial \xi} d\xi - \frac{1}{\sin\vartheta} \int_0^{\xi_2(\lambda)} \mu_w \left(\frac{\partial u}{\partial \eta}\right)_w d\xi \end{aligned} \tag{19}$$

$$\begin{aligned} \Theta = \int_0^{s_1} ds \int_0^{n_2} \bar{\rho}\bar{u}(1-\bar{u})\, dn &+ \int_{s_1}^{s_{2e}} ds \int_0^{n_e} \bar{\rho}\bar{u}(1-\bar{u}) dn - \int_{s_{2w}}^{s_{2e}} ds \int_0^{n_0} \bar{\rho}_0\bar{u}_0(1-\bar{u}_0)\, dn \\ = \int_0^{\xi_1(x)} d\xi \int_0^{\eta_2(\lambda)} (1/\bar{\rho})\bar{u}(1-\bar{u}) d\eta &+ \int_{\xi_1(x)}^{\xi_2(\lambda)} d\xi \int_0^{\eta_e(\xi,x)} (1/\bar{\rho})\bar{u}(1-\bar{u}) d\eta \end{aligned} \tag{20}$$

An expression analogous to (20), but with the integrand $(1/\bar{\rho})[(1/\bar{\rho}) - \bar{u}]$, can be written for Δ^*.

Specialization for Zero Streamwise Pressure Gradient

Up to this point, our discussion of the momentum integral equation, Eq. (9), has not been limited to constant-pressure flows. In fact the treatment of flows with streamwise pressure gradients, particularly those which would generate similar velocity profiles in the undisturbed regions, appears to be quite feasible (see reference 11). For zero heat transfer and $P = 1$ the Crocco integral, Eq. (5), would be employed; whereas the formation of an energy integral equation from Eq. (3) would be required for treating surface heat transfer and/or $P \neq 1$.

Hereafter, in this paper we shall deal only with constant-pressure flows (u_e and ρ_e constant). In this case the momentum integral equation analogous to (9), with the density transformation taken into account, assumes the form

$$\begin{aligned} \frac{\partial\Theta}{\partial x} - \frac{\partial}{\partial x}\left[\int_0^{\eta_1(x)} d\eta \int_0^{\xi_2(\lambda)} \frac{1}{\bar{\rho}}\, \bar{u}(1-\bar{u}_0) d\xi\right] - \int_0^{\eta_1(x)} d\eta \int_0^{\xi_2(\lambda)} \frac{1}{\bar{\rho}}\, \bar{u}\, \frac{\partial \bar{u}_0}{\partial x} d\xi = \left(\frac{\mu_e}{\rho_e u_e}\right) \frac{2}{\sin^2\vartheta} \times \\ \left[\cos\vartheta \int_0^{\xi_1(x)} \bar{u}_0 \frac{\partial \bar{u}_0}{\partial \xi}\, d\xi + \int_0^{\xi_2(\lambda)} \bar{u}_w \left(\frac{\partial \bar{u}}{\partial \eta}\right)_w d\xi\right] \end{aligned} \tag{21}$$

where Θ is given by Eq. (20).

Further restricting our attention to cases of $h_w =$ constant and $P = 1$, we rewrite the applicable Crocco relation, Eq. (6), as follows:

$$\bar{h} = \bar{h}_w + (1 - \bar{h}_w + c)\bar{u} - c\bar{u}^2 \qquad (22)$$

where $c = u_e^2/2h_e \approx (\gamma - 1)M_e^2/2$.

In addition the assumption is made that

$$1/\bar{\rho} \approx \bar{h} \qquad (23)$$

a relation which is strictly true only for constant specific heats, and it is assumed that

$$\bar{\rho}\bar{\mu} = 1 \qquad (24)$$

Assumed Velocity Profiles

On the basis of reasoning analogous to that employed for constant density in reference 1, symmetric velocity profiles are assumed in terms of ξ and η as follows:

$$\bar{u} = \bar{u}(g) \qquad (25)$$

where
$$g = \frac{\xi}{\xi_1(x)} \cdot \frac{\eta}{\eta_1(x)} \cdot \frac{1}{\varphi} \qquad (26)$$

$$\xi_1(x) = \eta_1(x) = \delta_0(x)/\sin\vartheta \qquad (27)$$

$$\xi_2(x) = \eta_2(x), \quad \varphi = \eta_2(x)/\eta_1(x) \qquad (28), (29)$$

For laminar flow, the transformed undisturbed boundary-layer thickness δ_0 has the following form:

$$\delta_0/x = (K/R_{ex})^{1/2} \qquad (30)$$

where K is on the order of 30 or 40. Its precise value depends upon the particular analysis or definition of the undisturbed boundary layer utilized.

At the solid surfaces we have $g = 0$, whereas at the outer edge of the boundary layer we may select $g = 1$, and thereby define the outer shape of the boundary layer as follows:

$$\eta_e/\eta_1(x) = \varphi\xi_1(x)/\xi \quad \text{or} \quad \xi_e/\xi_1(x) = \varphi\eta_1(x)/\eta \qquad (31)$$

for $\xi_1 < \xi < \xi_2$ and $\eta_1 < \eta < \eta_2$

For $\eta = \eta_2$ we have $g = \xi/\xi_1$, and for $\xi = \xi_2$ we have $g = \eta/\eta_1$, indicating the merging of the corner and undisturbed profiles.

If the velocity profiles at a station x are to be similar with respect to a single scale-length, say ξ_1, it is necessary that

$$\varphi = \text{constant} \qquad (32)$$

Specific functions $\bar{u}(g)$ may be selected to satisfy a number of boundary conditions. The following profiles are considered here for comparative purposes:

$$\bar{u} = 2g - g^2; \quad \bar{u}(0) = 0, \quad \bar{u}(1) = 1, \quad u'(1) = 2, \quad u'(1) = 0 \qquad (33)$$

$$\bar{u} = 2g - 2g^3 + g^4; \quad \bar{u}(0) = 0, \bar{u}(1) = 1, \quad u'(0) = 2, u'(1) = 0, u''(1) = 0 \qquad (34)$$

$$\bar{u} = 2g - 5g^4 + 6g^5 - 2g^6; \quad \bar{u}(0) = 0, \bar{u}(1) = 1, u'(0) = 2, u''(0) = 0, \quad u'(1) = 0, u''(1) = 0, u'''(1) = 0 \qquad (35)$$

Associated with each form of profile is a value of K [Eq. (30)] which can be obtained by a comparable integral method analysis of the undisturbed compressible boundary layer. Several values are given as follows:

Analysis		K
Integral method:	second-degree profile	30.0
Integral method:	fourth-degree profile	34.0
Integral method:	sixth-degree profile	36.6
Exact solution: Blasius profile (for $\bar{u} = 0.995$ at δ_0)		28.0

Solution of Integral Equation

The alternative substitution of Eqs. (33) and (34) into the integral equation (21) does not produce significant differences in the numerical coefficients which depend upon the profiles. However, appreciable differences in the values of φ obtained in the solution are found when the value of K consistent with a given profile is utilized to evaluate δ_0. That is, the results for φ are influenced more by the value of K used than by the functional form of the cited profiles.

In the present calculation only the fourth-degree profile is used to evaluate the integral equation (21), but K is permitted to remain in the resulting equations at first.

Substitution of Eq. (34) into Eq. (20) yields an expression for the momentum loss parameter:

$$\Theta/\xi_1^2(x) = (0.0667 + 0.0813\bar{h}_w + 0.0287c)\varphi(x) + (0.0671 + 0.0504\bar{h}_w + 0.0221c) \times \left\{\varphi(x)\ln\varphi(x) + 2\left[\varphi(\lambda)\frac{\xi_1(\lambda)}{\xi_1(x)} - \varphi(x)\right]\right\} \qquad (36)$$

The corresponding expression for the displacement parameter is

$$\Delta^*/\xi_1^2(x) = (0.4730\bar{h}_w^2 + 0.1480\bar{h}_w + 0.1568c\bar{h}_w + 0.07259c + 0.2704c^2)\varphi + (3.576 - 4.059\bar{h}_w + 5.440c)\varphi\ln\varphi + 2\left[\varphi(\lambda)\frac{\xi_1(\lambda)}{\xi_1(x)} - \varphi(x)\right](0.06709 + 2.238c^2 + 0.1007c\bar{h}_w + 0.1175\bar{h}_w + 0.1825\bar{h}_w^2) \qquad (37)$$

Likewise, the bracket on the right side of Eq. (21) yields:

$$(0.0900 + 0.9100\bar{h}_w + 0.1700c)\cos\vartheta - \bar{h}_w\varphi(x) + 2\bar{h}_w\varphi(\lambda)\frac{\xi_1(\lambda)}{\xi_1(x)} \qquad (38)$$

The contribution of the last two terms on the left side of Eq. (21) is $-\varphi(x)\xi_1^2(x)/(180x)$ and is negligible.

When Eqs. (36) and (38) are substituted into Eq. (21) it can be seen by inspection that a solution of the form $\varphi(x) = \varphi(\lambda) = \text{constant}$ can be obtained only if $\xi_1 \sim \sqrt{x}$, as will be the case when the undisturbed boundary layer corresponds to laminar flat-plate flow [Eqs. (27) and (30)]. Thus, assuming $\varphi = \text{constant}$ (independent of x) and $\xi_1 \sim \sqrt{x}$, the following solution is obtained from Eq. (21):

$$(K/2)[(0.0671 + 0.0504\bar{h}_w + 0.0221c)\ln\varphi + (0.0667 + 0.0813\bar{h}_w + 0.0287c)] = (0.0900 + 0.9100\bar{h}_w + 0.1700c)[\cos\vartheta^-/\varphi] + 3\bar{h}_w \qquad (39)$$

The solution for φ having been obtained, values of Θ and Δ^* may be determined by setting $x = \lambda$ in Eqs. (36) and (37), and thereafter treating x and λ as syn-

TABLE 1a

Values of φ for Fourth-Degree Polynomial With $K = \delta_0^2(u_e/\nu_e x) = 34.0$

c	$\sqrt{5c+1}$	$\bar{h}_w$ \ ϑ →	30°	60°	90°	120°	150°
0	0	1.0	1.645	1.470	1.274	1.000	1.000
		2.0	1.427	1.245	1.000		
0.4	1.41	1.0	1.524	1.363	1.150		
		1.4	1.446	1.276	1.020		
		2.8	1.331	1.110	1.000		
0.8	2.00	1.0	1.407	1.264	1.050		
		1.8	1.317	1.148	1.000		
		3.6	1.233	1.015	1.000		
1.6	2.83	1.0	1.252	1.108	1.000		
		2.6	1.190	1.017			
		5.2	1.155	1.000			
2.4	3.46	1.0	1.140	1.004	1.000		
		3.4	1.125	1.000			
		6.8	1.115	1.000			

$\varphi = n_w \sin\vartheta/\delta_0$

TABLE 1b

Values of φ for Sixth-Degree Polynomial With $K = \delta_0^2(u_e/\nu_e x) = 36.6$

K	c	$\bar{h}_w$ \ ϑ →	30°	60°	90°	120°	150°
36.6	0	1.0	1.500	1.352	1.144	1.000	1.000
		2.0	1.312	1.140	1.000		
	0.4	1.0	1.382	1.240	1.040		
		1.4	1.322	1.164	1.000		
		2.8	1.210	1.025	1.000		
	0.8	1.0	1.286	1.152	1.000		
		1.8	1.214	1.064			
		3.6	1.141	1.000			
	1.6	1.0	1.155	1.017	1.000		
		2.6	1.105	1.000			
		5.2	1.061	1.000			
	2.4	1.0	1.060	1.000	1.000		
		3.4	1.046				
		6.8	1.040				

$\varphi = n_w \sin\vartheta/\delta_0$

onymous. In interpreting the meaning of the values of Θ and Δ^*, it must be realized that the area of integration covered in their definition varies with the parameters ϑ, c, and $\bar{h}_w$, since this area covers only the portion of the flow presumed to be disturbed by the corner. It will be recalled that the integration limits have been specified explicitly in the transformed ξ, η plane and therefore must be determined a posteriori in the physical s, n plane. Key points, n_{2e} and n_{2w}, on the physical limit curves are given by the relatively simple expressions (18b) and (18c)

The integration areas A_p in the physical plane and A_t in the transformed plane are given at $x = \lambda$ as follows:

$$\frac{A_p}{\sin\vartheta} = \int_0^{s_1} ds \int_0^{n_2(s)} dn + \int_{s_1}^{s_{2e}} ds \int_0^{n_e(s)} dn - \int_{s_{1w}}^{s_{2e}} ds \int_0^{n_0(s)} dn$$

$$= \int_0^{\xi_1} d\xi \int_0^{\eta_2} (\bar{\rho})^{-2}\, d\eta + \int_{\xi_1}^{\xi_2} d\xi \int_0^{\eta_e(\xi)} (\bar{\rho})^{-2}\, d\eta \quad (40a)$$

$$\frac{A_t}{\sin\varphi} = \int_0^{\xi_1} d\xi \int_0^{\eta_2} d\eta + \int_{\xi_1}^{\xi_2} d\xi \int_0^{\eta_e(\xi)} d\eta = \xi_1^2\varphi(1 + \ln\varphi) \quad (40b)$$

Evaluation of Eq. (40a) for the representative case $\bar{h}_w = 1$ yields:

$$A_p/\xi_1^2\vartheta \sin\vartheta = 1 + \ln\varphi + 0.302c(1 + 0.0950c) \times \left[1 + 0.831\left(\frac{1 + 0.0880c}{1 + 0.0950c}\right)\ln\varphi\right] \quad (41)$$

Likewise, for $\bar{h}_w = 1$,

$$\Theta \sin\vartheta/\xi_1^2\,\varphi \sin\vartheta = 0.1480(1 + 0.1940c)(1 + 0.7941 \ln\varphi) \quad (42)$$

$$\Delta^* \sin\vartheta/\xi_1^2\varphi \sin\vartheta = 0.585(1 + 0.392c + 0.462c^2) \times \left[1 + \left(\frac{-0.826 + 9.30c}{1 + 0.392c + 0.462c^2}\right)\ln\varphi\right] \quad (43)$$

Division of (42) and (43) by (41) achieves normalization of the momentum and displacement areas with respect to the integration area. The resulting expressions for the "specific" momentum and displacement areas, $\Theta \sin\vartheta/A_p$ and $\Delta^* \sin\vartheta/A_p$, are functions of c and $\ln\varphi$. It will be seen from the results to be presented that the condition $\ln\varphi \ll 1$ holds for high Mach numbers for all corner angles, and for oblique corners on the order of 120° or higher at all Mach numbers. For this simplified case the specific momentum and displacement areas are functions of c alone. These are shown in Fig. 6, to be discussed later.

In the undisturbed two-dimensional constant-pressure boundary layer, the following expressions for the displacement thickness δ_0^* and momentum thickness ϑ_0^* may be used for $\bar{h}_w = 1$:

$$\delta_0^*/\delta_{0P} = 0.300(1 + 0.391c)/(1 + 0.126c) \quad (44a)$$

$$\vartheta_0^*/\delta_{0P} = 0.126/(1 + 0.126c) \quad (44b)$$

where an estimate for the undisturbed boundary-layer thickness is given by the following relation for $\bar{h}_w$ constant:

$$\delta_{0P}/\delta_0 = n_1/\eta_1 = 1 + 0.33(\bar{h}_w - 1) + 0.126c \quad (45a)$$

where

$$(\delta_0/x)R_{ex}^{1/2} = 5.3 \quad (45b)$$

For comparison, the effects of Mach number on the two-dimensional momentum and displacement thicknesses are also shown in Fig. 6.

By using (45a) for $\bar{h}_w$ constant, the following expression is obtained from (18):

$$n_{2e}/n_{2w} = [1 + 0.33(\bar{h}_w - 1) + 0.126c]/\bar{h}_w \quad (46)$$

The surface shear stress and heat flux at a station $x = \lambda$ are given by the following relation for constant $\bar{h}_w$:

$$\tau_w/\tau_{0w} = 2q_w/q_{0w} = \eta_w/\eta_2 = n_w/n_{2w} \quad (47)$$

Finally, we can derive the following relation for the physical boundary-layer thickness r_{eP} in the symmetry plane:

$$r_{eP}/\delta_{0P} = \sqrt{\varphi}/\sin(\vartheta/2) \quad (48)$$

(III) Results

Values of φ, with which the remaining flow properties can be evaluated, have been computed from the solution expressed by Eq. (39). They are listed in Table 1 for the following variety of conditions:

$$0 \leq c \leq 2.4, \text{ or approximately, } 0 \leq M_e \leq 3.48$$

$$\bar{h}_w = \begin{cases} 1, & \text{surface cooling} \\ 1 + c, & \text{insulated surface for } Pr = 1 \\ 2(1 + c), & \text{surface heating} \end{cases}$$

$$30^\circ \leq \vartheta \leq 150^\circ$$

$$K = \begin{cases} 34.0, & \text{fourth-degree polynomial} \\ 36.6, & \text{sixth-degree polynomial} \end{cases}$$

Table 2 gives the corresponding values of the momentum loss parameter $(\Theta R_{ex} \sin^2 \vartheta)/x^2$ and displacement parameter $(\Delta^* R_{ex} \sin^2 \vartheta)/x^2$, obtained by setting $x = \lambda$ in Eqs. (36) and (37) and, for $\bar{h}_w = 1$, the integration area $(A_p R_{ex} \sin \vartheta)/x^2$ obtained from Eq. (41).

The Case of Constant Density

For the special case of constant density and $\bar{h}_w = 1$, it is of interest to compare some of the present results with those of other analyses. Fig. 2 shows values of φ versus corner angle ϑ obtained from Eq. (39) for values of $K = 36.6$, 34.0, and 30.0, which correspond to sixth-, fourth-, and second-degree polynomials, respectively. These are compared with the results obtained by Loitsianskii and Bolshakov[1] with sixth- and second-degree profiles, but without the use of oblique coordinates, as mentioned previously. The qualitative agreement is good and the quantitative agreement fair.

The difference in the coordinate systems vanishes for $\vartheta = 90^\circ$; for this case the sixth-degree and second-degree values of the present analysis should coincide with those of reference 1. The differences which appear in Fig. 2 for $\vartheta = 90^\circ$ are due to the use of the fourth-degree polynomial in evaluating the coefficients in Eq. (39). Consistent use of the appropriate profiles in deriving Eq. (39) would lead to better agreement between the two analyses in the range $60^\circ < \vartheta < 120^\circ$. For larger and smaller corner angles the influence of the difference in the coordinate systems becomes more pronounced. Remaining differences in the values of φ obtained with different profiles are clearly due to the different values of K. A value of φ for $\vartheta = 90^\circ$ has been estimated from Carrier's results[2] considering the isovel $\bar{u} = 0.999$, and is shown in Fig. 2. It agrees with the present $K = 36.6$ value.

It is of particular interest to compare values and trends obtained by the present and other methods when the influence of the different representations of the *undisturbed* portions of the flow, implied for example by different values of K, are eliminated by normalization. This can be done by considering the velocity distributions in the plane of symmetry obtained in the present analysis, and those of Levy[3] and Cheng and Levy[9] obtained by a more complex solution of the Navier-Stokes equations.

At a given value of x, the distance along the symmetry axis measured from the apex is denoted as r, while r_e denotes the value of r at the outer edge of the viscous layer and corresponds to a coordinate value ξ_e. On this axis we have $\xi = \eta$ and the following relations hold in the present analysis (no distinction is made between physical and transformed coordinates in the constant-density case):

$$r(u_e/\nu_e x)^{1/2} = \sqrt{K}\,(\xi/\xi_1) \sin(\vartheta/2)$$

$$\xi_e/\xi_1 = \sqrt{\varphi}$$

$$r_e(u_e/\nu_e x)^{1/2} = \sqrt{K\varphi}/\sin(\vartheta/2)$$

$$g = (r/r_e)^2$$

Thus the present centerline profiles $\bar{u}(g)$ can be expressed as functions of r/r_e alone, and are independent of corner angle. The fourth- and sixth-degree profiles are shown in Fig. 3. Analogous profiles taken from the plots of reference 9 for $\vartheta = 60^\circ$, 90°, and 120°,

TABLE 2

Momentum Area, Displacement Area, and Disturbed Corner-Flow Area for $K = 34.0$
(NOTE: Values obtained with $K = 36.6$ differed at most by 10 per cent from those given here.)

			30°			60°			90°			120° and 150°		
$\sqrt{2}\xi/\xi_1 = H_e$	c	$\bar{h}_w$	$\frac{\Theta R_{ex}\sin^2\vartheta}{x^2}$	$\frac{\Delta^* R_{ex}\sin^2\vartheta}{x^2}$	$\frac{A_p R_{ex}\sin\vartheta}{x^2}$									
			(a)	(b)	(c)	(a)	(b)	(c)	(a)	(b)	(c)	(a)	(b)	(c)
0	0	1.0	11.55	19.21	83.74	9.30	19.95	65.23	7.64	20.28	53.80	5.03	19.89	34.00
		2.0	14.14	20.84		11.33	44.41		7.79	69.50		7.80	69.50	
1.41	0.4	1.0	11.21	95.50	84.07	9.19	76.34	67.68	6.53	53.16	50.04	5.42	35.18	35.36
		1.4	12.29	50.59		9.67	70.73		6.76	56.00		6.53	54.86	
		2.8	16.26	132.2		12.40	147.2		10.40	152.6		10.40	152.6	
2.00	0.8	1.0	10.36	108.3	79.89	8.71	79.50	66.57	6.34	36.84	47.10	5.81	32.07	42.84
		1.8	12.73	103.4		10.16	86.73		8.02	72.68		8.02	72.68	
		3.6	18.36	229.2		13.33	233.6		13.00	233.5		13.00	233.5	
2.83	1.6	1.0	9.71	149.3	80.16	7.90	94.28	64.34	6.59	56.44	52.92	6.59	56.44	52.92
		2.6	14.75	206.4		11.34	167.0		11.02	163.2		11.02	163.2	
		5.2	22.96	526.3		18.20	498.9		18.20	498.9		18.20	498.9	
3.46	2.4	1.0	9.27	169.9	83.05	7.43	94.88	64.79	7.37	93.02	64.26	7.37	93.02	64.26
		3.4	17.07	340.7		14.01	291.53		14.01	291.5		14.01	291.5	
		6.8	26.00	920.1		23.40	865.8		23.40	865.8		23.40	865.8	

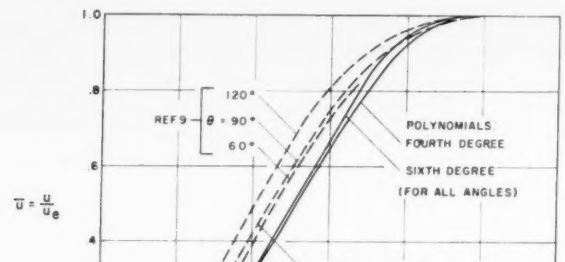

FIG. 3. Centerline velocity profiles compared with constant-density values of Levy-Cheng[9] and Carrier.[2]

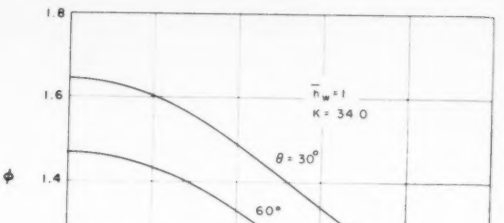

FIG. 5b. Representative values of φ versus M_e for various corner angles.

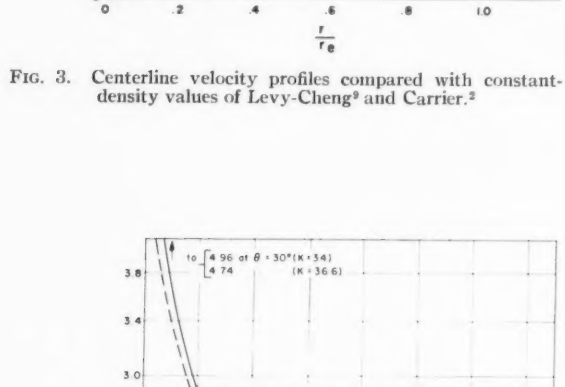
to [4.96 at θ = 30° (K = 34)
4.74 (K = 36.6)
integral method – present theory
4th degree profile (K = 34.0)
6th degree profile (K = 36.6)
C = 0
h̄_w = 1
ESTIMATED
FROM REF 9
√φ / sin θ/2 = r_e/δ_0
θ

FIG. 4. Normalized boundary-layer thickness in median plane versus corner angle for constant density.

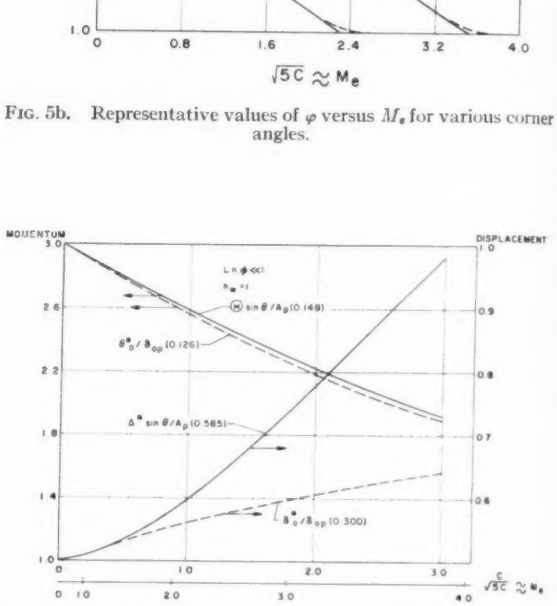

FIG. 6. Effect of Mach number on momentum and displacement parameters and comparison with two-dimensional values.

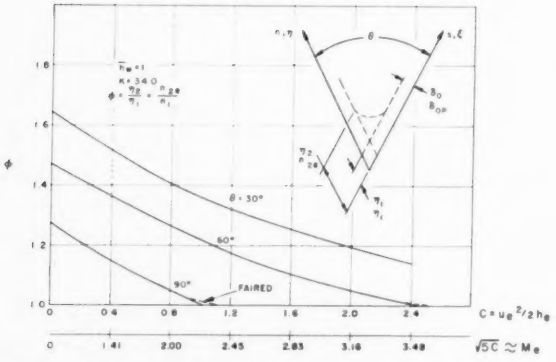

FIG. 5a. Representative values of φ versus c for various corner angles.

CURVE ①: $\bar{h}_w = 1$, parameter $\left[\frac{n_2(S,\lambda)}{\eta_2(\lambda)} - 1\right] \Big/ (0.126)C$

CURVE ②: $\bar{h}_w = 1 + C$, paramter $\left[\frac{n_2(S,\lambda)}{\eta_2(\lambda)} - 1\right] \Big/ C$

NOTE: $\eta_2(\lambda) = \phi\,\eta_1(\lambda) = \phi\,\delta_0/\sin\theta$

$$S/S_1 = \left[\int_0^{\xi/\xi_1} \bar{h}_0\, d(\xi/\xi_1)\right] \Big/ \left[\int_0^{1} \bar{h}_0\, d(\xi/\xi_1)\right]$$

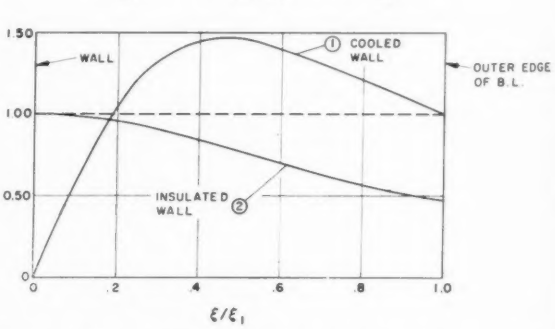

FIG. 7. Shape of curves at which corner and undisturbed boundary layers join.

which indicate the outer edge values $r_e(u_e/\nu_e x)^{1/2} = 10.5$, 7.6, and 6.3, shown with rather large differences in reference 9, are seen to be correlated quite closely in terms of r/r_e although they exhibit minor differences due to ϑ. Values estimated from Carrier's relaxation solution of the boundary-layer equations for $\vartheta = 90°$ fall somewhat lower and closer to the present solution than do those of reference 9 for $\vartheta = 90°$.

The major variations due to corner angle are due to changes in r_e with ϑ. This is shown in Fig. 4, which gives values of r_e/δ_0 versus for the present fourth- and sixth-degree polynomials, and values estimated from the 60°, 90°, and 120° cases of reference 9 with $\delta_0(u_e/\nu_e x)^{1/2} = 5.3$, corresponding to an undisturbed Blasius velocity ratio $\bar{u} = 0.995$. The present values are in excellent qualitative agreement and reasonable quantitative agreement with those of Levy and of Cheng and Levy. Evidently it is possible to extrapolate the curves to the value $r_e/\delta_0 = 1$ at $\vartheta = 180°$.

Oman[11] treated the constant-pressure 90° case by an integral method with more elaborate profiles of asymptotic nature in the form of a product of identical functions of the coordinates ξ and η. He obtained excellent agreement with the velocity profiles of Carrier. It is of interest to examine the implication of a profile-assumption of this type with respect to the velocity distributions in the symmetry plane.

For this purpose, assume

$$\bar{u} = F(\xi/\xi_\delta)\ F(\eta/\eta_\delta)$$

where $F = F(\zeta)$ is the Blasius function, for example, and $\zeta = \eta_B/5.3$ is the normalized Blasius variable. Now for

$\xi < \xi_1$: $\eta_\delta = \eta_2$, a constant
$\xi_1 < \xi < \xi_2$: $\eta_\delta = \eta_e(\xi)$, a curve defining the outer edge of the viscous layer
$\xi > \xi_2$: $\eta_\delta = \eta_1$, a constant

where analogous definitions hold for η. If we *assume* a boundary-layer edge shape $\eta_e = \xi_2\eta_1/\eta$, for example, it can be shown that on the centerline

$$\bar{u} = F[(r/r_e)(1/\sqrt{\varphi})]^2, \quad 0 < r/r_e < 1/\sqrt{\varphi}$$

$$\bar{u} = F[(r/r_e)^2]^2, \quad 1/\sqrt{\varphi} < r/r_e < 1$$

Furthermore, to avoid a full solution, if we assume that values of $\sqrt{\varphi} = (r_e/\delta_0)\sin(\vartheta/2)$ can be estimated from the results of reference 9, taken from Fig. 4 here, we obtain velocity distributions close to those of Levy and Cheng-Levy (Fig. 3) and the secondary variation due to ϑ exhibited by their results.

On the basis of the above comparisons of constant-density flow properties, the present theory can be expected to yield at least the proper qualitative and relative effects of compressibility.

Compressible Flow

Fig. 5 shows values of φ versus c and $\sqrt{5c} \approx M_e$ for the representative cases $\bar{h}_w = 1$, $\vartheta = 30°$, 60°, and 90°, calculated with $K = 34.0$. In this approximate theory φ is 1.0 for $\vartheta \gtrsim 120°$. For the insulated and heated, surfaces the trends are the same, however, the values of φ are closer to 1.0 at higher surface temperatures, as shown in Table 1. Fig. 5b shows the slow initial decrease in φ at subsonic speeds, and the more abrupt decrease at higher Mach numbers. This trend of φ to unity is analogous to the effect of increasing the corner angle in constant-density flow.

Although the present approximate theory does not predict the asymptotic approach to unity which would be expected on physical grounds, this is not believed to be a serious shortcoming. Thus, φ is seen to reach 1.0 at distinct values of c. The Mach numbers corresponding to $\varphi = 1.0$ when $\bar{h}_w = 1$ are about 3.5 for $\vartheta = 60°$ and 2.1 for $\vartheta = 90°$, decreasing with increasing ϑ.

The approach of φ to 1.0 indicates the increasingly sharp junction of the outermost isovels of u at the symmetry plane. The depth to which this trend persists depends upon the surface heat-transfer conditions. This may be seen by considering the nature of the corner-interference limit curve in terms of physical coordinates as typified by the ratio n_{2w}/n_{2e} [see Eq. (46)]. For a fixed $\bar{h}_w$ this ratio decreases with increasing c, indicating that, at the surface, the undisturbed shear stress τ_{w0} persists to positions closer to the apex as c increases. For example, at $c = 3$, for $\bar{h}_w = 1$, $n_{2w}/n_{2e} = 0.725$. On the other hand, for an insulated surface,

$$n_{2w}/n_{2e} = (1 + c)/(1 + 0.46c)$$

This ratio increases from unity at $c = 0$ and is 1.68 at $c = 3.0$, indicating a spreading of the corner influence in the region near the wall due to the dependence of $\bar{h}_w$ on c.

At some points within the boundary layer the average density may be lower—i.e., the average enthalpy may be higher than along the surface or in the undisturbed boundary layer along the matching line. Therefore intermediate points on the matching line $n_2(s, \lambda)$ may be greater than either n_{2e} or n_{2w}.

Representative values of parameters n_2 for the cases $\bar{h}_w = 1$ and $1 + c$ are shown in Fig. 7. The abscissa of Fig. 7 is not expressed in terms of physical scale, whereas the ordinate is. The curves shown are independent of Mach number. The values at $\xi/\xi_1 = 0$ and 1.0 correspond to n_{2w} and n_{2e}, respectively. As the ordinate parameters show, the effect of raising c is to magnify the ordinate affinely. Therefore, after φ has approached unity in the cooled-wall case, the point $n_{2e} = n_1$ moves further from n_{2w} and from the apex, owing to the enlargement of the undisturbed boundary layer. However, aside from the effect of the fixed surface temperature, there is no additional interior confinement of the disturbed flow at higher Mach numbers. In fact, with increasing c there is a moderate increase in the ratio $n_2(s, \lambda)/n_{2e}$ which ultimately approaches a limiting value. Similar effects hold for any fixed surface temperature.

In the insulated case, after φ has approached unity,

the corner influence expands relative to n_{2e} even at the wall, as previously noted.

Although values of the momentum area, displacement area, and integration area are listed in Table 2, interesting trends are observed from Fig. 6 for the simplified cases in which $\ln \varphi \ll 1$ and $\bar{h}_w = 1$. It is seen from Table 1 that the condition $\ln \varphi \ll 1$ applies at sufficiently high Mach numbers at all the corner angles taken into account here, and at all Mach numbers for sufficiently oblique angles. In Fig. 6 the "specific" quantities, momentum loss per unit area and displacement per unit area, are plotted to show the effect of increasing c or M_e. For comparison, the analogous two-dimensional quantities are shown. The corner and two-dimensional momentum parameters show virtually the same decrease with c. However, the corner-displacement parameter indicates a greater dilation of the streamtubes than is shown by the two-dimensional values. The merging of displacement parameters at the lower Mach numbers indicates that, for the more oblique angles, the displacement effect is essentially two-dimensional.

It is noted that the surface shear stress τ_w and heat transfer q_w go to zero at the apex of the corner. This behavior does not appear to be influenced by the corner angle within the range of angles covered by this analysis. It may be conjectured that this approach to zero will persist for angles $\vartheta \leq 180°$. In this case a transition must be made to the simple flat plate results, which yield nonzero shear (or heat flux) everywhere for $\vartheta = 180°$. The details of this transition are outside the scope of the present paper. We may simply observe here that this type of situation is common in potential problems. For example, in classical inviscid hydrodynamics a stagnation point must exist at the discontinuous junction of two surfaces, regardless of the closeness of the junction angle to 180°. However, for a perfectly smooth surface the stagnation point must vanish.

It is seen from Eq. (47) that, for constant $\bar{h}_w$, the surface shear and heat flux vary linearly with distance from the apex, being zero at $n = 0$ and increasing to the undisturbed two-dimensional values at $n = n_{2w}$. This type of variation leads to the result that the friction drag of the disturbed surface area is one half the drag due to undisturbed shear over an equal area, while the heat flux through the disturbed surface area in one fourth the undisturbed heat flux over an equal area.

From Eq. (48) it is seen that the boundary-layer thickness in the symmetry plane varies as $\sqrt{\varphi}$ for a given corner angle. Therefore, the trends for this parameter are roughly like those for φ shown in Fig. 5.

It is recalled that the flows are similar in cross planes.

It should be noted that the present choice of a curve $\eta_e = \eta_2\xi_1/\xi$ to represent the outer edge of the merger region would not permit the detection of a thinning of the merger region with respect to the undisturbed boundary layer. This can be seen by considering the nature of the outer edge in physical coordinates. For this purpose it can be shown that $n_e/n_1 = \xi_2/\xi > 1$. That is, the outer edge curve will not dip below the undisturbed boundary-layer thickness according to the present assumption. This assumption appears reasonable, but nevertheless is arbitrary and deserves further study. The isovels calculated by Krzywoblocki[10] for insulated surfaces at Mach 2 do not indicate the occurrence of dipping for $\bar{u} \leq 0.8$, although it might be expected to arise under the cited conditions. Thus, the present assumption is in agreement with Krzywoblocki's result.

Remark on Turbulent Flow

An integral method treatment of constant-density turbulent corner flow has been given by Loitsianskii and Bolshakov,[1] who assumed $\bar{u} = g^{1/7}$ and that the surface shear can be related to the boundary-layer thickness by a well-known relation for turbulent shear. The results for $\varphi(\vartheta)$ are almost identical to those obtained for laminar flow with a sixth-degree profile. It would be interesting to investigate the applicability of this correspondence at high speeds as well.

(IV) Conclusions

(1) Equations are presented for treating compressible laminar flow in a symmetric corner with varying angles and with streamwise pressure gradient, by a boundary-layer integral method. The integral equations also are applicable in turbulent flow.

(2) Results are obtained for the case of constant pressure, constant corner angle, and isothermal surfaces. Simplifying assumptions limit the corner angle range to about 60° to 120°, although the general nature of the results is expected to hold for larger and smaller angles as well.

(3) As the Mach number increases, the approach of φ to unity indicates the increasingly sharp merger of the outermost isovels of streamwise velocity. That is, the corner effect on the streamwise velocity at the outer region of the boundary layer becomes increasingly confined to the neighborhood of the median plane. For example, within the present approximations, the outermost isovels join sharply at about Mach 3.5 for $\vartheta = 60°$, Mach 2.2 for $\vartheta = 90°$, and Mach zero for $\vartheta = 120°$ when $h_w = h_e$. The effect becomes more pronounced for adiabatic or heated surfaces.

(4) After φ has approached unity, at intermediate depths within the boundary layer the region affected by corner merging, measured relative to the undisturbed boundary-layer thickness, expands with increasing Mach number. For a fixed wall temperature, the relative growth reaches a limiting value; for insulated surfaces, the growth continues. Near the surface, for a fixed surface temperature, the extent of the disturbed region does not vary after φ has approached unity, whereas for insulated surfaces it continues to expand.

(5) The surface shear stress and heat flux, related by Reynolds analogy in the disturbed region, increase linearly (in this approximation) from zero at the apex

to their undisturbed two-dimensional values. The drag of the surface area disturbed by the merging is one half the drag due to two-dimensional shear over the same area. The total heat flux over this area is one fourth the two-dimensional heat flux over an equal area.

(6) Values of momentum area, displacement area, and integration area are given. However, for the special conditions in which φ is approximately unity (i.e., high Mach numbers or wide corner angles), the "specific" momentum area decreases with increasing Mach number in virtually the same manner as the ratio of two-dimensional momentum thickness to boundary-layer thickness. However, the analogous displacement parameter, which is a measure of stream-tube dilation, increases more rapidly with Mach number than its two-dimensional counterpart.

(7) A comparison of results of the integral method with those obtained for constant density by more complex calculations indicates reasonable agreement with regard to properties such as boundary-layer thicknesses and velocity profiles in the median plane, normalized with respect to two-dimensional values.

References

[1] Loitsianskii, L. G., and Bolshakov, V. P., *On Motion of Fluid in Boundary Layer Near Line of Intersection of Two Planes*, NACA TM 1308 (Translation), 1936.

[2] Carrier, G., *The Boundary Layer in a Corner*, Quarterly of Applied Mathematics, Vol. IV, No. 4, p. 367, January, 1947.

[3] Levy, R., *The Boundary Layer in a Corner*, Ph.D. Thesis, Princeton University, Contract No. AF 49(638)-465, January, 1959.

[4] Dowdell, R., *Corner Boundary Layer*, M.Sc. Thesis, Brown University, Division of Engineering, May, 1952.

[5] Kemp, N., *The Laminar Three-Dimensional Boundary Layer, and a Study of the Flow Past a Side Edge*, M.Ae.S. Thesis, Cornell University, Graduate School of Aeronautical Engineering, ASTIA AD 45462, June, 1951.

[6] Sowerby, L., and Cooke, J., *The Flow of Fluid Along Corners and Edges*, Quarterly Journal of Mechanics and Applied Mathematics, Vol. 6, Part 1, p. 50, 1953.

[7] Gersten, K., *Corner Interference Effects*, DFL-Bericht Nr. 108, Braunschweig (Germany), 1959.

[8] Stainback, P. C., *An Experimental Investigation at a Mach Number of 4.95 of Flow in the Vicinity of a 90° Interior Corner Aligned With the Free-Stream Velocity*, NASA TN D-184, February, 1960.

[9] Cheng, S-I., and Levy, R. H., *The Boundary Layer in a Corner*, Princeton University, AFOSR TN 59-1165, November, 1959.

[10] Krzywoblocki, M. Z. *On the Boundary Layer in a Corner by Use of the Relaxation Method*, University of Illinois. Ganita (India). Vol. VII, No. 2, December, 1956.

[11] Oman, R. A., *The Three-Dimensional Laminar Boundary Layer Along a Corner*, D.Sc. Thesis, Massachusetts Institute of Technology, Dept. of Mechanical Engineering, Army OOR Contract DA-19-020-ORD-4538, January, 1959.

[12] Irvine, T. F., and Eckert, E. R. G., *Laminar Skin Friction and Heat Transfer on Flat Plates with Wedge-Shaped Grooves in Flow Direction*, ASME Paper 59-A-143, November-December, 1959.

Rolling Aircraft (*Continued from page 140*)

curacy can come both from the inclusion of terms neglected in Eq. (59) and from a better choice of coordinates. For instance, a reasonable set of coordinates to choose would be typical amplitudes found in a standard flexible-aircraft stability analysis where roll is neglected. Since the motion in this case is always damped we cannot speak of *normal* modes associated with these typical amplitudes. There are, nevertheless, mode shapes and damping factors which can be determined.

Reference

[1] Phillips W. H., *Effect of Steady Rolling on Longitudinal and Directional Stability*, NACA TN 1627, 1948.

✦ ✦ ✦

Plasma Flow (*Continued from page 144*)

The Coulomb drag for the specific thin conductor treated here with its fore and aft symmetry was found to be zero. The fluid drag corresponded to the neutral-particle continuum value of Ackeret at the plasma Mach number, and was independent of the charge on the body.

The above general behavior of the plasma flow over a conductor can be expected also in axisymmetric and three-dimensional cases. The detailed behavior of the electrostatic potential within the Debye layer can be expected to be locally similar in the different cases, but the hyperbolic ion flow would, of course, depend on the dimensionality of the problem.

References

[1] Kraus, L., and Watson, K., *Plasma Motion Induced by Satellites in the Ionosphere*, Convair Report ZPh-016, March, 1958.

[2] Kraus, L., and Yoshihara, H., *Electrogasdynamic Motion of a Charged Body in a Plasma*, Journal of the Aerospace Sciences, Vol. 27, No. 3, pp. 229–233, March, 1960.

[3] Chapman, S., and Cowling, T. G., *The Mathematical Theory of Nonuniform Gases*, pp. 77–81, Cambridge University Press, London, 1952.

[4] Spitzer, L., *Physics of Fully Ionized Gases*, p. 62; Interscience Publishers, New York, 1956.

✦ ✦ ✦

Supersonic Boom (*Continued from page 118*)

References

[1] Whitham, G. B., *The Flow Pattern of a Supersonic Projectile*, Com. on Pure and Appl. Math., p. 301, 1952.

[2] Sears, W. R., *General Theory of High Speed Aerodynamics*, in *High Speed Aerodynamics and Jet Propulsion*, Vol. VI, p. 239, Princeton Univ. Press, Princeton, N. J., 1954.

[3] Lighthill, M. J., *Supersonic Flow Past Bodies of Revolution*, ARC Reports and Memoranda No. 2003, 1945.

[4] Sears, W. R., *On Projectiles of Minimum Wave Drag*, Quart. Appl. Math., Vol. 14, p. 361, 1947.

[5] Haack, W., *Geschossformen kleinsten Wellenwiderstandes*, Lilienthal-Gesellschaft, Bericht 139, 1941.

Readers' Forum

BRIEF REPORTS of investigations in the aerospace sciences and discussions of papers published in the JOURNAL are presented in this special department. Entries must be restricted to a maximum of 1,300 words or the equivalent of one JOURNAL page including formulas and illustrations. Publication is completed as soon as possible after receipt of the material. The Editorial Committee does not hold itself responsible for the opinions expressed by the correspondents.

Contents

A Comment on "Radiation From Hot Air and Its Effect on Stagnation-Point Heating" ..... R. GOULARD 158

Derivation of Meyer's Inlet Criteria for Real-Gas Flows ..... C. W. HARTSELL AND W. HAYS 159

An Estimate of the Minimum Reynolds Number for Transition From Laminar to Turbulent Flow by Means of Energy Considerations ..... NEAL TETERVIN 160

A Method of Four-Point Interpolation Especially Adapted for Treating End Conditions of Wings and Other Elastic Surfaces ..... JAMES A. GRIFFIN, JR. 161

Rational Approximations Formed From Chester's Series for the Body Behind a Given Axially Symmetric Bow Shock Wave ..... A. H. VAN TUYL 162

Comment on "Inviscid Hypersonic Flow Over Unyawed Circular Cones" ..... S. A. POWERS 163

Additional Comment ..... HAIM KENNET AND SAINSBURY L. STRACK 163

Author's Reply ..... LEMBIT POTTSEPP 163

Comment on "Influence of Shock-Wave Attenuation by Boundary-Layer Growth on Contact-Surface Motion in a Shock Tube" ..... CHUL PARK 164

Author's Reply and Erratum ..... JAN ROSCISZEWSKI 164

On the Calculation of Natural Modes of Free-Free Structures ..... JOHN DUGUNDJI 164

A Note on Laminar Boundary-Layer Skin Friction Under the Influence of Foreign-Gas Injection ..... C. R. FAULDERS 166

On the Inclusion of Engine Effects in a Flutter Analysis ..... W. P. RODDEN AND R. S. ALBERT 167

Hypersonic Flow Around Bodies of Revolution ..... JAN ROSCISZEWSKI 168

Local Normal-Force Ratio Around an Expansion Corner ..... JOSEPH L. SIMS AND LEE M. SAUNDERS 170

On the Lift, Drag, and Moment on a Ring Concentric to a Cylindrical Body in Supersonic Flow ..... F. EDWARD EHLERS 170

A Note on the Canonical Form of the Thrust-Programming Problem for Power-Limited Flight ..... CHARLES SALTZER 172

Effect of Deceleration on Pressure Distribution Along a Slender Cone in Supersonic, Transonic, and Subsonic Flight ..... C. T. HSU AND D. A. ANDERSON 173

Shock Response to Downstream Disturbances ..... ROY M. GUNDERSEN 174

Comments on "Space Vehicle Environment" ..... KENNETH L. GOLDMAN 176

A Comment on "Radiation From Hot Air and Its Effect on Stagnation-Point Heating"

R. Goulard

Bendix Products Division, Advanced Development Laboratories, Chicago, Ill.

July 7, 1960

In a paper in this issue of the Aerospace Sciences,[1] the relative importance of radiation and convection energy transfer is discussed in the case of stagnation flow at hypersonic speeds. Air emissivities are obtained from convenient tables,[2] and radiation fluxes are illustrated for a wide range of altitude and velocities. It is shown that convection dominates in ballistic trajectories and that radiation does in planetary probes, as has also been previously established.[3] Finally, the validity of the physical model used (an adiabatic, optically thin shock layer in chemical equilibrium) is discussed at some length.

The purpose of this note is to define more accurately one of the limitations discussed,[1] on the basis of existing work.

Radiation Energy Losses in the Shock Layer

As correctly pointed out,[1] the assumption of a near-isothermal adiabatic shock layer loses its validity whenever the radiation level is comparable with the energy content of the flow. This is because the loss of radiated energy from the particles in their motion past the body reduces their stored energy and, consequently, their temperature. Since the radiated energy is itself a strong function of the temperature, it then gradually decreases downstream of the shock. As a result, the total radiation flux q_R from the shock layer is less than calculated assuming a constant stagnation temperature throughout. Furthermore, the inviscid flow near the wall being cooler, the

Contributors Please Note

Readers' Forum items must be confined to the equivalent of one page in the *Journal*. Contributions that exceed this limit will be returned to the authors for condensation and rewrite. To avoid inconvenience and delay, please adhere to the following specifications:

(1) Five, double-spaced, typewritten, manuscript pages (8½ by 11 in.), including wide margins, formulas, and headings, equal one printed page.

(2) For every illustration, deduct at least one-half or as much as one manuscript page, depending on the size of the illustration.

energy convected to the wall across the thin boundary layer is also reduced.

This coupling between radiation and convection in the shock layer has been analyzed.[4] It is shown in reference (4) that the ratio of the actual radiation flux q_R to that obtained on the basis of a uniform stagnation temperature $q_R{}^0$ is, in first approximation

$$\bar{q}_R = q_R/q_R{}^0 = 1 - \alpha\Gamma$$

where α is an optical parameter of order 10 for air, and Γ is the nondimensional ratio of the energy $q_R{}^0$ to the stored energy E of the flow. It can be concluded that a value of $\Gamma = (1/\alpha) \cong 10^{-1}$ will characterize an important deviation from the result of Eq. (1). This condition is therefore more stringent than the requirement $\Gamma < 1$ put forward in (1). It is seen on Fig. 1, extracted from reference (4), that the condition $\Gamma < 10^{-1}$ corresponds to velocities below 35 kft./sec., only.

Note that the parameter Γ also plays an important role in star turbulence[5] and gasdynamics of radiant media in general.[6] Similarly, the possibility of self-absorption mentioned in reference (1) is usually characterized by such concepts as optical thickness[5] and penetration length.[7]

References

[1] Kivel, B., *Radiation From Hot Air and Its Effect on Stagnation-Point Heating*, Journal of the Aerospace Sciences, Vol. 28, No. 2, pp. 96–102, February, 1961.

[2] Kivel, B., and Bailey, K., *Tables of Radiation from High Temperature Air*, Avco-Everett Research Laboratory, Res. Rept. 21, December, 1957.

[3] Meyerott, R. E., *Radiation Heat Transfer to Hypersonic Vehicles*, Third AGARD Combustion and Propulsion Panel Colloquium, Palermo, Sicily, March 17–21, 1958.

[4] Goulard, R., *The Coupling of Radiation and Convection in Detached Shock Layers*, Bendix Products Division, Advanced Development Laboratories, Res. Note 23, December, 1960.

[5] Unsöld, A., *Physik der Sternatmosphären*, Springer Verlag, 1955.

[6] Adrianov, V. N., and Shorin, S. N., *Radiant Energy Transfer From the Flow of Radiative Media*, Izvestia Akademii Nauk SSSR, Otdelenie Tehnitcheskih Nauk, Vol. 5, p. 46, 1958. (Translation available from Purdue University, School of Aeronautical Engineering.)

[7] Goulard, R. and M., *One Dimensional Energy Transfer in Radiant Media*, International J. Heat and Mass Transfer, July, 1960.

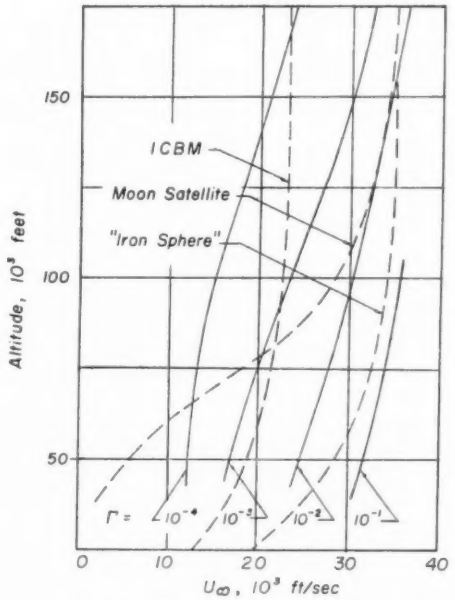

FIG. 1. Curves of constant ratio $\Gamma = q_R{}^{(0)}/E$ for a hemispheric nose (R = 1 ft.) shock layer.

Derivation of Meyer's Inlet Criteria for Real-Gas Flows†

C. W. Hartsell and W. Hays

Technical Staff, Space Technology Laboratories, Inc., Los Angeles, and Astro Division, The Marquardt Corporation, Van Nuys, Calif., Respectively

July 11, 1960

Symbols

A = area
h = enthalpy
P = pressure
R = universal gas constant
T = temperature
u = velocity
ρ = density
mw = molecular weight

Subscripts

0 = reference conditions
2, ∞ = stations, see Fig. 1
R = centerbody projected area

Superscripts

$-$ = average value—i.e., $\bar{P} = \int P dA_R/A_R$

THE ANALYSIS of Meyer[1] is of fundamental importance in the study of supersonic inlet performance. This note presents an extension of Meyer's analysis to handle real-gas flows. An equation is derived in a form which is useful for numerical computations.

A schematic of the configuration to be analyzed is shown in Fig. 1. The control volume of ABCDEFA is to be considered. The momentum theorem for steady-state operation, inviscid fluid and uniform flow at station (2) may be written as follows:

$$\int_\infty^2 \rho u^2\, dA = -\int_\infty^2 P\, dA \tag{1}$$

$$\rho u^2 A)_2 - \rho u^2 A)_\infty = -\int_\infty^2 P\, dA \tag{2}$$

If we restrict our interest to the forces in the axial direction

$$-\int_\infty^2 P dA = P_\infty A_\infty - \bar{P}A_R - P_2 A_2 \tag{3}$$

where $\bar{P}$ is the average pressure over the spike surface and A_R is the centerbody projected area.

$$\text{thus,}\quad \rho u^2 A)_2 + P_2 A_2 - \rho u^2 A)_\infty - P_\infty A_\infty + \bar{P}A_R = 0 \tag{4}$$

If we introduce the continuity equation and assume adiabatic flow, we obtain

$$\rho u\, A)_\infty = \rho u\, A)_2 \tag{5}$$

$$h_\infty + (1/2)u_\infty{}^2 = h_2 + (1/2)u_2{}^2 \tag{6}$$

Combining Eqs. (5) and (6), we have

$$u_\infty{}^2 = \frac{2(h_2 - h_\infty)}{1 - [(\rho_\infty/\rho_2)(A_\infty/A_2)]^2} \tag{7}$$

and inserting Eqs. (5) and (7) into Eq. (4) eliminating u, we get

$$\left(\frac{A_\infty\, \rho_\infty}{A_2\, \rho_2}\right)^2 \rho_2 A_2 \left\{\frac{2(h_2 - h_\infty)}{1 - [(\rho_\infty/\rho_2)(A_\infty/A_2)]^2}\right\} - \rho_\infty A_\infty \times$$

$$\frac{2(h_2 - h_\infty)}{1 - [(\rho_\infty/\rho_2)(A_\infty/A_2)]^2} + P_2 A_2 - P_\infty A_\infty + \bar{P}A_R = 0 \tag{8}$$

from the geometry

$$A_R/A_\infty = 1 - (A_2/A_\infty)$$

By a series of manipulations nondimensionalize using conditions of the gas at the reference state (0) used in reference (2).

† This work was completed while both authors were connected with The Marquardt Corporation.

FIG. 1.

$$\frac{2(h_2 - h_\infty)}{(R_0/mw_0)T_0} \times \frac{\rho_\infty/\rho_0}{1 + [(\rho_\infty/\rho_2)(A_\infty/A_2)]} = \frac{P_2}{P_0}\frac{A_2}{A_\infty} - \frac{P_\infty}{P_0} + \frac{\bar{P}}{P_0}\left(1 - \frac{A_2}{A_\infty}\right) \quad (9)$$

Solve Eq. (9) by iteration as follows:

(1) Select u_∞, altitude
(2) Find $\bar{P}$ from knowledge of compression surface geometry
(3) Select T_2, vary sets of P_2, h_2, ρ_2 values from the tabulated data[2]
(4) Iterate from Eq. (9) for a solution
(5) Compute a free-stream velocity that satisfies the above solution from Eq. (7)
(6) Vary T_2 until u_∞(selected) = u_∞[from step (5)]

It is of interest to note that Eq. (9) when applied to a normal shock case ($A_2/A_\infty = 1$) degenerates to the form given in reference (3).

REFERENCES

[1] Meyer, Rudolph C., *Flow-Turning Losses Associated with Zero-Drag External Compression Supersonic Inlets*, NACA TN 4096, 1957.

[2] Hilsenrath, Joseph, and Beckett, Charles W., *Tables of Thermodynamic Properties of Argon-Free Air to 15,000°K.*, AEDC TN-56-12, September, 1956.

[3] Huber, Paul W., *Tables and Graphs of Normal-Shock Parameters at Hypersonic Mach Numbers and Selected Altitudes*, NACA TN 4352, September, 1958.

An Estimate of the Minimum Reynolds Number for Transition From Laminar to Turbulent Flow by Means of Energy Considerations*

Neal Tetervin
U.S. Naval Ordnance Laboratory, White Oak, Silver Spring, Md.
July 11, 1960

IN ORDER to obtain a rough estimate of the minimum Reynolds number for turbulent flow in a pipe, Lin[1] used the minimum dissipation property of the fully developed laminar flow in a pipe to show that the turbulent-friction coefficient must be larger than the laminar coefficient. This result establishes a lower Reynolds-number limit for a turbulent-friction formula, and by inference, a lower limit for turbulent flow. The lower limit obtained in this way is 597 when the Blasius turbulent-friction formula for a pipe[2] is used; the Reynolds number is based on the radius of the pipe and on the average velocity. The experimental value is about 1,000.

Although it follows from the equations of motion for the fully developed laminar incompressible flow in a pipe that this flow is a minimum dissipation flow, it does not follow from the boundary-layer equations that the laminar boundary-layer flow is a minimum dissipation flow. Consequently, a slightly different method is used to obtain a rough estimate of the smallest Reynolds number at which transition to turbulent flow can occur in a boundary layer. In this method, the rate of dissipation of mean-flow mechanical energy by the shear stress is first split into the portion caused by the viscous stress and the portion caused by the Reynolds stress, and then it is noted that in a turbulent boundary layer the total dissipation of mechanical energy is large enough to supply both the direct viscous and the Reynolds-stress dissipation. Hence, it is inferred that transition cannot begin unless the Reynolds number is large enough for the rate of dissipation of the turbulent boundary layer to exceed that of the laminar boundary layer. The indication from the boundary-layer kinetic-energy equation and the momentum equation is that the boundary-layer parameters at the smallest Reynolds number at which transition can begin are those for the laminar boundary layer. In this way, the result is obtained that, at the minimum Reynolds number for transition, the friction coefficient calculated by the formula for laminar flow is equal to the friction coefficient calculated by a formula for turbulent flow. A suitable Reynolds number is that based on the boundary-layer momentum thickness. Details of the analysis are presented in a forthcoming Bureau of Naval Weapons publication.

The application of this criterion leads to the result that transition cannot begin on a plate, cylinder, or cone, if the Reynolds number based on the momentum thickness is less than about 44, when the Mach number is zero, and the flow properties are all constant. The effect of Mach number and wall-to-stream temperature ratio on the minimum Reynolds number is found by first using the reference-enthalpy method[3] to find the effect of Mach number and wall-to-stream temperature ratio on the skin-friction coefficient for both laminar and turbulent flow. The results for the insulated wall and for the wall temperature equal to the stream temperature are shown in Figs. 1 and 2. For the insulated wall, the minimum momentum-thickness Reynolds number for transition, $Re_{\theta,\,m}$ increases by a factor of 4.9 as the Mach number is increased from zero to ten; the Reynolds number based on the distance from the origin of the boundary layer, $Re_{x,\,m}$ increases by a factor of 57. When the wall temperature is equal to the stream temperature, the effect of Mach number is less; this result is, however, in doubt because there seems to be a question about the ability of the reference-enthalpy method to predict the turbulent skin-friction coefficient correctly when the wall temperature is much less than the insulated wall temperature.[4]

An investigation of the effect of pressure gradient by a combination of the incompressible boundary-layer flow over wedges with the reference-enthalpy method indicates that the ratio of the minimum boundary-layer Reynolds number with pressure gradient to that without, depends only on the value of the nondimensional pressure-gradient parameter for wedges[5] when the Mach number and ratio of wall-to-stream temperature are fixed. Computations indicate that the largest nondimensional pressure gradient that can be obtained on wedges in incompressible flow

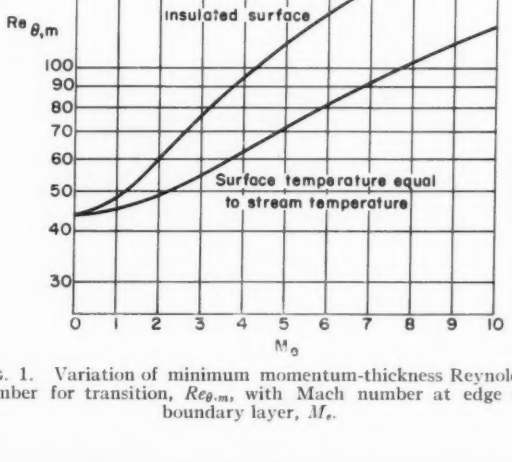

FIG. 1. Variation of minimum momentum-thickness Reynolds number for transition, $Re_{\theta,m}$, with Mach number at edge of boundary layer, M_e.

* The research discussed in this paper was sponsored by Special Projects, U. S. Department of the Navy.

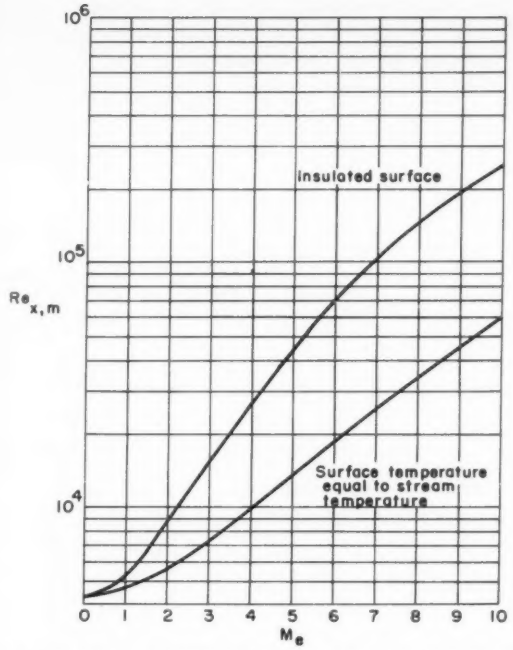

FIG. 2. Variation of minimum Reynolds number for transition based on distance to leading edge, $Re_{x,m}$, with Mach number at edge of boundary layer, M_e.

multiplies the minimum Reynolds number for the zero pressure-gradient case by about 1.4, and also that the minimum Reynolds number for incompressible flow is about 54 at the stagnation point of a body of revolution, and about 57 at the stagnation point of a two-dimensional body.

The estimated values of the minimum momentum-thickness Reynolds numbers for transition are found to be close to the momentum-thickness Reynolds numbers calculated for the most forward transition locations that were observed by Gregory and Walker[6] when particles were placed near the leading edge of airfoils.

REFERENCES

[1] Lin, C. C., *Note on a Modification of a Method of Kampe de Feriet for Estimating the Critical Reynolds Number of Turbulence*, NAVORD Report 2243, 1952.

[2] Goldstein, S., Ed., *Modern Developments in Fluid Dynamics*, Vol. II Fluid Motion Panel of the Aeronautical Research Committee and Others, The Clarendon Press (Oxford), 1938.

[3] Eckert, Ernst R. G., *Survey on Heat Transfer at High Speeds*, TR. 54-70, Aero. Res. Lab., WADC Contract AF 33(616)-2214, 1954.

[4] Winkler, Eva M., and Cha, Moon H., *Investigation of Flat-Plate Hypersonic Turbulent Boundary Layers with Heat Transfer at a Mach Number of 5.2*, NAVORD Report 6631, 1959.

[5] Goldstein, S., Ed., Fluid Motion Panel of the Aeronautical Research Committee and Others, *Modern Developments in Fluid Dynamics*, Vol. I, pp. 139–142, The Clarendon Press (Oxford), 1938.

[6] Gregory, J., and Walker, W. J., *The Effect on Transition of Isolated Surface Excrescences in the Boundary Layer*, Part I, A.R.C. R&M No. 2779, 1956.

A Method of Four-Point Interpolation Especially Adapted for Treating End Conditions of Wings and Other Elastic Surfaces

James A. Griffin, Jr.
Engineer, McDonnell Aircraft Corporation, St. Louis, Mo.

June 27, 1960

A METHOD of four-point interpolation has been developed by this writer which is felt to be superior to other methods of four-point interpolation (e.g., cubic and least-square parabolic methods) due to continuity of slope between successive intervals. Although applicable in other ways, it is particularly useful in the mapping of wing-mode shapes, in tensor transformations of the elastic stiffness and/or influence-coefficient matrices from one set of control points or stations to another set, and in determining slope angles at one or more points of an elastically distorted body. An attempt has also been made by this writer to simplify the treatment of unequal intervals whenever they occur in connection with interpolation.

Consider $n + 1$ points, $P_1, P_2, \ldots, P_{n+1}$, lying on a smooth curve in the region from X_1 to X_{n+1}, as shown in Fig. 1, of which P_{i-1}, P_i, P_{i+1} and P_{i+2} are four typical consecutive points. Let

$$\theta_i = [(X - X_1)/\Delta X] + 1 - i, \quad i = 1, 2, 3, \ldots, \quad n \tag{1}$$

where θ_i is the ratio of the distance in the X-direction of some variable point P from P_i to ΔX. Let $f_i(\theta_i)$ and $f_{i+1}(\theta_i)$ be the two parabolas through the two sets of points, P_{i-1}, P_i, P_{i+1}, and P_i, P_{i+1}, P_{i+2}, respectively, as shown. Then

$$F_i(\theta_i) = (1 - \theta_i)f_i(\theta_i) + \theta_i f_{i+1}(\theta_i), \quad 0 \le \theta_i \le 1 \tag{2}$$

constitutes a formula for interpolating between P_i and P_{i+1}.

The two parabolas of Eq. (2) are

$$f_i(\theta_i) = -(1/2)\theta_i(1 - \theta_i)Y_{i-1} + (1 - \theta_i^2)Y_i + (1/2)\theta_i(1 + \theta_i)Y_{i+1} \tag{3}$$

and

$$f_{i+1}(\theta_i) = (1/2)(1 - \theta_i)(2 - \theta_i)Y_i + \theta_i(2 - \theta_i)Y_{i+1} - (1/2)\theta_i(1 - \theta_i)Y_{i+2} \tag{4}$$

Substitution of Eqs. (3) and (4) into Eq. (2) yields the diparabolic formula for the ith interval:

$$F_i(\theta_i) = -(1/2)\theta_i(1 - \theta_i)^2 Y_{i-1} + (1/2)(1 - \theta_i) \times (2 + 2\theta_i - 3\theta_i^2)Y_i + (1/2)\theta_i(1 + 4\theta_i - 3\theta_i^2)Y_{i+1} - (1/2)\theta_i^2(1 - \theta_i)Y_{i+2}, \quad i = 2, 3, 4, \ldots, \quad n - 1 \text{ and } 0 \le \theta_i \le 1 \tag{5}$$

The slope, $\tan \alpha_i$, of the diparabolic function in the ith interval is

$$\tan \alpha_i = (1/2\Delta X)[(3\theta_i - 1)(1 - \theta_i)Y_{i-1} + \theta_i(9\theta_i - 10)Y_i + (9\theta_i + 1)(1 - \theta_i)Y_{i+1} + \theta_i(3\theta_i - 2)Y_{i+2}] \tag{6}$$

and is continuous between adjacent intervals—i.e.,

$$F_i'(\theta_i)\big|_{\theta_i = 1} = F_{i+1}'(\theta_{i+1})\big|_{\theta_{i+1} = 0}, \quad i = 2, 3, 4, \ldots, \quad n - 2$$

Consider the case for which $i = 1$. If no special condition exists for this interval, then the interpolation is given by Eq. (4) with i set equal to 1. That is,

$$F_1(\theta_1) = f_2(\theta_1) = (1/2)(1 - \theta_1)(2 - \theta_1)Y_1 + \theta_1(2 - \theta_1)Y_2 - (1/2)\theta_1(1 - \theta_1)Y_3 \tag{7}$$

and

$$\tan \alpha_1 = (1/\Delta X)[(1/2)(2\theta_1 - 3)Y_1 + 2(1 - \theta_1)Y_2 + (1/2)(2\theta_1 - 1)Y_3] \tag{8}$$

If the actual curve through $P_1, P_2, P_3, \ldots, P_{n+1}$ is known to be symmetric about the Y-axis, then the existence of a fictitious point, P_0, may be assumed, as shown in Fig. 1, with $Y_0 = Y_2$.

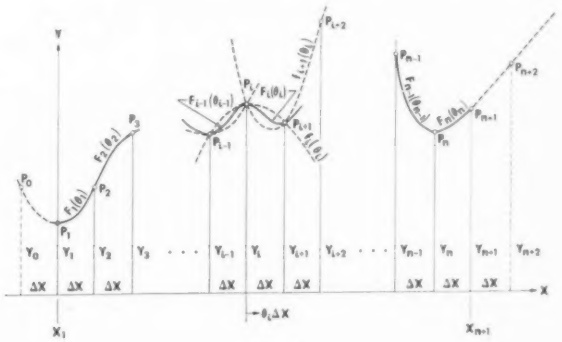

FIG. 1.

Setting $i = 1$ and $Y_0 = Y_2$ in Eq. (5), the interpolation function for the symmetric root condition is

$$F_1(\theta_1) = (1/2)(1 - \theta_1)(2 + 2\theta_1 - 3\theta_1^2)Y_1 + \theta_1^2(3 - 2\theta_1)Y_2 - (1/2)\theta_1^2(1 - \theta_1)Y_3 \quad (9)$$

and

$$\tan \alpha_1 = (1/\Delta X)[(1/2)\theta_1(9\theta_1 - 10)Y_1 + 6\theta_1(1 - \theta_1)Y_2 + (1/2)\theta_1(3\theta_1 - 2)Y_2] \quad (10)$$

In like manner, the antisymmetric root condition is obtained by setting $Y_0 = -Y_2$ and $Y_1 = 0$ in Eq. (5):

$$F_1(\theta_1) = \theta_1(1 + \theta_1 - \theta_1^2)Y_2 - (1/2)\theta_1^2(1 - \theta_1)Y_3 \quad (11)$$

and

$$\tan \alpha_1 = (1/\Delta X)[(3\theta_1 + 1)(1 - \theta_1)Y_2 + (1/2)\theta_1(3\theta_i - 2)Y_3] \quad (12)$$

When Y_1 is set equal to zero, then Eqs. (9) and (10) represent the cantilever root condition.

Next, consider the case for which $i = n$. If no special condition exists for this interval, then the interpolation is given by Eq. (3) with i set equal to n. That is,

$$F_n(\theta_n) = f_n(\theta_n) = -(1/2)\theta_n(1 - \theta_n)Y_{n-1} + (1 - \theta_n^2)Y_n + (1/2)\theta_n(1 + \theta_n)Y_{n+1} \quad (13)$$

and

$$\tan \alpha_n = (1/\Delta X)[(1/2)(2\theta_n - 1)Y_{n-1} - 2\theta_n Y_n + (1/2)(2\theta_n + 1)Y_{n+1}] \quad (14)$$

If P_{n+1} is located at the tip of a deflected surface, it can be assumed that the curvature at the tip is zero. For small deflections, this is equivalent to saying that

$$F_n''(\theta_n)\big|_{\theta_n=1} = 0$$

where $F_n(\theta_n)$ is obtained from Eq. (5) by setting i equal to n and assuming the existence of a fictitious point, P_{n+2}, which makes the curvature at P_{n+1} zero. For this condition, the interpolation becomes

$$F_n(\theta_n) = -(1/4)\theta_n(1 - \theta_n)(2 - \theta_n)Y_{n-1} + (1/2)(1 - \theta_n) \times (2 + 2\theta_n - \theta_n^2)Y_n + (1/4)\theta_n(2 + 3\theta_n - \theta_n^2)Y_{n+1} \quad (15)$$

and

$$\tan \alpha_n = (1/4\Delta X)[-(3\theta_n^2 - 6\theta_n + 2)Y_{n-1} + 6\theta_n(\theta_n - 2)Y_n + (2 + 6\theta_n - 3\theta_n^2)Y_{n+1}] \quad (16)$$

In all the above formulas, the region from X_1 to X_{n+1} is divided into n equal intervals of length ΔX. Consider the case of n unequal intervals, and let X_{01} and $X_{0(n+1)}$ be the lower and upper limits, respectively, of the interpolation region with X_{02}, X_{03}, ..., X_{0n} as the intermediate stations. Let

$$\bar{X}_{i+1} = X_{01} + i[(X_{0(n+1)} - X_{01})/n], \quad i = 0, 1, 2, \ldots, n \quad (17)$$

These $n + 1$ stations, $\bar{X}_1$, $\bar{X}_2$, ..., $\bar{X}_{n+1}$ are at equal intervals and their range coincides with that for

$$X_{01}, X_{02}, \ldots, X_{0(n+1)}$$

A square matrix, $[\xi]$, can therefore be calculated by successive application of Eq. (5) to all intermediate intervals of common length $(X_{0(n+1)} - X_{01})/n$, by application of Eqs. (7), (9), or (11) to the root interval, and by application of Eqs. (13) or (15) to the tip interval, such that

$$\{Y_0\} = [\xi]\{\bar{Y}\} \quad (18)$$

where $\{Y_0\}$ is a column matrix of values of the function at X_{01}, X_{02}, ..., $X_{0(n+1)}$, and $\{\bar{Y}\}$ is a column matrix of values of the function at $\bar{X}_1$, $\bar{X}_2$, ..., $\bar{X}_{n+1}$. If the inequality of the intervals between X_{01}, X_{02}, ..., $X_{0(n+1)}$ is not too great, then

$$\{\bar{Y}\} = [\xi]^{-1}\{Y_0\} \quad (19)$$

This can be justified by thinking of the intervals between X_{01}, X_{02}, ..., $X_{0(n+1)}$ as approaching equality. Then $[\xi]$ approaches the identity matrix which is obviously nonsingular. Another matrix, $[\eta]$, can be calculated such that

$$\{q\} = [\eta]\{\bar{Y}\} \quad (20)$$

where $\{q\}$ is a column matrix of desired interpolated values (e.g., deflections and/or slopes at one or more points of an elastically distorted body). Substitution of Eq. (19) into Eq. (20) yields

$$\{q\} = [\eta][\xi]^{-1}\{Y_0\} \equiv [\xi]\{Y_0\} \quad (21)$$

where $[\xi]$ is the interpolation matrix for the original unequal intervals.

It should be noted, in passing, that the above method for handling unequal intervals is by no means restricted to diparabolic interpolation, but can be applied to any method of interpolating for equal intervals. Moreover, numerical integrating coefficients for unequal intervals can be obtained by postmultiplying the row matrix of integrating coefficients for $\{\bar{Y}\}$ using, say, Simpson's Rule by $[\xi]^{-1}$.

Rational Approximations Formed From Chester's Series for the Body Behind a Given Axially Symmetric Bow Shock Wave

A. H. Van Tuyl
U.S. Naval Ordnance Laboratory, White Oak, Silver Spring, Md.
July 14, 1960

IN REFERENCE 1, Chester has given a method for finding the body which would produce a given bow shock wave when the free-stream Mach number M is large, and for values of the adiabatic exponent γ near 1. The equation of the body and the pressure on the body are obtained as double power series in M^{-2} and $d^{1/2} = [M^{-2} + (\gamma - 1)/(\gamma + 1)]^{1/2}$. Let x and r be cylindrical coordinates with origin at the nose of the shock, with x measured in the downstream direction. Let x_0 be the abscissa of the nose of the body, and let R and R_b be the radii of curvature of the shock and body noses, respectively. In reference 1, double power series are given for x_0/R and R/R_b in the case of a paraboloidal shock up to and including terms of degree 5 in M^{-1} and $d^{1/2}$.

In reference 2, Van Dyke has plotted x_0/R_b as a function of γ when $M = \infty$ in the case of a paraboloidal shock, using Chester's series. On comparison with numerical calculations by the method of reference 2, it is found that the series for x_0/R and R/R_b converge slowly beyond $\gamma = 1.1$, and that the accuracy obtained from the given terms of the series decreases rapidly as γ increases. Further results obtained by Van Dyke in the case of a paraboloidal shock, using the method of reference 2, are given in reference 3. In the present note, it is shown that the use of Padé fractions[4,5] formed from the power series in M^{-2} and $d^{1/2}$ gives results for the body shape in good agreement with numerical calculations by the method of reference 2 when M is larger than about 3 and γ lies between 1 and 5/3. When Padé fractions are used in connection with the series for the pressure on the body, however, accurate results are obtained only for very small values of M^{-1} and $\gamma - 1$.

Let the shock be the paraboloid $x = r^2/(2R)$, and let $k = \sqrt{8d/3}$. Then from reference 1, we have

$$x_0/R = A_0 + A_1M^{-2} + A_2M^{-4} + \ldots \quad (1)$$

and

$$R/R_b = B_0 + B_1M^{-2} + B_2M^{-4} + \ldots \quad (2)$$

where

$$A_0 = d - kd[1 - (39/40)k + (463/488)k^2] + \ldots \quad (3)$$

$$A_1 = -(3/8)k^2 + (13/32)k^3 + \ldots \quad (4)$$

$$A_2 = 1 - (3/2)k + \ldots \quad (5)$$

and

$$B_0 = 1 + (19/6)\,d[1 - (94/95)k + (33{,}519/21{,}280)k^2 - (2{,}593/1{,}064)k^3] + \ldots \quad (6)$$

TABLE 1

x_0/R for $\gamma = 7/5$ in the Case of a Paraboloidal Bow Shock

M	Case I	Case II	Van Dyke[3]
4	0.1215	0.1244	0.1196
10	0.1019	0.1036	0.10165

TABLE 2

R_b/R for $\gamma = 7/5$ in the Case of a Paraboloidal Bow Shock

M	Case I	Case II	Case III	Van Dyke[3]
4	0.6589	0.6614	0.6749	0.647
10	0.7211	0.7230	0.7301	0.712

TABLE 3

x_0/R_b at $M = \infty$ in the Case of a Paraboloidal Bow Shock

γ	Rational Approximations	Van Dyke[3]
6/5	0.0728 − 0.0734	0.073
7/5	0.1318 − 0.1353	0.135
5/3	0.1960 − 0.2073	0.207

$$B_1 = (2/3) - (25/28)k^2 + (861/160)k^3 + \ldots \quad (7)$$

$$B_2 = (23/6) - (47/10)k + \ldots \quad (8)$$

As in references 4 and 5, we obtain the rational approximations

$$A_0 \cong d\left[1 - k\left(\frac{1 + 0.084981685k}{1 + 1.0599817k}\right)\right] \quad (9)$$

$$A_0 \cong d\left(\frac{1 + 0.049180328k}{1 + 1.0491803k + 0.074180328k^2}\right) \quad (10)$$

$$B_0 \cong 1 + (19/6)d\left[1 - (94/95)k\left(\frac{1 - 0.044715601k}{1 + 1.5471822k}\right)\right] \quad (11)$$

$$B_0 \cong 1 + (19/6)d\left(\frac{1 + 0.48426373k}{1 + 1.4737374k - 0.073880712k^2}\right) \quad (12)$$

$$B_0 \cong \frac{1 + 0.50138967k + 0.10847091k^2}{1 + 0.50138967k - 1.0790291k^2 + 0.57959977k^3} \quad (13)$$

and

$$B_1 \cong \frac{2}{3}\left(\frac{1 + 6.0270000k}{1 + 6.0270000k + 1.3392857k^2}\right) \quad (14)$$

Because of the small number of terms in Eqs. (4), (5), and (8), it is necessary to use the partial sums shown as rational approximations. Thus, M and γ must be restricted to values such that k is sufficiently small.

Finally, after calculating the A_i and B_i, we obtain x_0/R and R/R_b from the rational approximations

$$x_0/R \cong [(A_0A_2 - A_1^2)M^{-2} - A_0A_1]/(A_2M^{-2} - A_1) \quad (15)$$

and

$$(R/R_b) \cong [(B_0B_2 - B_1^2)M^{-2} - B_0B_1]/(B_2M^{-2} - B_1) \quad (16)$$

The results obtained from the previous approximations are compared with Van Dyke's results[3] in Tables 1, 2, and 3. In Table 1, Cases I and II are computed from Eqs. (9) and (10), respectively, together with Eqs. (4), (5), and (15). In Table 2, Cases I, II, and III are computed from Eqs. (11), (12), and (13), respectively, together with Eqs. (8), (14), and (16). Finally, in Table 3, the range of values of x_0/R_b for each given value of γ at $M = \infty$ obtained from the six possible combinations of the approximations for A_0 and B_0 is compared with the results of reference 3.

REFERENCES

[1] Chester, W., *Supersonic Flow past a Bluff Body with a Detached Shock, Part II, Axisymmetrical Body*, J. Fluid Mech., Vol. 1, pp. 490–496, November, 1956.

[2] Van Dyke, Milton D., *The Supersonic Blunt Body Problem—Review and Extension*, Journal of the Aero/Space Sciences, Vol. 25, No. 8, pp. 485–496, August, 1958.

[3] Van Dyke, Milton D., and Gordon, Helen M., *Supersonic Flow past a Family of Blunt Axisymmetric Bodies*, NASA Report R-1, 1959.

[4] Wall, H. S., *Continued Fractions*, D. Van Nostrand, New York, 1948.

[5] Shanks, Daniel, *Non-Linear Transformations of Divergent and Slowly Convergent Sequences*, J. Math. & Phys., Vol. 34, pp. 1–42, April, 1955.

Comment on "Inviscid Hypersonic Flow Over Unyawed Circular Cones"[1]

S. A. Powers
Senior Engineer, Research and Advanced Systems Group, Norair Division of the Northrop Corp., Hawthorne, Calif.

July 18, 1960

REFERENCE 1 presents a simple solution to the hypersonic conical flow equation. However, the same solution[2] was published in 1959. This in no way detracts from the usefulness of the approximation, but merely points up how often two identical solutions to the same problem are obtained independently.

REFERENCES

[1] Pottsepp, L., *Inviscid Hypersonic Flow Over Unyawed Circular Cones*, Journal of the Aero/Space Sciences, Readers' Forum, Vol. 27, No. 7, pp. 558–559, July, 1960.

[2] Sidorov, O. P., *On the Calculation of the Flow Around a Cone*, Journal of the Institute of Advanced Studies (Izvestiya Vyssmikh Uchebnykh Zavedenii), MVO, SSSR, Aviation Technology Div., No. 2, pp. 144–146, 1959.

Additional Comment[1]

Haim Kennet and Sainsbury L. Strack
Research Engineer and Research Specialist, Respectively, Aero-Space Div., Boeing Airplane Co., Seattle, Wash.

August 12, 1960

WE HAVE READ WITH INTEREST the note by Pottsepp[1] on the inviscid hypersonic flow over unyawed circular cones. It seems to us, however, that essentially the same results have previously been obtained by Feldman[2] in 1957. Further, the physical reasoning which underlies Pottsepp's formulation of the approximate Taylor-Maccoll equation is precisely that which motivated the constant-density solution—viz., that the shock layer is thin (reference 3, p. 139).

REFERENCES

[1] Pottsepp, L., *Inviscid Hypersonic Flow Over Unyawed Circular Cones*, Journal of the Aero/Space Sciences, Readers' Forum, Vol. 27, No. 7, pp. 558–559, July, 1960.

[2] Feldman, S., *Hypersonic Conical Shock for Dissociated Air in Thermodynamic Equilibrium*, Jet Propulsion, Vol. 27, No. 12, pp. 1253–1255, December, 1957.

[3] Hayes, W. D., and Probstein, R. F., *Hypersonic Flow Theory*; Academic Press, New York, 1959.

Author's Reply

Lembit Pottsepp
Aero/Astrodynamics Section, Missiles and Space Systems Engineering Dept., Douglas Aircraft Company, Inc., Santa Monica, Calif.

September 12, 1960

I APPRECIATE THE INFORMATION contained in the comment of S. A. Powers. However, I wish to point out that the linearization technique which I used in my paper has been considered by other investigators previous to O. P. Sidorov (reference 2 of Powers' comment).

Additional literature study has shown that, in 1956, Fettis[1] used the same approach and compared the values of the velocity

components with those of the exact solution. In an earlier publication, Hord[2] states that "this approximation, which gives good results when $v^2 \ll a^2$, was recognized as a good approximation in the hypersonic speed range a number of years ago by several persons, independently, at the Langley Aeronautical Laboratory."

In addition, and in reply to the comment of Messrs. Kennet and Strack, I should like to emphasize that the constant-density approximation used by Hayes,[3] Feldman[4] and others, leads to the same form of the potential equation. The difference, however, lies in the manner in which the constants appearing in the solution are evaluated, and in that the constant-density assumption requires the use of constant-density energy equation for computing the pressure coefficients. As a consequence, the range of validity of the constant-density approximation is somewhat narrower. Of course, at higher Mach numbers the two approximations yield very nearly the same results.

REFERENCES

[1] Fettis, Henry E., *An Approximate Solution to Supersonic Conical Flow*, Journal of the Aeronautical Sciences, Readers' Forum, Vol. 23, No. 12, pp. 1122–1123, December, 1956.

[2] Hord, Richard A., *An Approximate Solution for Axially Symmetric Flow Over a Cone With an Attached Shock Wave*, NACA TN 3485, p. 19, October, 1955.

[3] Hayes, W. D., and Probstein, R. F., *Hypersonic Flow Theory*, p. 148; Academic Press, New York, 1959.

[4] Feldman, S., *Hypersonic Conical Shock for Dissociated Air in Thermodynamic Equilibrium*, Jet Propulsion, Vol. 27, No. 12, pp. 1253–1255, December, 1957.

Comment on "Influence of Shock-Wave Attenuation by Boundary-Layer Growth on Contact-Surface Motion in a Shock Tube"

Chul Park
Instructor of Aerodynamics,
Department of Aeronautical Engineering,
Republic of Korea Air Force Academy, Seoul, Korea

July 13, 1960

THE FOLLOWING COMMENTS pertain to reference 1.

If γ is defined as

$$(d/d\gamma) = (\partial/\partial t) + U(\partial/\partial x)$$

$d\gamma$ is not an element of arc length in the direction of U, but the element of displacement in t direction in $x-t$ plane.

Equation (14)

$$\frac{D\epsilon_V}{Dt} = (U^o - V^o)\frac{d\Omega}{d\xi} + P\left(\frac{d\epsilon_U}{d\gamma}\right)_A \frac{a^o}{V^o + a^o - U^o} \times \sqrt{\frac{{a_0}^2 - {V^o}^2}{{a_0}^2 - (V^o + a^o)^2}} - R\left(\frac{d\epsilon_U}{d\gamma}\right)_B \frac{a^o}{U^o - V^o + a^o} \times \sqrt{\frac{{a_0}^2 + {V^o}^2}{{a_0}^2 + (V^o + a^o)^2}}$$

should read

$$\frac{D\epsilon_V}{Dt} = (U^o - V^o)\frac{d\Omega}{d\xi} + P\left(\frac{d\epsilon_U}{d\gamma}\right)_A \times \frac{a^o}{V^o + a^o - U^o} - R\left(\frac{d\epsilon_U}{d\gamma}\right)_B \frac{a^o}{U^o - V^o + a^o}$$

because the change of ϵ_V due to a change of $(P\epsilon_U)_A$ is

$$\Delta\epsilon_{V_A} = [(\epsilon_V)_c' - (\epsilon_V)_c]_A = (P\epsilon_U)_{A'} - (P\epsilon_U)_A = \Delta(P\epsilon_U)_A$$

and no multiplication factor is necessary.

REFERENCE

[1] Rosciszewski, Jan, *Influence of Shock-Wave Attenuation by Boundary-Layer Growth on Contact-Surface Motion in a Shock Tube*, Journal of the Aero/Space Sciences, Readers' Forum, Vol. 26, No. 6, pp. 388–389, June, 1959.

Author's Reply and Erratum

Jan Rosciszewski
Division of Engineering and Applied Physics,
Harvard University, Cambridge, Mass.

July 29, 1960

I AGREE with the comments that there is no need for the multiplication factor in my paper, referenced above. However, this does not change the main result of the paper.

I also wish to avail myself of the opportunity to correct Eq. (5) of my paper.

Initially, instead of

$$\frac{1}{c_p}\frac{DS}{Dt} = \left\{ \quad \right\} \cdots\cdots \tag{5}$$

it should read

$$\frac{1}{c_p}\frac{DS}{Dt} = \left\{ \quad \right\} \cdots\cdots \tag{5}$$

On the Calculation of Natural Modes of Free-Free Structures

John Dugundji
Assistant Professor of Aeronautics and Astronautics,
Massachusetts Institute of Technology, Cambridge, Mass.

July 11, 1960

THE STANDARD MATRIX METHOD for calculating the natural modes and frequencies of free-free (unrestrained) structures is described, among other places, in references (1), (2), (3). It is the purpose of this note to review this method and to indicate certain interesting relations which may not have been generally apparent heretofore.

Consider the "flattened" aircraft structure indicated in Fig. (1), where the only important displacement is perpendicular to the x-y plane. The structure is considered as a series of n lumped point masses m_i with weightless elastic structure between. Masses possessing concentrated moments of inertia as well, such as fuselages, can be represented by two point masses separated by a rigid link—i.e., "dumbells" [see reference (3)]. Fixing an axis system x, y at any arbitrary reference point 0 on the structure, the equations of motion are

$$[m_i \ \ldots\ ]\begin{Bmatrix} w_i \\ \cdot \\ \cdot \\ \cdot \end{Bmatrix} = 0 \tag{1}$$

$$[m_i y_i \ \ldots\ ]\begin{Bmatrix} w_i \\ \cdot \\ \cdot \\ \cdot \end{Bmatrix} = 0 \tag{2}$$

$$[m_i x_i \ \ldots\ ]\begin{Bmatrix} w_i \\ \cdot \\ \cdot \\ \cdot \end{Bmatrix} = 0 \tag{3}$$

$$\begin{Bmatrix} w_i \\ \cdot \\ \cdot \\ \cdot \end{Bmatrix} - \begin{Bmatrix} 1 \\ \cdot \\ \cdot \\ \cdot \end{Bmatrix} w_0 - \begin{Bmatrix} y_i \\ \cdot \\ \cdot \\ \cdot \end{Bmatrix} \theta_x - \begin{Bmatrix} x_i \\ \cdot \\ \cdot \\ \cdot \end{Bmatrix} \theta_y = \omega^2[C][m_i]\begin{Bmatrix} w_i \\ \cdot \\ \cdot \\ \cdot \end{Bmatrix} \tag{4}$$

Here, the notation $[\ \ldots\ ]$ represents a row matrix, while $\begin{Bmatrix} \cdot \\ \cdot \\ \cdot \end{Bmatrix}$ represents a column matrix. w_i is the absolute vertical deflec-

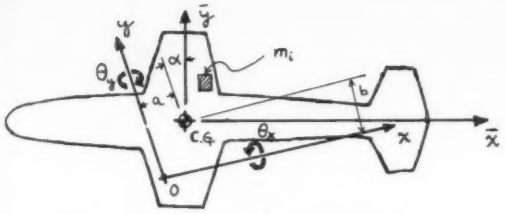

FIG. 1. Axis system of "flattened" aircraft.

tion (positive up) of mass m_i, w_0, θ_x, θ_y, the deflection and rotation of the structure at point 0, ω the natural frequency, $[m_i]$ a diagonal matrix of the mass elements m_i, and $[C]$ the influence coefficients matrix measured relative to clamping at point 0. The first three equations represent rigid-body force equilibrium of the unrestrained structure (note that Eq. (1) was used in establishing Eqs. (2), and (3) since x_i, y_i are not measured from c.g.), while Eq. (4) represents elastic deformation equilibrium of the vibrating structure. Multiplying Eq. (4) by the row matrices $[m_i \ldots]$, $[m_i y_i \ldots]$, $[m_i x_i \ldots]$, respectively, and utilizing Eqs. (1), (2), (3), one obtains three equations from which w_0, θ_x, θ_y can be determined. Substituting these values back into Eq. (4), one then obtains the matrix iteration equations,

$$[R][C][m_i]\{w_i\} = (1/\omega^2)\{w_i\} \tag{5}$$

where the rigid-body mode-modifying matrix $[R]$ is an operator defined as

$$[R] = \left[\left[\,[1] - \begin{bmatrix} 1 & y_i & x_i \\ \cdot & \cdot & \cdot \\ \cdot & \cdot & \cdot \\ \cdot & \cdot & \cdot \end{bmatrix} \begin{bmatrix} M & S_x & S_y \\ S_x & I_x & I_{xy} \\ S_y & I_{xy} & I_y \end{bmatrix}^{-1} \begin{bmatrix} 1 & \ldots \\ y_i & \ldots \\ x_i & \ldots \end{bmatrix} [m_i]\right]\right] \tag{6}$$

Here, [1] is the unity matrix and M, S_x, S_y, I_x, I_y, I_{xy} represent the total mass, static moment about x and y axes, moment of inertia about x and y axes, and product of inertia, respectively.

It is often convenient to locate the reference point 0 at the c.g. and to align the axes along principal axis directions (the plane of symmetry in Fig. 1). For this case, $S_x = S_y = I_{xy} = 0$, and the [R] matrix of Eq. (6) reduces simply to

$$[R] = \left[\left[\,[1] - \frac{1}{M}\begin{Bmatrix} 1 \\ \cdot \\ \cdot \\ \cdot \end{Bmatrix} [m_i \ldots] - \frac{1}{I_{\bar{x}}}\begin{Bmatrix} \bar{y}_i \\ \cdot \\ \cdot \\ \cdot \end{Bmatrix} [m_i \bar{y}_i \ldots] - \frac{1}{I_{\bar{y}}}\begin{Bmatrix} \bar{x}_i \\ \cdot \\ \cdot \\ \cdot \end{Bmatrix} [m_i \bar{x}_i \ldots]\right]\right] \tag{7}$$

It is seen, therefore, that premultiplication by $[R]$ of the restrained structure dynamic matrix $[C][m_i]$, acts to "free" the restrained structure and give free-free modes rather than restrained modes. In the $[R]$ matrix given in Eq. (7), the second, third, and fourth terms represent freeing the structure with respect to vertical translation, roll, and pitch, respectively. Leaving out any of these terms suppresses the corresponding rigid-body freedom. As formulated here, the $[C]$ matrix of Eq. (5) is considered to be the influence coefficients measured for the structure clamped at the reference point 0 (at the c.g. if Eq. (7) is used for $[R]$). Closer examination will reveal, however, that this is actually a much too stringent restriction on the $[C]$ matrix. This fact is not generally apparent in the engineering literature on this subject. This restriction is now further examined.

Consider the case where the reference point 0 is not located at the c.g. The $[C]$'s, as mentioned above, are measured for clamping at this point 0, and the general expression, Eq. (6), is used for $[R]$. Now if one expresses the x, y coordinates in terms of the c.g. coordinates $\bar{x}$, $\bar{y}$,

$$\begin{bmatrix} 1 & y_i & x_i \\ \cdot & \cdot & \cdot \\ \cdot & \cdot & \cdot \\ \cdot & \cdot & \cdot \end{bmatrix} = \begin{bmatrix} 1 & \bar{y}_i & \bar{x}_i \\ \cdot & \cdot & \cdot \\ \cdot & \cdot & \cdot \\ \cdot & \cdot & \cdot \end{bmatrix} \begin{bmatrix} 1 & b & a \\ 0 & \cos\alpha & \sin\alpha \\ 0 & -\sin\alpha & \cos\alpha \end{bmatrix} \tag{8}$$

and then substitutes this into $[R]$ of Eq. (6), it will turn out, after some matrix manipulation, that the $[R]$ as given by Eq. (7) will result. The matrix $[R]$ is thus a numerically invariant quantity regardless of the location of the reference point 0 and the orientation of the axis system for which it is computed. This implies then that any set of influence coefficients $[C]$ for the structure clamped at any point can be used in Eq. (5) together with $[R]$ computed at any other reference point since all values of $[R]$ will be numerically equal. It is simplest to compute $[R]$ at the c.g. and in the plane of symmetry using Eq. (7).

Further, it can be shown that if a set of influence coefficients $[C]$ for the structure simply supported at any three points A, B, C is used, the same $[R]$ matrices as before will result. To show this, one returns to Eqs. (1)–(4) and re-expresses the elastic deformation [the left-hand side of Eq. (4)] in terms of the deflections of the three points w_A, w_B, w_C, instead of w_0, θ_x, θ_y. Proceeding in a similar manner as before will result in the same equations as previously, Eqs. (5), (6), (7).

Summarizing then, one arrives at the interesting result that for the calculation of the free-free modes of a structure, one need only premultiply the dynamic matrix $[C][m_i]$ of any restrained structure (restrained in any way—cantilevered, simply supported, and at any arbitrary points) by the invariant $[R]$ matrix, which is most easily computed at the c.g. and along principal axes by Eq. (7). The resulting matrix $[R][C][m_i]$ is then iterated for the modes and frequencies. Although the $[C]$'s are so vastly different in all these cases, and will, in fact result in vastly different modes and frequencies for the restrained structures, premultiplication by the identical $[R]$ matrix will make all of them have the exact same free-free (unrestrained) modes and frequencies. Thus, the restriction mentioned earlier on the $[C]$ matrix used in Eq. (5) is considerably relaxed—any consistent set of influence coefficients for the structure restrained in any way is permissible.

The removal of the restriction on influence coefficients allows one to pick those most convenient for the problem. Notice that clamping at a mass point will introduce a column and row of zeros into the $[C]$ matrix, and a column of zeros into the $[R][C][m_i]$ matrix. This means that only n-1 of the w_i's need be iterated, the w_i at the clamped mass results from the row corresponding to the column of zeros, and need only be found after the other n-1 w_i's have iterated. Similarly, for simply supporting at three mass points, three columns of zeros are introduced into $[R][C][m_i]$, and iteration need be done only on n-3 of the w_i's.

The orthogonality relations for the free-free modes of these point mass systems are

$$[w_i^{(r)} \ldots][m_i]\begin{Bmatrix} w_i^{(s)} \\ \cdot \\ \cdot \\ \cdot \end{Bmatrix} = 0$$

These can be used in the standard fashion of sweeping to obtain the higher modes of the $[R][C][m_i]$ matrix. Notice that the $[R]$ matrix contains three rigid-body modes and hence is degenerate of rank 3. The resulting $[R][C][m_i]$ matrix yields only n-3 elastic modes.

Advantage can be taken of symmetry considerations to reduce the size of the matrices. This would restrict the choice of $[C]$'s permissible. Also, it would be necessary to suppress the appropriate rigid-body degrees of freedom in the $[R]$ matrix.

The procedure outlined here for flattened two-dimensional structures is readily extendable to three-dimensional structures. Returning to Eqs. (1) to (4), one would add the displacements in

the other two directions, u, v as well as a θ_z, thus resulting in six rigid-body equilibrium equations and one elastic equation involving the unknowns u_0, v_0, w_0, θ_x, θ_y, θ_z. These unknowns are found as before and the analogous $[R]$ matrix determined. Again, it would probably result that any arbitrary set of restrained influence coefficients $[C]$ could be used.

References

[1] **Kappus, R., and Clerc, D.,** *Remarks on Systematizing the Calculations of the Natural Modes of a Free Structure*, Journal of the Aero/Space Sciences, Vol. 25, No. 4, pp. 276–278, April, 1958.

[2] **Mack, C. E.,** *Tensor Analysis of Aircraft Structural Vibration*, Presented at the I.A.S. 16th Annual Meeting, N.Y., January 26–29, 1958 (Fairchild Fund Paper No. 104).

[3] **Bisplinghoff, R. L., Ashley, H., and Halfman, R. L.,** *Aeroelasticity*; Addison-Wesley Publishing Company, Inc., Cambridge, Mass., 1955.

A Note on Laminar Boundary-Layer Skin Friction Under the Influence of Foreign-Gas Injection

C. R. Faulders

Aero-Space Laboratories, Missile Division, North American Aviation, Inc., Downey, Calif.

July 11, 1960

Symbols

c = mass concentration
D_{12} = binary-diffusion coefficient
m = molecular weight
w = mass flow rate of injected gas
$\eta = \frac{1}{2}\sqrt{\frac{u_\infty}{x\nu_\infty}}\int_0^y \frac{\rho}{\rho_\infty}\,ds$
$\lambda = \rho\mu/\rho_\infty\mu_\infty$
$\xi = \mu/\rho D_{12}$
$\psi = \sqrt{u_\infty x \nu_\infty}\, f(\eta)$

Subscripts

w = wall value
1 = injected gas
2 = free-stream gas
∞ = free-stream value

In the case of a compressible laminar boundary layer flowing over a flat porous plate, the skin friction at the wall corresponding to a particular rate of injection is dependent on the variation of the density-viscosity product across the boundary layer. The purpose of this note is to present some numerical results for the relationship between skin friction and blowing rate when the $\rho\mu$ variation is due to the injection of foreign gas. Primary assumptions are that each component of the resulting binary system is a perfect gas and that the viscosity of the mixture varies linearly with temperature and is independent of concentration. The latter assumption is not overly restrictive as long as the molecules are monatomic, diatomic, or of the simple polyatomic variety.[1]

The continuity and momentum equations can be combined through the introduction of a stream function ψ and a similarity parameter η, to obtain

$$ff'' + (\lambda f'')' = 0 \tag{1}$$

where primes denote differentiation with respect to η. The boundary conditions are

$$\eta = 0: \quad f = f_w \qquad \eta = \infty: \quad f' = 2$$
$$f' = 0$$

due to

$$u = (u_\infty/2) f'(\eta) \tag{2}$$

Writing Eq. (1) in integral form and evaluating the constants of integration from the boundary conditions,

$$f_w'' \equiv \frac{2}{\int_0^\infty \frac{\lambda_w}{\lambda} \exp\left\{-\int_0^\eta \frac{f}{\lambda}\,ds\right\} d\eta} \tag{3}$$

$$f' = f_w'' \int_0^\eta \frac{\lambda_w}{\lambda} \exp\left\{-\int_0^s \frac{f}{\lambda}\,dt\right\} ds \tag{4}$$

$$f = f_w + \int_0^\eta f'\,ds \tag{5}$$

Eqs. (3)–(5) can be solved by an iterative procedure, starting with an assumed $f(\eta)$, once λ is known as a function of η. From the assumptions of perfect gas and viscosity proportional to temperature,

$$\lambda = \rho T/\rho_\infty T_\infty = m/m_2 \tag{6}$$

where the absence of a subscript indicates a property of the mixture. Introducing the Gibbs-Dalton Law and $c_i = \rho_i/\rho$, Eq. (6) can be reduced to

$$\lambda = \frac{1}{1 + [(m_2/m_1) - 1]c_1} \tag{7}$$

For a Schmidt number for binary diffusion of unity, the concentration of the injected gas is related to the velocity[2] by

$$c_1 = c_{1w}[1 - (u/u_\infty)] \tag{8}$$

With actual Schmidt-number variations through the boundary layer corresponding to gases having simple, compact molecules, Eq. (8) is still a reasonable approximation, particularly at high blowing rates. Here the Schmidt number varies between values less than one to values greater than one across the boundary layer, thus tending toward an average value of unity. A comparison of velocity and concentration profiles for helium injection appearing in reference 2, for example, indicates favorable agreement with Eq. (8). Combining Eqs. (2), (7), and (8),

$$\lambda = \frac{1}{1 + c_{1w}[(m_2/m_1) - 1][1 - (f'/2)]} \tag{9}$$

Numerical integrations of Eqs. (3)–(5), with λ given by Eq. (9), were carried out for selected values of f_w and λ_w. First approximations for $f(\eta)$ were obtained from solutions to the Blasius equation,[3] for which λ is unity. Three or four iterations were generally required to obtain acceptable convergence on f_w'', with a mean accuracy of convergence estimated to be 4 per cent. Curves of constant f_w have been faired through the calculated points in Fig. 1.

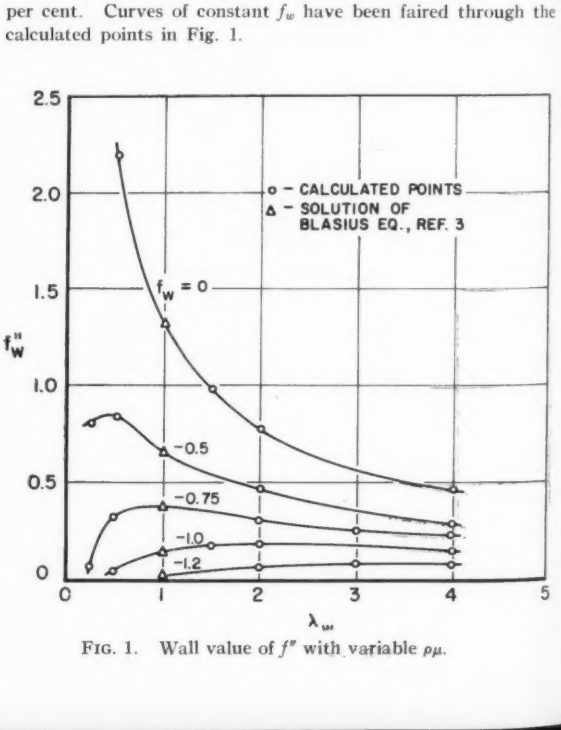

Fig. 1. Wall value of f'' with variable $\rho\mu$.

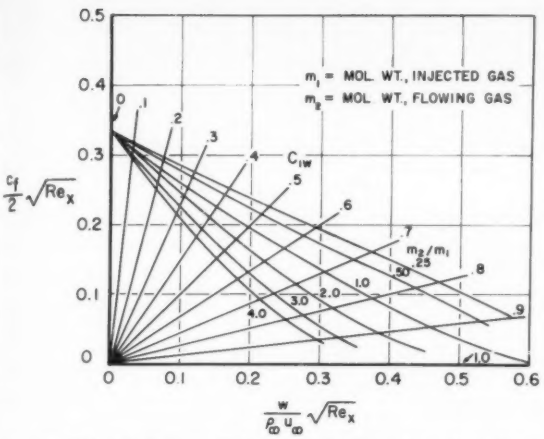

FIG. 2. Skin-friction coefficient for laminar boundary layer with foreign-gas injection, Schmidt No. = 1.

The wall skin-friction coefficient and the blowing rate are, according to the definition of the stream function,

$$(c_f/2)\sqrt{Re_x} = \lambda_w(f_w''/4) \tag{10}$$

$$(w/\rho_\infty u_\infty)\sqrt{Re_x} = -(f_w/2) \tag{11}$$

The mass flow rate of injected fluid is related to the wall concentration and the concentration gradient at the wall by means of the binary-diffusion coefficient.[2] That is, considering concentration to be a function of velocity and introducing the Schmidt number ξ_w,

$$\frac{w}{\rho_\infty u_\infty} = -\frac{c_f}{2\xi_w}\frac{u_\infty}{(1 - c_{1w})}\left(\frac{dc_1}{du}\right)_w \tag{12}$$

Assuming the concentration derivative to be given by Eq. (8)

$$\frac{w}{\rho_\infty u_\infty} = \frac{c_f}{2\xi_w}\frac{c_{1w}}{(1 - c_{1w})} \tag{13}$$

The data of Fig. 1 were combined with Eqs. (9)–(11) and (13) to obtain skin-friction coefficient as a function of dimensionless blowing rate, Fig. 2, for a wall Schmidt number of unity and a range of molecular-weight ratios from 0.25 to 4. Included in Fig. 2 are lines of constant wall concentration. Similar curves could, of course, be obtained for other values of the wall Schmidt number and for more exact relationships between concentration and velocity. Fig. 2 illustrates the significant effect that the $\rho\mu$ variation corresponding to various molecular-weight ratios has upon wall friction. It would be expected that the influence on heat-transfer coefficient would be similar.

REFERENCES

[1] Jeans, J., *An Introduction to the Kinetic Theory of Gases*, p. 183, The University Press, Cambridge, England, 1952.

[2] Baron, J. R., *The Binary-Mixture Boundary Layer Associated with Mass Transfer Cooling at High Speeds*, M.I.T. Naval Supersonic Laboratory TR 160, May, 1956.

[3] Emmons, H. W., and Leigh, D., *Tabulation of the Blasius Function with Blowing and Suction*, Harvard University Division of Applied Sciences, Combustion Aerodynamics Laboratory Interim TR 9, November, 1953.

On the Inclusion of Engine Effects in a Flutter Analysis

W. P. Rodden and R. S. Albert
Dynamics and Loads Branch, Norair Division, Northrop Corporation, Hawthorne, Calif.

July 18, 1960

THE EFFECTS OF A TURBOJET ENGINE on the dynamic stability of an aircraft have been considered in references 1 and 2. These results can be transformed directly into the form necessary for inclusion in a flutter analysis. We consider three effects: the gyroscopic coupling of the rotor, the engine-intake effect, and the Coriolis damping from the flow through the engine. We make the transformations necessary for the collocation formulation of the flutter problem given in reference 3. The harmonic control-point force amplitudes $\{F\}$ in the aeroelastic system have been written as

$$\{F\} = \omega^2([M] + \rho b^2 s[C_h])\{h\} \tag{1}$$

where $[M]$ is the mass matrix, $[C_h]$ is the (complex) matrix of aerodynamic influence coefficients ($AICs$), $\{h\}$ is the set of control-point deflection amplitudes, ω is the circular frequency, ρ is the atmospheric density, and b and s are the reference semichord and span, respectively. The present derivation will lead us to an incremental mass matrix $[M_g]$ to account for the gyroscopic effect, and two incremental matrices of $AICs$, $[C_{h_i}]$ for the intake effect and $[C_{h_c}]$ for the Coriolis damping. The coordinate system, control-point deflections, and control-point forces are shown in Fig. 1. From references 1 and 2, the force vector, $\mathbf{F} = \mathbf{j}Y + \mathbf{k}Z$, and the moment vector, $\mathbf{G} = \mathbf{j}G_y + \mathbf{k}G_z$, are known. (We are not presently concerned with a drag force or a rolling moment, although the basic vibration analysis should consider the fore-and-aft degree of freedom.) The equivalence between the control-point forces and the vector components is given by (cf. Fig. 1)

$$\begin{Bmatrix} F_1 \\ F_2 \\ P_1 \\ P_2 \end{Bmatrix} = \begin{bmatrix} 0 & 1 + e/d & -1/d & 0 \\ 0 & -e/d & 1/d & 0 \\ 1 + e/d & 0 & 0 & 1/d \\ -e/d & 0 & 0 & -1/d \end{bmatrix} \begin{Bmatrix} Y \\ Z \\ G_y \\ G_z \end{Bmatrix} \tag{2}$$

Once the vector component matrix in Eq. (2) is placed in terms of the control-point deflections, the desired matrices are known by comparison of Eq. (2) with Eq. (1).

We first consider the gyroscopic effects. The moment components are given by the rotor terms in Eq. (9) of reference 1, and (after setting $\alpha_{CL} = 0$ and reversing the sign to give the applied loads) become

$$G_y = -Jr\omega_0 \tag{3}$$

$$G_z = Jq\omega_0 \tag{4}$$

where J is the rotor moment of inertia, ω_0 is its angular velocity, positive clockwise looking forward, and q and r are the pitching and yawing velocities, respectively. In terms of the control-point deflections, the angular velocities are

$$q = (\dot{h}_2 - \dot{h}_1)/d \tag{5}$$

$$r = (\dot{s}_1 - \dot{s}_2)/d \tag{6}$$

If we substitute Eqs. (5) and (6) into Eqs. (3) and (4), *assume harmonic motion*, and note there are no transverse forces associated with gyroscopic precession, we may write the vector component matrix:

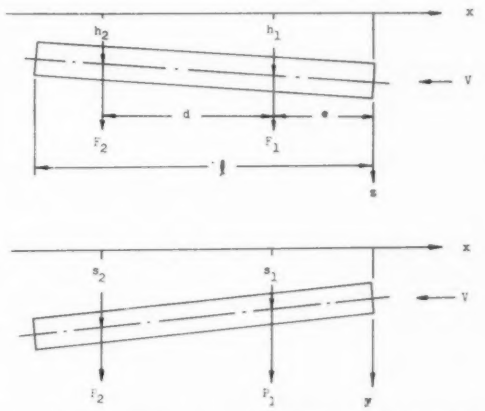

FIG. 1. (a) *Top:* Elevation. (b) *Bottom:* Plan view of engine geometry and force system.

$$\begin{Bmatrix} Y \\ Z \\ G_y \\ G_z \end{Bmatrix} = iJ\omega_0(\omega/d)\begin{bmatrix} 0 & 0 & 0 & 0 \\ 0 & 0 & 0 & 0 \\ 0 & 0 & -1 & +1 \\ -1 & +1 & 0 & 0 \end{bmatrix}\begin{Bmatrix} h_1 \\ h_2 \\ s_1 \\ s_2 \end{Bmatrix} \quad (7)$$

where i is now the imaginary unit. Substituting Eq. (7) into Eq. (2) and identifying the result with Eq. (1) yields the mass matrix

$$[M_g] = i(J/d^2)(\omega_0/\omega)\begin{bmatrix} 0 & 0 & +1 & -1 \\ 0 & 0 & -1 & +1 \\ -1 & +1 & 0 & 0 \\ +1 & -1 & 0 & 0 \end{bmatrix} \quad (8)$$

We note that this increment is imaginary and is frequency-dependent. This frequency dependence will necessitate a modification in the methods of vibration and flutter analysis since the eigenvalue problems are now explicitly dependent on the frequency.

We next consider the intake effect. The force components are found in Eq. (5) of reference 2, and the moment components vanish in our coordinate system. The perturbation force components are

$$Y = -(\rho_i A_i V_i)V_i \sin\beta \quad (9)$$

$$Z = -(\rho_i A_i V_i)V_i \sin\alpha \quad (10)$$

where ρ_i, A_i, and V_i are the density, area, and velocity at the intake, respectively, and the total unsteady angles of attack and sideslip are given by

$$\sin\alpha = (h_2 - h_1)/d + [(1 + e/d)\dot{h}_1 - (e/d)\dot{h}_2]/V \quad (11)$$

$$\sin\beta = (s_1 - s_2)/d + [(1 + e/d)\dot{s}_1 - (e/d)\dot{s}_2]/V \quad (12)$$

If we substitute Eqs. (11) and (12) into Eqs. (9) and (10), and again *assume harmonic motion*, we may write the vector component matrix:

$$\begin{Bmatrix} Y \\ Z \\ G_y \\ G_z \end{Bmatrix} = \rho_i A_i V_i^2\begin{bmatrix} 0 & 0 & -1/d - i(\omega/V)(1 + e/d) & 1/d + i(\omega/V)(e/d) \\ 1/d - i(\omega/V)(1 + e/d) & -1/d + i(\omega/V)(e/d) & 0 & 0 \\ 0 & 0 & 0 & 0 \\ 0 & 0 & 0 & 0 \end{bmatrix}\begin{Bmatrix} h_1 \\ h_2 \\ s_1 \\ s_2 \end{Bmatrix} \quad (13)$$

where i is again the imaginary unit. Substituting Eq. (13) into Eq. (2) and identifying the result with Eq. (1) yields the intake AIC matrix:

$$[C_{hi}] = (1/k^2)(MFR)(V_i/V)(A_i/bs)\begin{bmatrix} C(B - ikC) & C(-B + ikA) & 0 & 0 \\ A(-B + ikC) & A(B - ikA) & 0 & 0 \\ 0 & 0 & C(-B - ikC) & C(B + ikA) \\ 0 & 0 & A(B + ikC) & A(-B - ikA) \end{bmatrix} \quad (14)$$

where k is the reduced frequency ($k = \omega b/V$), MFR is the mass-flow ratio ($MFR = \rho_i V_i/\rho V$), and $A = e/d$, $B = b/d$, $C = 1 + e/d$.

Our last consideration is of the Coriolis damping. In Eq. (6) of reference 1 we find our force and moment components given in dimensionless coefficient form. If we derive the dimensional force and moment coefficients (taking into account the differences in notation and geometry, e.g., $\alpha_{CL} = 0$, $h = l$, $a = d = 0$, etc., noting that the ram drag is equal to $(\rho_i A_i V_i)V$, and neglecting the added fuel mass), we obtain the following:

$$Y = 2(\rho_i A_i V_i)lr \quad (15)$$

$$Z = -2(\rho_i A_i V_i)lq \quad (16)$$

$$G_y = -(\rho_i A_i V_i)l^2 q \quad (17)$$

$$G_z = -(\rho_i A_i V_i)l^2 r \quad (18)$$

If we substitute Eqs. (5) and (6) into Eqs. (15) through (18), and *assume harmonic motion*, we obtain the vector component matrix:

$$\begin{Bmatrix} Y \\ Z \\ G_y \\ G_z \end{Bmatrix} = i\omega(\rho_i A_i V_i)(l/d)\begin{bmatrix} 0 & 0 & 2 & -2 \\ 2 & -2 & 0 & 0 \\ +l & -l & 0 & 0 \\ 0 & 0 & -l & +l \end{bmatrix}\begin{Bmatrix} h_1 \\ h_2 \\ s_1 \\ s_2 \end{Bmatrix} \quad (19)$$

Substituting Eq. (19) into Eq. (2) and identifying the result with Eq. (1) yields the Coriolis AIC matrix:

$$[C_{hc}] = i(1/k)(MFR)(l/d)(A_i/bs)\begin{bmatrix} D & -D & O & O \\ E & -E & O & O \\ O & O & D & -D \\ O & O & E & -E \end{bmatrix} \quad (20)$$

where $D = 2(1 + e/d) - l/d$, and $E = l/d - 2e/d$.

Although these effects are admittedly small, they represent an important addition to a flutter analysis because the intake effect is destabilizing for the usual wing-mounted engine configuration and the gyroscopic effect can cause an adverse coupling with the wing.

References

[1] Vetter, Hans C., *Effect of a Turbojet Engine on the Dynamic Stability of an Aircraft*, Journal of the Aeronautical Sciences, Vol. 20, No. 11, pp. 796–797, November, 1953.

[2] Rodden, W. P., Surber, T. E., and Wykes, J. H., *An Extension of "Effect of a Turbojet Engine on the Dynamic Stability of an Aircraft,"* Journal of the Aeronautical Sciences, Vol. 23, No. 3, pp. 284–286, March, 1956.

[3] Rodden, William P., *A Matrix Approach to Flutter Analysis*, IAS Paper No. FF-23, May, 1959.

Hypersonic Flow Around Bodies of Revolution

Jan Rosciszewski
Division of Engineering and Applied Physics, Harvard University, Cambridge, Mass.
July 13, 1960

IN THE PRESENT NOTE an approximate method of calculation of the shock-wave shape and pressure distribution around bodies not very different from conical bodies is given. This method is an extension of applications of the method developed in the author's previous paper.[1] This method leads to the relation between shock-wave slope and body shape without the need to solve the entire flow between the shock wave and the body.

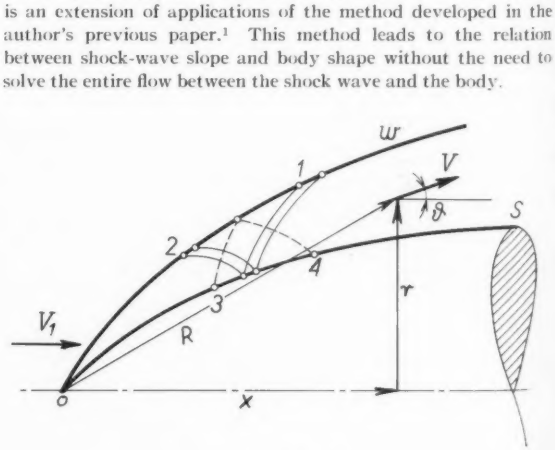

FIG. 1. Notation.

In the supersonic symmetrical flow around the body of revolution the following expressions must be fulfilled (see Dorodnitzin[2] along the characteristics of first and second families:

$$d\vartheta = d[f(\alpha)] + [1/k(k-1)](d\ln\varphi/M) - (1/M)(dr/r) \quad (1)$$

$$d\vartheta = -d[f(\alpha)] - [1/k(k-1)](d\ln\varphi/M) + (1/M)(dr/r) \quad (2)$$

where ϑ, r (see Fig. 1)

$$f(\alpha) = \sqrt{\frac{k+1}{k-1}}\left[\frac{\pi}{2} - \arctan\left(\sqrt{\frac{k+1}{k-1}}\tan\alpha\right) - \left(\frac{\pi}{2} - \alpha\right)\right] \quad (3)$$

α = Mach angle
$\varphi = p/\rho^k$, entropy function
$k = c_p/c_v$, specific-heat ratio

Integrating these expressions respectively along characteristics of the first and second families passing through points 1 and 2 (see Fig. 1), and adding obtained relations, we go to

$$\vartheta_w^{(1)} + \vartheta_w^{(2)} - 2\vartheta_s = f^{(1)}(\alpha_w) - f^{(2)}(\alpha_w) + \frac{1}{k(k-1)}\int_{\ln\varphi_r}^{\ln\varphi_w^{(1)}}\frac{d\ln\varphi}{M} - \frac{1}{k(k-1)}\int_{\ln\varphi_s}^{\ln\varphi_w^{(2)}}\frac{d\ln\varphi}{M} + \int_{r_s}^{r_w^{(2)}}\frac{dr}{Mr} - \int_{r_s}^{r_w^{(1)}}\frac{dr}{Mr} \quad (4)$$

where suffixes w and s denote shock wave and body surface.

Writing the same expressions for the neighboring pair of characteristics (see Fig. 1) and subtracting an obtained expression from previous ones, we obtain in the limit when both pairs match one another

$$d\vartheta_w^{(1)} + d\vartheta_w^{(2)} - 2d\vartheta_s = f'^{(1)}(\alpha_w)\,d\alpha_w - f'^{(2)}(\alpha_w)\,d\alpha_w^{(2)} + \frac{1}{k(k-1)}\,d(\ln\varphi_w^{(1)})\frac{1}{M_w^{(1)}} + \frac{1}{k(k-1)}\left(\frac{dM}{M^2}\right)_m(\ln\varphi_w^{(1)} - \ln\varphi_r) - \frac{1}{k(k-1)}\,d\ln\varphi_w^{(2)}\frac{1}{M_w^{(2)}} - \frac{1}{k(k-1)}\left(\frac{dM}{M^2}\right)_m(\ln\varphi_w^{(1)} - \ln\varphi_r) - dr_w^{(1)}\left(\frac{1}{Mr}\right)_w^{(1)} - \left[\frac{d(Mr)}{M^2r^2}\right]_m(r_w^{(1)} - r_s) + dr_w^{(2)}\left(\frac{1}{Mr}\right)_w^{(2)} + \left[\frac{d(Mr)}{M^2r^2}\right]_m(r_w^{(2)} - r_s) \quad (5)$$

where suffix m marks the mean value in the considered interval of integration. For high Mach numbers $M \gg 1$ and for not very thin bodies we can omit all terms with suffix m as small values of second order.

Expressing all parameters on the shock wave by shock-wave slope angle, we have[3]

$$\left.\begin{aligned} d\vartheta_w &= \frac{d\vartheta_w}{d\gamma}\,d\gamma = \xi(\gamma)d\gamma \\ \text{where}\qquad \xi(\gamma) &= 2M_\infty^2\left[\cos 2\gamma + \frac{1}{M_\infty^2\sin^2\gamma} + \frac{4\cos^2\gamma(M_\infty^2\sin^2\gamma - 1)}{2 + M_\infty^2(k + \cos 2\gamma)}\right] \\ M_w = M_w(\gamma) &= \sqrt{\frac{(k+1)^2M_\infty^4\sin^2\gamma - 4(M_\infty^2\sin^2\gamma - 1)(kM_\infty^2\sin^2\gamma + 1)}{[2kM_\infty^2\sin^2\gamma - (k-1)][(k-1)M_\infty^2\sin^2\gamma + 2]}} \end{aligned}\right\} \quad (6)$$

Velocity must be tangential to the body surface; hence we have

$$d\vartheta_s = (d\vartheta_s/dx)dx = \vartheta_s'(x_s)dx \quad \text{where} \quad \vartheta_s = \arctan r_s'(x)$$

is given by body-surface shape.

Introducing expressions (6) to Eq. (5) and omitting, according to the previous remark, the mean-value terms, we obtain

$$[\xi(\gamma_2) + F(\gamma_2)]\left(\frac{d\gamma}{dx}\right)_2 - \frac{G(\gamma_2)}{r_w^{(2)}} - 2\vartheta'(x_s) = [F(\gamma_1) - \xi(\gamma_1)]\left(\frac{d\gamma}{dx}\right)_1 - \frac{G(\gamma_1)}{r_w^{(1)}} \quad (7)$$

where

$$F(\gamma) = \frac{d[\sin^{-1}(1/M_w)]}{d\gamma}f'(\alpha_w) + \frac{1}{k(k-1)}\frac{1}{M_w}\frac{d\ln\varphi_w}{d\gamma}$$

$$G(\gamma) = (\tan\gamma/M_w)$$

Functions $F(\gamma)$, $G(\gamma)$, $\xi(\gamma)$ could be tabulated using relations (6) and $\varphi_w(\gamma)$ from reference 3. Eq. (7) gives the relation between the shock-wave slope at point (2), the body shape $\vartheta_s(x_s)$, and the shock-wave slope at point (1). Knowing the parameters in point (2) and the body shape, we can find the shock-wave slope at point (1) if we know the form of the characteristics.

Similarly, and as previously outlined, from expressions along characteristics intersecting on the shock wave (see Fig. 1), we obtain by the same assumptions as before

$$\Psi^{(3)}(M_s)\left(\frac{dM_s}{dx}\right)_4 = \Psi^{(3)}(M_s)\left(\frac{dM_s}{dx}\right)_2 + \left(\frac{dr_s}{dx}\right)_4\left(\frac{1}{M_sr_s}\right)_4 - \left(\frac{dr_s}{dx}\right)_2\left(\frac{1}{M_sr_s}\right)_2 + 2\xi(\gamma)\left(\frac{d\gamma}{dx}\right)_w - \vartheta_3'(x_s) + \vartheta_3'(x_s) \quad (8)$$

where

$$\Psi = -f'(\alpha)\frac{1}{M\sqrt{M^2-1}}$$

First solving Eq. (7), we can obtain from Eq. (8) the distribution of Mach number along the body surface and from Bernoulli's equation, pressure distribution.

To obtain an approximate form of characteristics, we assume that body has a shape little different from a circular cone. We neglect the entropy-change influence on the shape of the characteristics and substitute to potential equation in spherical coordinates $\Phi = \Phi_c + \epsilon_\Phi$, $V_R = V_{Rc} + \epsilon_{VR}$ etc., where Φ_c, V_R, etc., potential and radial velocity corresponding to conical-flow solution; $\epsilon_\Phi \ll \Phi_c$, $\epsilon_R \ll V_{Rc}$ etc., small deviations from conical-flow solution. In this way we obtain an approximate equation for characteristics

$$R = e^{\pm\int(V_{Rc}/a_c)d\vartheta}$$

For V_{Rc}, a_c, we can substitute the solution recently discussed by L. Pottsepp[4] or the simplest solution discussed by H. Zienkiewicz[5]:

$$V_{Rc} = V_{Rc_s}\cos\sqrt{2}(\vartheta - \vartheta_s)$$

where ϑ_s, V_{Rc_s} semivertex cone angle, and velocity on the cone surface, respectively.

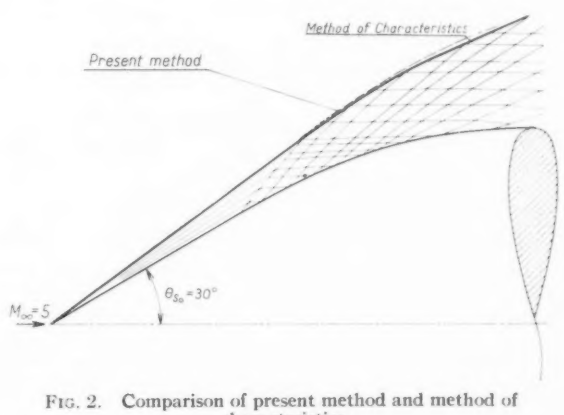

FIG. 2. Comparison of present method and method of characteristics.

Comparison of the result of calculation of the shock-wave shape by the use of the present method and method of characteristics are given in Fig. 2. The nose part of the body is a cone of semivertex angle 30°, and then, parabolic arc given by equation

$$r = 4.04 + 0.31(x - 7)[2 - 0.1(x - 7)]$$

In the rear part, this body does not consist of a small deviation from a cone. These calculations were made by Mr. Rzetelski.

References

[1] Rosciszewski, J., *Nonuniform Shock Waves*, J. Fl. Mech., Vol. 8, No. 3, 1960.

[2] Dorodnitzin, A. A., *Collection of Theoretical Works of Aerodynamics* (in Russian), p. 116, Moscow, 1957.

[3] Ames Research Staff, *Equations, Tables and Charts for Compressible Flow*, NACA TR No. 1135, pp. 613–694, 1953.

[4] Pottsepp, L., *Inviscid Hypersonic Flow Over Unyawed Circular Cone*, Journal of the Aero/Space Sciences, Vol. 27, No. 7, pp. 558–559, July, 1960.

[5] Zienkiewicz, H. K., *Flow About Cones at Very High Speeds*, Aero. Quart., Vol. 8, pp. 384–394, 1957.

Local Normal-Force Ratio Around an Expansion Corner

Joseph L. Sims and Lee M. Saunders
Aeroballistics Laboratory, Army Ballistic Missile Agency, Redstone Arsenal, Ala.

July 18, 1960

A STUDY of the local normal-force ratio around an expansion corner of a lifting body reveals that, for certain Mach numbers and body shapes, completely isentropic calculations may differ considerably from rotational-flow results. In assuming isentropic flow, the effects of the entropy gradient around the body due to an axially asymmetrical shock wave are neglected. These effects can be considerable even for small angles of attack. A solution is presented here which considers rotational flow and assumes an entropy distribution described by Ferri,[2] for small angles of attack. This entropy distribution is valid only outside the vortical layer but is quite satisfactory for the normal-force calculations since there is no pressure gradient across the vortical layer.

Ferri describes the small-angle-of-attack flow characteristics as perturbations on the zero-angle-of-attack case, and the total flow at any point is described by

$$M^* = M^*_1 + \alpha M^*_2 \cos\phi \qquad \varphi = \varphi_1 + \alpha\varphi_2 \cos\phi$$
$$M^*_w = \alpha M^*_{w2} \sin\phi \qquad \Delta S = \Delta S_1 + \alpha S_2 \cos\phi$$

where

M^* = V/a^*, and a^* is the critical speed of sound
M^*_w = the velocity normal to the meridian plane
φ = the flow-direction angle
ΔS = the entropy change

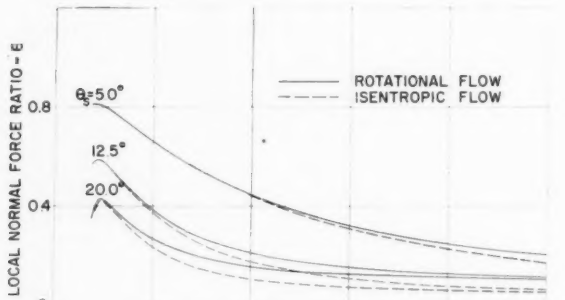

FIG. 1. The local normal-force ratio around the corner of a cone-cylinder juncture.

Subscripts 1 indicate zero-angle-of-attack values
Subscripts 2 denote angle-of-attack quantities which are independent of the meridian angle, ϕ, and the angle of attack, α.

A derivation of the local normal-force equation is given in reference 1. The resulting expression is

$$\frac{d(dC_N/d\alpha)_{\alpha=0}}{dx} = \frac{8}{\gamma M^2_\infty D^2_{REF.}} \times \left\{\frac{P}{P_\infty} r\left[\frac{-2\gamma M^*_1 M^*_2}{(\gamma+1)-(\gamma-1)M^{*2}_1} - \frac{S_2}{R}\right]\right\}$$

A ratio, ϵ, of the local normal-force value immediately downstream of the corner to the value immediately upstream of the corner yields

$$\epsilon = \frac{P_{1d}\,(-2\gamma M^*_{1d} M^*_{2d})/[(\gamma+1)-(\gamma-1)M^{*2}_{1d}] - (S_2/R)}{P_{1u}\,(-2\gamma M^*_{1u} M^*_{2u})/[(\gamma+1)-(\gamma-1)M^{*2}_{1u}] - (S_2/R)}$$

where

P_1 = the zero-angle-of-attack pressure
γ = the ratio of specific heats. Value used in the calculations was $\gamma = 1.4$

Subscripts u and d denote values immediately upstream and downstream of the corner, respectively

The downstream value M^*_{2d} may be calculated by

$$M^*_{2d} = M^*_{2u}\frac{(dM^*_1/d\theta)_d}{(dM^*_1/d\theta)_u} = M^*_{2u}\frac{M^*_{1d}}{M^*_{1u}}\sqrt{\left[\frac{M^{*2}_{1u}-1}{M^{*2}_{1d}-1}\right]\left[\frac{(\gamma+1)-(\gamma-1)M^{*2}_{1d}}{(\gamma+1)-(\gamma-1)M^{*2}_{1u}}\right]}$$

The value $dM^*/d\theta$ is the slope of the Prandtl-Meyer curve.

Several calculations were made of the local normal-force ratio around a cone-cylinder juncture using both isentropic- and rotational-flow equations. A comparison of the results is presented as Fig. 1, where curves were plotted for three values of θ_s, the cone semivertex angle. It is readily seen that, for large values of θ_s, the curves differ considerably even for fairly low Mach numbers.

References

[1] Sims, Joseph L., *Supersonic Flow Around Right Circular Cones – Tables for Small Angle of Attack*, Army Ballistic Missile Agency Report DA TR-19-60, April 27, 1960.

[2] Ferri, Antonio, *The Method of Characteristics for the Determination of Supersonic Flow Over Bodies of Revolution at Small Angles of Attack*, NACA Report 1044, 1951.

On the Lift, Drag, and Moment on a Ring Concentric to a Cylindrical Body in Supersonic Flow

F. Edward Ehlers
Mathematics Research, Boeing Scientific Research Laboratories Seattle, Wash.

July 20, 1960

BECAUSE OF CONTINUED INTEREST in the ring-wing configuration (see, for example, references 1 and 2), it seems worthwhile to correct and improve the theory presented by the author in reference 3. Formulas for the lift and moment in reference 3 are limited to a length l and ring radius R for which the Mach wave from the ring leading edge is not reflected back to the ring. In the following, we shall extend the analysis to a length where multiple reflections of the Mach lines occur.

It has been called to the attention of the author by H. Thommen[4] and B. Friedman[5] that the term $H(O)R'(x)/\beta$ was omitted from Eq. (3.2).* Because part of the function $H(x)$, Eq. (3.6),*

* All equation numbers refer to equations in reference 3.

is periodic of period $2\beta(R-1)$, $H(x)$ has jumps of magnitude 2 at $x = 2n\beta(R-1)$, $n = 1, 2, 3, 4, \ldots$ Then, for $2m\beta(R-1) \leq x \leq 2(m+1)\beta(R-1)$, we gave

$$H'(x) = 1/\beta(R+1) + 2\sum_{n=1}^{m} \delta[x - 2n\beta(R-1)]$$

where $\delta(x)$ is the delta or impulse function. Substituting into the corrected Eq. (3.2)* and also noting the periodic property of the cross-flow solution, we obtain the following relation for the pressure coefficient on the interior of the ring in place of Eq. (4.6)*:

$$C_{p_i} = 2[R(O) - R_i(x)]/\beta^2(R+1) - 2R_i'(x)/\beta - (4/\beta)\sum_{n=1}^{m} R_i'[x - 2n\beta(R-1)] - 2(R^2-1)[x/\beta(R-1) - 2m - 1]\alpha\cos\theta/\beta R^2 \quad (A)$$

for $2m\beta(R-1) < x < 2(m+1)\beta(R-1)$, $m = 0, 1, 2, 3, \ldots$. Thus, the drag produced by the pressure distribution on the interior of the ring, for $2m\beta(R-1) < l < 2(m+1)\beta(R-1)$, is given by

$$C_{D_i} = (1/2Rl)\int_0^l\int_0^{2\pi} C_{p_i}R_i'(x)R_i(x)d\theta\,dx \quad (B)$$

$$= \frac{R(0)[3S_i(l) - S(0)] - 2R_i(l)S_i(l)}{3\beta^2Rl(R+1)} - \frac{1}{\beta Rl}\int_0^l R_i'(x)S_i'(x)dx - \frac{2}{\beta Rl}\sum_{n=1}^{m}\int_{2n\beta(R-1)}^{l} R_i'[x - 2n\beta(R-1)]S_i'(x)dx \quad (C)$$

where $S_i(x) = \pi R_i^2(x)$ is the cross-sectional area enclosed by the inner surface of the ring at x. The exterior drag is found by applying Eq. (B), with the sign changed, to C_p given by Eq. (4.8).* For the drag in the wind direction, we multiply Eq. (C) by $\cos\alpha \cong 1 - \alpha^2/2$ and add the drag due to lift αC_{LW_i}. Using Eq. (6.1)* and Eq. (A) yields for the contribution to the coefficient of lift from pressures on the interior of the ring, for $2m\beta(R-1) \leq l \leq (2m+2)\beta(R-1)$

$$C_{LW_i} = -[\pi\alpha(R^2-1)/\beta R^3][\beta(R-1)/l]\left\{\sum_{n=0}^{m-1}\int_0^2 R_i(x_n)(t-1)dt + \int_0^{l/\beta(R-1)-2m} R_i(x_m)(t-1)dt\right\}$$

where $x_n = \beta(R-1)(t+2n)$. If $R_i(x) \equiv R$ a constant, then with $\tau = l/\beta(R-1)$

$$C_{LW_i} = [\pi\alpha(R^2-1)/2\beta R^2\tau][1 - (\tau - 2m - 1)^2] \quad (D)$$

for $2m < \tau < 2m+2$. This equation reduces to Eq. (6.2)* for $m = 0$. Similarly for the coefficient of lift on the body in the range $\beta(R-1)$ to $l + \beta(R-1)$, we have in place of Eq. (6.4)*

$$C_{LB} = [\pi\alpha(R^2-1)/2\beta R^{5/2}\tau][(\tau - 2m - 1)^2 - 1] \quad (E)$$

for $2m < \tau < 2m+2$. The coefficient of lift for the exterior pressures on the ring is given by Eq. (6.3)* but with βR^2 in the denominator of the first fraction instead of βR. By comparing Eqs. (D) and (E), we find that the lift on the body is $-1/R^{1/2}$ times the lift on the interior of the ring. Thus the combined interior lift force is always positive.

For $x > l + \beta(R-1)$ on the cylindrical body, the vortex sheet behind the trailing edge of the ring influences the pressure distribution. Let $\varphi_1^{(o)}$ and $\varphi_1^{(i)}$ be the exterior cross-flow potential (for $r > R$) and the interior cross-flow potential, respectively, for the range $x > l + \beta(r-R)$ for $r > R$, and $x > l - \beta(r-R)$ for $r < R$. Making the same assumptions as in Section V, page 243, of reference 3, we obtain for the continuity of pressure on the vortex sheet, instead of Eq. (5.3),* the relation

$$\bar{\varphi}_1^{(o)} - \bar{\varphi}_1^{(i)} = \Delta\varphi_1 \quad (F)$$

where $\Delta\varphi_1$ is the difference in potential between the exterior and interior solutions at the wing trailing edge, considered as the origin in x for the transform. The quantity $\Delta\varphi_1$ may be found by integrating the pressure coefficients for the cross-flow solutions and is given by

$$\Delta\varphi_1 = (R - 1/R)\{L(l/\beta R) - (1 - 1/R) \times [l/\beta(R-1) - 2m - 1]^2/2 + (1 - 1/R)/2\} \quad (G)$$

Using Eqs. (5.4)* and (5.5)* in the boundary conditions, we obtain the following transform of the perturbation potential for the flow between the vortex sheet and the cylindrical body:

$$\bar{\varphi}_1^{(i)} = \Delta\varphi_1 p\beta R\, e^{-pl}[K_1'(p\beta R)/K_1'(p\beta)][I_1(p\beta r)K_1'(p\beta) - I_1'(p\beta)K_1(p\beta r)] \quad (H)$$

where the origin of x has been shifted to the ring leading edge by the factor e^{-pl}. The lift on the cylinder for a length $x > l + \beta(R-1)$ is

$$L/(1/2)\gamma pM^2 = 2\alpha\int_{l+\beta(R-1)}^{x}\int_0^{2\pi}\cos^2\theta(\partial\varphi_i^{(i)}/\partial x)dx$$

or

$$C_{LB_S} = -[\pi\alpha/Rl]\{\varphi_1^{(i)}[l + \beta(R-1)] - \varphi_i^{(i)}(x)\}$$

Setting $r = 1$ in Eq. (H), we get

$$\bar{\varphi}_1^{(i)} = -R\Delta\varphi_1 e^{-pl}\, K_1'(p\beta R)/K_1'(p\beta)$$

When we alter the contour of integration for the inversion to the negative p-axis by a cut from the branch point $p = 0$, the function $\varphi_1^{(i)}$ consists of the residue at the origin, the residues at the zeros of $K_1'(z) = 0$ (see p. 232, Ward[6]), and an infinite real integral. For x becoming infinite all terms vanish except the residue at $p = 0$. Thus, $\varphi_1^{(i)}(\infty) = -\Delta\varphi_1/R$. Since for large p,

$$\bar{\varphi}_1^{(i)} \cong -\Delta\varphi_1 e^{-p[l+\beta(R-1)]}\sqrt{R}$$

then

$$\varphi_1^{(i)}[l + \beta(R-1)] = -\Delta\varphi_1\sqrt{R}$$

Therefore, the coefficient of lift on the infinite cylinder induced by the trailing vortex sheet is

$$C_{LB_S} = (\pi\Delta\varphi_1\alpha/Rl)(\sqrt{R} - 1/R)$$

Now the potential difference $\Delta\varphi_1$ from Eq. (G) is positive for $2m\beta(R-1) < l < (2m+2)\beta(R-1)$. Thus, the contribution to the lift on the body from the influence of the vortex sheet is also positive.

In like manner, for $2m < l/\beta(R-1) < 2m+2$, the coefficients of moment about $x = 0$ from the interior of the flat ring and from the cylinder in the range $2\beta(R-1) \leq x \leq l + 2\beta(R-1)$ become

$$C_{m_o w_i} = [\pi\alpha(R^2-1)/6\beta R^2\tau^2]\{-2m + 2(\tau - 2m)^3 - 3(\tau - 2m)^2 + 6m(\tau - 2m - 1)^2\}$$

$$C_{m_o b} = -[\pi\alpha(R^2-1)/3\beta R^{5/2}\tau^2]\{2 - m + (\tau - 2m + 1)^3 - 3(\tau - 2m + 1)^2 + 3m(\tau - 2m - 1)^2\}$$

For $m = 0$, the first expression reduces to Eq. (6.6)* and the second to Eq. (6.8).*

References

[1] Schindel, L. H., *Supersonic Wind Tunnel Tests of Ring-Wing Configurations*, WADC TR 58-220, ASTIA Document No. AD 155534, Dec., 1958.

[2] Crimi, P., *Flutter Analysis of a Supersonic Ring Wing*, AFOSR TN-59-685, Cornell University, Graduate School of Aero. Engrg., June, 1959.

[3] Ehlers, F. E., *The Lift and Moment on a Ring Concentric to a Cylindrical Body in Supersonic Flow*, Journal of the Aeronautical Sciences, Vol. 22, No. 4, pp. 239–248, April, 1955.

[4] Thommen, H. U., Personal Communication, Brown Univ., March 1, 1957.

[5] Friedman, B., Unpublished Lectures on "*Operational Techniques in Compressible Flow*," August, 1956.

[6] Ward, G. N., *Flow past a Quasi-Cylindrical Tube*, Quart. J. Mech. & Appl. Math., Vol. 1, pp. 225–245, June, 1948.

A Note on the Canonical Form of the Thrust-Programming Problem for Power-Limited Flight

Charles Saltzer
Professor of Applied Mathematics, University of Cincinnati, and Thompson Ramo Wooldridge Inc., Cleveland, Ohio
July 20, 1960

THE POWER-LIMITED ROCKET ENGINE is defined by Irving and Blum[1, 2] as an engine for which the rate of mass flow and exhaust velocity can both be varied, subject only to the condition that the jet power is not to exceed a fixed value. It was shown by Irving and Blum[1-4] that the problem of determining a thrust program, i.e., the thrust as a function of the time for which the burn-out mass is maximized, can be formulated as a classical problem of the calculus of variations, namely, to minimize the integral

$$J = {}^1/_2 \int_0^T f^2\, dt \tag{1}$$

where f is the thrust force per unit mass, T is the mission duration and t is the time. In this note the method of Ostrogradsky[5] will be used to construct the Hamiltonian function for some special cases of this problem. The two integrals of the variational equations which were obtained by Irving and Blum will be identified as the Hamiltonian and a component of generalized momentum corresponding to an ignorable coordinate. An integral for nonplanar trajectories will also be given. While the problem considered here is for powered trajectories in a central field, this method is applicable to more general problems if Lagrange multipliers are used and makes it possible to obtain certain integrals quite readily.

The equations of motion of a rocket in inverse-square-law central field of strength μ with the origin at the center are

$$f_r = \ddot{r} - r\dot{\theta}^2 + (\mu/r^2) \tag{2}$$

$$f_\theta = r\ddot{\theta} + 2\dot{r}\dot{\theta} \tag{3}$$

where r and θ are the polar coordinates of the rocket, and f_r and f_θ are the radial and transverse components of the thrust per unit mass, respectively. The thrust per unit mass is

$$f^2 = f_r^2 + f_\theta^2 \tag{4}$$

The first problem considered is the powered transfer between two points given prescribed initial and terminal velocities. The generalized coordinates used are defined by

$$q_1 = r \tag{5}$$

$$q_2 = \dot{r} \tag{6}$$

$$q_3 = \theta \tag{7}$$

$$q_4 = \dot{\theta} \tag{8}$$

Following Ostrogradsky,[5] the corresponding generalized momenta are

$$p_1 = \partial/\partial\dot{r}({}^1/_2 f^2) - (d/dt)(\partial/\partial\ddot{r})({}^1/_2 f^2) = 2\dot{\theta} f_\theta - \dot{f}_r \tag{9}$$

$$p_2 = (\partial/\partial\ddot{r})({}^1/_2 f^2) = f_r = \ddot{r} - r\dot{\theta}^2 + (\mu/r^2) \tag{10}$$

$$p_3 = (\partial/\partial\dot{\theta})({}^1/_2 f^2) - (d/dt)(\partial/\partial\ddot{\theta})({}^1/_2 f^2) = 2\dot{r} f_\theta - 2r\dot{\theta} f_r - (d/dt)(r f_\theta) \tag{11}$$

$$p_4 = (\partial/\partial\ddot{\theta})({}^1/_2 f^2) = r f_\theta = r^2\ddot{\theta} + 2r\dot{r}\dot{\theta} \tag{12}$$

The generalized velocities are obtained from Eqs. (6), (8), (10), and (12) as

$$\dot{q}_1 = q_2 \tag{13}$$

$$\dot{q}_2 = \ddot{r} = p_2 + q_1 q_4^2 - (\mu/q_1^2) \tag{14}$$

$$\dot{q}_3 = q_4 \tag{15}$$

$$\dot{q}_4 = (1/q_1^2)(p_4 - 2q_1 q_2 q_4) \tag{16}$$

The Hamiltonian H, defined in the usual way

$$H = \sum_{k=1}^{4} p_k \dot{q}_k - {}^1/_2 f^2 \tag{17}$$

becomes

$$H = (1/2)[p_2^2 + (p_4^2/q_1^2)] + p_1 q_2 + p_2[q_1 q_4^2 - (\mu/q_1^2)] + p_3 q_4 - (2q_2 q_4 p_4/q_1) \tag{18}$$

The Euler equations take the canonical form

$$\dot{q}_k = (\partial H/\partial p_k) \quad (k = 1, 2, 3, 4) \tag{19}$$

$$\dot{p}_k = -(\partial H/\partial q_k) \quad (k = 1, 2, 3, 4) \tag{20}$$

Since q_3 does not appear in the Hamiltonian, p_3 is constant. If the angular momentum per unit mass

$$h = r^2\dot{\theta} \tag{21}$$

is introduced, Eq. (11) gives one integral of the motion as

$$-p_3 = r\dot{f}_\theta - \dot{r} f_\theta + (2h f_r/r) = C_1 \tag{22}$$

In addition, since the Hamiltonian is also independent of the time, it is an integral. In terms of the original parameters and the constant of integration C_1, this integral can be written in the form

$${}^1/_2 f^2 - \dot{r}\dot{f}_r + f_r[(h^2/r^3) - (\mu/r^2)] - (h/r^2)C_1 = C_2 \tag{23}$$

If, instead of specifying the initial and terminal values of r, $\dot{r}$, θ and $\dot{\theta}$, the initial and terminal values of r, $\dot{r}$, and h are specified, the equations of motion may be written as

$$f_r = \ddot{r} - (h^2/r^3) + (\mu/r^2) \tag{24}$$

$$f_\theta = (1/r)(dh/dt) \tag{25}$$

The generalized coordinates are now defined by

$$q_1 = r \tag{26}$$

$$q_2 = \dot{r} \tag{27}$$

$$q_3 = h \tag{28}$$

and the corresponding generalized momenta are

$$p_1 = (\partial/\partial\dot{r})({}^1/_2 f^2) - (d/dt)(\partial/\partial\ddot{r})({}^1/_2 f^2) = -\dot{f}_r \tag{29}$$

$$p_2 = (\partial/\partial\ddot{r})({}^1/_2 f^2) = f_r = \ddot{r} - (h^2/r^3) + (\mu/r^2) \tag{30}$$

$$p_3 = (\partial/\partial h)({}^1/_2 f^2) = (f_\theta/r) = (\dot{h}/r^2) \tag{31}$$

Hence, the generalized velocities are

$$\dot{q}_1 = q_2 \tag{32}$$

$$\dot{q}_2 = p_2 + (q_3^2/q_1^3) - (\mu/q_1^2) \tag{33}$$

$$\dot{q}_3 = q_1^2 p_3 \tag{34}$$

and the Hamiltonian is

$$H = \sum_{k=1}^{3} p_k \dot{q}_k - {}^1/_2 f^2 = {}^1/_2(p_2^2 + p_3^2 q_1^2) + p_2[(q_3^2/q_1^3) - (\mu/q_1^2)] + p_1 q_2 \tag{35}$$

This Hamiltonian is again an integral of the Euler equations, and in the original parameters is

$${}^1/_2 f^2 - \dot{r}\dot{f}_r + f_r(h^2/r^3) - (\mu/r^2) = C_2 \tag{36}$$

For powered trajectories in three dimensions, the equations of motion in Cartesian coordinates are

$$f_k = \ddot{x}_k + (\mu x_k/r^3) \quad (k = 1, 2, 3) \tag{37}$$

where

$$r^2 = x_1^2 + x_2^2 + x_3^2 \tag{38}$$

x_1, x_2, x_3 are the Cartesian coordinates of the rocket, f_1, f_2, and f_3 are the components of thrust per unit mass parallel to the coordinate axes, and

$$f^2 = f_1^2 + f_2^2 + f_3^2 \tag{39}$$

If the generalized coordinates are defined by

$$q_{2k-1} = x_k, \quad q_{2k} = \dot{x}_k \quad (k = 1, 2, 3) \tag{40}$$

the generalized momenta are

$$p_{2k-1} = \frac{\partial}{\partial\dot{x}_{2k-1}}({}^1/_2 f^2) - (d/dt)(\partial/\partial\ddot{x}_{2k-1})({}^1/_2 f^2) = -f_k, \quad (k = 1, 2, 3) \tag{41}$$

$$p_{2k} = \frac{\partial}{\partial \dot{x}_{2k-1}} (1/2 f^2) = f_k \quad (k = 1, 2, 3, \qquad (42)$$

Hence, the generalized velocities are

$$\dot{q}_{2k-1} = q_{2k}, \quad \dot{q}_{2k} = p_{2k} - [\mu q_{2k-1}/(q_1^2 + q_3^2 + q_5^2)^{3/2}](k = 1, 2\ 3) \qquad (43)$$

The Hamiltonian

$$H = \sum_{k=1}^{6} p_k \dot{q}_k - 1/2 f^2 \qquad (44)$$

is independent of the time and is again an integral of the motion. In the original coordinates this integral is

$$1/2 f^2 - \sum_{k=1}^{3} \dot{x}_k \dot{f}_k - (\mu/r^3) \sum_{k=1}^{3} x_k f_k = C \qquad (45)$$

It may be noted that the transformation of the thrust-programming problem to the Hamiltonian form makes it possible to apply the Hamilton-Jacobi theory to this problem.

References

[1] Irving, J. H., *Low-Thrust Flight: Variable Exhaust Velocities in Gravitational Fields*, Space Technology, H. Seifert, Ed., pp. 10-01 to 10-54, John Wiley and Sons, Inc., New York, 1959.

[2] Irving, J. H., and Blum, E. K., *Comparative Performance of Ballistic and Low-Thrust Vehicles for Flight to Mars*, 2nd Annual AFOSR Astronautics Symposium, Denver, Colo., April, 1958.

[3] Blum, E. K., *Optimal Rocket Trajectories*, June, 1957 (unpublished).

[4] Saltzer, C., Craig, R. T., and Fetheroff, C. W., *Comparison of Chemical and Electric Propulsion Systems for Interplanetary Travel*, Proc. I.R.E., Vol. 48, No. 4, April, 1960.

[5] Whittaker, E. T., *A Treatise on the Analytical Dynamics of Particles and Rigid Bodies* 4th Ed., pp. 265-267, Dover Publications, New York, 1944.

Effect of Deceleration on Pressure Distribution Along a Slender Cone in Supersonic, Transonic, and Subsonic Flight†

C. T. Hsu and D. A. Anderson
Associate Professor and Instructor, Respectively, Department of Aeronautical Engineering, Iowa State University, Ames, Iowa

July 20, 1960

Symbols

$A(X)$	=	cross-sectional area
a	=	speed of sound in the undisturbed fluid
$2b$	=	constant deceleration
M_0	=	instantaneous Mach number at $t = 0$
$S(x, t)$	=	source strength
x, r	=	cylindrical coordinates fixed in the undisturbed fluid
$U(t)$	=	instantaneous velocity of the body along negative x-axis
β	=	$(bx/a^2) > 0$, deceleration parameter
ξ, τ	=	variables of x and t, respectively
ϕ	=	perturbation velocity potential

† This work was partially supported by Sandia Corporation, New Mexico.

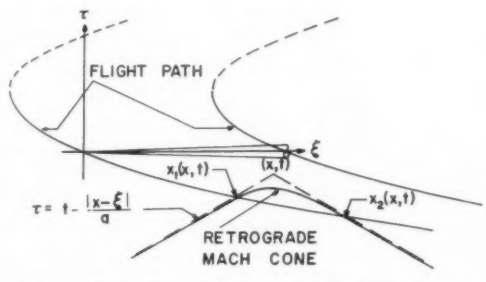

FIG. 1. Body flight path and retrograde Mach cone.

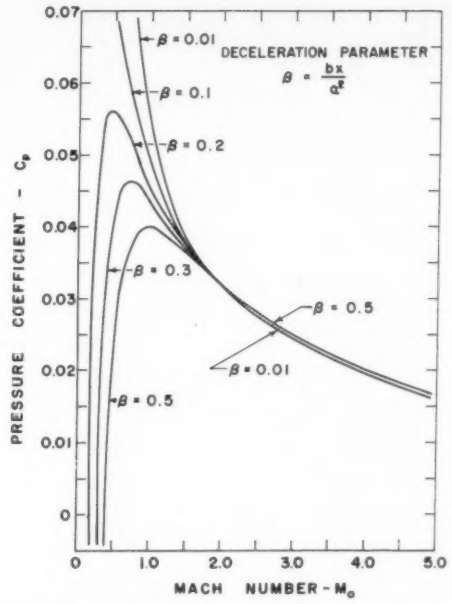

FIG. 2. Effect of deceleration on pressure coefficient, $\delta = 5°$.

IN THE PRESENT NOTE, the effect of constant deceleration on pressure distribution along a slender cone is analyzed for arbitrarily large values of β in all flight speed ranges. Simple approximate expressions for pressure coefficients are also given.

The asymptotic potential (valid near the body) for a slender body of revolution performing arbitrary motion along its axis was obtained by Cole[1,2]

$$\phi(x, r, t) = (1/2\pi)S(x, t) \log (r/2) - (1/4\pi)\{S[x_1, t - (x - x_1)/a] \log (x - x_1) + S[x_2, t - (x_2 - x)/a] \times \log (x_2 - x)\} - \frac{1}{4\pi} \int_{x_1}^{x_2} \left[\frac{1}{a} \frac{\partial S(\xi, \tau)}{\partial \tau} + \operatorname{sgn}(x - \xi) \frac{\partial S(\xi, \tau)}{\partial \xi} \right] \times \log |x - \xi| \, d\xi + \ldots \qquad (1)^*$$

where

$$\tau \doteq t - (|x - \xi|)/a \qquad (2)$$

is the retrograde Mach cone. The integral in Eq. (1) is evaluated for those values of ξ which are intersected by the flight path of the cone apex** given by

$$\xi = -M_0 a\tau + b\tau^2 \qquad (3)$$

and the surface of the retrograde Mach cone[1, 2] (see Fig. 1). Therefore, the integration limits x_1 and x_2 can be determined by solving ξ from Eqs. (2) and (3), i.e.,

$$x_1 = x - at + (a^2/2b)[M_0 + 1 - \sqrt{(M_0 + 1)^2 + (4b/a^2)(x - at)}] \qquad (4)$$

$$x_2 = x + at + (a^2/2b)[-(M_0 - 1) + \sqrt{(M_0 - 1)^2 + (4b/a^2)(x + at)}] \qquad (5)$$

The source strength $S(x, t)$ is known for a given body shape[2]

$$S(x, t) = U(t)A'(X) \qquad (6)$$

where

* It is believed to be a misprint that Cole has $[\partial S(\xi, \tau)/\partial t]$ and $[\partial S(\xi, \tau)/\partial x]$ in the integral term of Eq. (1).

** For supersonic flight, the retrograde Mach cone from the body will never intersect the flight path of the base of the cone. For subsonic flight, the results are valid where the retrograde Mach cone from the body never intersects the flight path of the base of the cone, i.e., $x < L - (a^2/4b)(1 - M_0)^2$. L is the length of the cone.

$$X = x + \int_0^t U(\tau)d\tau$$

is a coordinate fixed in the body. In our case

$$U(\tau) = -d\xi/d\tau = M_0 a - 2b\tau \tag{7}$$

and

$$A(x, t) \doteq \pi\delta^2(x + M_0 at - bt^2)^2 \tag{8}$$

Substituting Eqs. (7) and (8) into Eq. (6), we have

$$S(x, t) = 2\pi\delta^2(M_0 a - 2bt)(x + M_0 at - bt^2) \tag{9}$$

Substituting Eqs. (4), (5), and (9) into Eq. (1) and performing the integration, the velocity potential ϕ can be obtained. The pressure coefficient in unsteady flow, including squared terms,[2] is

$$C_p = -(2/U^2)(\partial\phi/\partial t) - (1/U^2)(\partial\phi/\partial r)^2 \tag{10}$$

Substituting ϕ and Eq. (7) into Eq. (10) and then setting $t = 0$, and $r \doteq \delta x$, the surface pressure coefficient of a slender cone moving at instantaneous Mach number M_0 with constant deceleration $2b$ is

$$C_p/\delta^2 = [1 - (2\beta/M_0^2)] \log \left\{ [-(M_0 + 1) + \sqrt{(M_0 + 1)^2 + 4\beta}]\,[-(M_0 - 1) + \sqrt{(M_0 - 1)^2 + 4\beta}]/\delta^2\beta^2 \right\} - \left(5 - \frac{1}{M_0^2} - \frac{6\beta}{M_0^2}\right) + \frac{M_0^3 + 2M_0^2 + M_0/2 - (1/2) + 4\beta M_0 - 2\beta}{M_0^2\sqrt{(M_0 + 1)^2 + 4\beta}} + \frac{M_0^3 - 2M_0^2 + (M_0/2) + (1/2) + 4\beta M_0 + 2\beta}{M_0^2\sqrt{(M_0 - 1)^2 + 4\beta}} + (2\beta/M_0)\left[\frac{1 - [1/\sqrt{(M_0 + 1)^2 + 4\beta}]}{-(M_0 + 1) + \sqrt{(M_0 + 1)^2 + 4\beta}} + \frac{1 + [1/\sqrt{(M_0 - 1)^2 + 4\beta}]}{-(M_0 - 1) + \sqrt{(M_0 - 1)^2 + 4\beta}}\right] \tag{11}$$

Eq. (11) is plotted in Fig. 2 for a cone of semiangle $\delta = 5°$. A few interesting results may be stated as follows: (1) The surface pressure (or, specifically, the drag) of a slender cone is reduced if deceleration occurs at a flight speed below $M_0 \doteq 2$, but it is increased if deceleration occurs above $M_0 \doteq 2$. (2) If C_p vs. β (or x) is plotted with M_0 as parameter, the curve will show that C_p increases slightly along the cone surface for $M_0 > 2$. This phenomenon is quite different from the steady supersonic flow which ensures constant C_p along the cone surface. (3) The effects of deceleration are much more pronounced in the subsonic and transonic ranges than the supersonic range.

Approximate Expressions for C_p

(1) *Supersonic Range:*—Eq. (11) may be expanded in terms of ζ. Retaining only the first-order terms, Eq. (11) becomes

$$C_p/\delta^2 = -2\left[\frac{1 - 2(M_0 - 1)^2\zeta}{M_0}\right] \log \frac{\delta}{2}\sqrt{M_0^2 - 1} - \frac{(M_0 + 1)^2 - [6M_0^2 - 22 - (4/M_0^2)]\zeta}{(M_0 + 1)^2 + 4(M_0^2 + 1)\zeta} \tag{12}$$

where $\zeta = \beta/(M_0 - 1)^2$. The deviation of Eq. (12) from the exact expression is insignificant. For example, at $M_0 = 1.1$, with $\beta = 0.05$ and $\delta = 5°$, Eq. (12) yields a value that is only 5 per cent less than that from Eq. (11). If we neglect $\zeta \ll 1$, Eq. (12) gives the steady supersonic C_p for a slender cone:

$$C_p/\delta^2 = -2 \log (\delta/2)\sqrt{M_0^2 - 1} - 1 \tag{13}$$

(2) *Transonic Range:*—For $M_0 = 1$, Eq. (11) may be further simplified by expanding β in a power series and retaining only the first-order terms. Therefore,

$$C_p/\delta^2 = -2(1 - 2\beta) \log \sqrt[4]{(\beta/4)}\delta - 1 + (27/4)\beta + 4\sqrt{\beta} \tag{14}$$

Eq. (14) yields an error of 0.14 per cent of the exact value for $\beta = 0.05$. If we assume $\beta \ll 1$ and neglect $\sqrt{\beta}$ with respect to one, Eq. (14) reduces to

$$C_p/\delta^2 = -2 \log \sqrt[4]{(\beta/4)}\delta - 1 \tag{15}$$

which was first obtained by Cole.[1] Eq. (15) gives an error of 4.3 per cent for $\beta = 0.01$, and 8 per cent for $\beta = 0.05$ which is evidently not too small.

(3) *Subsonic Range:*—Eq. (11) may be expanded in terms of η and, neglecting η with respect to one,

$$C_p/\delta^2 = -2 \log (\delta/2)\sqrt{\eta(1 - M_0^2)} - (4M_0^2 - 2M_0 - 1)/M_0^2 \tag{16}$$

where $\eta = [\beta/(1 - M_0)^2] \ll 1$. Generally, the deviation from the exact values is greater for the subsonic case than it is for either transonic or supersonic cases.

References

[1] Cole, J. D., *Note on Nonstationary Slender-Body Theory.* Journal of the Aeronautical Sciences, Readers' Forum, Vol. 20, No. 11, pp. 798–799, November, 1953.

[2] Cole, J. D., *Acceleration of Slender Bodies of Revolution through Sonic Velocity,* J. Appl. Phys., Vol. 26, No. 3, pp. 322–327, March, 1955.

Shock Response to Downstream Disturbances*

Roy M. Gundersen
Associate Professor of Mathematics,
Illinois Institute of Technology, Chicago, Ill.
July 21, 1960

A problem of interest in diffuser dynamics is to determine the effect of downstream (behind the shock) perturbations on a normal shock in a channel flow. In reference 1, the forcing variable is a pressure perturbation downstream of the shock, and the imposed transient is obtained as a Laplace transfer function. Entropy perturbations behind the shock are not considered and only transients that are slow relative to the transit times for sonic waves are considered, so that the partial derivatives with respect to time are omitted from the linearized equations.

In the present paper, a linearized analysis, based on small area variations,[2] is utilized to discuss a problem which differs from Hurrell's analysis in that the response to an arbitrary perturbation is determined, entropy perturbations are considered, and general solutions to the complete perturbation equations are used. Further, it is assumed that the gas in front of the shock is at rest, which results in a slight simplification without overly restricting the results, since a downstream disturbance does not affect the upstream flow. Attention is focused on determining the shock-velocity perturbation from which the shock-position perturbation may be obtained by integration. Use of the linearized equations allows the solution to be obtained as the superposition of the perturbations of the shock due to the area variations and the downstream perturbation. The results of any interaction between these would be of second order and thus neglected. It is found that the shock-velocity perturbation is singular for sonic flow just behind the shock with the singularity contained in terms due to the downstream perturbation. This singularity occurs for a shock strength, defined as the pressure jump across the shock, of about 4.83, a rather strong shock. This singularity may mask large nonlinear disturbances.

When the equations which govern the one-dimensional, unsteady flow of an inviscid, ideal compressible gas in a tube of variable cross section are linearized in the neighborhood of a known (isentropic) solution, the general solution for an initially uniform state is

* This work was supported by a grant from the National Science Foundation.

$$H_0 = 2R'(x - u_0t)$$

$$A \equiv u_1/2 + c_1/(\gamma - 1) = F[x - (u_0 + c_0)t] + c_0^{-1}R(x - u_0t) - u_0c_0E_1/2E_0(u_0 + c_0)$$

$$B \equiv -u_1/2 + c_1/(\gamma - 1) = G[x - (u_0 - c_0)t] + c_0^{-1}R(x - u_0t) - u_0c_0E_1/2E_0(u_0 - c_0) \quad (1)$$

where u, c, s, E_0, E_1, and γ are the particle velocity, local speed of sound, specific entropy, original uniform cross-sectional area, area perturbation, and ratio of the specific heats at constant pressure c_p and at constant volume c_v. $H_0c_v\gamma(\gamma - 1) = c_0^2s_{1x}$, P is the pressure, ρ the density, the subscript zero denotes the basic (known) flow, the subscript 1 the terms of first order, and F, G, and R are arbitrary functions of one variable.

For the present problem, denote the rest state in front of the shock by the subscript 0, and the state behind by the subscript 2. Let w be the shock velocity

$$v_2 = w - u_2, \qquad m_0 = w/c_0,$$

$$m_1 = v_2/c_2, \qquad m = u_2/c_2.$$

Perturbations of a base quantity will be denoted by a bar.

The pressure perturbation behind the shock was first given by Chester,[3] using a different analysis. The present analysis has led to the same result,[2] and leads to the following expression for the shock-velocity perturbation due to the area variations:

$$\bar{w}/c_0 = \bar{m}_0 = -(m_0^2 - 1)E_1/m_0E_0(1 + m)(1 + 2m_1 + m_0^{-2}) \quad (2)$$

Now, suppose that at a point downstream of the shock, say, $x = a$, an arbitrary perturbation is given, viz.,

$$u = u_2 + 2\xi(t), \quad s = s_2 + \psi(t), \quad p = p_2 + \phi(t)$$

where u_2, s_2, and p_2 are constants. Expressing $\bar{c}_2$ in terms of these quantities, gives

$$\bar{c}_2 = c_2\psi(t)/2c_v\gamma + c_2(\gamma - 1)\phi(t)/2\gamma p_2 \equiv (\gamma - 1)\beta(t) \text{ on } x = a$$

Applying these subsidiary conditions to the general solution for the nonisentropic perturbation of a constant state, Eqs. (1), yields the perturbed flow due to the downstream perturbation. Since, in general

$$\bar{c}_2/c_2(\gamma - 1) - s_2/\nu = \bar{p}_2/2\gamma p_2$$

the pressure perturbation is easily determined, and the shock-velocity perturbation, due to this pressure perturbation, is determined by evaluating the general solution on the shock—i.e., for $x = wt$ and utilizing the result that

$$\bar{p}_2/\gamma p_2 = 4m_0\bar{m}_0/(2\gamma m_0^2 - \gamma + 1)$$

This gives:

$$4m_0\bar{m}_0 = (2\gamma m_0^2 - \gamma + 1)\{c_2^{-1}\eta[(a/c_2 + (1 - m_1)t)/(1 + m)] + c_2^{-1}\xi[(a/c_2 - (1 + m_1)t)/(m - 1)] - \nu^{-1}\psi[(a/c_2 + (1 - m_1)t)/(1 + m)] - \nu^{-1}\psi[(a/c_2 - (1 + m_1)t)/(m - 1)] + [E_1(a) - E_1(wt)]m^2/E_0(m^2 - 1)\} \quad (3)$$

where

$$\eta(t) \equiv \zeta(t) + \beta(t) \qquad \xi(t) \equiv \beta(t) - \zeta(t) \qquad \text{and} \qquad \nu = 2c_v\gamma(\gamma - 1)$$

From Eqs. (2) and (3), since $\bar{m}_0 = \bar{w}m_0/w$, it follows that the total shock-velocity perturbation may be written as:

$$\bar{w}/w = -[(1 - m_0^{-2})/(1 + m)(1 + 2m_1 + m_0^{-2}) + \{m^2[2\gamma - (\gamma - 1)m_0^{-2}]/4(m^2 - 1)\}E_1(wt)/E_0 + \{c_2^{-1}\eta[(a/c_2 + (1 - m_1)t)/(1 + m)] + c_2^{-1}\xi[(a/c_2 - (1 + m_1)t)/(m - 1)] - \nu^{-1}\psi[(a/c_2 + (1 - m_1)t)/(1 + m)] - \nu^{-1}\psi[(a/c_2 - (1 + m_1)t)/(m - 1)] + m^2E_1(a)/E_0(m^2 - 1)\}[2\gamma - (\gamma - 1)m_0^{-2}]/4 \quad (4)$$

For discussion, Eq. (4) is specialized to the case that on

$$x = a, \ \bar{u}_2 = 0, \ \bar{s}_2 = 0 \text{ so that } \psi \equiv 0, \quad \xi \equiv 0, \quad \eta \equiv \xi \equiv \beta \equiv \phi/2\rho_2.$$

Then

$$\bar{w}/m_0c_0 = -(1 - m_0^{-2})E_1(wt)/E_0(1 + m)(1 + 2m_1 + m_0^{-2}) + [2\gamma - (\gamma - 1)m_0^{-2}][E_1(a) - E_1(wt)]m^2/4E_0(m^2 - 1) + \{\beta[(a/c_2 + (1 - m_1)t)/(1 + m)] + \beta[(a/c_2 - (1 + m_1)t)/(m - 1)]\}(\gamma + 1)/4m_1c_0 \quad (5)$$

For $\gamma = 7/5$, with the shock strength defined as the pressure ratio $p_2/p_0 = z$, the term $[-(1 - m_0^{-2})/(1 + m)(1 + 2m_1 + m_0^{-2})]$, due to area variations only, is a monotonic decreasing function of z with only a small range of variation from zero, for a very weak shock, to an asymptotic limit of -0.238, for a very strong shock. The term $[2\gamma - (\gamma - 1)m_0^{-2}]/4$ is a monotonic increasing function of z with a variation from 0.6 to 0.7. The term $m^2/(m^2 - 1)$ is zero for a very weak shock and, for $m < 1$, is a monotonic decreasing function of z and singular for $z = 4.83$. For $m > 1$, it is a monotonic increasing function of z with an asymptotic limit of 1.39. The coefficient $(\gamma + 1)/4m_1$ is a monotonic increasing function of z varying between the limits of 0.6 and 1.59. Several particular cases of Eq. (5) are the following, where the number in the parentheses following $\bar{w}$ represents the shock strength:

$$\bar{w}(2) = 0.125c_0E_1(wt)/E_0 - 0.289c_0E_1(a)/E_0 + 1.08\{\beta(0.833a/c_0 + 0.166t) + \beta(-2.35a/c_0 + 3.34t)\}$$

$$\bar{w}(3) = 1.01c_0E_1(wt)/E_0 - 1.235c_0E_1(a)/E_0 + 1.51\{\beta(0.802a/c_0 + 0.202t + \beta(-5.08a/c_0 + 6.08t)\}$$

$$\bar{w}(4) = 4.78c_0E_1(wt)/E_0 - 5.08c_0E_1(a)/E_0 + 1.89\{\beta(0.79a/c_0 + 0.212t) + \beta(-14.5a/c_0 + 15.5t)\}$$

For the particular case of the constant-area duct—i.e., $E_1 \equiv 0$, it is seen that the shock velocity changes as long as there is a pressure disturbance.

A direct comparison with the results of reference 1 is difficult due to differences in formulation and solution. There, the time dependence has essentially been neglected save that $\bar{w} = d\bar{x}/dt$. The term E_1 written as $(E_1/\bar{x})\,\bar{x}$ and $(E_1/\bar{x})$ was replaced by the derivative of the cross-sectional area evaluated at the steady-state shock position. Also, the flow in front of the shock was not at rest so that there was a $\bar{p}_0$ due to the area variations. The Laplace transform was taken to what corresponded to Eq. (5) of the present paper with the result that $\bar{x}(\lambda)/\bar{p}_x(\lambda) = k/(1 + \sigma\lambda)$, where λ was the transform parameter and k and σ were defined in terms of a dimensionless quantity σ' which varied only slightly for m_0 between 1 and 3.

Further, the pressure perturbation was given at a station just behind the shock, whereas in the present paper it is given for an arbitrary position downstream of the shock.

Thus, when a shock moving through a tube of a slowly varying cross-sectional area was subjected to an arbitrary downstream perturbation, the shock-velocity perturbation was obtained as the sum of the perturbations due to the area variations alone, and those due to the downstream perturbation. One of the terms due to this latter disturbance changed signs according as $m > 1$ or $m < 1$ and was singular at $m = 1$. It is felt that this singularity may mask a large nonlinear disturbance, and a second-order theory might be useful in examining this result.

References

[1] Hurrell, H. G., *Analysis of Shock Motion in Ducts During Disturbances in Downstream Pressure*, NACA TN 4090, 1957.

[2] Gundersen, R., *The Flow of a Compressible Fluid with Weak Entropy Changes*, J. Fluid Mech., Vol. 3, p. 553, 1958.

[3] Chester, W., *The Quasi-Cylindrical Shock Tube*, Phil. Mag., Ser. 7, Vol. 45, p. 1293, 1954.

Comments on "Space Vehicle Environment"

Kenneth L. Goldman
Technical Staff, Space Technology Laboratories, Inc., Los Angeles, Calif.
July 28, 1960

In the discussion of Thermal Radiations in the paper "Space Vehicle Environment,"[1] the problem of heat losses from manned vehicles at distances from the Sun appreciably greater than from the Earth was briefly treated. It was stated that, for the extreme case where solar radiation is negligible compared to surface heat loss, an internal heat generation of about 100 watts/sq.m. would be required with about 1 in. of good insulation between the interior and the outer surface. This approach ignores the use of low-emissivity surface optical properties discussed earlier in the paper.[1]

If one were to coat the vehicle with a low-emissivity material such as vacuum-plated aluminum, $\epsilon = 0.05$, the required internal heat generation for an interior temperature of 75°F. would be reduced to 20 watts/sq.m. without any insulation whatsoever—i.e., thin-walled skin. The use of an insulating material such as multiple layers of reflective aluminum foil evacuated to space ($k \sim 3\text{–}5 \times 10^{-5}$ B.t.u./hr.-ft.-°R.) would permit a further reduction of the required heat generation to less than 2 watts/sq.m. for half inch of insulating thickness. This approach is analogous to that of a low-α/ϵ spinning sphere orbiting about a near planet, Fig. 6 of reference 1, where the planetary radiation input is replaced by the manned-space-vehicle internal heat generation.

Reference

[1] Gazley, Carl, Jr., Kellogg, W. W., and Vestine, E. H., *Space Vehicle Environment*, Journal of the Aero/Space Sciences, Vol. 26, No. 12, pp. 770–782, 814, December, 1959.

✦ ✦ ✦

Subsonic Nonplanar Lifting Surface Problems (*Continued from page 112*)

chord. The overall agreement between the experimental and theoretical results shown here compares well with that for the plane wing of Fig. 6.

The comparisons shown above establish the validity of the proposed method for wing loading calculations. It may also be concluded that the results of such calculations have an accuracy well within the requirements for most aircraft design studies.

Computation Time

Most engineers, after a more than casual perusal of the analytical development of the proposed method, are horrified to note that the innocuous appearing downwash relationship (19) really contains a number of quintuple and sextuple summations. They immediately envision the prospect of years of hand calculation, or days of electronic computer calculation, required to achieve a single solution. A meaningful solution might, indeed, require years of hand calculation. However, the running time required on an IBM 704 computer is measured in minutes, as indicated in Fig. 9. The time per control point shown includes data input, computation and print out of the solution. As seen from Fig. 9, the 45 control point solution of Fig. 8 required 25 minutes of computer time, a nominal expenditure for a solution not otherwise available.

References

[1] Blenk, H., *Der Eindecker als Tragende Wirbelfläche*, ZAMM, Vol. 5, 1925, translated as NACA TM 1111, 1947.

[2] Weissinger, J., *Über die Auftriebsverteilung von Pfeilflügeln* F.B. 1553, 1942, translated as NACA TM 1120, 1947.

[3] Multhopp, H., *Methods for Calculating the Lift Distribution of Wings (Subsonic Lifting Surface Theory)*, Aeronautical Research Council, R&M No. 2884, 1950.

[4] van de Vooren, A. I., *An Approach to Lifting Surface Theory*, Netherlands NLL Report F. 129, 1953.

[5] Bisplinghoff, R. L., Ashley, H., and Halfman, R. L., *Aeroelasticity*, pp. 221–227; Addison-Wesley Publishing Co., Cambridge, Mass., 1955.

[6] Birnbaum, W., *Die Tragende Wirbelfläche als Hilfsmittel zur Behandlung des ebenen Problems der Tragflügeltheorie*, ZAMM, Vol. 3, 1923.

[7] Falkner, V. M., *The Solution of Lifting Plane Problems by Vortex Lattice Theory*, Aeronautical Research Council, ARC 10, 895, 1947.

[8] Dickson, R., *The Relationship Between the Compressible Flow Round a Swept Back Aerofoil and the Incompressible Flow Round Equivalent Aerofoils*, British RAE Aero 2146, 1946.

[9] Grobner, W., and Hofreiter, N., *Integraltafel*, Vol. 2, pp. 112–113; Springer–Verlag, Vienna, Austria, 1950.

[10] Ursell, F., *Notes on the Linear Theory of Incompressible Flow Round Symmetrical Swept-Back Wings at Zero Lift*, The Aeronautical Quarterly, Vol. 1, Part 1, May, 1949.

[11] Garner, H. C., *Theoretical Calculations of the Distribution of Aerodynamic Loading on a Delta Wing*, Aeronautical Research Council, R&M No. 2819, March, 1949.

[12] Malavard, L., Duquenne, R., Enselme, M., and Grandjean, C., *Propriétés Calculées D'Ailes en Delta Echancré ou Non. Calcul par Analogies Electriques*, ONERA, TN No. 25, 1955.

[13] Kolbe, C. D., and Boltz, F. W., *The Forces and Pressure Distribution at Subsonic Speeds on a Plane Wing Having 45° of Sweepback, an Aspect Ratio of 3, and a Taper Ratio of 0.5*, NACA RM L51G31, October, 1951.

[14] Boltz, F. W., and Kolbe, C. D., *The Forces and Pressure Distribution at Subsonic Speeds on a Cambered and Twisted Wing Having 45° of Sweepback, an Aspect Ratio of 3, and a Taper Ratio of 0.5*, NACA RM A52D22, July, 1952.

INTERNATIONAL AEROSPACE ABSTRACTS

New IAS Periodical—First Issue, January 1961

This new monthly combines, in improved format, the abstracts and books sections formerly printed in *Aerospace Engineering*. For uninterrupted abstract service, enter your subscription now.

REQUIREMENTS *for* CONTRIBUTIONS

to the publications of the

INSTITUTE *of the* AEROSPACE SCIENCES

The Institute of the Aerospace Sciences invites both members and nonmembers from any country to submit papers for publication in the JOURNAL OF THE AEROSPACE SCIENCES and AEROSPACE ENGINEERING. The Institute, following the practice of other societies, does not pay for contributions.

The following directions for the preparation of papers, if followed by authors, will save correspondence, avoid the return of papers for changes, minimize the work of preparation for the printer, and save the expense due to the charges made for "author's corrections."

MANUSCRIPTS: The original typewritten copy of the paper is desired. **To expedite review, an additional copy of both the manuscript and figures should be submitted.** The manuscript must be double or triple spaced on one side of white paper sheets, consecutively numbered. There should be wide margins to allow for the marking of directions to the printer. Correcting, changing, or adding to papers after they are in type is costly. It is, therefore, imperative that papers submitted be in final form. Typographical errors may be corrected on proofs, but if authors wish to add material, they may do so at their own expense. In mailing, drawings may be rolled, but manuscripts should be sent flat. Send by first-class mail (register if you wish for your own protection) to the Editorial Office, Institute of the Aerospace Sciences, 2 East 64th Street, New York 21, N.Y. All manuscripts will be examined by the Editorial Committee and by the Editor. Authors will be advised as promptly as possible whether the paper is acceptable for publication.

TITLES: The title of the paper should be brief. The name and initials of the author should be written as he prefers. The use of the full name of an author is advocated because of the frequent duplication of initials and surnames which sometimes makes it difficult to establish the identity of the author. This is particularly important for large annual indexing and abstracting services. All titles and degrees or honors are omitted. The name of the organization with which the author is associated should be placed after his name on a separate line. The date on which the paper is received will be inserted by the Editor. The author's title or position should be indicated in a footnote.

SUMMARIES OR ABSTRACTS: An abstract to be printed at the beginning should accompany each article. It should be adequate as an *index* and as a *summary*. It should contain a statement of major conclusions reached, since summaries in many cases constitute the only source of information used in compiling scientific reference indexes. Abstracts printed in other journals, especially foreign, in most cases consist of summaries from printed papers. The summary should explain as adequately as possible the major conclusions to a nonspecialist in the subject and should contain from 100 to 300 words, depending on the length of the paper.

SUBHEADINGS: Subheadings should be inserted by the author at frequent intervals. The work of editorial preparation will be simplined by the author's provision of many subheadings.

MATTER USUALLY DELETED: Photographs or illustrations of little technical interest and not showing advances in general practice. Too detailed tabular matter (general results of such tables may be included in the text). Lengthy descriptions of materials or processes or of preliminary experiments or theories that preceded final results; salient features only are of interest.

REFERENCES: References should be numbered consecutively and grouped together at the end of the manuscript, with only the corresponding number being mentioned in the text. The arrangement should be as follows. For books: [1]Durand, W. F., *Aerodynamic Theory*, 1st Ed., Vol. 1, p. 23; Julius Springer, Berlin, 1934. For magazines: [1]England, C. R., Crawford, A. B., and Mumford, W. W., *Some Results of a Study of Ultra-Short-Wave Transmission Phenomenon*, Proc. IRE, Vol. 20, No. 12, pp. 481–482, March, 1933. Please give author, title edition, volume, number, page, publisher, and place and date of publication as indicated. Omission of one required fact causes much extra editorial work and possible inaccuracies.

ILLUSTRATIONS: Illustrations should accompany manuscripts, and each should always be referred to in the text by number. Drawings or graphs should not be larger than 12 × 16 inches, and must be made with jet black India ink on white paper or tracing cloth, the latter being preferred. *Do not use typewriter for lettering.* The smallest lettering on 8 × 10 inch figures should be no less than $^1/_4$ inch high. Cross-section paper (white with black lines) may be used, but it should not have more than 4 lines per inch. If finer ruled paper is used, the major division lines should be drawn in with black ink, omitting the finer divisions. In the case of finely ruled paper, only blue-lined paper can be accepted. *Tracing paper and blueprints* are not acceptable. Lettering and all markings must be large enough to be readable after reduction to single-column width ($3^3/_{16}$ in.). Mail rolled or flat; never fold. Drawings that cannot be reproduced (including pencil drawings) will be returned to the author for redrawing, thus delaying publication of the paper. Photographs should be distinct and show clear black and white contrasts. They must be on glossy white paper. Avoid round or oval photographs.

CAPTIONS AND LEGENDS: Legends or captions must accompany each drawing or photograph submitted. If written on the drawing or photograph they should be placed below and well outside the part to be reproduced. Each table should have a caption such as Table 1, Table 2, Table 3, etc. Captions should be complete in themselves so as to make the data intelligible to the reader without reference to the text. A duplicate list of captions for figures should be included as the last page of the manuscript. Use "Fig. 1" (not Figure 1), "Figs. 3 and 4," etc., in both the text and the numbering of illustrations. In the text, "Eq. (1)" or "Eqs. (1) and (2)" is used, not "Equation (1)." In captions, legends, and in table headings, write all words in full; do not abbreviate, except for "Fig." and "Eq."

MATHEMATICAL WORK: Formulas may be typewritten or carefully written in pen and ink, the writing to be large enough so that it can be marked for the printer. Considerable space for marking should be allowed above and below all equations. All complicated equations should be repeated on separate sheets with adequate space left for marking. The solidus should be used for simple fractions appearing within the text. Make all expressions clear to the typesetter. Greek letters used in formulas should be clearly designated by name in the margin of the manuscript. The difference between capital and lower-case letters should be clearly distinguished and care taken to avoid confusion between zero (0) and the letter (o), between the numerical (one) and the letter (ell) and the prime (′), between alpha and a, kappa and k, u and mu, v and nu, n and eta. All subscripts and exponents should be clearly distinguished. Avoid complicated exponents and subscripts. Dots and bars over letters or mathematical expressions should also be avoided. When it is necessary to repeat a complicated expression, it should be represented by some convenient symbol.

SYMBOLS AND ABBREVIATIONS: The symbols recommended in the American Standard Association "Letter Symbols for Aeronautical Sciences," ASA Y10.7—1954, should be used wherever practicable. All symbols should be clearly written and carefully checked. Standard abbreviations should be used, and it should be noted that most abbreviations are lower case.

CORPORATE MEMBERS

OF THE

INSTITUTE OF THE AEROSPACE SCIENCES

AC SPARK PLUG DIVISION, GENERAL MOTORS CORPORATION

ACADEMY OF AERONAUTICS

AEROJET-GENERAL CORPORATION

AERONCA MANUFACTURING CORPORATION

AERONUTRONIC, DIVISION OF FORD MOTOR COMPANY

AGAWAM AIRCRAFT PRODUCTS, INC.

ALLIED RESEARCH ASSOCIATES, INC.

ALLISON DIVISION, GENERAL MOTORS CORPORATION

ALUMINUM COMPANY OF AMERICA

AMERICAN AIRLINES, INC.

AMERICAN BOSCH ARMA CORPORATION

AMERICAN OIL COMPANY

AMOCO CHEMICALS CORPORATION

AMPHENOL-BORG ELECTRONICS CORPORATION

ARDE ASSOCIATES

ASTRO-ELECTRONIC PRODUCTS DIVISION, RADIO CORPORATION OF AMERICA

AUTOMATION INDUSTRIES, INCORPORATED

AVCO-EVERETT RESEARCH LABORATORY

AVIEN, INC.

BEECH AIRCRAFT CORPORATION

BELL AEROSPACE CORPORATION

THE BENDIX CORPORATION

BOEING AIRPLANE COMPANY

BOOZ, ALLEN APPLIED RESEARCH, INC.

BULOVA RESEARCH AND DEVELOPMENT LABORATORIES, INC.

CANADAIR, LTD.

CHANCE VOUGHT AIRCRAFT, INCORPORATED

THE CHASE MANHATTAN BANK

CHICAGO AERIAL INDUSTRIES, INC.

THE CLEVELAND PNEUMATIC INDUSTRIES, INC.

CLIFFORD MANUFACTURING DIVISION, STANDARD-THOMSON CORPORATION

CONTINENTAL MOTORS CORPORATION

CORNELL AERONAUTICAL LABORATORY, INC

COX & COMPANY, INC.

CURTISS-WRIGHT CORPORATION

DANIEL, MANN, JOHNSON, & MENDENHALL

THE DECKER CORPORATION

DEFENSE ELECTRONIC PRODUCTS DIVISION, RADIO CORPORATION OF AMERICA

DEFENSE SYSTEMS DIVISION, GENERAL MOTORS CORPORATION

DEL MAR ENGINEERING LABORATORIES

DELCO-RADIO DIVISION, GENERAL MOTORS CORPORATION

DELCO-REMY DIVISION, GENERAL MOTORS CORPORATION

DOAK AIRCRAFT COMPANY, INC.

DOUGLAS AIRCRAFT COMPANY, INC.

DZUS FASTENER COMPANY, INC.

EASTERN AIRLINES, INC.

EATON MANUFACTURING COMPANY

EDO CORPORATION

ELASTIC STOP NUT CORPORATION OF AMERICA

ENGINEERING SUPERVISION COMPANY

FAIRCHILD CAMERA AND INSTRUMENT CORPORATION

FAIRCHILD ENGINE AND AIRPLANE CORPORATION

THE GARRETT CORPORATION

GENERAL APPLIED SCIENCE LABORATORIES, INC.

GENERAL DYNAMICS CORPORATION

GENERAL ELECTRIC COMPANY

GENERAL PRECISION, INC.

GIANNINI CONTROLS CORPORATION

THE B. F. GOODRICH COMPANY

GOODYEAR AIRCRAFT CORPORATION

GRUMMAN AIRCRAFT ENGINEERING CORPORATION

HOFFMANN AIRCRAFT COMPANY

HUGHES AIRCRAFT COMPANY

INSURANCE COMPANY OF NORTH AMERICA COMPANIES

INTERNATIONAL BUSINESS MACHINES CORPORATION FEDERAL SYSTEMS DIVISION

THE INTERNATIONAL NICKEL COMPANY, INC.

ITT FEDERAL LABORATORIES, A DIVISION OF INTERNATIONAL TELEPHONE AND TELEGRAPH CORPORATION

JANITROL AIRCRAFT DIVISION, MIDLAND-ROSS CORPORATION

JOHNS-MANVILLE SALES CORPORATION

KOLLSMAN INSTRUMENT CORPORATION

LAVELLE AIRCRAFT CORPORATION

LEAR, INCORPORATED

C. W. LEMMERMAN, INC.

THE LIQUIDOMETER CORPORATION

ARTHUR D. LITTLE, INC.

LOCKHEED AIRCRAFT CORPORATION

THE MARQUARDT CORPORATION

THE MARTIN CORPORATION

McDONNELL AIRCRAFT CORPORATION

MELETRON CORPORATION

MINNEAPOLIS-HONEYWELL REGULATOR COMPANY

MOBIL OIL COMPANY

NATIONAL CREDIT OFFICE, INC.

NORTH AMERICAN AVIATION, INC.

NORTHROP CORPORATION

NUCLEAR DEVELOPMENT CORPORATION OF AMERICA

PAN AMERICAN WORLD AIRWAYS, INC.

THE RALPH M. PARSONS COMPANY

PIASECKI AIRCRAFT CORPORATION

POLY INDUSTRIES, INC.

REPUBLIC AVIATION CORPORATION

ROHR AIRCRAFT CORPORATION

RYAN AERONAUTICAL COMPANY

SANDBERG-SERRELL CORPORATION

SHELL OIL COMPANY

SIMMONDS PRECISION PRODUCTS, INC.

SOLAR AIRCRAFT COMPANY

SOUTHWEST PRODUCTS COMPANY

SPACE TECHNOLOGY LABORATORIES, INC.

R. DIXON SPEAS ASSOCIATES

SPERRY GYROSCOPE COMPANY, DIVISION OF SPERRY RAND CORPORATION

STANLEY AVIATION CORPORATION

THERM, INCORPORATED

THIOKOL CHEMICAL CORPORATION

THOMPSON RAMO WOOLDRIDGE INC.

TRANS WORLD AIRLINES, INC.

UNION CARBIDE METALS COMPANY, DIVISION OF UNION CARBIDE CORPORATION

UNITED AIR LINES, INC.

UNITED AIRCRAFT CORPORATION

UNITED STATES AVIATION UNDERWRITERS, INC.

VEHICLE RESEARCH CORPORATION

VITRO CORPORATION OF AMERICA

WESTERN GEAR CORPORATION

WESTINGHOUSE ELECTRIC CORPORATION

WYMAN-GORDON COMPANY

YOUNG RADIATOR COMPANY